AN INVESTIGATION OF MULTI-SATELLITE STRATOSPHERIC MEASUREMENTS ON TROPOSPHERIC WEATHER PREDICTIONS OVER CONTINENTAL UNITED STATES

by

Min Shao

A Dissertation
Submitted to the
Graduate Faculty
of
George Mason University
in Partial Fulfillment of
The Requirements for the Degree
of
Doctor of Philosophy
Earth System and GeoInformation Sciences

Committee:

_____	Dr. John J. Qu, Dissertation Director
_____	Dr. Michael Summers, Committee Member
_____	Dr. Jianjun Xu, Committee Member
_____	Dr. Donglian Sun, Committee Member
_____	Dr. Anthony Stefanidis, Department Chair
_____	Dr. Donna M. Fox, Associate Dean, Office of Student Affairs & Special Programs, College of Science.
_____	Dr. Peggy Agouris, Dean, College of Science
Date: _____	Spring Semester 2017 George Mason University Fairfax, VA

An Investigation of Multi-Satellite Stratospheric Measurements on Tropospheric Weather Predictions over Continental United States

A Dissertation submitted in partial fulfillment of the requirements for the degree of Doctor of Philosophy at George Mason University

by

Min Shao
Master of Environmental Science
Nanjing University, 2013

Director: John J. Qu, Professor
Department of Geography and GeoInformation Science, College of Science

Spring Semester 2017
George Mason University
Fairfax, VA

DEDICATION

This is dedicated to my wonderful grandfather Kaiquan Shao with gratitude and love.

ACKNOWLEDGEMENTS

This work would have been impossible without the great support from a number of people.

First and foremost, I would like to thank my advisor, Dr. John J. Qu, for his guidance, support and endless patience. He always encourages me to explore my research ideas, providing thorough instructions and insightful advices. It is him who led me into this spectacular field of remote sensing. Without him, I would not have gone this far.

I would also like to send my special thanks to Dr. Michael E. Summers, one of my committee members, who enlightens me on the field of atmospheric physics and gives me insightful suggestions on the troposphere-stratospheric coupling. I am so happy to have him as one of my committee members as he always lovely to share the beauties from Pluto with me.

My great thanks go particular to Dr. Jianjun Xu. We share a lot of time discussing about research ideas, publications, etc. It is him that brought me into the field of data assimilation and weather modeling. And it is also him who teaches me to live happily. He uses his precious time to give valuable advice and critical comments on my publications. I extend my thanks to Dr. Donglian Sun, another committee member, for her endless patience helping me research into the unknown. I also would like to convey special thanks to Dr. Ruixing Yang, Dr. Eugenia Kalnay, Dr. Arie Croitoru and Dr. Xianjun Hao who encouraged me a lot when I started my career in this field and helped me so many times with endless patience.

Warm thanks go to all the team members in the Global Environment and Natural Resources Institute (GENRI), Environmental Science and Technology Center (ESTC) and EastFIRE Lab: Drs. Rui Zhang, Taeyoung Choi, Laurel Gutenberg, Di Wu, Chenyang Xu, Adel Al-Shomrany. They have been great colleagues and friends. Especially thanks to Min Sun, despite she is in China, she helped me a lot on my way to the academic life. I also would like to thank my wonderful roommates Han Qin, and Di Wu for their support and friendship. Also, I thank my friends in both China and the United States, for their understanding, encouragement and all the sweet memories we had in the past years. I can’t live without your friendships.

My family deserves special mention for their inseparable support. Special thanks go to my dearest grandfather Kaiquan Shao for his enlightenment on my life. I taste the sweet and sorrow as I read his books, and make deeper understandings of this world. Also, many thanks to my parents Bai Shao and Hongmei Wang for their unconditional love, encouragement, and understandings. They sincerely raise me and heal me with great love. If not for them, I couldn't live so far. I also would like to thank my cousin sister Ting Yao, who also gave me lots of help.

TABLE OF CONTENTS

LIST OF TABLES

LIST OF FIGURES

LIST OF EQUATIONS

LIST OF ABBREVIATIONS AND SYMBOLS

Advanced Microwave Sounding Unit-A ..... AMSU-A
Advanced Technology Microwave Sounder ..... ATMS
Advanced Research Weather Research and Forecasting system ..... WRF-ARW
Air Force Weather Agency ..... AFWA
Advanced Microwave Sounding Unit-A ..... AMSU-A
Analysis error covariance ..... $\boldsymbol{P}_a$
Atmospheric Infrared Sounder ..... AIRS
Background Field ..... $\boldsymbol{x}_b$
Background error covariance ..... $\boldsymbol{B}$
Boundary Condition ..... BC
Brewer-Dobson Circulation ..... BDC
Binary Universal Form for the Representation of meteorological data ..... BUFR
Community Radiative Transfer Model ..... CRTM
Community Gridpoint Statistical Interpolation system ..... GSI
Correlation Coefficient CC
Cross-track Infrared Sounder ..... CrIS
Data Assimilation ..... DA
Defense Meteorological Satellite Program ..... DMSP
Developmental Testbed Center ..... DTC
El Niño and Southern Oscillation ..... ENSO
Ensemble Kalman Filter ..... EnKF
Environmental Modeling Center ..... EMC
European Center for Medium range Weather Forecasting ..... ECMWF
Extended Kalman Filter ..... EKF
Ferrel Cell ..... FC
Forecast Sensitive to Observations ..... FSO
Forward Observational Operator ..... H
Four-Dimensional Variational assimilation 4D-Var
General Circulation Models ..... GCM
Geostationary Operational Environmental Satellite ..... GOES
Global Forecast System ..... GFS
Global Land Data Assimilation System ..... GLDAS
Global Modeling and Assimilation Office ..... GMAO
Global Positioning System ..... GPS
Greenhouse Gases ..... GHG
Hadley Cell ..... HC

High Resolution Infrared Sounder ..... HIRS
Infrared Atmospheric Sounding Interferometer ..... IASI
Initial Condition IC
Japanese Meteorological Agency Global Spectral Model ..... JMAGSM
Joint Center for Satellite Data Assimilation ..... JCSDA
Kalman Filter ..... KF
Kalman Gain Matrix ..... $\boldsymbol{K}$
Meteorological Operational ..... MetOp
Microwave Humidity Sounder ..... MHS
Model error covariance ..... $\boldsymbol{Q}$
Moderate Resolution Imaging Spectroradiometer ..... MODIS
National Aeronautics and Space Administration ..... NASA
National Center for Atmospheric Research ..... NCAR
National Meteorological Center ..... NMC
National Oceanic and Atmospheric Administration ..... NOAA
Northern Annular Mode ..... NAM
Numerical Weather Prediction ..... NWP
North Hemisphere ..... NH
Observations ..... $\boldsymbol{y}_o$
Observation error covariance ..... $\boldsymbol{R}$
Observing System Experiments ..... OSE
Optimal Interpolation ..... OI
Optimum analysis of a field ..... $\boldsymbol{x}_a$
Partial Differential Equations ..... PDEs
Particle Matters ..... PM
Polar Cell ..... PC
Polar Front Jet ..... PFJ
Polar Night Jet ..... PNJ
Quality Control ..... QC
Relative Humidity ..... RH
Relative Operating Characteristics ..... ROC
Root Mean Square ..... RMS
Root Mean Square Deviation ..... RMSD
Sub-tropical Jet ..... SJ
South Hemisphere ..... SH
Spatial Correlation Coefficient ..... SCC
Special Sensor Microwave Imager/Sounder ..... SSMI/S
Spectral Statistical Interpolation ..... SSI
Suomi National Polar-Orbiting Partnership ..... Suomi-NPP
Sudden Stratospheric Warming ..... SSW
Three-Dimensional Variational assimilation 3D-Var
Tropical Convection ..... TC
Ultra Violet ..... UV
United States ..... U. S.

U. S. Geological Survey..... USGS
Weight..... $\boldsymbol{W}$
WRF Preprocessing System..... WPS

ABSTRACT

AN INVESTIGATION OF MULTI-SATELLITE STRATOSPHERIC MEASUREMENTS ON TROPOSPHERIC WEATHER PREDICTIONS OVER CONTINENTAL UNITED STATES

Min Shao, Ph.D.

George Mason University, 2017

Dissertation Director: Dr. John J. Qu

The troposphere and stratosphere are the two closest atmospheric layers to the Earth's surface. These two layers are separated by the so-called tropopause. On one hand, these two layers are largely distinguished, on the other hand, lots of evidences proved that connections are also existed between these two layers via various dynamical and chemical feedbacks. Both tropospheric and stratospheric waves can propagate through the tropopause and affect the down streams, despite the fact that this propagation of waves is relatively weaker than the internal interactions in both atmospheric layers. Major improvements have been made in numerical weather predictions (NWP) via data assimilation (DA) in the past 30 years. From optimal interpolation to variational methods and Kalman Filter, great improvements are also made in the development of DA technology. The availability of assimilating satellite radiance observation and the

increasing amount of satellite measurements enabled the generation of better atmospheric initials for both global and regional NWP systems.

The selection of DA schemes is critical for regional NWP systems. The performance of three major data assimilation (3D-Var, Hybrid, and EnKF) schemes on regional weather forecasts over the continental United States during winter and summer is investigated. Convergence rate in the variational methods can be slightly accelerated especially in summer by the inclusion of ensembles. When the regional model lid is set at 50-mb, larger improvements (10~20%) in the initials are obtained over the tropopause and lower troposphere. Better forecast skills (~10%) are obtained in all three DA schemes in summer. Among these three DA schemes, slightly better (~1%) forecast skills are obtained in Hybrid configuration than 3D-Var. Overall better forecast skills are obtained in summer via EnKF scheme. An extra 22% skill in predicting summer surface pressure but 10% less skills in winter are given by EnKF when compared to 3D-Var. The different forecast skills obtained between variational methods and EnKF are mainly due to the opposite incremental features over ocean and mountainous regions and the inclusion of ensembles. Diurnal variations are observed in predictions. Variations in temperature and humidity are mainly produced by the one-time assimilation in a day and the variations in wind predictions are mainly come from model systematic errors.

The assimilation of microwave and infrared satellite measurements alone is compared. Compared to microwave measurements, less than 1% extra performance skill is obtained over the tropopause when infrared measurements are assimilated alone. Large differences are observed in winter analysis when Hybrid scheme is applied. Compared to infrared

measurements, an averaged extra 5% performance skill is obtained when microwave measurements are assimilated alone. Predictions made by microwave configuration (MW) shows an extra 3% forecast skill than infrared configuration (IR) at early forecasts. Major differences between MW and IR are located over the tropopause and lower troposphere. Extra 3% and 15% forecast skills for the tropopause wind and temperature are obtained by assimilating microwave measurements alone, respectively. Infrared measurements show slightly better forecast skills at lower troposphere at later forecast lead times.

The impacts of the extended stratospheric layers by raising regional model lid from 50-mb to 10-mb and then to 1-mb and the assimilated stratospheric satellite measurements on tropospheric weather predictions are explored in the last section. An extra 10% performance skill over the initial tropopause is obtained by extending the model top to 1-mb. Significant improvements (15~50%) in initials are obtained over tropopause and lower troposphere by assimilating stratospheric measurements. In the predictions, the stratospheric information can propagate through the tropopause layers and affect the lower troposphere after 2-3 days' propagation. The major improvements made by the extended stratospheric layers and measurements are located in the tropopause. An averaged extra 5% forecast skill is obtained by raising the model lid from 10-mb to 1-mb. An extra 7% forecast skill is obtained in the tropospheric humidity by assimilating stratospheric measurements.

Significant improvements in the tropopause and tropospheric predictions are observed when multi-satellite stratospheric measurements extended to 1-mb are assimilated in

regional NWP system. Major positive impacts on the tropospheric weather predictions are observed in the first 72-h forecast lead times due to the downward propagation of the microwave stratospheric measurements. A two-season comparison study shows that the assimilation of microwave stratospheric measurements extended to 1-mb will lead to an adjusted stratospheric temperature distribution which may related to an adjusted BDC. Small impacts on the tropospheric general circulations are also found. The tropospheric forecast skills are slightly improved in response to the stratospheric initial conditions and adjusted tropospheric general circulations. For the prediction of heavy precipitation events, an extra 14% forecast skill is obtained when the microwave stratospheric measurements extend to 1-mb are assimilated. The results obtained in this thesis indicate that the assimilation of satellite microwave measurements has the advantages for short-term regional weather forecast using ensemble related data assimilation scheme. Also, this thesis proposed that the assimilation of microwave stratospheric measurements extended to 1-mb can slightly improve the tropospheric weather forecast skills as a result of the tropospheric general circulations responded to the adjusted stratospheric initials.

CHAPTER ONE INTRODUCTION

Downward propagation of stratospheric waves is relatively weaker the internal interactions in the troposphere. However, perturbations existed in both troposphere and stratosphere can strongly affect the circulations in both atmospheric layers (Garcia, and Randel, 2008; Calvo, et al., 2010; Kolstad, et al., 2010). The propagation of stratospheric perturbations may have significant impacts on the tropospheric weather forecasts.

In the fact that most of the major weather phenomena are occurred in the troposphere, weather forecasts are mainly based on tropospheric atmospheric states. In this study, the impacts of the stratospheric information on the tropospheric weather forecasts are investigated by assimilating remote sensed stratospheric observations.

1.1 Brief Introduction of Numerical Weather Prediction

For a considerable period of time, weather forecasting is mainly relied on the subjective intuition of weather forecasters until the illumination of numerical weather prediction (NWP) systems in 1950s (Bergovind and Döös, 1955; John, and Peter, 2006, Chapter 7). Different from other fields of natural sciences, controlled experiments are hard to perform in meteorology. As a result, numerical experimentation becomes more and more important. NWP systems view the weather as a dynamical system which is strongly related to physics, fluid dynamics, and meteorology and governed by a set of hydrodynamic partial differential equations (PDEs) which governs the motions of atmosphere. Multiple range of weather forecast products are carried out by national

meteorological centers all over the world using state-of-the-art supercomputers. As the dramatic development of computing power, the magnitude of modern NWP system has reached ~10^9 dimensional space with over 60 vertical layers and as fine as 12 km horizontal grid resolution (e.g., the Global Forecast System (GFS) initially developed by J. Sela (1980, 1982)). Some of the world leading NWP centers are operationally providing global products with considerable quality to give a better description of the atmospheric dynamics and even atmosphere chemistry. These products such as GFS atmospheric predictions, European Center for Medium-Range Weather Forecasts (ECMWF) products (Gibson, 1997; Gregory, et al., 2000), Japanese Meteorological Agency Global Spectral Model (JMAGSM) (Saito, et al., 2006; Rajendran, et al., 2007), etc. again can be downscaled to regional applications as initial conditions (IC) and boundary conditions (BC) with even higher temporal (~1 hour) and spatial (~3 km) resolutions (Schwartz, et al., 2009) for a better understanding of the regional coupling impacts between atmosphere, chemistry, topography, etc.

1.2 Data Assimilation in Numerical Weather Prediction

As the developing of atmospheric physics, fluid dynamics, the use of governing equations with fewer and fewer approximations and significant improvements in parameterization application for some physics processes (e.g., cumulative physics, (Wootten, et al., 2016)), the NWP is becoming more and more accurate and also harder to make any further progresses. Hence, the accuracy of initial conditions became increasingly important. In another word, how could we get the right results if the inputs are wrong? The demand for the generation of initial conditions with better qualities has developed to a new branch of data analysis science: Data Assimilation. The development

of DA experienced the steps of simple spatial polynomial interpolation of observations, then to more sophisticated statistical methods namely variational methods and Kalman Filter (KF), etc. (Anderson, et al., 1998; Courtier, et al., 1998; Houtekamer P. L., and H. L. Mitchell, 1998; Rabier, et al., 1998; Klinker, et al., 2000; Mahfouf, et al., 2000; Rabier, et al., 2000; Anderson, 2001). Researchers also found that the information assimilated in the upstream regions can propagate down toward the downstream regions (Bergthorsson and Döös, 1955). Associated with the techniques of data thinning, nudging (Storch, et al., 2000), etc., the problem of non-uniformly geographic distributed observations (e.g., there are relatively dense observations over the densely-populated regions such as North America while fewer or non-existent at all over less-populated regions such as oceans, mountainous regions, polar regions, etc.) can be adjusted. The objective analysis produced by the data assimilation process greatly helped the forecasters to notify the detailed information within a limited region. With the steady increase of computing power, today's operational NWP system can assimilate ~10^6 observations four times per day in order to lead to an optimal analysis of the atmospheric state. The rapid growth of numerous observations especially the radiance/brightness temperature remote sensed from satellite instruments has driven the question of how to effectively assimilate new types of observations. The involve of the technology of innovation (as Kalman gain in Kalman Filter) (Migliorini, et al., 2008) calculations which lead to the direct assimilation of satellite radiances rather than indirect assimilation (direct and indirect assimilation will be introduced in section 4) of the retrievals (which

brings more uncertainties into the systems) have significantly improved the NWP forecasts.

Dramatic improvements have been made in NWP forecasts since the use of the advancements described above. Figure 1 from the ECMWF center showed the improvements of 500 hPa geopotential height anomaly correlation coefficients when using data assimilation in global NWP forecast. The blue, red, greed, and yellow represent the forecast lead times of 3, 5, 7, and 10 days, respectively. The thick lines represent the northern hemisphere (NH) score, and the thin lines represent the southern hemisphere (SH). Larger improvements are made over the southern hemisphere (SH) with 2011 7-day forecast reaching the skill of 1980 3-day forecast. For the northern hemisphere (NH), significant improvements are also made such as 2011 5-day forecast can reach the skill of 1980 3-day forecast, and the 10-day forecast can reach the level of 0.4. The improvements of forecast skills in southern hemisphere relative to the northern hemisphere (Fig. 1) is believed to be attributed to the large contributions of satellite observations over the southern hemisphere rather than conventional observations – for the truth that there are fewer conventional observations over the southern hemisphere (Simmons and Hollingsworth, 2002; Rabier, 2005). An overview of the DA algorithms will be described in chapter 2.

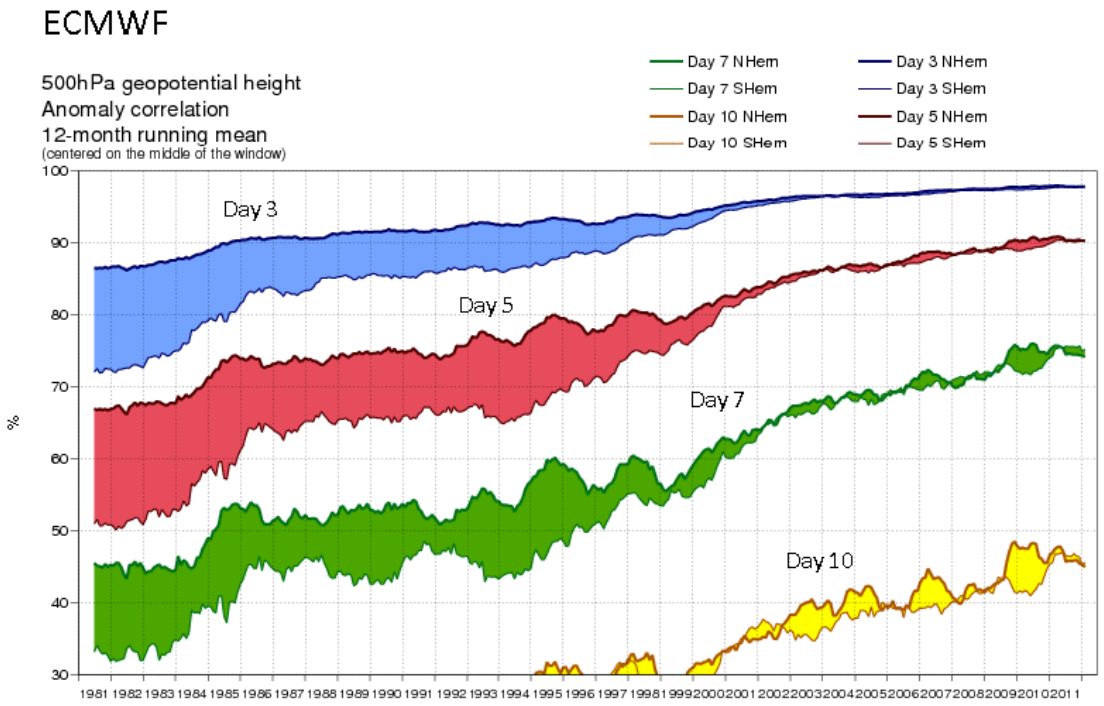

Figure 1 Improvements made at the 500 hPa geopotential height by assimilating satellite measurements starting from 1980s in global NWP forecast in the ECMWF center. (Collard et al., 2011).

1.3 Regional Weather Predictability

As defined by Delsole (2004), the predictability is the study of the extent to which events can be predicted. A so-called saturation value is defined as the mean square error increases with lead time and asymptotically approaches a finite value. When the errors are comparable to the saturation value, it is said that all the predictability is lost. The lack of atmospheric predictability is mainly due to the non-linear amplification (Garcia-Moya, et al., 2011). Also, a system becomes unpredictable when the climatological and forecast distributions are identical in every way. The degree of predictability depends on the degree to which the prior and posterior distributions differ. In modern NWP systems, the predictability is a problem of two dominant source of errors in the initial and boundary

conditions, which these uncertainties may amplify and spoil the forecast at a given lead time (Collins, and Allen, 2002).

Many measurements have been developed to measure the predictability of weather forecasts. The most utilized measure of predictability is the mean square error or the root-mean square deviation (RMSD) of a forecast model. Other measurements such as relative operating characteristics (ROC) (Kharin, and Zwiers, 2003), Brier skill score and ranked probability skill score (Andreas, et al., 2007) also can give out the quantized values representing the predictability of weather forecasts. Delsole (2004 & 2005) discussed the usage of some of the popular measurements and pointed out the connections between these metrics.

Data assimilation has significant impacts on the predictability of weather forecasts due to its contribution to the smaller errors in the initial and boundary conditions. Gelaro et al. (2000) showed that by assimilating geostationary satellite winds, the 48-h forecast skill in a downstream area can be improved due to the large positive impacts on the reduction of analysis errors. Hu et al. (2007) investigated that the assimilation of radar observations can improve the predictability of thunderstorms. And some recent researches showed that by using ensemble forecasting or involving in ensembles via data assimilation, the predictability can be improved due to a probabilistic representation of the atmospheric forecasts (Garcia-Moya, et al., 2011; Reinecke, and Durran, 2009).

1.4 Distinct and Coupled Stratosphere and Troposphere

One of the satellite observation advantages is the better representing of atmospheric profiles exceeding into high altitudes. This means the use of satellite

observations involves the connections between different atmospheric layers. Here we first introduce the differences and connections between the troposphere and stratosphere.

1.4.1 The Distinctions between Stratosphere and Troposphere

As we know that the troposphere and the stratosphere are the two closest atmospheric layers to the Earth's surface. Until the found of the so-called tropopause by Léon Teisserenc de Bort and Richard Assmann in 1902 (Hoinka, 1997), the stratosphere is departed from the troposphere. These two layers are greatly distinguished by their thermal dynamics, chemistry compositions, and aerodynamics characteristics. For the differences of thermal dynamics, troposphere is usually known with a negative lapse rate (decrease of temperature with height) while stratosphere is known with a positive lapse rate (increase of temperature with height) mainly due to the strong absorption of the Ultra Violet (UV) bands of radiation by stratospheric ozone layer (Stocker, et al., 2001; Liao, 2002). Due to the decreasing of temperature structure in troposphere, the large potential for atmospheric instability associated with convection lead to the happening of most of the synoptic phenomena or as known as weather systems (e.g., front systems, storms, hurricanes/typhoons). Because of the totally inverse temperature lapse rate, the stratosphere is thermally stable with significantly stronger horizontal motion than the vertical motion.

Also, the troposphere and stratosphere are significantly difference in chemical composition mainly due to the gravity of the Earth (John, and Peter, 2006). Over 80% of the total air mass constructed the troposphere layer including the most important chemical species for us human beings. It is worth noting that almost all the greenhouse

gases (GHG) which contributed a lot to the global climate effect (e.g., carbon dioxide, water vapor, methane, etc.) have much higher concentration in the troposphere than that in the stratosphere except ozone which is primarily generated by the photochemical processes in the stratosphere (Chapman, 1930).

On the aerodynamic aspect, different atmospheric circulations are the main reason for the distinguishing of the troposphere and the stratosphere. Atmospheric waves which spread on a broad range of scales play the main rolls in influencing the atmospheric circulations via the wave-mean flow interaction (Andrews, et al., 1987). Researches showed that most of the waves including the planetary waves resulted by the large scale topography and land-sea contrast, the gravity waves due to orographic perturbations, and the synoptic waves caused by regional baroclinic instability are generated in the lower troposphere because of the relatively unstable conditions in the troposphere favors the propagation of the waves throughout the vertical column at most scales (Dickinson, 1968; Sato, and Nomoto, 2015). While in the stratosphere, most of the waves are suppressed by the generally stable conditions and only some of the synoptic waves are active in the lowermost stratosphere (Justus, and Woodrum, 1973).

1.4.2 The Connections between Stratosphere and Troposphere

In addition to the differences between the troposphere and stratosphere, these two layers are also coupled through various dynamic and chemical interactions with increasing evidence even though this kind of coupling is much weaker than the inner actions among these two layers (Stohl, et al., 2003; Black, et al., 2006; Grise, et al., 2009). The connection between these two layers are mainly controlled by the dynamic propagating of waves which across the tropopause into another layer, or the overshoots

pumping of momentum and energy from the troposphere into the stratosphere via diabatic processes (Matsuno, 1971; Xu, and Powell, 2015). The major atmospheric circulations and jet streams in the troposphere and lower stratosphere are concluded in Fig. 2 (Yang, 2015). These meridional circulations and jet streams are strongly related to those major climate variabilities (e.g., volcanic eruption caused global cooling, etc.) and large scale synoptic events due to the significant transport of air mass and chemical components between different latitudes and longitudes. The primary circles in troposphere are the Hadley Cell (HC) in the lower latitudes, the Ferrel Cell (FC) in the mid-latitudes, and the Polar Cell (PC) in the high latitudes which are formed due to the unbalance of the radiation absorption in different latitudes and the Coriolis effect (John, and Peter, 2006). The subtropical jet (SJ) and the polar front jet (PFJ) are formed at the poleward edge of the Hadley Cell and roughly at the boundary between the Ferrel Cell and the Polar Cell, respectively. These two tropospheric jets (TJ) merge at some locations and times, while at other times they are well separated (Reiter, and Whitney, 1969). In the stratosphere, the major circulation is the Brewer-Dobson circulation (BDC) discovered by Brewer (1949) and Dobson (1956). At the lowermost stratosphere, the BDC is observed as hemispherically one cell with upwelling in tropics related to the tropical convections (TC) and downwelling in mid/high altitudes as showed in Fig. 2. While in the upper stratosphere, the BDC is usually observed as one cell over the globe with slightly upwelling towards the summer hemisphere and downwelling in the extratropical winter hemisphere. These circulations in both troposphere and stratosphere are influencing each other through different scales of perturbations (Cohen, et al., 2014).

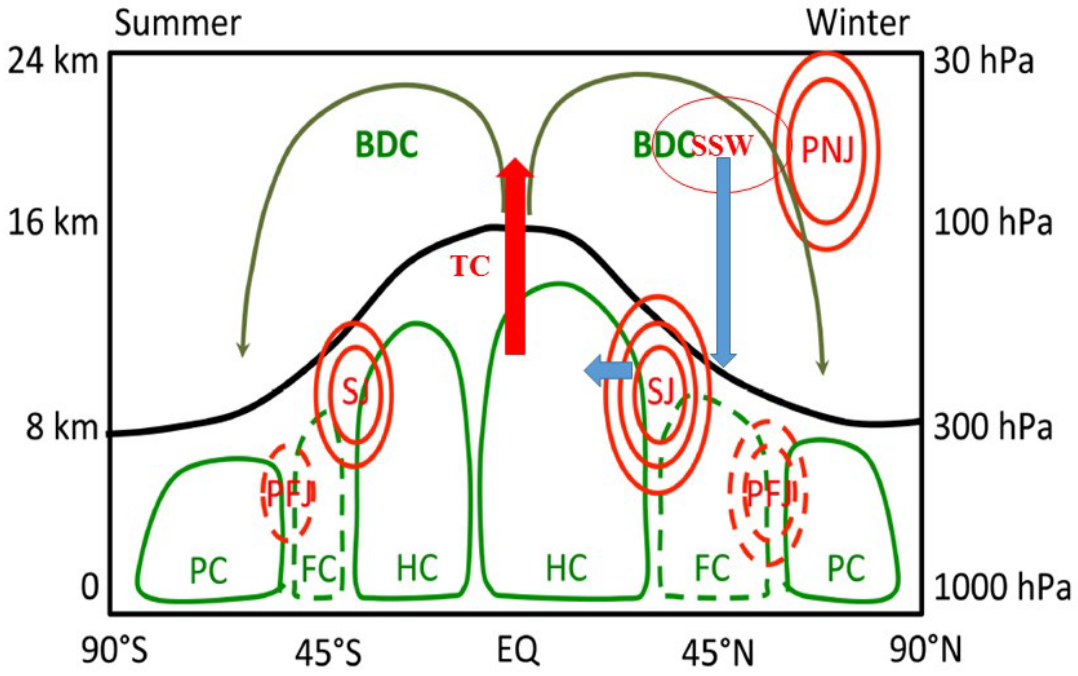

Figure 2 General atmospheric circulations, jet streams, and synoptic phenomena in troposphere and lower stratosphere during North Hemisphere winter. (Yang, 2015).

Firstly, as most of the waves are generated in the troposphere and some of them can propagate into the stratosphere, the stratosphere circulations are strongly influenced by the perturbations originated within these tropospheric waves. As Haynes, et al. (1991) investigated that a “downward control” principle can express the critical part of the dynamical transportations of ozone and water vapor between troposphere and stratosphere, and the extratropical pump of planetary eddies in tropospheric baroclinic zones (Holton et al. 1995) and the tropical pump of planetary and gravity eddies associated with tropospheric deep convection (Norton, 2006) are the main factors for the

driven of stratospheric BDC. And recently, the discovery of the acceleration of BDC caused by the anomalies resulted from large-scale climate events such as GHGs related Global warming, and the El Niño and Southern Oscillation (ENSO) highlighted the impacts from troposphere on stratosphere circulations (Garcia, and Randel, 2008; Calvo, et al., 2010). Also, Sjoberg and Birner (2012) found that the sudden stratospheric warming (SSW) events are normally generated by strong heat flux anomalies in the troposphere, and this SSW information also has impacts on later tropospheric weather predictions (Hamilton, 1993; Charlton, et al., 2004).

Similarly, stratospheric perturbations also have significant impacts on some tropospheric events. The stratospheric perturbations are usually connected with the Northern Annular Mode (NAM) such as sudden stratospheric warming can interact with the tropospheric circulation by weakening the NAM which leads to the deceleration and equator shifts of the tropospheric jets (Lee, and Feldstein, 2013), and weak polar vortex in the stratosphere also can interact with the NAM and the Northern Atlantic Oscillation (NAO) in the troposphere which can lead to extremely cold winters (Kolstad, et al., 2010).

1.4.3 Assimilation of the Stratospheric Observations

The troposphere and stratosphere are highly isolated from each other with a so-called tropopause between these two layers while at the same time these two layers are also connected with a lot of interactions happening between them such as some of the planetary waves can propagate through the tropopause into the other layer. As the valuable information obtained in the stratosphere and the impact on the weather forecasts, and because of the abundance satellite observations in the early 2000s, most of the NWP

models have raised their model lids for a better assimilation of the stratospheric radiance/brightness temperature and ozone data sets (Swinbank, and O'Neill, 1994).

In the 1990s, some meteorological centers began to assimilate the stratospheric constituents. Strong attentions have been paid to the assimilation of ozone in order to develop the ozone and UV-forecasting capabilities, to monitor stratospheric ozone to track the evolution of the stratospheric composition, and to improve the skills of stratospheric and tropospheric forecasts by a better representation of stratospheric temperature and winds (Kalnay, 2003; Lahoz, et al., 2007).

The stratosphere meteorological data is also assimilated by some meteorological centers. It has been evaluated that the assimilation of stratospheric information has a positive impact on the tropospheric weather forecasts by generating a better initial condition including valuable stratospheric information. In 1990, beside the beginning of assimilation of stratospheric constituents, Boville and Baumhefner found that both Root Mean Square (RMS) and systematic errors can develop rapidly in the lower stratosphere with some propagation into the troposphere for mid-range forecasts (10-30 days) while the errors will be relatively small during the first 10 days using the general circulation models (GCM) with both 15 vertical levels below and above 10-mb (Boville, and Baumhefner, 1990), and when the model is set up with a lower upper boundary, the error growth in the troposphere is slightly greater than the model with higher lids.

1.5 Satellite Measurements

With the rapid development of technology, a group of satellites including polar satellites and geostationary satellites are observing the entire globe continuously. Remote

sensing technology is now capable of observing land surface parameters, such as surface reflectance, soil moisture, as well as estimating atmospheric products such as wind, precipitable water, etc. (Smith, et al., 2015).

In the latest NWP systems, most of the observations used for global data assimilation are remote sensed via satellite sensors (Thépaut, 2003; Migliorini, et al., 2008). With the help of over 35 geostationary and polar satellites including the newly launched Suomi National Polar-Orbiting Partnership (Suomi-NPP) carrying Advanced Technology Microwave Sounder (ATMS) and Cross-track Infrared Sounder (CrIS), NWP centers can continuously receive key Earth system parameters for a better generation of forecasting products. (Smith, et al., 2015). As shown in Fig. 1.1, the dramatic improvements have been made in the global NWP system with the help of satellite data assimilation especially over the southern hemisphere. Also, some researches showed that satellite radiance data assimilation has the potential advantages in improving the forecast of weather systems in regional models (Wan, et al., 2009; Xu, et al., 2009; Wan, and Xu, 2011; Xu, and Powell, 2012; Bao, et al., 2015).

1.6 Objectives and Outlines

As shown in Fig. 3, we will achieve three objectives by rising the model lid step-by-step to 1-mb with the help of data assimilation. The first goal of this study is to evaluate the performance of three major DA schemes namely the 3D-Var, Hybrid, and EnKF on regional weather forecast system. To reach this goal, we perform DA experiments on a U. S. continental domain configuration with a general model lid at 50-

mb during both winter and summer. The statistics results will be analyzed to evaluate the predictabilities of these three major DA schemes.

The second goal is to investigate the impacts of infrared and microwave satellite measurements on regional NWP system when assimilated alone. The satellite instruments will be classified into infrared and microwave classes and then be brought into the weather forecast system separately via DA system. The model lid firstly be raised here from 50-mb to 10-mb to include more satellite stratospheric observations.

The third goal, also the major goal of this study is to elucidate the quantified impacts of assimilated microwave stratospheric measurements on regional NWP systems. To reach this goal, part of the results from the first two goals will be involved here. The regional model lid is raised again from 10-mb to 1-mb. The microwave satellite channels are classified into stratospheric and tropospheric channels. The results are brought out via a comparison of the stratospheric channels and tropospheric channels when assimilated alone.

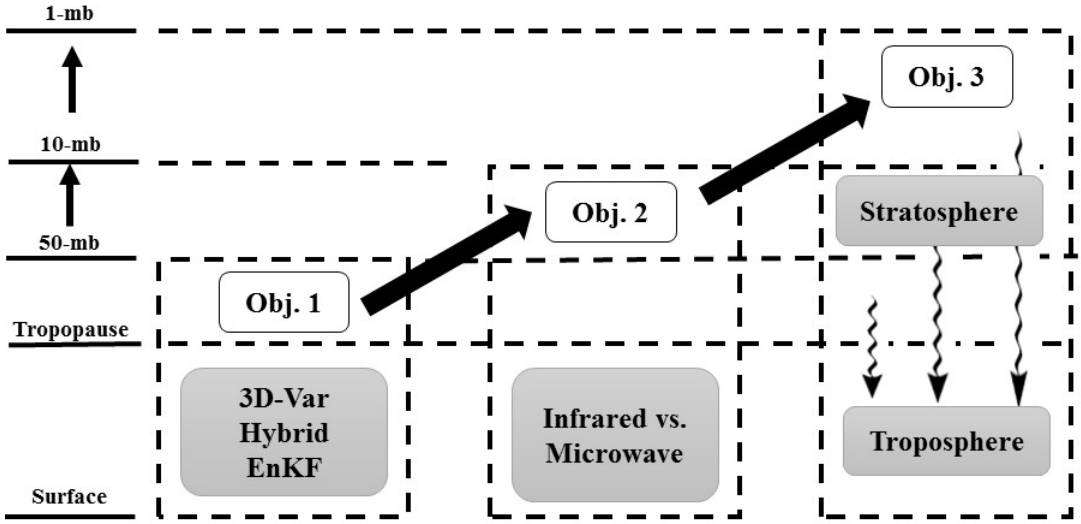

Figure 3 Flow chart of this thesis.

Chapter 2 reviews the development of some major data assimilation algorithms, satellite observations, and the assimilation of satellite radiance/brightness temperature in NWP system. Chapter 3 introduces the regional weather model, the data assimilation system, data and experimental set-up. Then the main subject of this thesis, to investigate the impacts of extra stratospheric microwave satellite observations on regional NWP system, is described in Chapter 4 to 6. Chapter 4 examines the performance of applying different DA algorithms on regional short-range weather forecasts in two seasons (winter and summer), and a selection of DA algorithms on specified conditions will be summarized in the end of Chapter 4. In Chapter 5, the model lid will be first raised from 50-mb to 10-mb, and the performance of infrared and microwave observations when assimilated alone will be examined. In chapter 6, the model lid will be raised again to 1-mb and the impacts of extra stratospheric information on regional NWP system will investigated. Extra experiments involving a selection of tropospheric and stratospheric

microwave channels will be taken out to investigate the impacts of extra stratospheric microwave information on tropospheric weather forecasts. At last, a diagnostic method called forecast sensitive to observations (FSO) technique is applied on the regional scale aiming at bringing out an optimal selection of microwave channels. A conclusion of the major findings of this thesis is given in Chapter 7.

CHAPTER TWO LITERATURE REVIEW OF DATA ASSIMILATION AND SATELLITE OBSERVATIONS

Data assimilation technology has been developed for years since its large contributions to NWP systems. In this chapter, some major DA algorithms are firstly reviewed. The theoretically advantages and disadvantages of each DA algorithm are compared. A set of satellite observations and the assimilation of these satellite observations are also reviewed in this chapter.

2.1 Review of the Data Assimilation Algorithms

With the less approximations and more sophisticated physical and dynamical processes, and the dramatic increased computational resources, NWP systems became more and more accurate and now is usually described as an initial value problem (Epstein, 1968; Berri, and Paegle, 1990; Badger, and Hoskns, 2001): do bad initial conditions lead to good forecasts? The answer is absolute no, the accuracy of the forecast is largely dependent on the quality of the initial atmospheric state because the forecast is produced by propagating forwards the estimated state of the atmosphere using physical and dynamical equations. So, a new branch of atmospheric science was born in the 1950s – Data Assimilation. DA can be described as the science of combining geo-physically measured observations and prior information to produce a statistically optimal estimate of the true state. The DA methods started from simple interpolation, to Optimal Interpolation (OI), then to more comprehensive Variational Data Assimilation, and

Kalman Filter, and now the involve of ensembles enabled the inclusion of flow-dependent information. In this section, we will review the optimal interpolation, some variational data assimilation algorithms, and Kalman Filter and Ensemble Kalman Filter.

2.1.1 Optimal Interpolation

The Optimal Interpolation (OI) equations are original developed by Eliassen (1954), and Gandin (1963) derived the multivariate OI equations and applied them to objective analysis in the former Soviet Union. It can be shown later that the three-dimensional variational is equivalent to the OI problem, except that the method to solve the problem is quite different and advantageous for operational systems.

Consider the complete NWP problem of finding an optimum analysis of a field of model variables $\boldsymbol{x}_a$ by giving a background field variable $\boldsymbol{x}_b$ at grid points and a set of p observations $\boldsymbol{y}_o$ available at irregularly spaced points $\boldsymbol{r}_i$ in which $\boldsymbol{x}_a$ and $\boldsymbol{x}_b$ are vectors of length n, the product of number of points times the number of variables, and the observational field $\boldsymbol{y}_o$ is a vector of p, the number of observations. The unknown analysis and the known background can be both 2-dimensional fields of a single variable and 3-dimensional fields of the initial conditions of all the model prognostic variables. And the observations $\boldsymbol{y}_o$ is different from the model variable by:

1) Being located at different points, and
2) By possibly being indirect measures of the model variables, such as radar reflectivity and Doppler radar radial velocity, satellite radiances, and Global Positioning System (GPS) atmospheric refractivity.

Then the OI equation (Eq. 1) is described as the background plus the innovation weighted by optimal weights which are determined to minimize the analysis error variance:

Equation 1 OI algorithm

$$\boldsymbol{x}_a = \boldsymbol{x}_b + \boldsymbol{W}\left(\boldsymbol{y_0} - H(x_{\boldsymbol{b}})\right) = \boldsymbol{x}_b + \boldsymbol{W}\boldsymbol{d}$$

The weights $\boldsymbol{W}$ are given by a matrix of dimension $(n \times p)$. H is the forward observational operator which can be nonlinear, converts the background field which is the model space into the observed first guesses which can be understood as the measurement space. The vector $\boldsymbol{d}$ with length p, is called the "innovation" or "observational increments" vector which is defined as the differences between the observation and the background mapped to the observational point via forward operator H. It is worth noting that in Kalman Filter process, the weight matrix $\boldsymbol{W}$ is also called the gain matrix $\boldsymbol{K}$, and the innovation is also called the Kalman gain matrix.

In this approach, the background errors (Eq. 2), analysis errors (Eq. 3) and observational errors (Eq. 4) can be defined as follows:

Equation 2 Background errors

$$\varepsilon_b(x, y) = \boldsymbol{x}_b(x, y) - \boldsymbol{x}_t(x, y)$$

Equation 3 Analysis errors

$$\varepsilon_a(x, y) = \boldsymbol{x}_a(x, y) - \boldsymbol{x}_t(x, y)$$

Equation 4 Observational errors

$$\varepsilon_{oi} = \boldsymbol{y}_o(\boldsymbol{r}_i) - \boldsymbol{y}_t(\boldsymbol{r}_i) = \boldsymbol{y}_o(\boldsymbol{r}_i) - H(\boldsymbol{x}_t)$$

As the truth is remained unknown, and thus we can't get the background errors, analysis errors, and observational errors directly but through a number of assumptions about their statistical properties:

1) The background and observations are assumed to be unbiased,
2) The background is a good approximation of the truth, so the analysis and the observations are equal to the background values plus small increments,
3) The background error covariance $\boldsymbol{B}$ (a matrix of size n × n) and the observation error covariance $\boldsymbol{R}$ (a matrix of size p × p) are assumed to be known in IO analysis, and
4) The observation and background errors are uncorrelated.

These four assumptions are the major assumptions in DA processes, and after these assumptions, the analysis error covariance $\boldsymbol{P}_a$ can be minimized through the optimal choice of weights.2

2.1.2 Three-Dimensional Variational Assimilation (3D-Var)

In OI analysis, it is the optimal weight matrix $\boldsymbol{W}$ that minimize the total analysis error variance $\boldsymbol{P}_a$. In 1986, Lorenc found that this analysis is equivalent to a specified variational assimilation problem which can be described as find the optimal analysis $\boldsymbol{x}_a$ field that minimizes a (scalar) cost function (Eq. 5). As shown in Eq. 5, the cost function is defined as the distance between the analysis variable $\boldsymbol{x}$ and the background $\boldsymbol{x}_b$,

weighted by the inverse of the background error covariance, plus the distance to the observations $\boldsymbol{y}_o$, weighted by the inverse of the observation error covariance (Courtier, et al., 1998):

Equation 5 3D-Var cost function

$$J(\boldsymbol{x}) = \frac{1}{2}(\boldsymbol{x} - \boldsymbol{x_b})^T \boldsymbol{B}^{-1}(\boldsymbol{x} - \boldsymbol{x_b}) + \frac{1}{2}\big(\boldsymbol{y}_o - H(\boldsymbol{x})\big)^T \boldsymbol{R}^{-1}(\boldsymbol{y}_o - H(\boldsymbol{x}))$$

Where: $\boldsymbol{B}$ is the background error covariance matrix, and $\boldsymbol{R}$ is the observational error covariance. The first term in the right-hand side of Eq. 5 denotes the background term, and the second term in the right-hand side of Eq. 5 denotes the observational term. In Lorenc (1986), to derive the idealized equations for finding the best analysis for NWP, the Bayesian probabilistic arguments are used. In practice, the solution for Eq. 5 is obtained by using iterative methods for minimization such as conjugate gradient or quasi-Newton. For non-linearity models, the uniqueness of the minimization is usually not guaranteed, and because the minimization process is an iterative process, it can be very costly.

In real operational systems, the use of 3D-Var involves a lot of advantages compared to OI method. For OI analysis, a number of approximations are required before the analysis processes, and analysis problem is solved locally, grid point by grid point, or small volume by small volume (Lorenc, 1981). This means a “radius of influence” is required and only the stations closest to the grid point or volume are selected to be analyzed. The background error covariance matrix has to be also locally approximated.

While for 3D-Var, due to the use of global minimization algorithms for minimization of the cost function (Lorenc, 1981), many simplifying approximations required by OI method are no longer necessary. The advantages of 3D-Var comparing to OI can be concluded as (more detailed are concluded in Dr. Xue's lecture: http://twister.caps.ou.edu/OBAN2016/):

1) No need for data selection and background error localization for 3D-Var

   The background error covariance matrix for 3D-Var, can be defined with a more general, global approach with fewer assumptions, rather than the local approximations used in OI analysis. While in 3D-Var, there is no data selection, all available data in the set-up time window are used simultaneously. This avoids jumpiness in the boundaries between regions that have selected different observations.

2) Easy incorporation of balance constraints

   In 3D-Var, add constraints to the cost function without increasing the cost of the minimization becomes available. NCEP global model spin up time has been reduced by more than an order of magnitude dur to the use of the global balance equation (Parish and Derber, 1992). With 3D-Var it became unnecessary for the first time to perform a separate initialization step in the analysis cycle.

3) Non-linear observation operators are available

   Nonlinear relationships between observed variables and model variables in the *H* operator in the minimization of the cost function are becoming available by performing the so-called "inner" and "outer" iterations, in which the "inner" iterations

with the linearized H observation operator kept constant and the "outer" iterations is updated.

The assimilation of radiances is now available using 3D-Var (Derber and Wu, 1998). Also, quality control of the observations becomes possible which can improve the preconditioning of the problem in an iterative solution.

2.1.3 Four-Dimensional Variational Assimilation (4D-Var)

4D-Var is the direct generalization of 3D-Var to handle observations that are distributed in time dimension. The cost function is similar to 3D-Var (Eq. 6) (Rabier, et al., 2000), in which a forecast model is included in the observation operators which allows the comparison between the model state and the observations at the appropriate time. In order to seek the initial condition which best fit the observations, 4D-Var tries to use all available observations in the assimilation time interval.

Equation 6 4D-Var cost function

$$J\left(\boldsymbol{x}(t_0)\right) = \frac{1}{2}\left(\boldsymbol{x}(t_0) - \boldsymbol{x}^b(t_0)\right)^T \boldsymbol{B}_0^{-1}\left(\boldsymbol{x}(t_0) - \boldsymbol{x}^b(t_0)\right) + \frac{1}{2}\sum_{i=0}^{N}(H(\boldsymbol{x}_i) - \boldsymbol{y}_i^o)^T \boldsymbol{R}_i^{-1}(H(\boldsymbol{x}_i) - \boldsymbol{y}_i^o)$$

Where observations are assumed to be distributed within a time interval (t_0, t_n), and the N indicates the number of observations distributed over the time interval.

In 4D-Var, the assumption that the model is perfect is used and this assumption is a disadvantage of this algorithm which 4D-Var tends to give the same to older

observations at the beginning of the interval as to newer observations at the end of the interval.

When compared to 3D-Var data assimilation systems, 4D-Var is a very suitable system for numerical forecasting as the forecast will be completely consistent with the model equations and the 4-dimensional of observations allowed the assimilate of observations at their correct time. However, because of the assumption of perfect model, 4D-Var may experience big problems if the model errors are large. Also, the tangent linear and adjoint models are required in 4D-Var processes. This can be a lot of work if the forecast model is complex (with more complete physical parameterizations). And because it tends to use all the observations in the 4-dimensional space, 4D-Var requires the assimilation to wait for the observations over the whole 4D-Var time interval to be available before the analysis procedure can begin, whereas sequential systems can process observations shortly after they are available. This can delay the availability of analysis.

2.1.4 Kalman Filter and Ensemble Kalman Filter (EnKF)

In the formal methods, OI minimizes the expected analysis error covariance, 3D-Var and 4D-Var solve essentially the same problem but minimizing a cost function. In all these methods, the forecast (or background) error covariance matrix is estimated once for all, as if the forecast errors were statistically stationary. However, there exists day-to-day variability dominated by baroclinic instabilities of synoptic time scales in the model forecast error (with a time scale of a few days) and the variability is about as large as the average error, this error is ignored in variational methods. Kalman Filter (KF) is an

advanced scheme which can deal with the evolution of the forecast error covariance and solve the errors caused by the day-to day variability (Kalman, 1960).

The major differences between KF and 3D-Var is that the background/forecast error covariance in KF is advanced using the model itself, rather than estimating it as a constant covariance matrix. The original KF equations are (subscripts denote the time steps) (Evensen, 2003):

Equation 7 Kalman Filter algorithms

$$x_n^f = \boldsymbol{M}_{n-1} x_{n-1}^a \quad (1)$$

$$\boldsymbol{P}_n^f = \boldsymbol{M}_{n-1} \boldsymbol{P}_{n-1}^a \boldsymbol{M}_{n-1}^T + \boldsymbol{Q}_{n-1} \quad (2)$$

$$\boldsymbol{K}_n = \boldsymbol{P}_n^f \boldsymbol{H}_n^T [\boldsymbol{R}_n + \boldsymbol{H}_n \boldsymbol{P}_n^f \boldsymbol{H}_n^T]^{-1} \quad (3)$$

$$x_n^a = x_n^f + \boldsymbol{K}_n [y_n - \boldsymbol{H}_n x_n^f] \quad (4)$$

$$\boldsymbol{P}_n^a = [\boldsymbol{I} - \boldsymbol{K}_n \boldsymbol{H}_n] \boldsymbol{P}_n^f \quad (5)$$

Where, x_n^f denotes the forecast, x_n^a denotes the analysis, $\boldsymbol{P}_n^f$ and $\boldsymbol{P}_n^a$ represent the forecast error covariance and analysis error covariance, respectively, $\boldsymbol{Q}_n$ is the model error covariance, $\boldsymbol{K}_n$ is the Kalman gain which is defined in Eq. 7 (3) and is obtained by minimizing the analysis error covariance with the same formula derived for OI except that the static background error covariance is replaced by the forecast error covariance generated by model itself. Eq. 7 (1) represents the forecast of the model fields from time step $n-1$ to time step n, while Eq. 7 (2) calculates the forecast error covariance from the analysis error covariance $\boldsymbol{P}_n^a$ and the model error covariance $\boldsymbol{Q}_n$. As the Kalman gain is defined in Eq. 7 (3), Eq. 7 (4) and Eq. 7 (5) are the analysis steps using the Kalman gain. For optimality, all errors such as analysis and model errors should be assumed

uncorrelated (Bouttier and Courtier, 1999). The original KF was developed for linear prediction model (Kalman, 1960), when a nonlinear model is used for the state variable prediction step, the filter is called Extended Kalman Filter (EKF) (Uhlmann, 1992). As theoretically proved, the EKF is the "gold standard" of data assimilation. It can provide the best linear unbiased estimate and its error covariance by going through an initial transient period of one week or two even when the system starts with a poor initial guess. The updating of the forecast error covariance matrix also ensures that the analysis takes into the flow-dependent errors. Nonetheless, if the system is very unstable or the observations are not frequent enough, it is possible for the linearization to become inaccurate, and the EKF may drift away from the true solution. And similarly, EKF is exceedingly expensive in computing resources.

In order to reduce the expensive of computing resources, a simplified version of KF is derived known as the Ensemble Kalman Filter (EnKF) (Evensen, 1994; Anderson, 2001). The basic idea of EnKF is using the mean of a set of ensembles as the best estimate, and the sample of covariance as a good estimate of the forecast error covariance of this best estimate. The estimate of the forecast error covariance from a set of ensembles is defined in Eq. 8 (Evensen, 2003):

Equation 8 Estimation of forecast error covariance for EnKF

$$\boldsymbol{P}^f \approx \frac{1}{N-1}\sum_{k=1}^{K}(\boldsymbol{x}_k^f - \overline{\boldsymbol{x}}^f)(\boldsymbol{x}_k^f - \overline{\boldsymbol{x}}^f)^T$$

It is worth noting that by using the mean of a set of ensembles as the best estimate, the Eq. 8 tends to underestimate the variance of the forecast errors because every forecast is used to compute of its own error covariance. The solution for this kind of underestimate of the analysis error covariance is to add random perturbations into the observations that are assimilated in each member of the ensemble, and this solution is usually called the stochastic EnKF. The advantages of using EnKF have been proved since the operational implantation in the Community Gridpoint Statistical Interpolation (GSI) system. The application of EnKF not only can save a lot of computational resource than Kalman Filter, but also make the tangent linear and adjoint model and the linearizing the evolution of the forecast error covariance unnecessary. Without the tangent linear and adjoint model, it may still provide excellent initial perturbations for ensemble forecasting.

2.1.5 Ensemble-Variational Hybrid Data Assimilation

EnKF only uses a set of limited ensembles (typically 40-120 members) to provide the best estimate (Ott, et al., 2004; Torn, 2010; Hamrud, et al., 2015). However, when compared to the much larger number of depth of field of the model, the limited sample of ensemble may come with the problem called rank deficient (Solonen, et al., 2014). One way to solve this problem is the combination of ensembles or the sequential EnKF and Variational DA methods by cooperating with the estimate calculated from many estimated forecast errors. It uses the background error covariance matrix which is completely static or only weakly coupled to the dynamics of the forecast, and at the same time involves in the fully flow-dependent background error covariance estimated from a

set of ensembles of short-range forecasts with the full nonlinear model (Wang, et al., 2013).

The cost function for this hybrid data assimilation can be described in the form of Eq. 9:

Equation 9 Hybrid cost function

$$J(x) = \frac{1}{2}\beta_1(\boldsymbol{x}-\boldsymbol{x}_b)^T\boldsymbol{B}_f^{-1}(\boldsymbol{x}-\boldsymbol{x}_b) + \frac{1}{2}\beta_2(\boldsymbol{x}-\boldsymbol{x}_b)^T\boldsymbol{B}_{ens}^{-1}(\boldsymbol{x}-\boldsymbol{x}_b) + \frac{1}{2}[\boldsymbol{y}_o - H(\boldsymbol{x})]^T\boldsymbol{R}^{-1}[\boldsymbol{y}_o - H(\boldsymbol{x})]$$

Where $\boldsymbol{B}_f$ and $\boldsymbol{B}_{ens}$ are the model static background error covariance and background error covariance estimated from a set of ensemble forecasts, respectively. And β_1 and β_2 are two factors whose inverse define the weights placed on the static covariance and the ensemble covariance, and these two factors satisfy the relation:$\frac{1}{\beta_1} + \frac{1}{\beta_2} = 1$.

In the hybrid method, flow-dependent ensemble error covariance estimated from a set of ensembles was taken into account with the variational minimization which makes the model background error covariance more reliable. However, more tests are needed for the choosing of number of ensembles and the factors for both weights of static and ensemble background error covariance.

In simple words, data assimilation is a method which uses the observations to adjust the model's initial guess in order to get an initial condition with better accuracy for further forecasting by physical and dynamical equations. From the OI method, to variational method and further to ensemble Kalman filter, data assimilation associated

with significantly improved computing resources have greatly helped in improving the NWP systems. Nowadays, DA systems can not only assimilate the physical-state variable such as temperature, pressure, humidity, etc., but also assimilate radiance observed by satellites, and chemical components such as ozone, aerosols, etc. These additional forcing can be brought into the model and propagating along with the forecast and which may significantly affect the downstream events (Rood, 2005).

2.2 Assimilation of Satellite Radiance/Brightness Temperature

Satellite instruments provide a large amount of observations varying from land surface parameters, vegetation coverages, atmospheric profiles, etc. Despite the fact that satellites can provide lots of products to enhance our scientific researches, the radiance/brightness temperature products are usually used in the NWP DA systems.

2.2.1 The Development of Satellite Observations

It has been over 50 years using instruments on weather satellite, in both polar orbit and geostationary orbit measuring key Earth system parameters (Smith, et al., 2015). By keep tracking the records of satellite remote sensing data, the field of satellite climatology has received considerable attention in recent years owing to the long term global coverage data sets.

Acting as the predecessor to today's hyperspectral sounders, the High Resolution Infrared Radiometer (HIRS) has provided more than two decades' worth of infrared observations with a global coverage since 1979 (Smith, et al., 2015) (https://poes.gsfc.nasa.gov/hirs4.html). And for today, there are four operational hyperspectral sounders observing the Earth and increased the frequency of space-based

hyperspectral soundings to at least 8 measurements (4 daytime and 4 nighttime) per day with an order of magnitude more in the polar zones. They are listed as below: 1), the Atmospheric Infrared Sounder (AIRS) launched in 2002 on Aqua (http://disc.sci.gsfc.nasa.gov/AIRS/documentation/airs_instrument_guide.shtml); 2), the Infrared Atmospheric Sounding Interferometer (IASI) launched in 2006 on the first satellite in the series of three of the Meteorological Operational satellite programme (MetOp-A), 3), another IASI launched in 2012 on MetOp-B (https://wdc.dlr.de/sensors/iasi/), and 4) the Cross-track Infrared Sounder (CrIS) launched in 2011 on the Suomi National Polar-Orbiting Partnership (S-NPP) satellite (https://jointmission.gsfc.nasa.gov/cris.html). These four very high spectral resolution infrared sensors significantly improved the vertical resolution and hence the accuracy of the atmospheric information by measuring the retrieved radiance from their top-of-atmosphere (TOA) compared the prior-generation multispectral sounders such as HIRS (Schwaerz and Kirchengast, 2003; Smith, et al., 2015). Despite their own high accuracy, their very high spectral resolution also has the advantages helping other instruments in both radiometric and spectral calibration (Tobin, et al., 2006; Wang and Cao, 2008; Wang, et al., 2009).

The AIRS instrument is a grating spectrometer with 2378 (independently calibrated) channels in the thermal bands and 4 bands in the visible (0.4 – 1.0 μm), and IASI and CrIS are interferometers with 8461 and 1305 channels, respectively. Their local sampling time (LST) is based on their satellite platforms. The detailed information of these three kinds of sensors are summarized in Table 1. As shown in Table 1, AIRS and

CrIS are in the same orbital planes (ascending) with a same 13:30 LST but operate at different altitudes. However, their instruments are totally different, a grating spectrometer and a Fourier transform infrared spectrometer (or interferometer) for AIRS and CrIS, respectively. While IASI and CrIS are both interferometer instruments and both operate at a similar orbital altitude but in the opposite orbital planes (descending for IASI) with an ~09:30 LST in the early morning for IASI. The spectral bands covered by these three instruments are slightly different in which IASI has the highest spectral resolution and the most channels without spectral gap. AIRS has 2378 infrared channels over three wavelength ranges, and it also has four visible bands. CrIS has 1305 infrared channels also over three wavelength ranges similar to AIRS, and here we call them LWIR (Long wavelength InfraRed: 9.13-15.5 μm), MWIR (Mid Wavelength InfraRed: 5.71-8.26 μm), and SWIR (Short Wavelength InfraRed: 3.92-4.64 μm). These three hyperspectral sensors are all capable for the detecting of lower troposphere temperature and humidity with considerable accuracy in which CrIS has the best accuracy in lower troposphere.

Table 1 Measurement characteristics of AIRS, IASI, and CrIS

Satellite Platform (time: LST Altitude: km)	Instruments	Nadir Spatial Resolution (km)	Spectral Resolution (bands)	Spectral Coverage (μm)	Spatial Sampling	Accuracy
Auqa (13:30) (705) (Ascending)	AIRS (Grating Spectrometer)	13.5	~1200 λ/△λ (2378 Infrared channels, and 4 Visible bands)	IR: 3.74-4.61 6.20-8.22 8.80-15.40 VIS: CH1:0.41-0.44 CH2:0.58-0.68 CH3:0.71-0.92 CH4:0.49-0.94	Contiguous cross-track scan: 3*3 footprints in a 50-km area	Atmospheric Temperature: 1 K in layers of 1 km thick Humidity: 20% in layers of 2 km thick (Both in troposphere)
MetOp-A/B (09:30) (817) (Descending)	IASI (Fourier transform infrared spectrometer)	12	0.5 cm^{-1} (8461 Infrared channels)	3.7-15.5 No Spectral gap	Contiguous cross-track scan: 2*2 footprints in a 50-km area	Atmospheric Temperature: 1 K in layers of 1 km thick Humidity: 10-15% in layers of 1-2 km thick (Both in the lower troposphere)
S-NPP (13:30) (833) (Ascending)	CrIS (Fourier transform infrared spectrometer)	14	0.625 cm^{-1} 1.25 cm^{-1} 2.5 cm^{-1} (1305 Infrared over 3 wavelength range)	LWIR: 9.13-15.5 MWIR: 5.71-8.26 SWIR: 3.92-4.64	Contiguous cross-track scan: 3*3 footprints in a 50-km area	Atmospheric Temperature: 0.3 K in layers of 1 km thick Humidity: 10-15% in layers of 1-2 km thick (Both in the lower troposphere)

In recent years, microwave data retrieved from microwave sensors have received considerable attention owing to the valuable information content contained in the microwave bands due to its ability to provide more accurate information under cloudy conditions. One typical application is that the retrieved global microwave radiance observations have been used to enhance the operational NWP via DA (English et al. 2000; Mahfouf et al. 2005; Kelly et al. 2008; Kulie, et al., 2010; Prigent, et al., 2006;

Weng, et al., 2012). Among lots of the microwave instruments will be talked later, we are highlighting here that the first application of microwave techniques for monitor the atmospheric temperature and water vapor was built by the Nimbus 5 (Nimbus E) Microwave Spectrometer (NEMS) experiment in 11 December 1982. The NEMS is the milestone of the applying microwave technologies in meteorological researches (Waters, 1975; Staelin, et al., 1976).

The pioneer microwave sounding instrument was the Microwave Sounding Unit (MSU), a cross-track scanner, flown on the National Oceanic and Atmospheric Administration (NOAA) polar-orbiting satellite platform named the Television and Infrared Observations Satellite (TIROS-N) in late 1978. During that time, MSU measures atmospheric temperature profiles using only four channels ranging from 50.3 to 57.95 GHz using the thermal emission from the atmospheric oxygen constitutes near 60 GHz (Mears and Wentz, 2008; Zou, et al., 2014). These four channels are sensitivity to the near surface, middle troposphere, near the tropopause, and the lower stratosphere, respectively. And within these four channels, only channel 2 and 4 have continuous data over the entire period of observation. These limitations caused large calibration issues and time-varying biases for the construction of MSU data sets.

The follow-on series of instruments for MSU is the AMSUs began operation in mid-1998 (Diak, 1995), in which the AMSU-A, is a cross-track, stepped-line scanning, and total power microwave radiometer with 15 channels ranging from 23-89 GHz providing a nominal spatial resolution at the nadir of 48 km (http://mirs.nesdis.noaa.gov/amsua.php). While AMSU-B (recently replaced by the

Microwave Humidity Sounder (MHS)) is a cross-track, continuous line scanning, total power radiometer with 5 channels ranging from 89-183.31 GHz where the frequencies are sensitive to atmospheric water vapor (http://mirs.nesdis.noaa.gov/mhs.php). The instantaneous field of view (FOW) is one third of the AMSU-A which is 1.1°and the spatial resolution at nadir is nominally 16 km (Also one third of the AMSU-A spatial resolution at nadir). The AMSU instruments have significantly higher spatial resolution comparing to MSU instruments such as the scan time reduced to 8 s instead of 25.6 s used by MSU instruments, and the nadir spot size has been reduced from 110×110 km to 48×48 km and for the near-limb view, the size has been reduced from 178×322 km to 80 ×150 km (the coarser spatial resolution at near-limb view is due both to the increased distance and to the oblique earth incidence angle). In 2011, a more advanced microwave radiometer the Advanced Technology Microwave Sounder (ATMS) is launched on S-NPP platform along with the hyperspectral infrared radiometer CrIS (https://jointmission.gsfc.nasa.gov/atms.html). ATMS is also a cross-track scanner and combined all the channels of AMSU-A and AMSU-B/MHS into a single package with considerable savings in mass (1/2 of AMSUs), power (1/2 of AMSUs), and volume (1/4 of AMSUs). ATMS has 22 channels ranging from 23-183 GHz, in which the first 16 channels are primarily for temperature soundings from the surface to about 1-mb (~50 km), and the remaining channels are associated with atmospheric humidity soundings in the troposphere from the surface to about 200-mb (10 km). The ATMS channels 4, 19 and 21 are new for better atmospheric temperature and moisture profiling and better data sets for NWP. Also, the ATMS noise equivalent differential temperature for temperature

sounding channels is higher than the AMSUs mainly because the ATMS sampling time is much shorter than that of AMSUs (the integration time for all ATMS channels is reduced to 18 ms), spatial coverage is also improved in ATMS which has no gaps between swaths now, and it was initially the intention to use the 118 GHz oxygen line for temperature sounding instead of 50-60 GHz used by AMSUs. Another microwave instrument, the Special Sensor Microwave Imager/Sounder (SSMI/S) carried onboard the Defense, is a 24-channel passive microwave radiometer which can detect radiative frequencies range from 19-183 GHz correspond to four main categories: Lower Atmospheric Sounding, Upper Atmospheric Sounding, Environmental and Imaging. The detailed channel information of SSMI/S can be found at the website: https://nsidc.org/data/docs/daac/ssmis_instrument/#bell_2006. A summary of the channel frequencies of the major microwave satellite sensors is shown in Table 2.

Table 2 Channel frequencies of AMUS-A, MHS, ATMS, and SSIMS

AMSU-A(ch1-15)/MHS(ch16-20)			ATMS			SSMI/S		
Ch	GHz	Pol	Ch	GHz	Pol	Ch	GHz	Pol
1	23.8	QV	1	23.8	QV	1	50.3	V
2	31.399	QV	2	31.4	QV	2	52.8	V
3	50.299	QV	3	50.3	QH	3	53.596	V
4	52.8	QV	4	51.76	QH	4	54.4	V
5	53.595±0.115	QH	5	52.8	QH	5	55.5	V
6	54.4	QH	6	53.596±0.115	QH	6	57.29	RCP
7	54.94	QV	7	54.4	QH	7	59.4	RCP
8	55.5	QH	8	54.94	QH	8	150	H
9	57.29	QH	9	55.5	QH	9	183.31±6.6	H
10	57.29±0.217	QH	10	57.29	QH	10	183.31±3	H
11	57.29±0.3222 ±0.048	QH	11	57.29±0.3222 ±0.217	QH	11	183.31±1	H
12	57.29±0.3222 ±0.022	QH	12	57.29±0.3222 ±0.048	QH	12	19.35	H
13	57.29±0.3222 ±0.01	QH	13	57.29±0.3222 ±0.022	QH	13	19.35	V
14	57.29±0.3222 ±0.0045	QH	14	57.29±0.3222 ±0.01	QH	14	22.235	V
15	89	QV	15	57.29±0.3222 ±0.0045	QH	15	37	H
16	89	QV	16	88.2	QV	16	37	V
17	157	QV	17	165.5	QH	17	91.655	V
18	183.31±1	QH	18	183.31±7	QH	18	91.655	H
19	183.31±3	QH	19	183.31±4.5	QH	19	63.283248 ± 0.285271	RCP
20	191.31	QV	20	183.31±3	QH	20	60.792668 ± 0.357892	RCP
			21	183.31±1.8	QH	21	60.792668 ± 0.357892 ± 0.002	RCP
			22	183.31±1	QH	22	60.792668 ± 0.357892 ± 0.0055	RCP
						23	60.792668 ± 0.357892 ± 0.016	RCP
						24	60.792668 ± 0.357892 ± 0.050	RCP

2.2.2 Compared to In-situ Observations

Satellite observations have many advantages compared to the in-situ observations: 1) better representative of an area (satellite observations usually provide a regional view instead of a point of view in in-situ observations); 2) larger spatial coverage (e.g., polar satellites can cover most of the Earth and the recently launched sensor ATMS has the advantage that it no longer has gaps between swaths. For geostationary satellite sensors, they usually have a continent scale coverage); 3) provide more information where there are few in-situ observations, such as plateaus, mountainous areas, oceans, polar regions (with the developing of polar satellites such as Aqua/Terra, we can get as many as 8 times of observations per day over the polar regions and 2 times per day over the equators), etc.; 4) by using the reflected radiance from the Earth and the atmosphere, satellite observations are some way cheaper and easier installation and maintenance comparing to the tower observations, and at the same time, satellite can detect multi-spectral radiance include Visible bands, Infrared bands and Microwave bands which located in a wide range of radiances sensitive to most of the key Earth system parameters; 5) satellite sensors also have multiple weighting features representing the vertical profile of the atmosphere which extending into higher altitudes such as 1-mb, and the abundance of observations located in the stratosphere is part of the reasons for the raising of NWP models lids. As a consequence of these satellite observations advantages, the accuracy of NWP systems has gone through dramatic improvements. However, when it is hard to significantly improve the skills of NWP forecasts, how to deal with the uncertainties became particularly important. On one hand, the advantages of satellite observations compared to in-situ observations can largely benefit the NWP systems via DA, on the

other hand, uncertainties of these observations will also be brought into the NWP systems simultaneously and sometimes may cause the misleading of atmospheric state. For example, Zou et al. (2011) found that degradation in quantitative precipitation forecasts skill in an all-data assimilation experiment (including the Geostationary Operational Environmental Satellite-11 and -12 (GOES-11/12), the Advanced Microwave Sounding Unit-A (AMSU-A), the Microwave Humidity Sounder (MHS), the Atmospheric Infrared Sounder (AIRS), and the High Resolution Infrared Sounder (HIRS)) was mainly caused by the using of MHS data. And therefore, it is necessary to investigate the uncertainties in NWP systems such as using different satellite spectral bands at different altitudes. It is also important to find out how much can be approved by using the stratospheric microwave data sets in NWP systems.

2.2.3 Direct Assimilation of Satellite Radiance/Brightness Temperature Using the Community Radiative Transfer Model (CTRM)

Unlike in-situ observations, no direct measurements of the atmospheric states can be provided by satellite observations. Instead of direct measuring of the atmospheric states, satellite observations are more sensitive to radiation emitted and reflected by the earth's atmosphere, surface, ocean, cloud, etc. So, two ways of assimilating satellite data are usually used in NWP systems namely direct assimilating and indirect assimilating satellite observations (Sasaki, and Goerss, 1982; Scott, et al., 2012). The indirect way uses the retrieved satellite products (including land surface/soil products and atmospheric state variables, e.g., the Moderate Resolution Imaging Spectroradiometer (MODIS) products) as the observations and then be assimilated in the DA systems with same processing as the assimilating of conventional observations.

Direct assimilating of satellite observations involves a radiative transfer forward model as the observation operator for radiance observations. The Community Radiative Transfer Model (CTRM) developed by Joint Center for Satellite Data Assimilation (JCSDA) is employed in the DA system to transfer control variables into simulated radiance/brightness temperature. The CRTM model calculates the absorption of atmospheric gases, scattering and absorption by both clouds and aerosols, and surface emissivity and reflectivity, and then solves the radiative transfer problem. In other words, the CRTM is used as the observation operator and when the uncertainties of the formation of radiative transfer equation or the unknown parameters in the radiative transfer equation, observed radiance data must be removed due to the low reliability. Typical examples include when clouds, trace gases, or aerosols exist in the observed column, and such radiance will be removed through the quality control (QC) steps (Anderson and Jarvinen, 1998).

The first QC step is the processing of radiance thinning which select the best quality observations. Then, the major QC steps are mainly focused on the capture of problematic satellite data. The main sources for the problematic satellite data are: 1) instrument problems, 2) clouds and precipitation simulation errors, 3) surface emissivity simulation errors, and 4) processing errors such as wrong height assignment, etc. It is believed that using the direct way of assimilating satellite radiance can bring less uncertainties into the NWP systems than using the indirect way which needs more complex steps associated with more uncertainties. Theoretically saying, direct radiance

assimilation is superior to indirect assimilation due to the more justified observational error statistics (Xu, J., et al., 2009).

CHAPTER THREE EXPERIMENTAL CONFIGURATION

A number of numerical experiments are designed to investigate the major purposes of this thesis. The advanced research core in weather research and forecasting (WRF-ARW) system is used as the regional weather forecasting system and the community gridpoint statistical interpolation (GSI) system is used as the data assimilation system. Three set of experiments with different DA configurations are designed with model lids at 50-mb, 10-mb, and 1-mb, respectively. This chapter mainly introduce the models used in this thesis, the data used for data assimilation over the U. S. continental, and the detailed experimental set-ups.

3.1 Advanced Weather Research and Forecasting System

The WRF-ARW is used for the regional study (Skamarock et al. 2008; Wang, et al., 2016). The WRF-ARW system is a non-hydrostatic, fully compressible, primitive equation model. Lead institutions involved in the WRF-ARW effort include the National Center for Atmospheric Research (NCAR), Air Force Weather Agency (AFWA), National Oceanic and Atmospheric Administration (NOAA), and other governmental agencies and universities. WRF is built around a software architectural framework in which different dynamical cores and model physics packages are accessible within the same code. Within the WRF framework, it is possible to mix the dynamical cores with differing physics packages to optimize performance since each core has strengths and

weaknesses in different areas. WRF-ARW uses a terrain-following pressure coordinate and the Arakawa C grid staggering approach. And the time integration schemes be used in WRF-ARW is the Runge-Kutta 2nd and 3rd order, and for both the horizontal and vertical, the 2nd to 6th order advection schemes are used (Wang, et al., 2016). The vertical levels in WRF model is set as eta levels. By using the eta coordinates system, we don't need to calculate the pressure gradient force in sigma coordinate system which can reduce the error in pressure gradient force calculation and improve the forecast of wind, temperature, and moisture in steeply sloping terrain due to its relatively horizontal surfaces at all times. A flow chart of WRF (Wang, et al., 2016) is shown in Fig. 4.

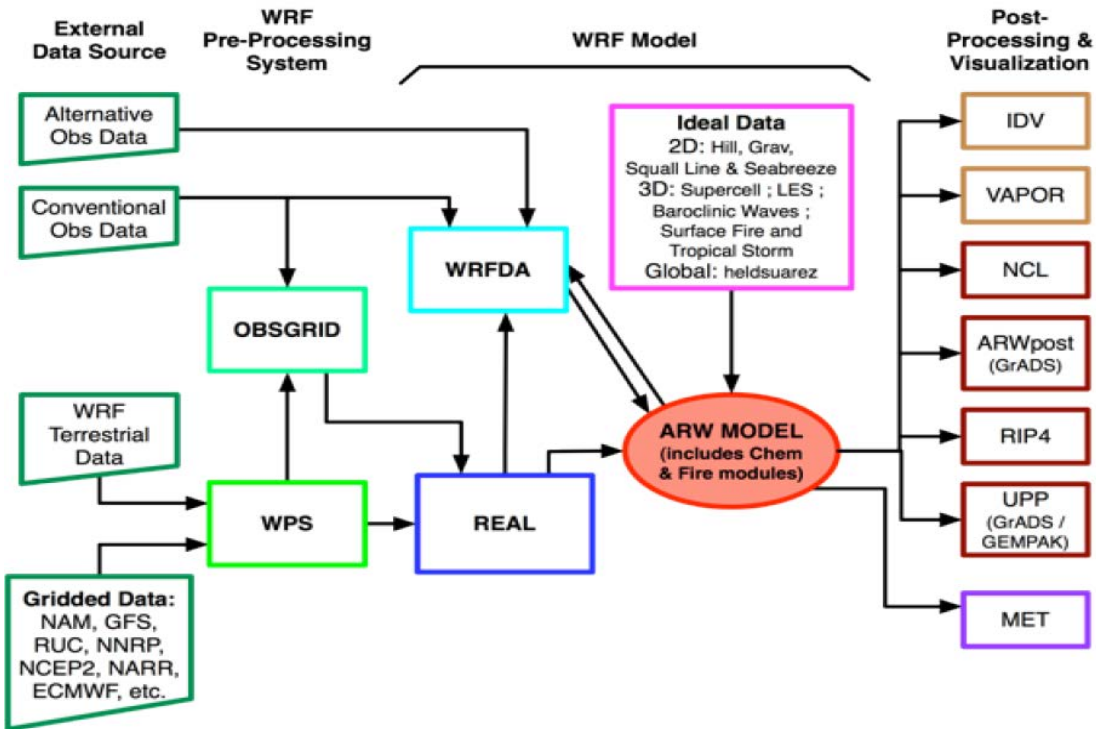

Figure 4 The WRF-ARW Modeling System Flow Chart (Wang, et al., 2016).

The major part of WRF-ARW including the WRF Preprocessing System (WPS) and the ARW solver. The simulation domain is defined in the WPS step. The domain design in this thesis is shown in Fig. 5 (shading indicates land (grey) and ocean (white)), and the domain configurations including map projection, central point, etc. are shown in Table 3. The model lid (top of the model) is raised step by step from 50-mb to 1-mb to involve more stratospheric information, and the number of vertical layers are increasing as the model lid increased. With the domain defined, WPS then interpolate terrestrial data and meteorological fields (usually comes from other regional or global models) to the designed domain to generate the meteorological field for further processes. The U. S. Geological Survey (USGS) 24 category is used for the land use option. Two tables describe the land use options and the detailed categories can be found in the Wang, et. al. (2016, Chapter 3).

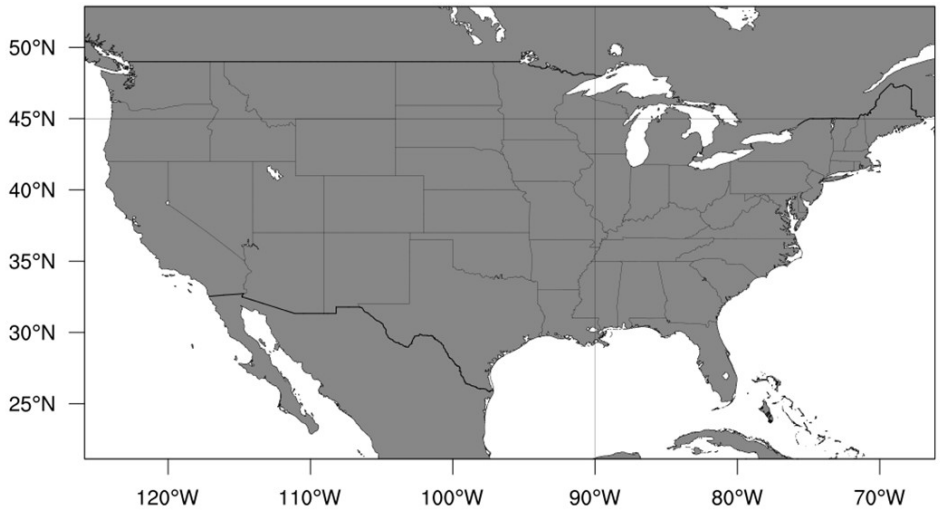

Figure 5 Study domain over the U. S. continental.

Table 3 Domain Configurations for WRF simulations

Central Point	(37°N，90°W)		
Projection	Lat-Lon		
Domain	Layer	Resolution (degree)	Grid (Lon*Lat)
	1	0.25	240*128
Experiment set 1 Vertical Layers (Eta levels with model top at 50-mb)	30 levels 1, 0.993, 0.983, 0.97, 0.954, 0.934, 0.909, 0.88, 0.8317505, 0.7835011, 0.7352517, 0.6870022, 0.6035514, 0.5279136, 0.4594781, 0.397675, 0.3419721, 0.2918729, 0.2469149, 0.2066672, 0.1707291, 0.1387277, 0.1103166, 0.08602321, 0.06535161, 0.04776186, 0.03279452, 0.02005862, 0.009221466, 0		
Experiment set 2 Vertical Layers (Eta levels with model top at 10-mb)	51 levels 1.000, 0.994, 0.986, 0.978, 0.968, 0.957,0.945, 0.931, 0.915, 0.897, 0.876, 0.854,0.829, 0.802, 0.772, 0.740, 0.705, 0.668,0.629, 0.588, 0.550, 0.513, 0.478, 0.445,0.413, 0.383, 0.355, 0.328, 0.303, 0.279,0.256, 0.234, 0.214, 0.195, 0.177, 0.160,0.144, 0.128, 0.114, 0.101, 0.088, 0.076,0.065, 0.055, 0.045, 0.036, 0.028, 0.020,0.012, 0.0056, 0.000		
Experiment set 3 Vertical Layers (Eta levels with model top at 1-mb)	63 levels 1, 0.993, 0.983, 0.97, 0.954, 0.934, 0.909, 0.88, 0.8413662, 0.8027326, 0.7640989, 0.7254651, 0.6569721, 0.5938299, 0.5356899, 0.4822229, 0.4331176, 0.3880801, 0.3468334, 0.309116, 0.2746814, 0.2432974, 0.2147456, 0.18882, 0.1653272, 0.1443878, 0.1260844, 0.1100854, 0.09610046, 0.08387615, 0.07319078, 0.06385061, 0.0556863, 0.04854981, 0.04231175, 0.03685901, 0.03209274, 0.02792649, 0.02428475, 0.02110147, 0.01831895, 0.01588672, 0.01376069, 0.01190231, 0.01027789, 0.008857966, 0.007616803, 0.006531891, 0.005583562, 0.004754621, 0.004030036, 0.003396671, 0.002843042, 0.002359111, 0.001936102, 0.001566348, 0.001243142, 0.0009606255, 0.0007136756, 0.0004978148, 0.0003091293, 0.0001441978, 0		

The regional initial and boundary conditions are generated using the key component of WRF-ARW – the ARW solver with the meteorological field generated in WPS. The physics schemes used in the WRF-ARW model are as follows: the WRF

Single-Moment 3-class scheme for the microphysics; the RRTM scheme for longwave radiation and the Goddard shortwave scheme for shortwave radiation; the Noah Land Surface Model for the land surface; the Yonsei University scheme for the planetary boundary layer; and the Grell-Devenyi (GD) ensemble scheme for the cumulus parameterization. The configurations of physics in WRF-ARW are the same for all the experiments in this thesis. More detailed descriptions of the physics schemes can be found at http://www2.mmm.ucar.edu/wrf/users/docs/arw_v3.pdf.

3.2 Community Gridpoint Statistical Interpolation (GSI) system

GSI is the DA system developed by the NCEP Environmental Modeling Center (EMC) as the next generation analysis system based on the Spectral Statistical Interpolation (SSI) analysis system and now serves as the currently operational DA system in NCEP (Kleist, et al., 2009b; Hu, et al., 2015). In SSI system, the system is constructed in the spectral space, while in the next generation, the GSI, the system is constructed in the physical space and is designed to be a flexible, state-of-art system that is efficient on available parallel computing platforms. In recent GSI version, the application of surface analysis, the basic 3D-Var, EnKF, ensemble-variational hybrid, and 4D-Var if coupled with an adjoint model of GSI supported forecast system (Kleist, 2012; Wang, et al., 2013; Hu, et al., 2015).

GSI can assimilate both conventional and satellite radiance data sets (with the help of Community Radiative Transfer Model (CRTM)). The detailed information can be found at the Developmental Testbed Center (DTC) website: http://www.dtcenter.org/. For

variational experiments in this thesis, two loops were used and the maximum iteration steps for both loops were set to 50.

3.3 Data

Three sets of data are used in this thesis: 1) the initial meteorological field and lateral boundary conditions for regional model WRF-ARW, 2) observations used in GSI DA system, and 3) observations used for verification.

3.3.1 Initial Meteorological Field and Lateral Boundary Conditions

The 3-hour interval products from the global forecast system (GFS) (the weather forecast model component of the NCEP's operational NWP system) are used as the initial meteorological and lateral boundary conditions for the regional weather forecasting system. The operational GFS covers the entire globe at a base horizontal resolution of T574 (a total wavenumber of 574 of the spherical harmonics which are triangularly truncated, or grid-spacing of ~28 km in the mid-latitude), and 64 vertical levels with model top at 0.3-mb. In our experiments, the GFS products with a horizontal resolution of 0.5°×0.5° and 26 unevenly distributed vertical levels (Table 3) with a top at 10-mb are used for the WRF-ARW experiments with model top under 10-mb, and the GFS whole atmospheric data with the same horizontal resolution but 47 unevenly distributed vertical levels (Table 4) with a top at 1-mb are used for the WRF-ARW experiments with model top at 1-mb. Detailed information can be obtained through the website below: https://www.ncdc.noaa.gov/data-access/model-data/model-datasets/global-forcast-system-gfs

Table 4 Vertical levels (mb) of GFS products

GFS products with 10-mb lid	Whole Atmospheric data with 1-mb lid
1000, 975, 950, 925, 900, 850, 800, 750, 700, 650, 500, 450, 400, 350, 300, 250, 200, 150, 100, 70, 50, 30, 20, 10	1000, 975, 950, 925, 900, 875, 850, 825, 800, 775, 750, 725, 700, 675, 650, 625, 600, 575, 550, 525, 500, 475, 450, 425, 400, 375, 350, 325, 300, 275, 250, 225, 200, 175, 150, 125, 100, 70, 50, 30, 20, 10, 7, 5, 3, 2, 1

3.3.2 Observations Used for Data Assimilation and Verification

The operationally available observations including conventional and satellite data were used for the research in this thesis. The observations are constructed in the Binary Universal Form for the Representation of meteorological data (BUFR) format and can be downloaded from the NCEP products website: http://www.nco.ncep.noaa.gov/pmb/products/gfs/. The conventional observations vary from in-situ observations cover both land and ocean, radiosondes, aircraft reports, to satellite retrievals, chemical compositions, etc. Typical coverages of the conventional observations including humidity, surface pressure, temperature and wind are shown in Fig. 6. Also, the conventional observations will be used to evaluate the model forecasts. The distribution of satellite observations depends on the time which DA is applied.

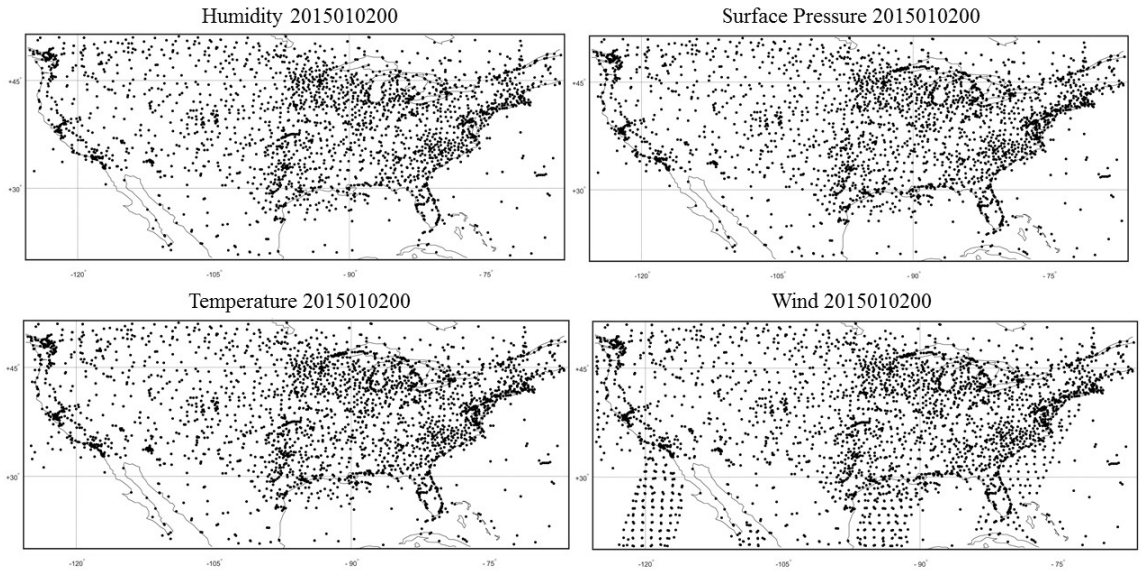

Figure 6 Typical conventional observation coverage over the U. S. at 00:00 UTC, January, 2015.

The satellite radiance/brightness temperature observations (level 1b) used in this thesis include both infrared and microwave satellite instruments. The microwave instruments used here include the AMSU-A (onboard NOAA-15, NOAA-18, NOAA-19, Meteorological Operational (MetOp)-A, MetOp-B, and Aqua), the MHS (onboard NOAA-18, NOAA-19, MetOp-A, and MetOp-B), the SSMI/S carried onboard the Defense Meteorological Satellite Program (DMSP-f16, -f17, -f18, -f19, and -f20), and the ATMS flown onboard the S-NPP satellite. The detailed microwave channel information is summarized in Table 2.

The infrared satellite instruments include the HIRS/4 (onboard NOAA-19, MetOp-A, and MetOp-B) (https://poes.gsfc.nasa.gov/hirs4.html), the AIRS (launched in 2002 on Aqua) (http://disc.sci.gsfc.nasa.gov/AIRS/documentation/airs_instrument_guide.shtml), the

IASI (onboard MetOp-A, and MetOp-B) (https://wdc.dlr.de/sensors/iasi/), and the CrIS launch along with the ATMS on S-NPP (https://jointmission.gsfc.nasa.gov/cris.html). A brief summary of the infrared instruments is concluded in Table 1. More detailed information can be found at the websites: https://www.nasa.gov/.

The data used for the verification of individual case studies includes the products from the Global Land Data Assimilation System (GLDAS) with a horizontal resolution of 0.125 degree and in-situ observations from individual stations. The GLDAS is generating a series of optimal land surface forcing (e.g, precipitation, surface meteorology and radiation), state (e.g., soil moisture and temperature, and snow), and flux (e.g., evaporation and sensible heat flux) data by integrating satellite- and ground-based observational data products, using advanced land surface modeling and data assimilation techniques (Rodell et al., 2004). The data set has been popularly used in many model simulations (Goncalves et al., 2006; Mueller et al., 2011; Wang et al., 2011).

3.4 Experimental Set-up

As shown in the flow chart (Fig. 3), three sets of experiments pointing to three objectives are designed to retrieve the goals of this thesis. The regional model lid is raised step by step from 50-mb to 1-mb. All three sets of experiments use the same observation forward operators and satellite bias correction algorithms as in the operational 3D-Var system (Wu, et al., 2002; Kleist, et al., 2009b). Also, the same quality control decisions are used for all experiments. The time window used in variational DA is set to 1.5-h before and after the assimilation time. All the computations are performed on the

Supercomputer for Satellite Simulations and Data Assimilation Studies (the “S4 supercomputer”) of the JCSDA.

The first set of experiments contains three configurations of GSI involving the basic 3D-Var, 3D-Var based Ensemble-Variational Hybrid (short for Hybrid) with a weight of 20% on the static background covariance and 80% on the ensemble covariance, and EnKF. The flow chart of the first set of experiments is shown in Fig. 7. For the first set of experiments, the regional model top is set at 50-mb. The regional ensembles for the Hybrid and EnKF configurations are prepared by adding random perturbations to the ICs using WRF-DA system at 18:00 UTC and propagating 6 hours forward with WRF-ARW thus the ensembles are flow dependent (Caya, et al., 2005; Meng, and Zhang, 2011). The data assimilation experiments are conducted during January, and February, 2015, and July, and August, 2015, representing winter and summer, respectively. A 6-h spin up is firstly made using WRF-ARW starting at 18:00 UTC, and then all operationally available observations including both conventional and satellite data are assimilated at 00:00 UTC. A 72-h forecast is applied using the newly generated ICs from DA system. A restart is applied every 24 hours and thus, over 50 samples were obtained each season. The forecasts verified against conventional observations at different forecast lead times with a 12-h increment to study the differences of predictabilities between three major DA configurations. Based on the evaluation results, the DA configuration which fit best for certain conditions is used for later studies.

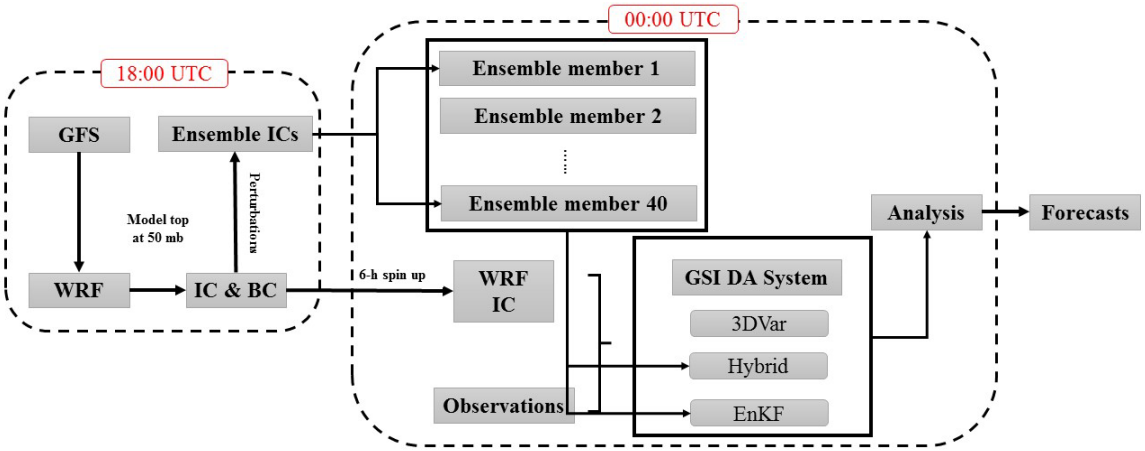

Figure 7 Flow Chart of the first part of experiment design.

The second set of experiments is designed to compare the impact of infrared and microwave satellite observations on regional NWP system. The flow chart of the second set of experiments is similar to the first set of experiments but with different data selection in DA system. The experiment period is the same as the in the first set of experiments. Also a 6-h spin up starting at 18:00 UTC is firstly made, DA is applied at 00:00 UTC with restarts being made every 24 hours and then a 72-h forecast is obtained using WRF-ARW. The model top of the second set of experiments is raised from 50-mb to 10-mb. The DA scheme selection is based on the results of the first set of experiments. Three configurations involving different observation sets are designed (similar to the traditional Observing System Experiments (OSE) method): the control experiment (CTRL) includes all operationally available observations, the infrared experiment (IR) includes all operationally available conventional observations and infrared satellite observations, and the microwave experiment (MW) includes all operationally available

conventional observations and microwave satellite observations. Also, the forecasts are verified against conventional observations at different forecast lead times with a 12-h increment.

The third set of experiments is designed to investigate the impacts of extra stratospheric information on regional NWP system. The regional model top is further raised to 1-mb associated with more model levels in the stratosphere. A selection of the stratospheric and tropospheric microwave channels is designed based on the vertical weighting functions for further studies. The experiment period is conducted during January, 2015. Also, a 6-h spin up is made first, and then a one-week forecast is made using WRF-ARW. Restarts are applied every 6 hours and thus over 120 samples. Three experiments without DA are designed first with model lids at 50-mb (WRF-50), 10-mb (WRF-10), and 1-mb (WRF-1), respectively. The systematic differences are studied through these three experiments. CTRL experiments with the selected DA configuration are also setup with all operational available observations with different model lids. The impacts of extra stratospheric information included via DA system can be obtained then. Another two configurations involving operationally available conventional observations and microwave observations are designed: the experiment with a selection of microwave channels at all levels (Whole), and a troposphere experiment (TRO) with a selection of only tropospheric microwave channels. The forecast results are also verified against conventional observations at different forecast lead times. After comparison of the inclusion of more stratospheric information in DA system, a forecast sensitive to observations (FSO) technique is applied on the regional model to give out a final

selection of the microwave channels which have positive impacts on regional NWP. A list of all the major experiment configurations is shown in Table 5.

Table 3 A list of major Experiment configurations

	Expt.	Description
The first set of experiments (Model top at 50-mb)	3D-Var	GSI 3D-Var configuration with all operationally available observations
	Hybrid	GSI 3D-Var based Ensemble-Variational Hybrid configuration using 40 ensemble members with all operationally available observations (20% weight on the static covariance and 80% weight on the ensemble covariance)
	EnKF	GSI Ensemble Kalman Filter configuration using 40 ensemble members with all operationally available observations
The second set of experiments (Model top at 10-mb)	CTRL	Experiment with the selected GSI DA configuration with all operationally available observations
	IR	Experiment with the selected GSI DA configuration with all operationally available conventional observations and infrared satellite observations only
	MW	Experiment with the selected GSI DA configuration with all operationally available conventional observations and microwave satellite observations only
The third set of experiments (Model top at 1-mb)	WRF-50, WRF-10, WRF-1	Experiments with different model lids at 50-mb, 10-mb, and 1-mb, respectively. No DA is applied.
	CTRL	Experiment with the selected GSI DA configuration with all operationally available observations
	Whole	Experiment with the selected GSI DA configuration with all operationally available conventional observations and a selection of all microwave satellite channels
	TROPO	Experiment with the selected GSI DA configuration with all operationally available conventional observations and a selection of tropospheric satellite channels only

For further evaluation of the results obtained in each set of experiments, two individual heavy precipitation events occurred in July, 2012 and Jan., 2015 are used. A list of the experiments configuration used for individual case studies are listed in Table 6.

Table 4 A list of Experiment configurations for individual case studies

	Expt.	Description
For the evaluation of the first set of experiments (Model top at 50-mb)	CTRL	WRF predictions without DA system
	3D-Var	GSI 3D-Var configuration with all operationally available observations
	Hybrid	GSI 3D-Var based Ensemble-Variational Hybrid configuration using 40 ensemble members with all operationally available observations (20% weight on the static covariance and 80% weight on the ensemble covariance)
	EnKF	GSI Ensemble Kalman Filter configuration using 40 ensemble members with all operationally available observations
For the evaluation of the second set of experiments (Model top at 10-mb)	CTRL	WRF predictions without DA system
	IR	GSI Hybrid configuration with all operationally available conventional observations and infrared satellite observations only
	MW	GSI Hybrid configuration with all operationally available conventional observations and microwave satellite observations only
	CON	GSI Hybrid configuration with conventional observations only
For the evaluation of the third set of experiments (Model top at 1-mb)	CTRL	WRF predictions without DA
	CTRL-DA	GSI Hybrid configuration with the same observations input in previous experiment
	Whole	GSI Hybrid configuration with all operationally available conventional observations and a selection of all microwave satellite channels
	TROPO	GSI Hybrid configuration with all operationally available conventional observations and a selection of tropospheric satellite channels only
	SELECTED	GSI Hybrid configuration with all operationally available conventional observations and the selected channels based on FSO results

CHAPTER FOUR EVALUTING THE PERFORMANCE OF DIFFERENT DA CONFIGURATIONS

The major goal of this chapter is to investigate the differences between three GSI DA configurations namely the 3D-Var, Hybrid, and EnKF which lead to an optimized selection of the DA algorithms under certain conditions.

4.1 Introduction

As DA algorithms developed, large improvements have been obtained in many global NWP systems (such as in Fig. 1). The differences between each DA algorithm are complex due to different ways of the observations assimilated into the system, the source of background error covariance, model forecast errors, the calculation of innovations, the processes of non-linear problems, the inclusion of ensembles, computational resources, etc. As described in chapter 2, EKF is theoretically proved the “gold standard” of DA. However, the large requirements of computational resources made the EKF not that “efficient” in data assimilation system. Thus, a simplified form of KF namely the EnKF and hybrid of ensemble-variational methods have been designed, tested and compared in many global NWP systems (Caya, et al., 2005; Wang, et al., 2013; Lorenc, et al., 2015). These comparisons show that the EnKF with proper pre-process (e.g., multi carefully selected schemes ensembles and covariance inflation in ensembles) usually have better performances in later DA cycles compared to variational methods, and the hybrid of ensemble-variational methods have the potential skills in improving NWP systems. Some

comparisons were also taken out in individual case studies (Meng, and Zhang, 2008; Schwartz, et al., 2013). The comparisons of applying DA algorithms on regional NWP systems are even more complex. Different DA algorithms have different impacts on regional scale, mesoscale, and convective scale systems. How the DA systems were configured also have large impacts on the results. Meng and Zhang found that significant improvements were obtained if three outer loops were used instead of one outer loop in 3D-Var. In this chapter, more detailed impacts of DA algorithms on regional NWP system such as the performance in different seasons, different layers, and different variables are investigated. The first set of experiments described in chapter 3 is used to test the performance of three major DA configurations namely 3D-Var, 3D-Var based ensemble-variational hybrid (Hybrid), and EnKF on regional weather predictions.

4.2 Statistical Results

4.2.1 Comparing the Convergence Rate during Variational Minimization

To investigate the impacts of the regional ensembles generated from WRF-ARW on the variational minimization, the convergence rate measured by the ratio of the gradient norm relative to the initial gradient norm averaged over winter and summer are compared. In Fig. 8, the convergence rate of the first outer loop during winter (Fig. 8a) is similar to what Wang et al. (2013) obtained. Hybrid shows slightly slower convergence rate at first few iterations and slightly faster convergence rate at later iterations than 3D-Var. For the second outer loop in winter (Fig. 8c), the result is similar to the first outer loop. In contrast, Dr. Wang (2013) found that the Hybrid scheme shows overall faster convergence rate in the second outer loop in his global experiment. For the convergence

rate obtained in summer (Fig. 8b, d), the Hybrid shows overall faster rates in both first and second outer loops than 3D-Var. The inclusion of ensembles showed better performance during summer.

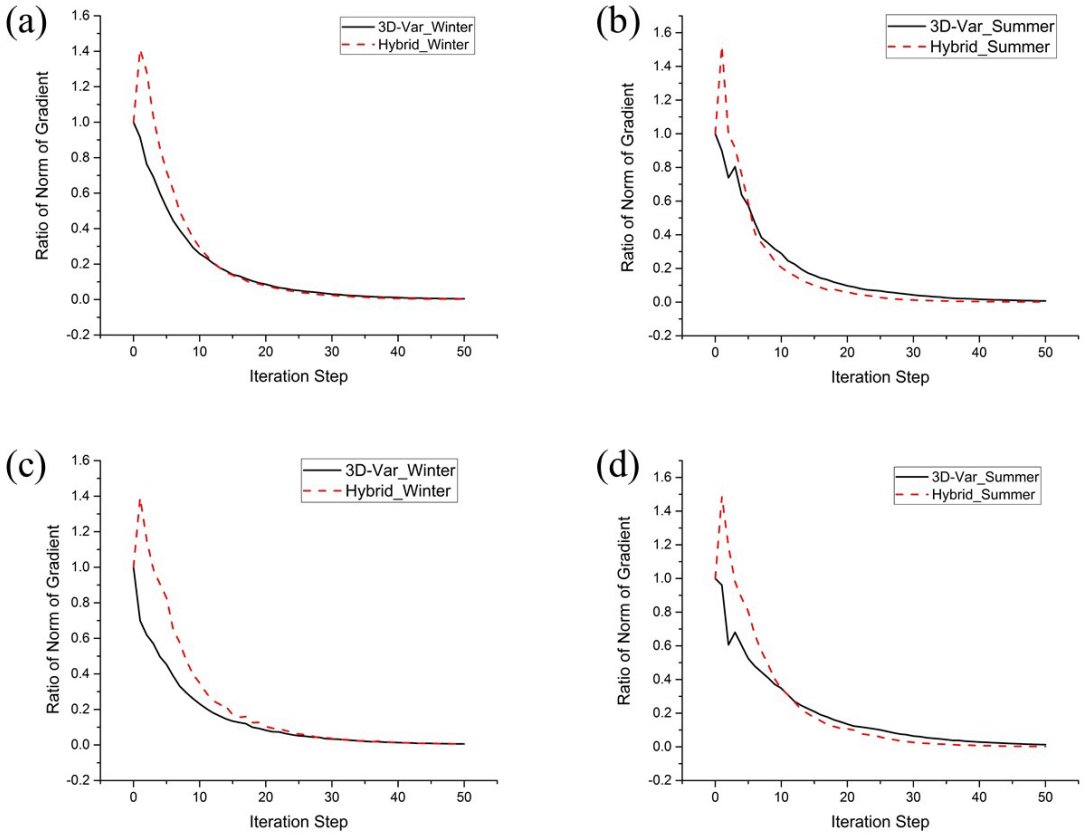

Figure 8 Variational DA convergence rate at different outer loops.

4.2.2 Fits of Analysis to Observations

Averaged bias and root mean square deviation (RMSD) over the study periods are calculated to investigate the performance of three tested DA configurations on WRF-ARW initial conditions. The absolute value of bias and RMSD of analyzed surface

pressure, all-level mean temperature, all-level mean wind, all-level mean relative humidity (RH), and precipitable water fit to conventional observations averaged over two seasons are shown in Table 7.

Table 5 Impacts of DA on WRF-ARW initial conditions

DA Algorithms	Surface Pressure (Pa)	Winter		Summer	
		Before DA	After DA	Before DA	After DA
3D-Var	Bias	0.1288	0.0143	0.0813	0.0376
	RMSD	1.3544	1.2926 (5%)	0.9054	0.8554 (6%)
Hybrid	Bias	0.1288	0.0222	0.0813	0.0104
	RMSD	1.3544	1.2190 (10%)	0.9054	0.7624 (16%)
EnKF	Bias	0.1288	0.0910	0.0813	0.1681
	RMSD	1.3544	1.3124 (3%)	0.9054	1.0204
	All-level mean Wind (m s^{-1})	Before DA	After DA	Before DA	After DA
3D-Var	Bias	0.3898	0.3789	0.9212	0.4730
	RMSD	3.6031	3.1920 (11%)	3.0588	2.6428 (14%)
Hybrid	Bias	0.3898	0.3989	0.9212	0.5493
	RMSD	3.6031	3.3356 (7%)	3.0588	2.7618 (10%)
EnKF	Bias	0.3898	0.2240	0.9212	0.4719
	RMSD	3.6031	3.2775 (9%)	3.0588	2.6435 (14%)
	All-level mean T (K)	Before DA	After DA	Before DA	After DA
3D-Var	Bias	0.6769	0.2474	0.9351	0.3518
	RMSD	1.9924	1.7081 (14%)	2.2060	1.8142 (18%)
Hybrid	Bias	0.6769	0.2394	0.9351	0.3749
	RMSD	1.9924	1.6376 (18%)	2.2060	1.7360 (21%)
EnKF	Bias	0.6769	0.1933	0.9351	0.1609
	RMSD	1.9924	1.8332 (8%)	2.2060	1.8139 (18%)
	All-level mean RH (%)	Before DA	After DA	Before DA	After DA
3D-Var	Bias	1.9233	0.9917	3.0161	1.6242
	RMSD	12.4896	9.8259 (21%)	10.1325	9.0011 (11%)
	All-level mean RH (%)	Before DA	After DA	Before DA	After DA
Hybrid	Bias	1.9233	1.1822	3.0161	2.7696
	RMSD	12.4896	10.285 (18%)	10.1325	8.8991 (12%)
EnKF	Bias	1.9233	1.8117	3.0161	3.3640
	RMSD	12.4896	12.0191 (4%)	10.1325	10.3190
	Precipitable Water (mm)	Before DA	After DA	Before DA	After DA

3D-Var	Bias	0.2876	0.7819	0.6652	0.9288
	RMSD	2.1697	2.4708	3.5967	3.9327
Hybrid	Bias	0.2876	0.3527	0.6652	0.5283
	RMSD	2.1697	2.2059	3.5967	3.5850
EnKF	Bias	0.2876	0.3348	0.6652	0.6894
	RMSD	2.1697	2.1942	3.5967	3.5310

Overall better performance is obtained in summer. Hybrid shows similar impacts on regional initials to those of 3D-Var. Both Hybrid and 3D-Var show better performance (3%) than winter. EnKF configuration shows some advantages in adjusting wind, summer temperature and precipitable water in the initial conditions.

The absolute value of analyzed wind, temperature, and RH profiles fit to conventional observations averaged over the two experimental periods (black solid lines for winter and red dashed lines for summer) are shown in Fig. 9. Solid square, solid circle, solid triangle, and × are for initial conditions, 3D-Var analysis, Hybrid analysis, and EnKF analysis, respectively. For different seasons, summer results show smaller RMSDs and larger improvements. For vertical variations, larger improvements are obtained over the lower boundary layers and the tropopause layers (150-250 hPa for winter, and 50-150 hPa for summer). For initial wind profiles, comparable biases are obtained for most of the layers except EnKF shows larger biases in the troposphere. In winter, 13%, 8%, and 11% improvements are obtained over the lower troposphere for 3D-Var, Hybrid, and EnKF, respectively. 22%, 9%, and 7% improvements are obtained over the tropopause layers for three DA schemes, respectively. An average extra 4% improvement is obtained in summer compared to winter results. 3D-Var shows larger improvements than Hybrid and EnKF. For initial temperature profiles, larger biases are

found in summer over lower troposphere and tropopause. Improvements made in temperature profiles are similar to wind profiles. 21%, 22%, and 5% improvements are obtained over lower troposphere for three DA schemes, respectively. 14%, 22%, and 23% improvements are obtained over tropopause layers, respectively. Greater improvements are also obtained during summer with extra 10% skills. For the initial RH profiles, only Hybrid shows overall improvements and better performance than 3D-Var. EnKF enlarges both bias and RMSDs in the initial RH profiles.

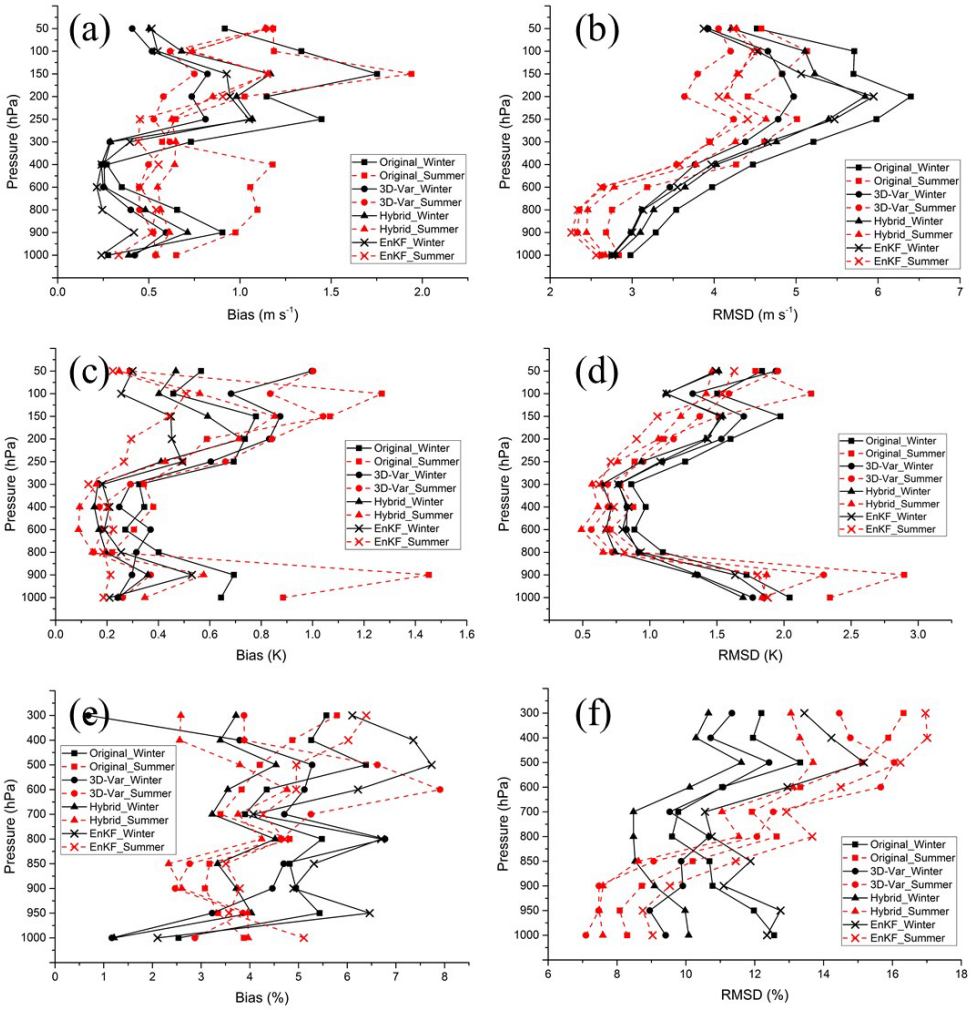

Figure 9 Averaged bias and RMSD of the analyzed wind, temperature, and RH profiles as a function of pressure.

The results of analyses show that Hybrid shows overall better performance than 3D-Var during both seasons especially in adjusting RH profiles in upper layers. EnKF performs better in adjusting lower level winds during winter and lower level temperature during summer. EnKF also gives out better precipitable water results despite the bad performances in adjusting RH profiles.

4.2.3 Verification of Tropospheric Forecasts

The absolute values of biases and RMSDs of predicted surface pressure, wind, temperature, and RH verified against the conventional observations at different forecast lead times over the continental U. S. are averaged during winter and summer.

4.2.3.1 Forecasts of Surface Pressure

The averaged bias and RMSD of the predicted surface pressure fit to conventional observations at different forecast lead times (12-, 24-, 36-, 48-, 60-, 72-h) are plotted in Fig. 10(a, b), respectively. Black lines indicate winter predictions and red lines indicate summer predictions. Solid, dashed, and dotted lines for predictions of 3D-Var experiment, Hybrid experiment, and EnKF experiment, respectively. As shown in Fig. 10, the Hybrid configuration performs similar forecast results to 3D-Var with extra 3% skill. In winter, 10% less skills in predicting surface pressure is observed in EnKF scheme. However, an averaged extra 22% skills is obtained in EnKF in summer compared to 3D-Var.

Generally, the predicting skills will fall as the lead time increases. For bias, 3D-Var and Hybrid perform very small increase of surface pressure biases during both seasons (both with slopes of ~0.03). In contrast, EnKF shows faster increase rate (with a larger slope of 0.11) during winter. For RMSDs, all three DA configurations show similar decrease rate of predicting skills during summer (with slopes of ~0.10). For winter surface pressure predictions, EnKF shows faster decrease rate (with a slope of 0.17) than 3D-Var and Hybrid (with slopes of ~0.14).

Diurnal bias variations are observed in all three experiments especially during summer. 3D-Var and Hybrid have better predictions at lead times of 24-h, 48-h and 72-h

during winter, but opposite results during summer. EnKF shows more stable prediction skills for daily variations in which the predictions at lead times of 12-h, 36-h, and 60-h are slightly better than the others.

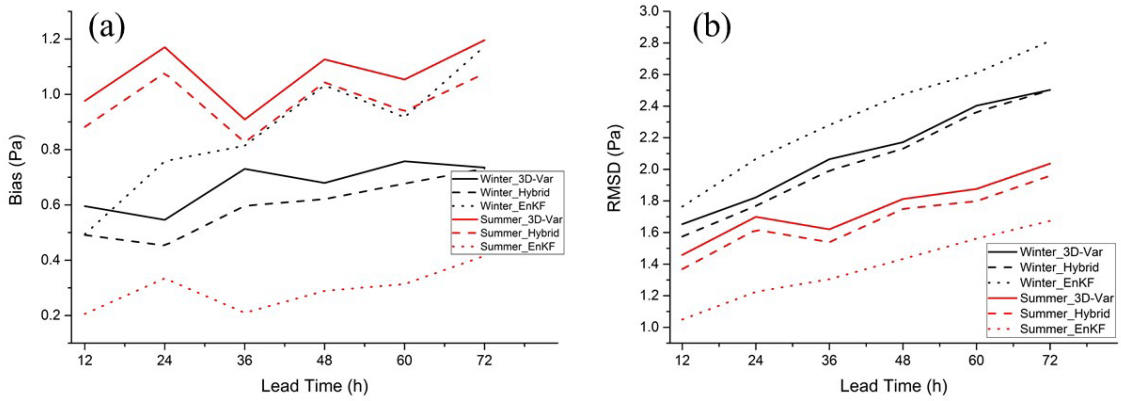

Figure 10 Averaged bias and RMSD of the predicted surface pressure.

For surface pressure predictions, Hybrid shows overall advantages in winter and EnKF shows better skills in summer. Also, the diurnal variations show that Hybrid predictions have better performance during the late afternoon (17:00-19:00 LST) in winter and better performance during the early morning (5:00-7:00 LST) in summer. In contrast, EnKF shows better skills in predicting surface pressure during the early morning (5:00-7:00 LST) without season variabilities.

4.2.3.2 Forecasts of Wind

The averaged biases and RMSDs of all-level mean wind and wind profile predictions during both seasons are plotted in Fig. 11(a, b), respectively. As shown in Fig. 11, summer has overall lower RMSDs but close values of biases than winter. EnKF shows

much lower biases (Fig. 11a) during the early forecast lead hours (12-, 24-, 36-h) in winter and then reaches equivalent levels to 3D-Var and Hybrid. However, EnKF has higher RMSDs (Fig. 11b) compared to 3D-Var and Hybrid. In summer, 3D-Var and Hybrid give close values of biases in the early forecast lead hours (12-, 24-, 36-h) and then Hybrid has a slightly increase of biases in the later forecasts. Hybrid and EnKF have very close RMSDs during the summer which are slightly smaller than 3D-Var. Hybrid showed better skills in predicting wind during summer and relatively longer predictions of wind during winter. EnKF has some advantages in 1-day wind prediction in winter, but higher RMSDs.

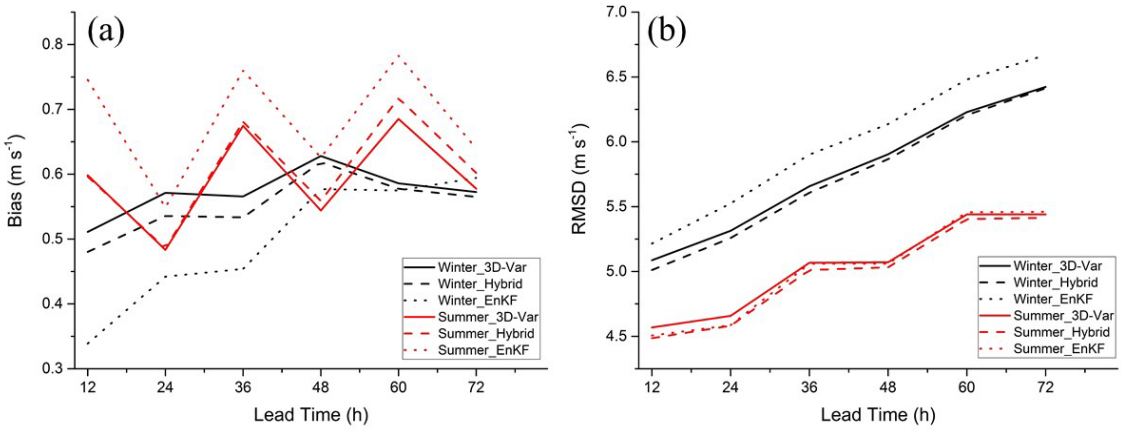

Figure 11 Averaged bias and RMSD of the predicted all-level mean wind.

Diurnal variations especially in summer are also observed when predicting wind. All three DA configurations show better skills in predicting wind in the early morning (5:00-7:00 LST) in winter while both biases and RMSDs are lower in the late afternoon (17:00-19:00 LST) in summer.

The averaged biases and RMSDs of wind profiles are plotted in Fig. 12(a, b), respectively. The wind predictions in summer have overall better skills (~10%) then the predictions in winter. All three DA configurations show the largest RMSDs in the tropopause layers (150-250 hPa for winter, and 50-150 hPa for summer). Compared to the 6-week global experiments starting in December 2010 did by Dr. Wang (2013), the results show that both global and regional models can't properly simulate the atmospheric state in the tropopause layers (150-250 hPa), and the regional predictions show larger RMSDs. Less than 2% differences are observed in 3D-Var and Hybrid in both seasons. EnKF shows slighter larger RMSDs than the other two DA configurations in winter. Larger increasing rate of RMSDs over the tropopause layers (150-250 hPa) are observed in EnKF. But these differences are getting smaller as lead time increases. EnKF and Hybrid have comparable RMSDs in summer and both RMSDs are slightly smaller than 3D-Var over all levels.

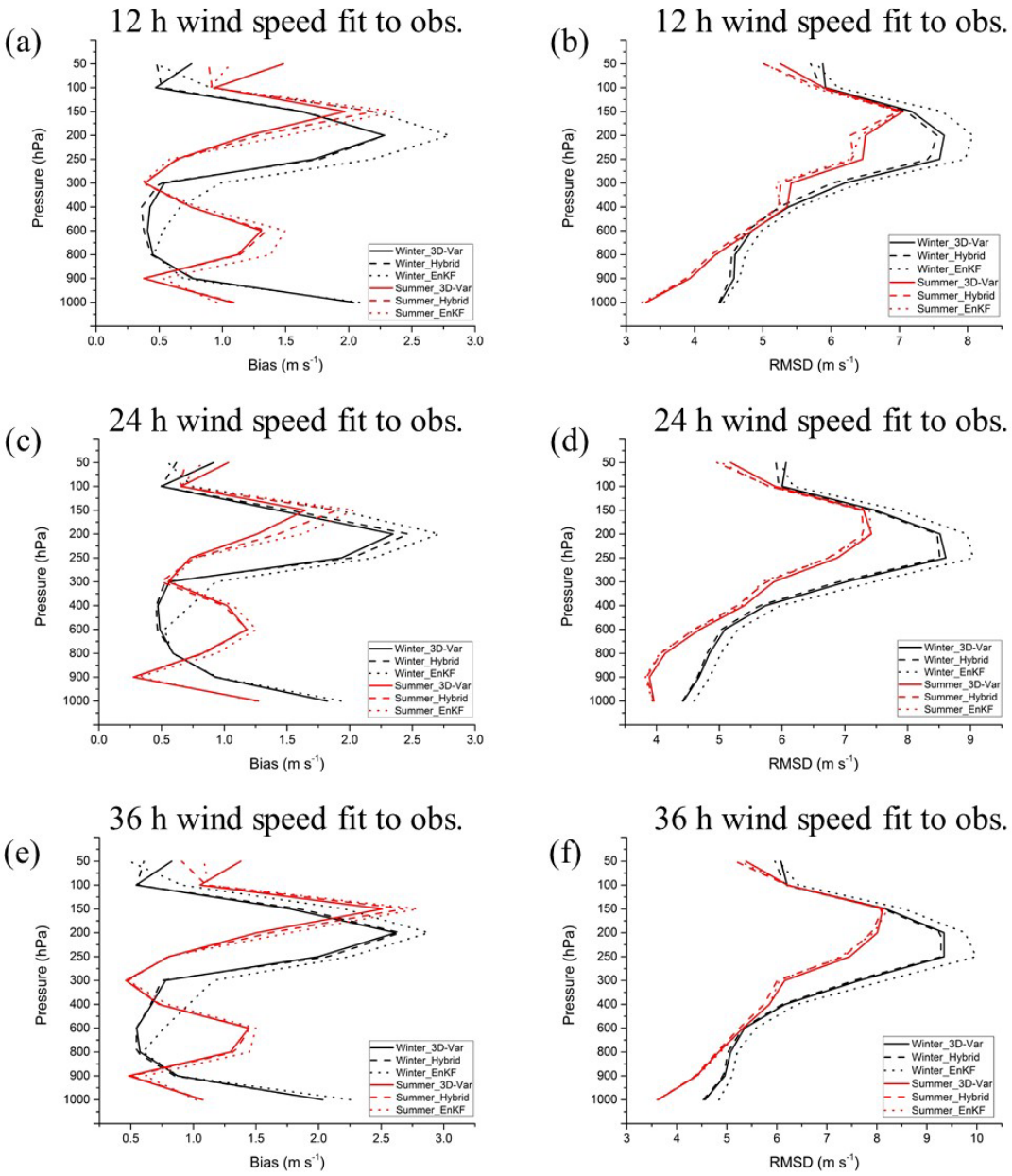

Figure 12 Continued

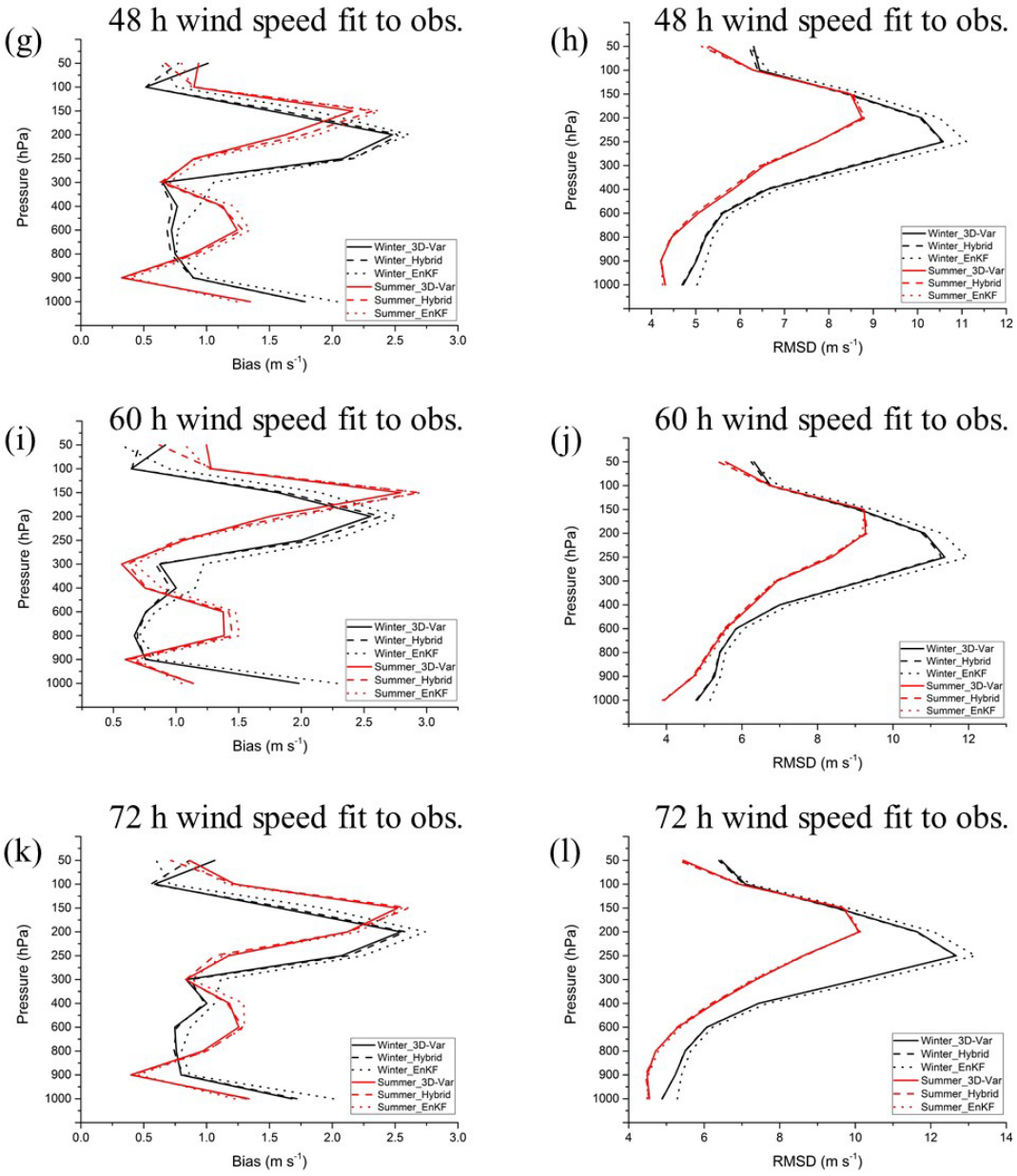

Figure 12 Averaged bias and RMSD of the predicted wind profiles.

The biases of wind profiles in three predictions are not decreasing as the increase of lead time. All three DA configurations show bimodal patterns in winter and tri-modal

patterns in summer. In winter, all three DA configurations show close values of biases in the near surface layers. As the height increases, EnKF shows a faster increase rate of bias especially at 800 hPa in the early morning and 600 hPa in the late afternoon. This feature is also obtained in the summer wind bias profiles with a faster increase rate of bias in the higher troposphere layers in the late afternoon. This feature indicates that when deeper convections exist, more uncertainties are brought into the system via ensembles used in EnKF. Also, the tropopause has the largest biases in all three DA configurations in both seasons. EnKF and Hybrid show better skills than 3D-Var at the model top in both seasons. In summer, one more bias peak is found at the middle layers of the troposphere (400-800 hPa) which means all three DA configurations lack the skills of predicting wind when deep convections exist compared to a more stable atmosphere in winter.

4.2.3.3 Forecasts of Temperature

The averaged biases and RMSDs of all-level mean temperature and temperature profile predictions at different forecast lead times during both seasons are plotted in Fig13 and Fig. 14. As shown in Fig. 13, again better predicting skills (~20%) are obtained in all three DA configurations in summer. In winter, 3D-Var and Hybrid show close results of both biases and RMSDs in which Hybrid shows slightly extra 1% skill. EnKF has faster growth of bias and larger RMSD in winter compared to 3D-Var and Hybrid. In summer, all three DA configurations show close skills (close values of RMSDs) in the predictabilities of temperature in which EnKF has better skills in the 12-h lead time predictions and the other two DA configurations have better skills in longer forecast lead time predictions. Diurnal variations are also observed in summer temperature predictions.

3D-Var and Hybrid show similar diurnal variations to those in surface pressure predictions, while EnKF shows the opposite features. Also, 3D-Var has larger amplitude of diurnal variations while EnKF has smaller ones.

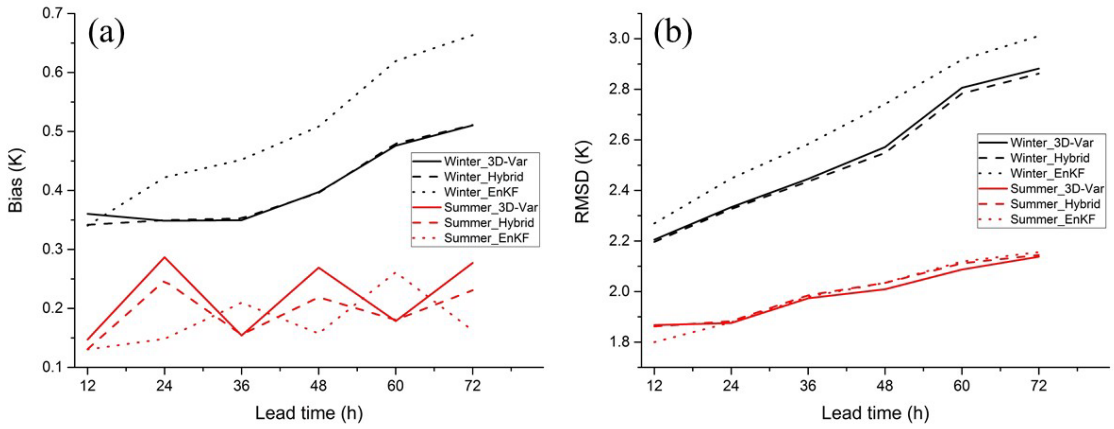

Figure 13 Averaged bias and RMSD of the predicted all-level mean temperature.

The predicted temperature profiles fit to conventional observations are plotted in Fig. 14. For different seasons, smaller biases are obtained in the troposphere and comparable values of biases are obtained in the tropopause layers. Similar structures are found in RMSD profiles. The predictabilities of winter tropospheric temperature drop faster than those in summer. About an extra 25% skill is found at 12- and 24-h forecast lead times and reaches 34% at 60- and 72-h forecast lead times. 3D-Var and Hybrid show close predictabilities in which Hybrid shows an extra 1% skill. EnKF shows less predictabilities (~7%) in lower troposphere in winter. In contrast, an extra 10% skill is obtained over the tropopause layers during both seasons in EnKF configuration.

Both biases and RMSDs of temperature profiles show a bimodal structure in both seasons. The first peak values of biases and RMSDs are obtained in the lower boundary layers (below 900 hPa), and the second peak is again obtained over the tropopause layers. The obtained RMSDs of temperature profile predictions at longer forecast lead times in winter show similar structure to the results obtained by Dr. Wang (2013) with the lowest predict skills in the lower boundary layers and then in the tropopause layers. The RMSDs in summer show that the predict skills at lower boundary layers and the tropopause layers are comparable. The bias profiles show that larger biases are occurred in the tropopause layers. The bias peaks in the tropopause layers are much larger than those in the lower level during summer.

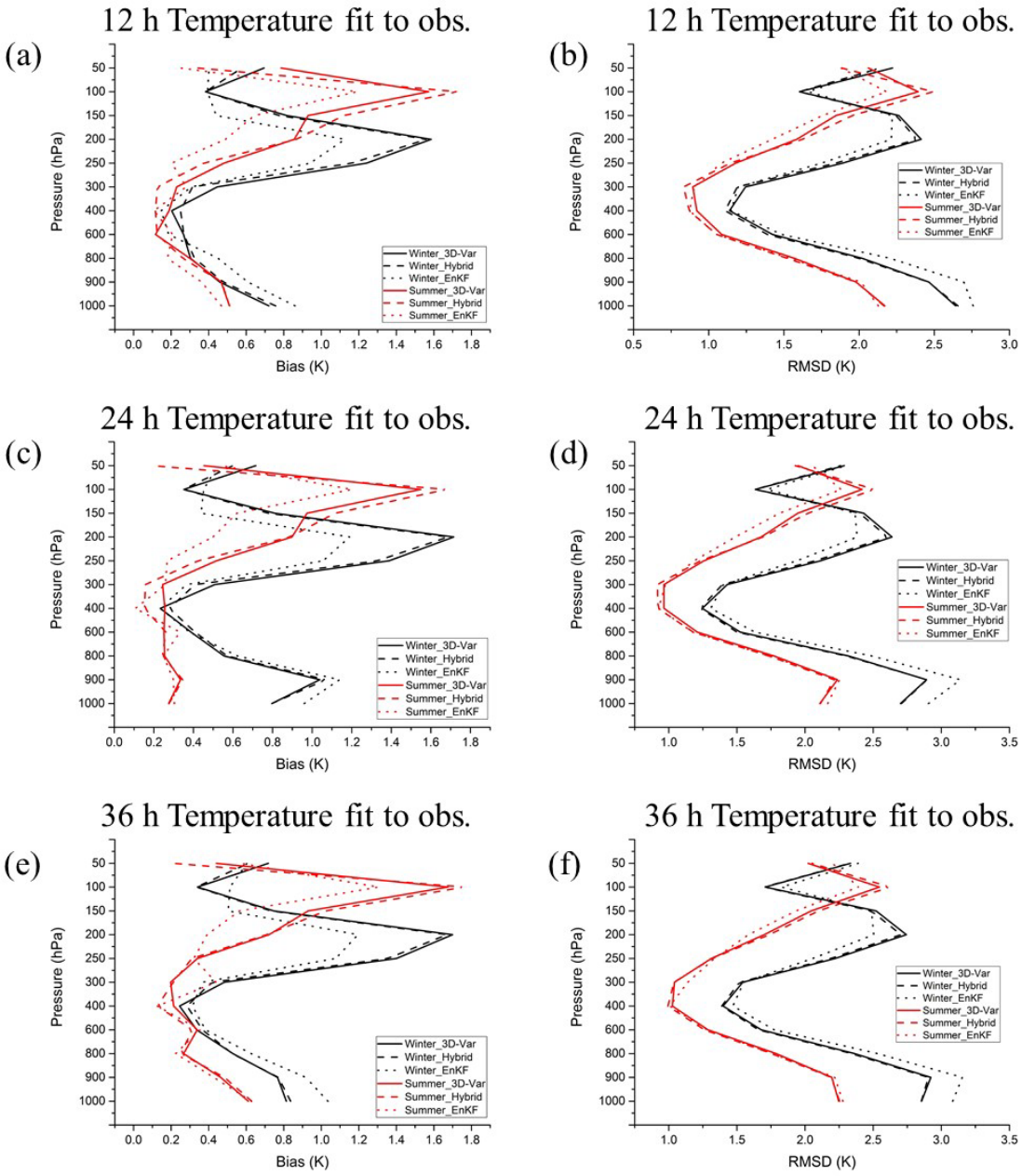

Figure 14 Continued

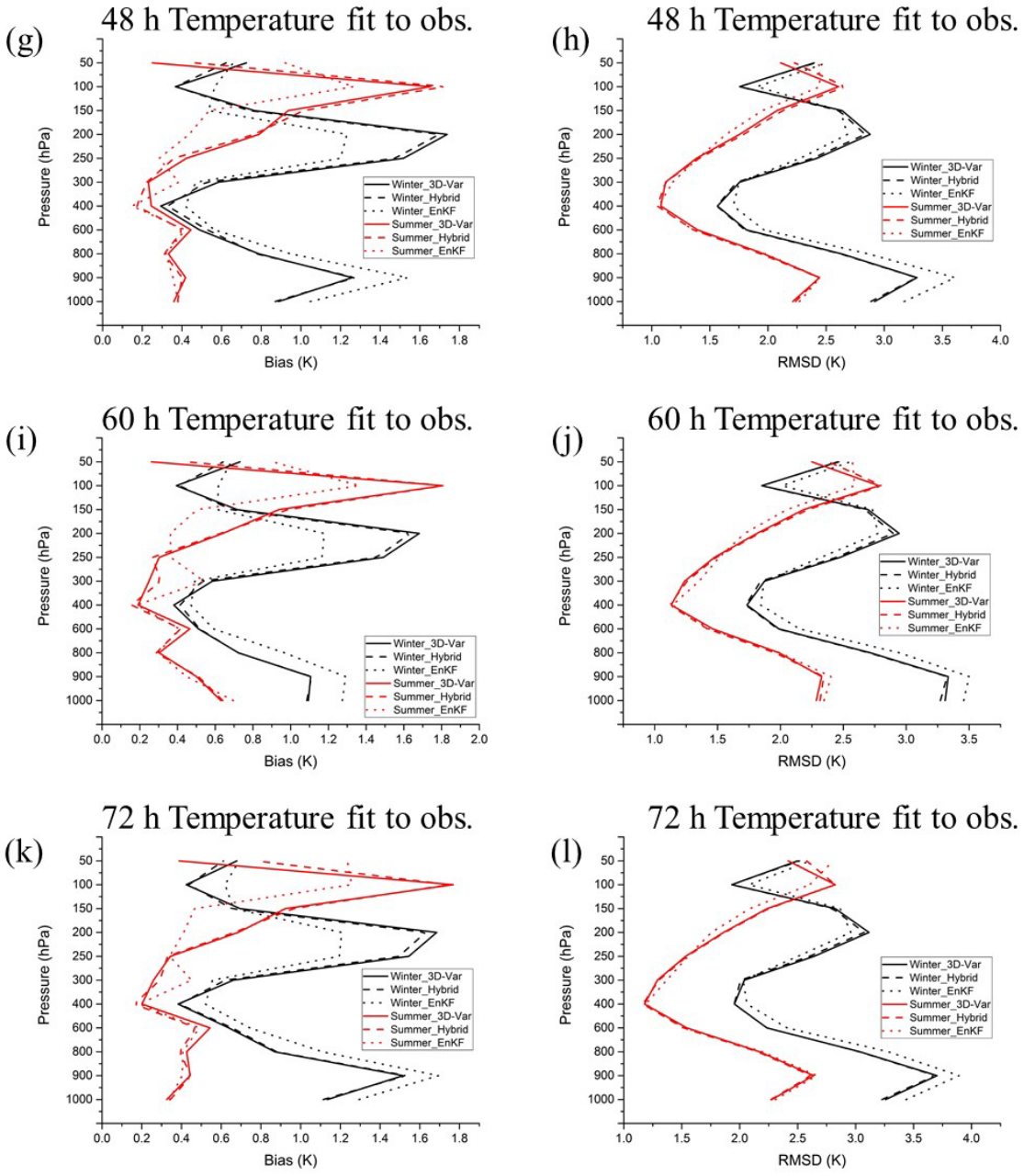

Figure 14 Averaged bias and RMSD of the predicted temperature profiles.

Above all, EnKF shows better predictabilities in predicting temperature. Smaller biases are obtained using EnKF at tropopause layers. While at lower troposphere, similar results are obtained in which Hybrid shows slightly better skills and lower biases.

4.2.3.4 Forecasts of Relative Humidity

Compared to the predictions of surface pressure, all-level mean wind and all-level mean temperature, the predicted RH have much larger biases and RMSDs (Fig. 15). Again, all three DA configurations have better performance during summer with much smaller bias growing rate (~0.64) than winter (~1.39) (Fig. 15a). 3D-Var and Hybrid show comparable results in which an extra 1% skill is obtained in Hybrid experiment. EnKF shows much larger biases and RMSDs than the other two DA configurations in winter. A drop of 10% skill is observed in EnKF scheme in winter. In summer, EnKF shows similar results to variational schemes with an extra 2% skill obtained during the 12- to 36-h forecast lead times compared to 3D-Var and then reaches a comparable level.

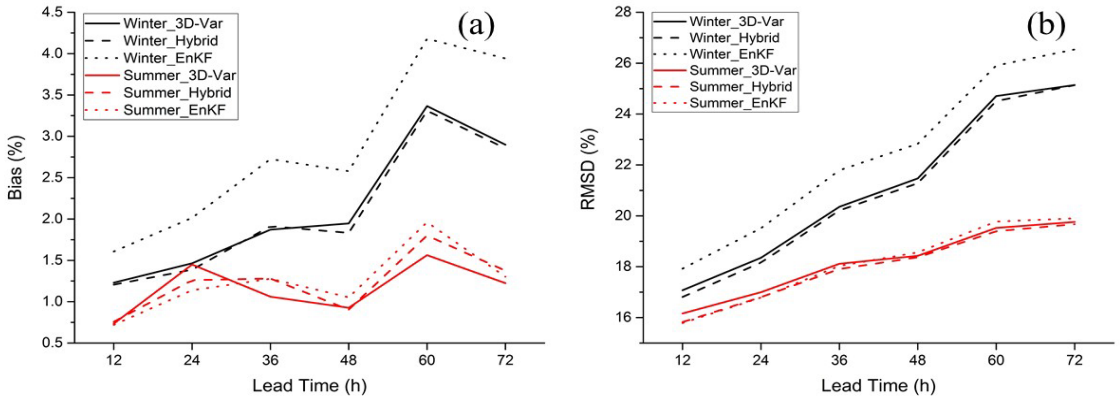

Figure 15 Averaged bias and RMSD of the predicted all-level mean RH.

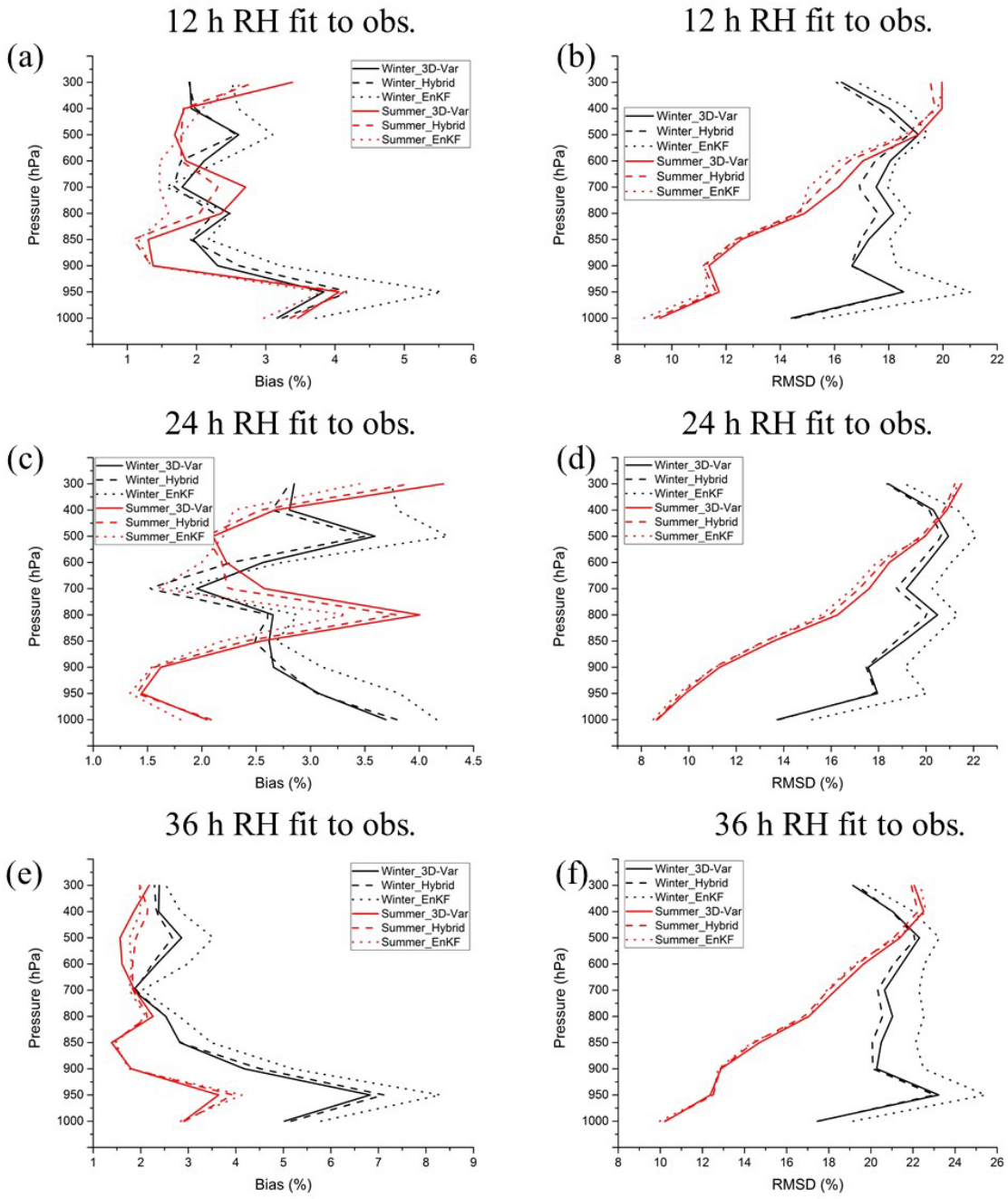

Figure 16 Continued

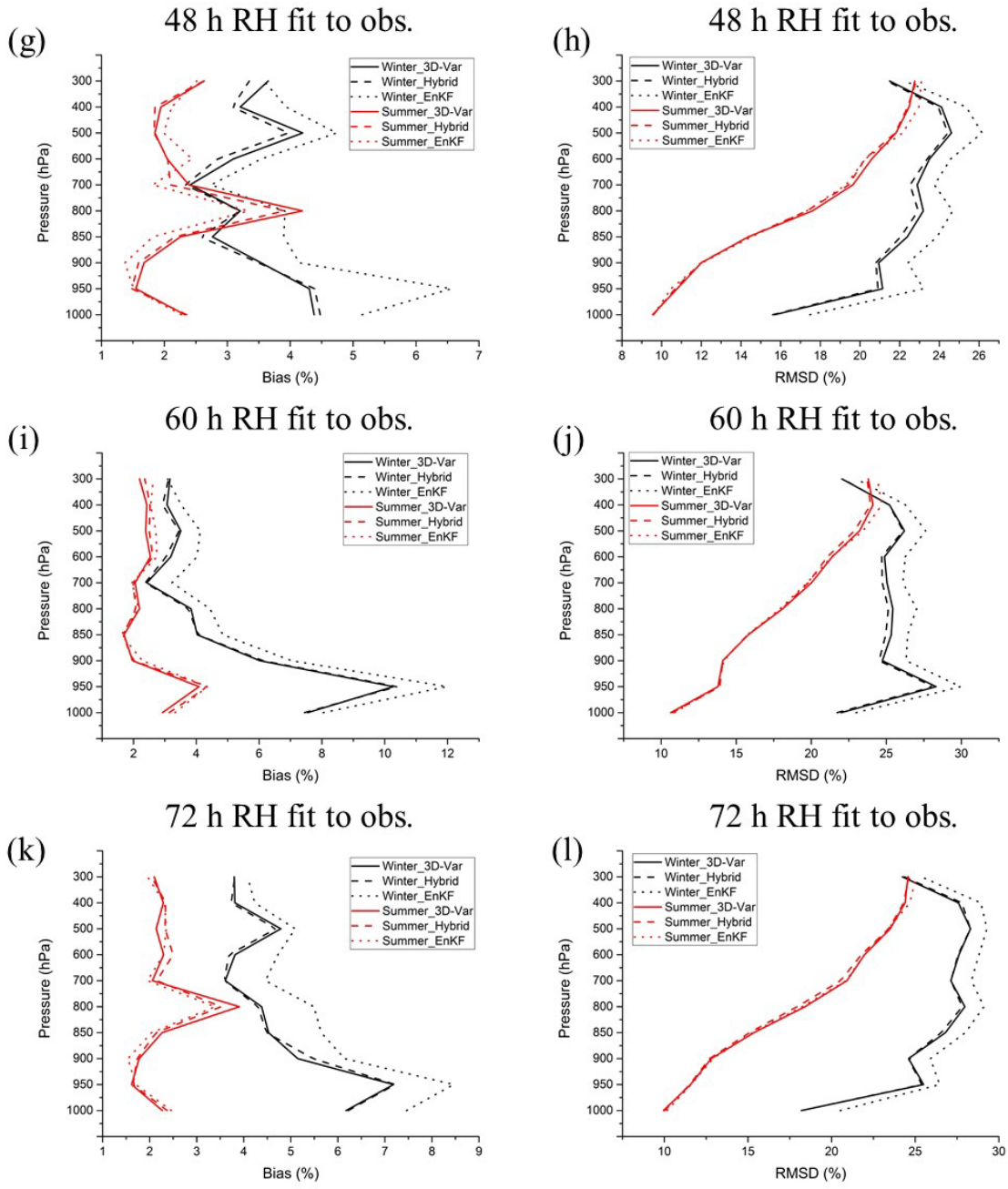

Figure 16 Averaged bias and RMSD of the predicted RH profiles.

The RH bias and RMSD profiles are plotted in Fig. 16. Generally, smaller biases and RMSDs are observed during summer. Beside the overall smaller biases observed in

summer in the left column in Fig. 16, larger biases are observed at 800 hPa level at 12-, 24-, and 48-h forecast lead times. Larger RMSDs are also observed above 400 hPa levels as shown in the right column in Fig. 16. In summer, all three DA configurations show close RMSDs in which EnKF shows slightly smaller results (extra 3% skill) over 800 hPa levels at 12-, and 24-h forecast lead times. In contrast, EnKF gives the lowest predicting skills in winter with much larger RMSDs over all levels (~6% less skill) while Hybrid gives more stable predicting skills in winter compared to 3D-Var. For biases, similar results are obtained. All three DA configurations show close results in summer with smaller biases obtained by EnKF at 800 level. In winter, EnKF gives much larger biases especially over the near surface levels.

The forecasts of RH profiles in all three DA configurations also show significant diurnal variations in summer. At 12-. 36-, and 60-h forecast lead times, larger biases are obtained over lower levels at 950 hPa while at 24-, 48-, and 72-h forecast lead times, larger biases are obtained at higher levels (800 hPa). Different from wind, and temperature, the diurnal variations in RH profiles are probably caused due to the insufficiency of dealing convections in the afternoon in regional weather forecasting model.

Similar to the forecasts of surface pressure and temperature, EnKF gives better results in summer especially at early forecast lead times. In contrast, EnKF shows much larger biases and RMSDs in winter compared to 3D-Var and Hybrid.

4.2.4 Discussion

4.2.4.1 Analysis Increments

The 3D-Var, Hybrid, and EnKF averaged analysis increments for wind, and temperature (wind results are slightly different from the other variables) in both seasons are compared at different layers.

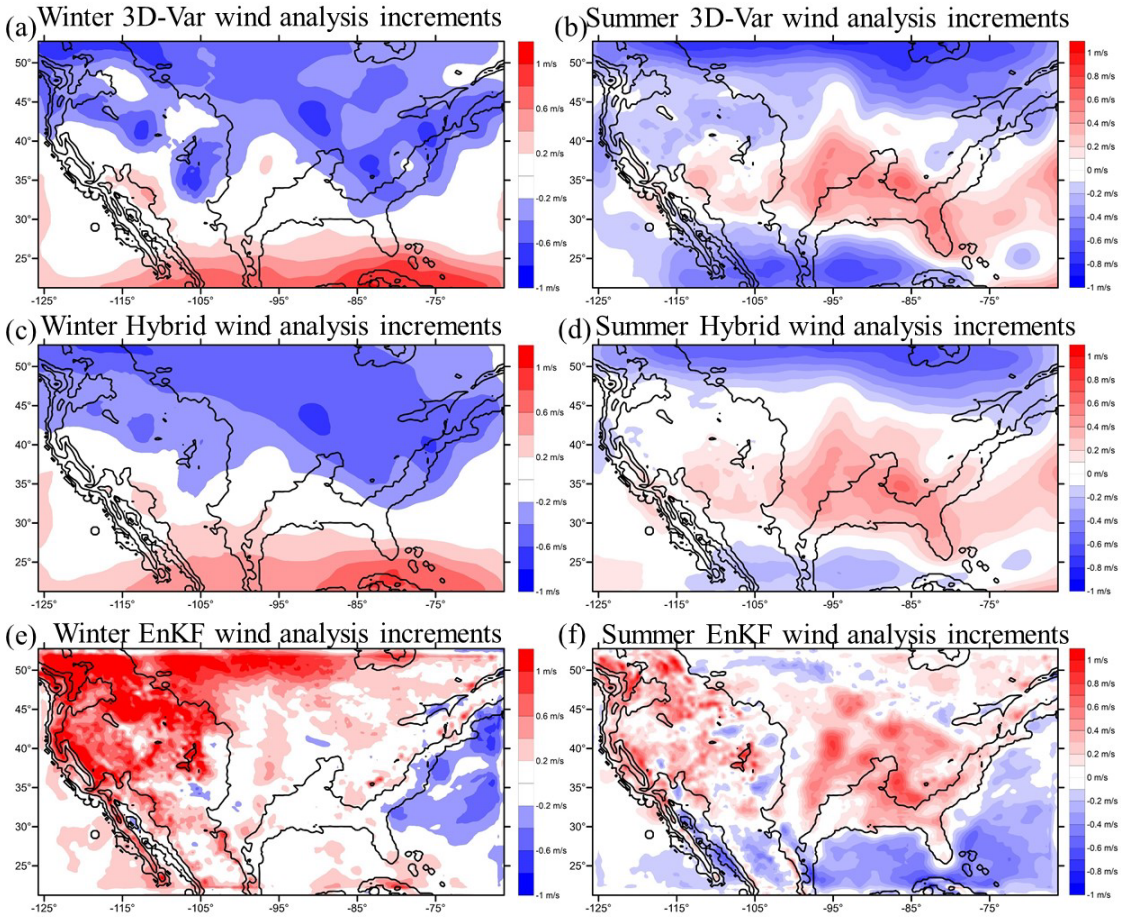

Figure 17 Column-averaged wind analysis increments.

Firstly, the column-averaged wind analysis increments of 3D-Var (Fig. 17a, b), Hybrid (Fig. 17c, d) and EnKF (Fig. 17e, f) in both seasons are compared. The seasonal variations are more obvious in 3D-Var and Hybrid configurations. Both 3D-Var and Hybrid show positive (red areas) increments in the south and negative (blue areas) increments in the north. In contrast, both 3D-Var and Hybrid show negative increments in both south and north but positive increment in the Great Plains and Florida. EnKF does not show much differences between winter and summer in which summer shows more negative increments over the oceans but less positive increments over the Rocky Mountains. By comparing between different DA configurations, Hybrid shows similar increments patterns to the 3D-Var configuration but with smaller magnitude. EnKF shows similar increments patterns to the other two configurations over the Great Plains and the Gulf of Mexico in summer. However, EnKF shows the opposite increments over the Atlantic Ocean and the north part of the Rocky Mountains during both seasons. The opposite characteristics of increments over the Atlantic Ocean and part of the Rocky Mountains may contribute to the differences showed in Table 7 and then propagate forward in the forecasts such as the results that smaller biases and larger RMSDs are obtained in Fig. 11.

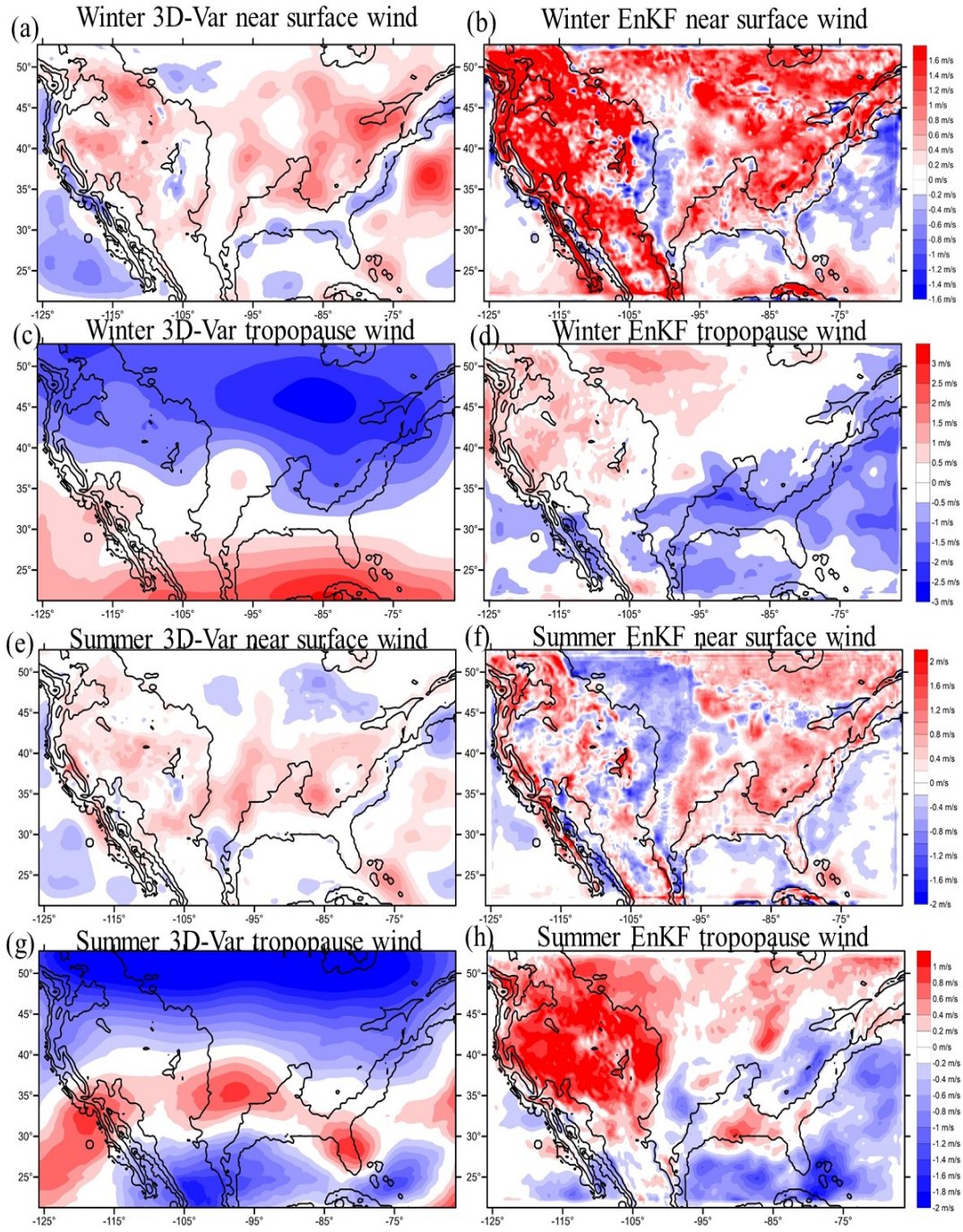

Figure 18 Column-averaged wind analysis increments over near surface and tropopause layers.

The wind analysis increments at near surface layer and tropopause layer are also compared. For the truth that Hybrid shows similar patterns to the 3D-Var configuration, here only 3D-Var (Fig. 18a, c, e, g) and EnKF (Fig. 18b, d, f, h) results are plotted. The patterns of the column-averaged wind analysis increments (Fig. 17) are similar to the patterns of tropopause wind analysis increments (Fig. 18) which means the column-averaged wind analysis increments in 3D-Var are mainly driven by the increments over the high altitudes. In contrast, EnKF shows similar patterns of increments in the near surface layer and the tropopause layer. The major differences between 3D-Var and EnKF wind analysis increments are the opposite impacts over the oceans in the near surface layer in which 3D-Var usually shows positive increments but EnKF usually shows negative increments. Different impacts are also obtained over the north Rocky Mountains over the tropopause layers in which 3D-Var shows all negative increments while EnKF shows large positive increments.

Secondly, the temperature analysis increments (Fig. 19) are compared to the wind analysis increments. The column-averaged temperature analysis increments from 3D-Var and Hybrid show smaller positive increments over the south oceans during winter and the magnitude becomes larger during summer. In contrast, EnKF shows overall negative increments especially over the mountainous areas. The temperature analysis increments at near surface layers and tropopause layers from 3D-Var and EnKF are also compared (Fig. 19). The results are largely different from the wind increments. At the near surface layer, EnKF shows similar patterns to 3D-Var scheme. Overall negative increments are observed at the near surface layer in both seasons in which EnKF shows larger negative

values. At the tropopause layers, overall positive increments are observed in the variational scheme. EnKF shows much smaller increments including negative increments in the Great Lakes area. Two observations over the troposphere in the south California and Oklahoma showed significant impacts on both 3D-Var and EnKF increments during both seasons. Different from wind increments, EnKF shows similar results to variational schemes but tends to have more negative increments.

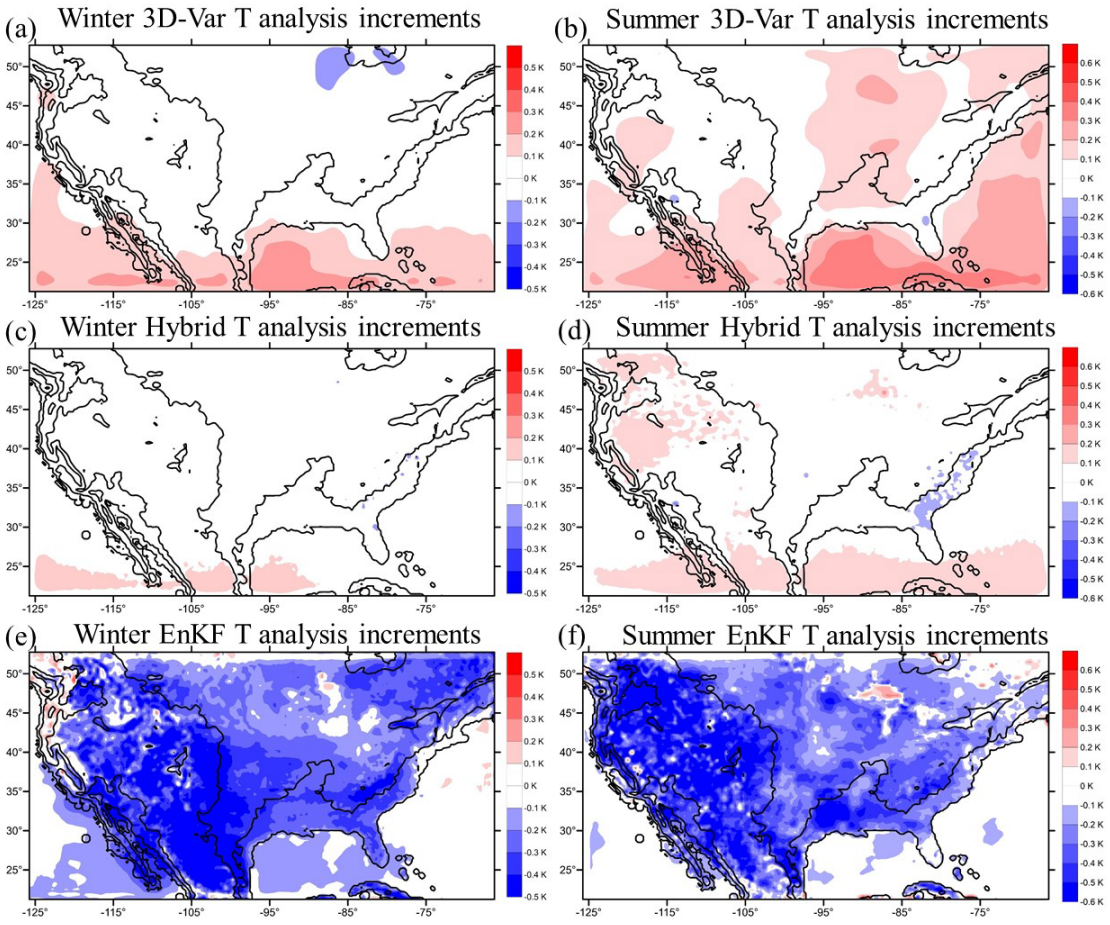

Figure 19 Column-averaged temperature analysis increments.

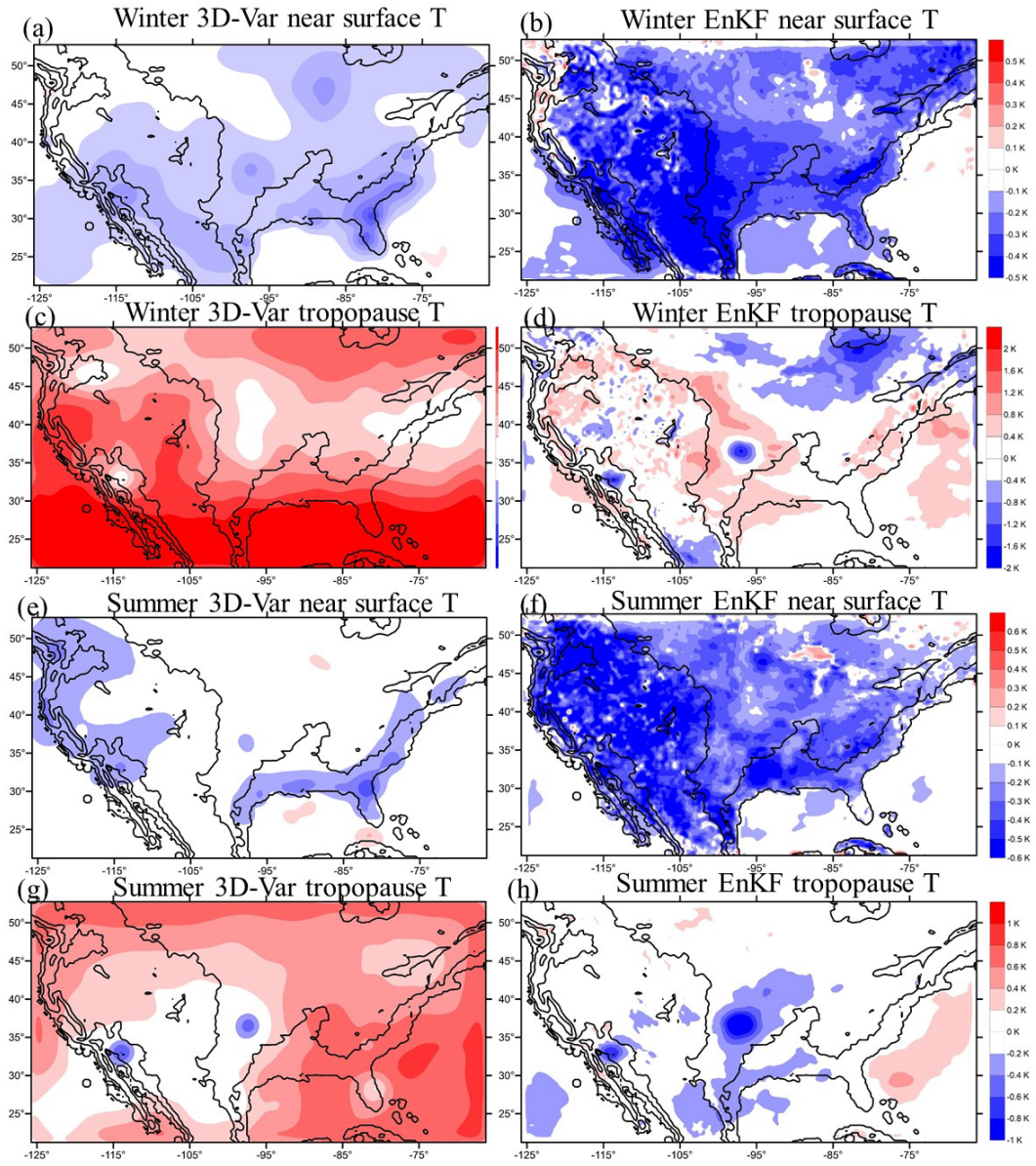

Figure 20 Column-averaged temperature analysis increments at near surface and tropopause layers.

4.2.4.2 Bias Variations

In previous sections, we found that after the application of DA especially when 3D-Var is applied, diurnal variations become more obvious in the predicted surface pressure, column-averaged wind and column-averaged temperature biases during

summer. Firstly, the system diurnal errors are brought out by perform a control (CTRL) experiment without the application of DA. Then, a 3D-Var configuration (3D-Var_4) during summer was applied to test if the diurnal variations are caused by the application of one-time DA in a day. In this experiment, the same observations, observation operators, satellite bias correction algorithms, and quality control decisions are used, but DA applications are applied four times a day at 00:00 UTC, 06:00 UTC, 12:00 UTC, and 18:00 UTC. Both experiments are conducted during the summer period. The averaged biases of surface pressure, all-level mean wind, and all-level mean temperature are obtained in Fig. 21. The averaged diurnal difference is used to represent the diurnal variations. The systematic diurnal variations for all three variables can be obtained in Fig. 20a in which ~0.13 Pa for surface pressure, ~0.16 m s^{-1} for wind and ~0.02 K for temperature. The diurnal variations of the 3D-Var experiment obtained from Fig. 9, Fig. 10 and Fig. 12 are ~0.18 Pa for surface pressure, 0.12 m s^{-1} for all-level mean wind and 0.12 K for all-level mean temperature. Compared to the systematic diurnal variations, it is obvious that one-time 3D-Var application has significant impacts on temperature diurnal variations and slightly smaller impacts on surface pressure, but no tend in increasing the magnitude of wind diurnal variations. The diurnal variations obtained in Fig. 20b are 0.08 Pa, 0.02 m s^{-1}, and 0.006 K for surface pressure, all-level mean wind and all-level mean temperature, respectively. Compared to the CTRL and one-time 3D-Var experiments, all diurnal variations are largely reduced which means the diurnal variations of biases obtained in the previous sections are the productions of one-time DA application and when the diurnal variations of the observations are brought into the system via DA four

times a day, the diurnal variations of biases caused by both system errors and one-time DA applications disappeared.

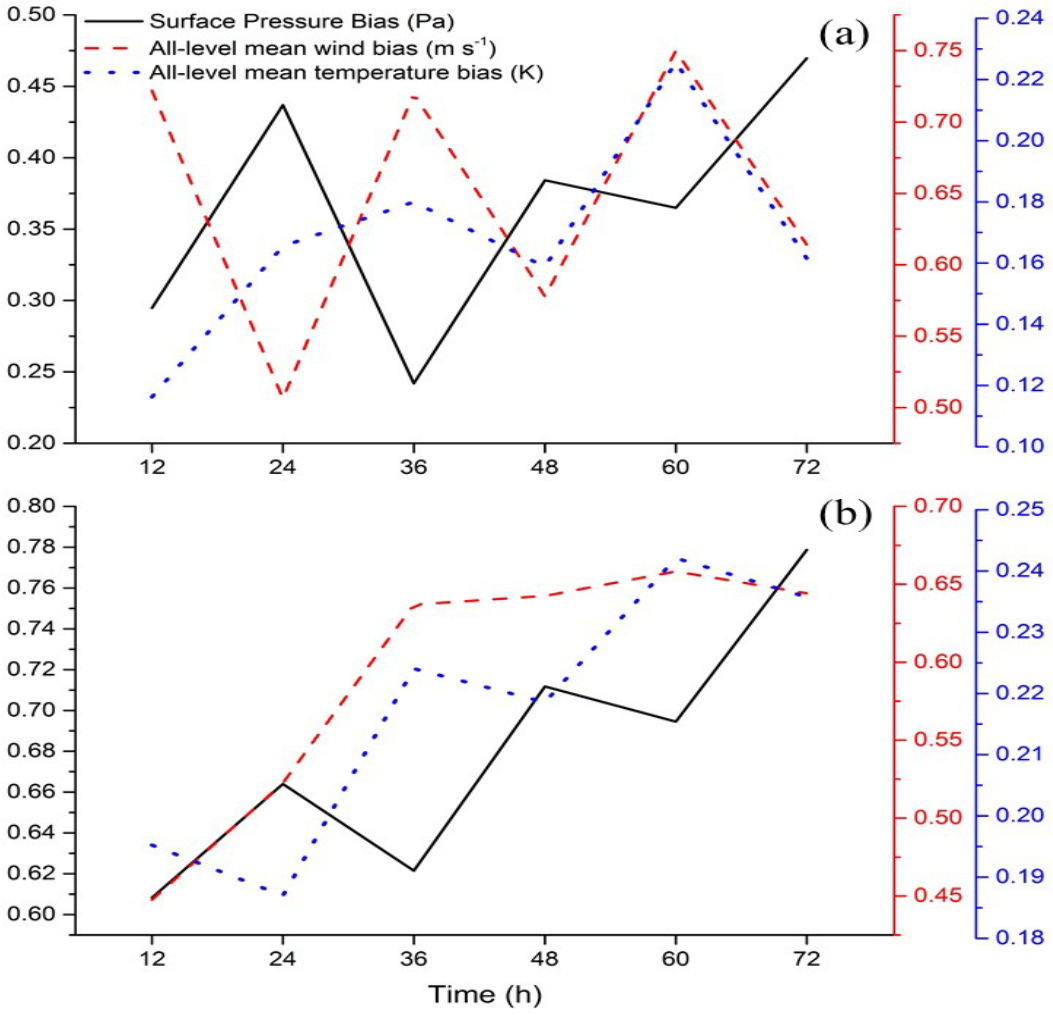

Figure 21 Averaged biases of the predicted summer surface pressure (Pa), all-level mean wind (m s^{-1}), and all-level mean temperature (K).

To further discuss the distribution of the diurnal variation of biases over the continental, the biases of surface pressure, all-level mean wind and temperature over the

Rocky Mountains (RM) and the Great Plains (GP) are plotted in Fig. 22. Generally, larger diurnal variations of biases are observed over the Great Plains especially in summer with variational data assimilation schemes. However, in winter, large diurnal variations of bias of temperature is observed over the Rocky Mountains with EnKF scheme (Fig. 22e). The major contribution of the diurnal variation of biases are from the mid-east of United Continental. Comparing different DA schemes, much smaller biases of surface pressure and wind and comparable bias of temperature are given in EnKF configuration in summer. In contrast, much larger biases of surface pressure and temperature are observed over the Rocky Mountains (Fig. 22a, e).

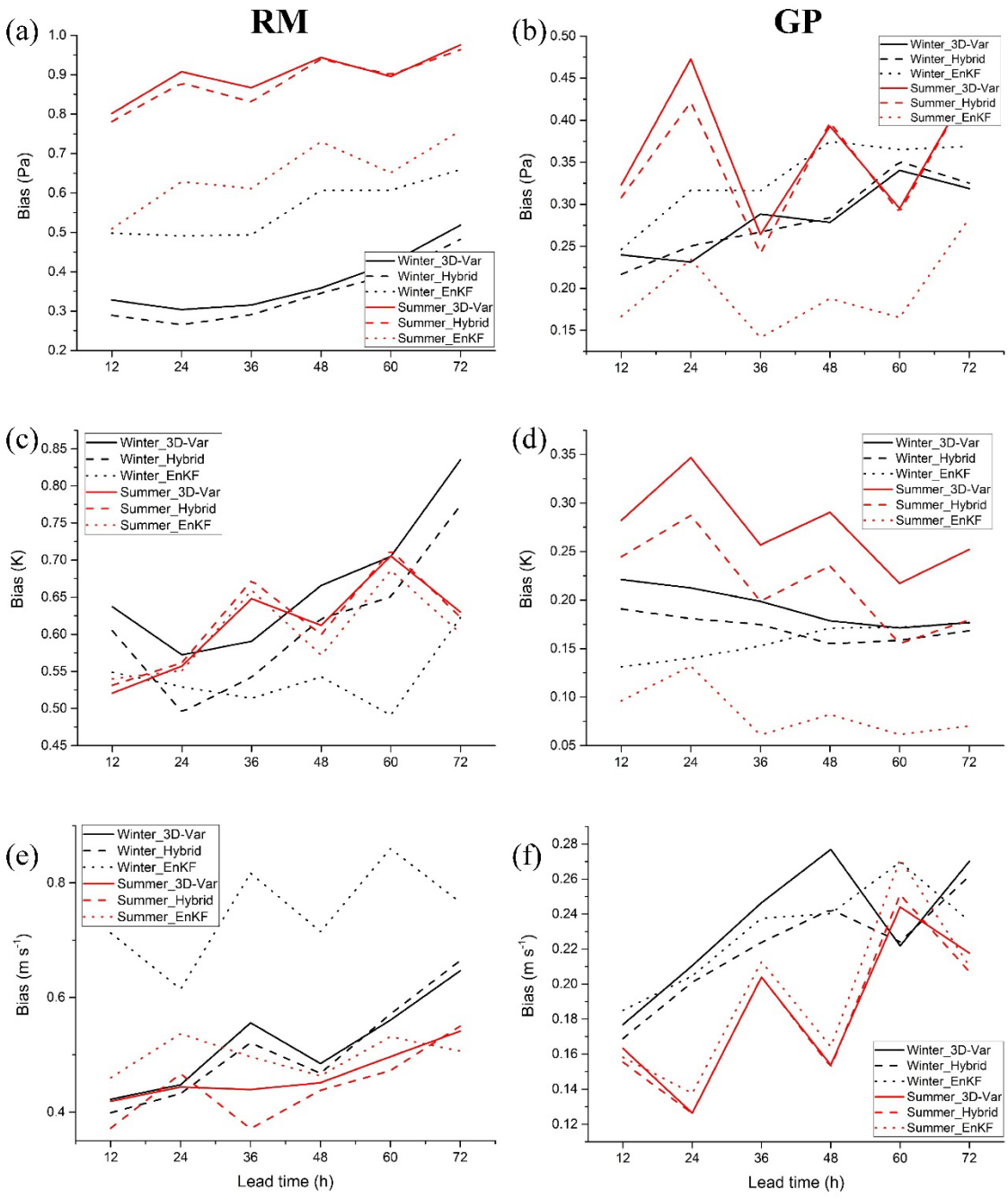

Figure 22 Averaged biases of the predicted surface pressure (a, b), all-level averaged wind (c, d), and all-level averaged temperature (e, f) over the RM and GP.

4.3 Individual Case study – A Summer Case

One bipolar event happened during the second week of July 2012 are used to evaluate the results obtained in former sections. As shown in Fig. 23 (from National Climatic Data Center, NOAA), over two-thirds of the U.S. continents especially over the corn-belt region (Di, et al., 2015) and southwest coast suffered extremely drought, while the southeast U.S. (divided by the solid black line in Fig. 23) suffered extreme heavy precipitation events.

The accompanying mean sea level pressure for the 2nd week of July, 2012 minus June-July-August (JJA) of 2012 (Fig. 24) shows a high pressure over the Great Lakes and relatively weaker high pressure over the Atlantic Ocean east of the Gulf of Mexico. The high pressure over the Great Lakes was the primary reasons for bringing in dry air from the north to the 'corn belt' region, and make this area extremely dry during the 2nd week of July. While the weaker one tended to prevent the dry air pushing southward to the southeast part of U.S. Under such a dynamic scenario, the drought was intensified in the 'corn belt' region and spread into the Texas. However, the cyclone located over the Gulf of Mexico strengthened the low-level jet carrying moisture from the Gulf of Mexico to the southern coastal areas and caused this heavy precipitation events during the 2nd week of July.

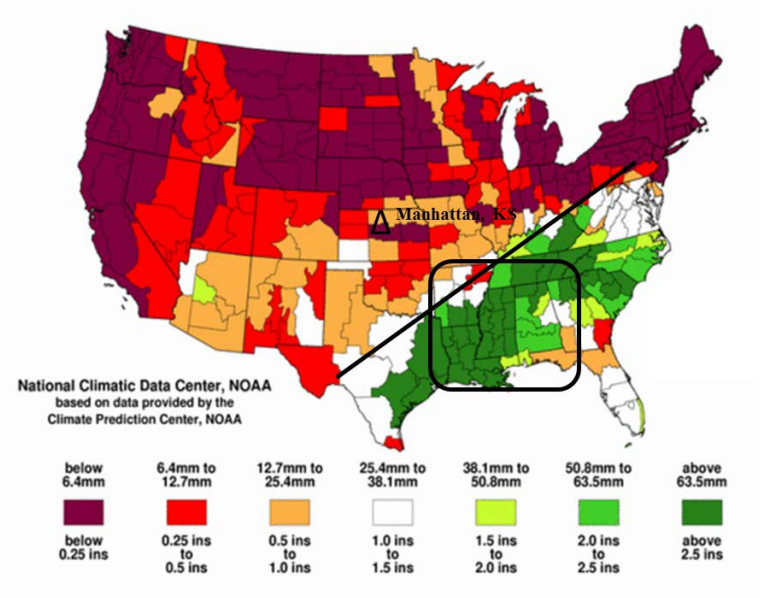

Figure 23 Total precipitation distribution of the second week of July, 2012. (From NOAA, National Climatic Data Center).

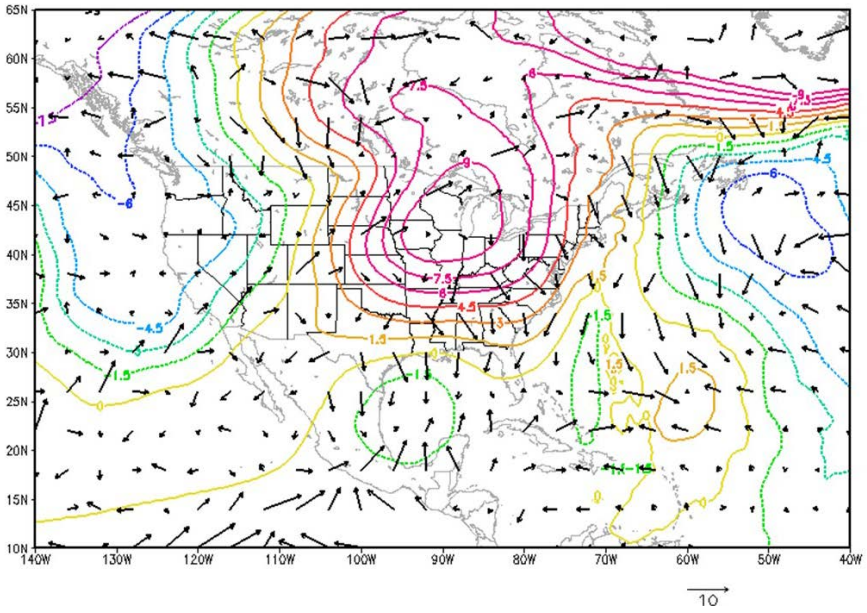

Figure 24 Sea level pressure (hPa) and 850-hPa wind vector (m s^{-1}) differences between the 2012 2nd week of July average and the 2012 JJA average from NCEP/NCAR reanalysis.

4.3.1 Verification of the Drought

A set of experiments involving a control experiment (CTRL) and three DA configurations including 3D-Var, Hybrid and EnKF are designed. The descriptions of these experiments are concluded in Table 6. The difference is that in the individual case study section, the DA is applied every 12-h continuously. The results are verified against in-situ observations and GLDAS products.

Firstly, a single station near surface temperature time series from Manhattan, Kansas (KS) located at the station (39.102°N, 96.609°W) shown in Fig. 23 ("Δ") is used to validate our model results. Fig. 25 compares the simulated 2 m temperatures from CTRL, 3DVar, Hybrid, and EnKF experiments with the in-situ observational near-surface temperature from Manhattan and shows all experiments overestimated the temperature during the first two days and then become more reliable in the rest days of the week. The correlation coefficients (CC) between the in-situ near surface observation and each model output 2 m temperature are calculated. The results showed that all DA configurations largely improved the model outputs with both higher CC and lower RMSDs. Among these three DA configurations, 3D-Var and Hybrid shows comparable results and EnKF gives better scores. The CTRL experiment showed better results during the first two days and then dropped dramatically from the third day. In contrast, EnKF shows comparable results at first few DA cycles and better results at later DA cycles compared to the other experiments in predicting near surface temperature.

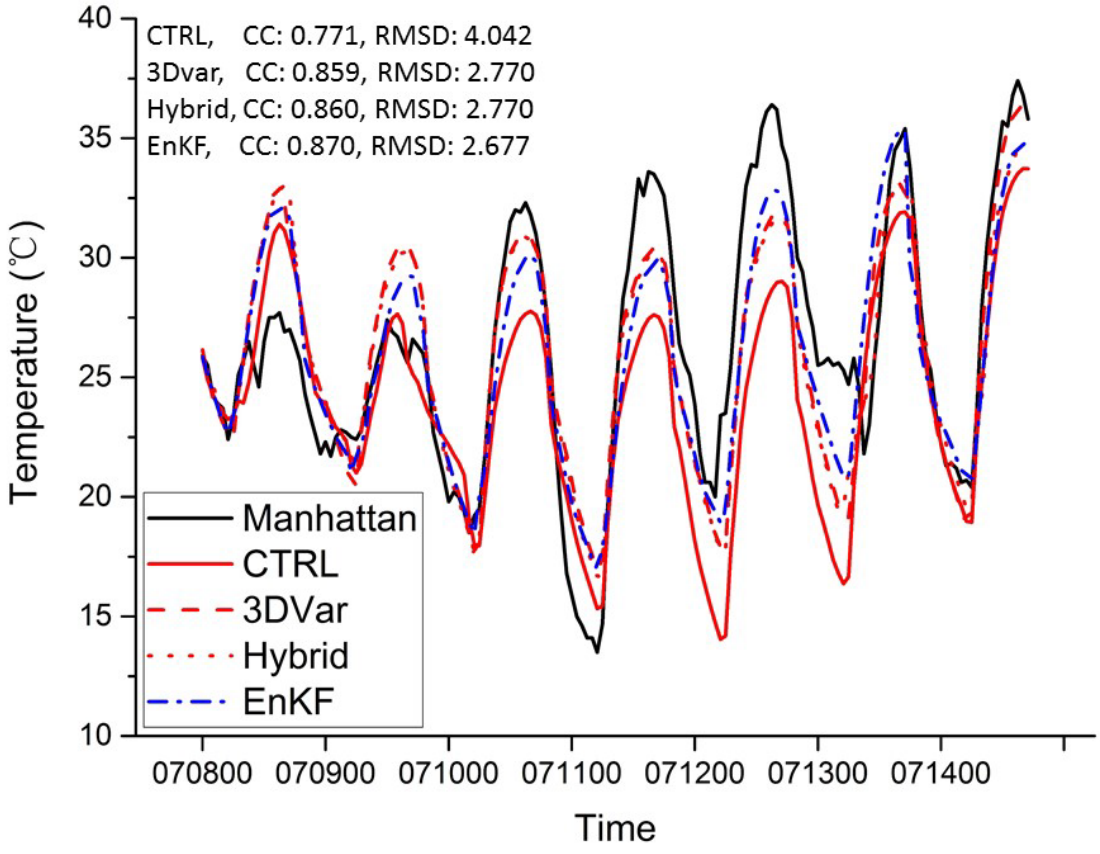

Figure 25 Time series of near-surface temperature from Manhattan, KS (39.102°N, 96.609°W) and the predicted 2 m temperature from different experiments.

The spatial correlation coefficients (SCC) and RMSDs between GLDAS hourly surface skin temperature and model hourly surface skin temperature over the drought area are obtained. The averaged SCC and RMSDs in CTRL experiment are 0.660 and 4.079, respectively. Compared to the CTRL experiment, all three DA configurations show great improvements in which the SCC and RMSD for 3D-Var are 0.754 and 3.515, respectively, 0.741 and 3.520 for Hybrid, respectively, and 0.773 and 3.382 for EnKF, respectively. EnKF shows better results among the three DA configurations. In Fig. 26,

the SCC and RMSD of the surface skin temperature obtained from the CTRL-GLDAS are used as basics and the differences of the SCC and RMSD between the DA-GLDAS experiments and the CTRL-GLDAS are calculated. The SCC above 0 in Fig. 26a and the RMSD under 0 in Fig. 26b indicate positive impacts, vice versa. Compared to 3D-Var, Hybrid shows the advantages in the first few DA cycles. The largest improvements were obtained after 6-7 DA cycles for all three DA configurations. Compared to the variational DA configurations, EnKF shows more advantages in the late DA cycles with both higher SCC and lower RMSDs in predicting surface skin temperature.

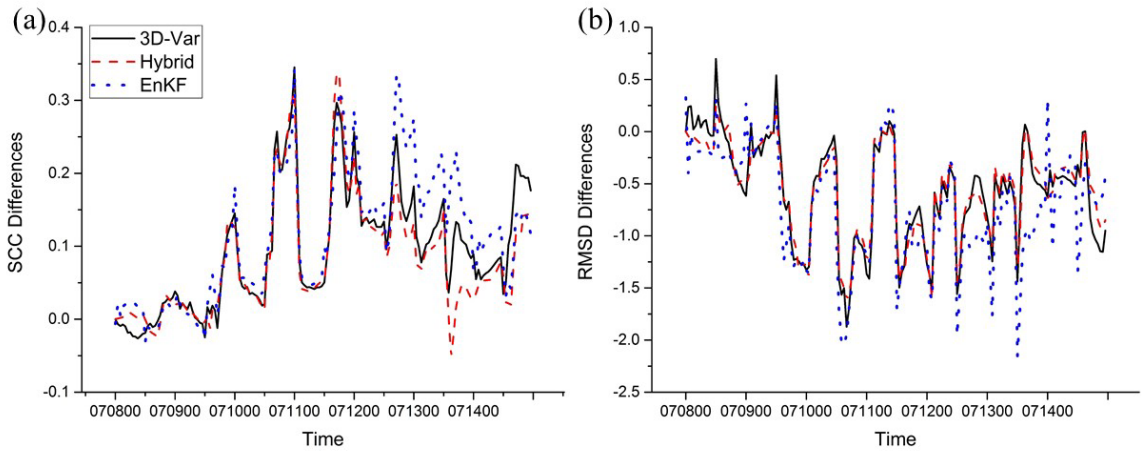

Figure 26 (a): Spatial correlation coefficients and (b): RMSD differences of surface skin temperature.

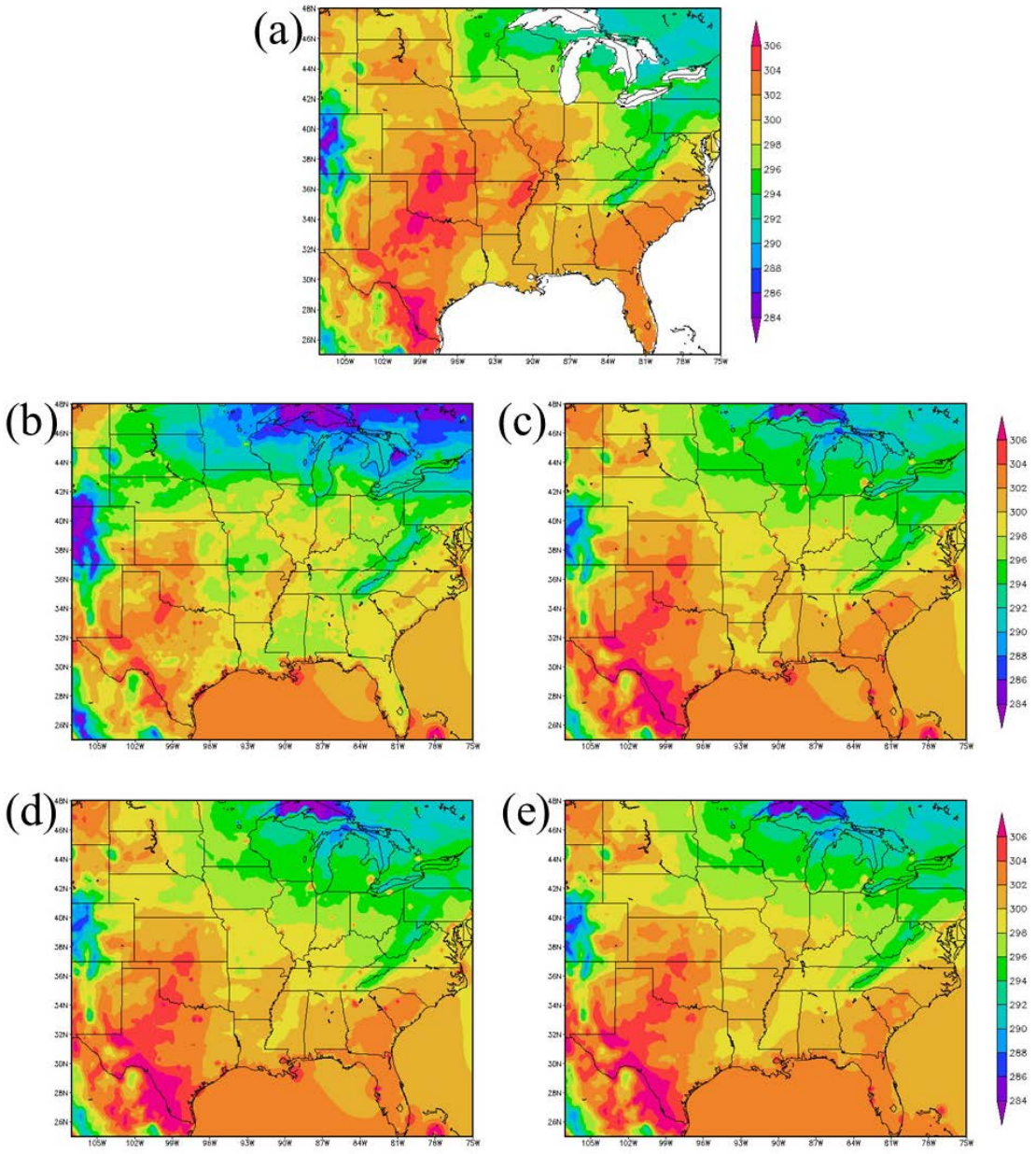

Figure 27 Distribution of averaged surface skin temperature (K) from different model results.

The extremely hot weather appeared over the southwest areas and the abnormally cold center near the northeast areas are clearly shown in GLDAS results (Fig. 27a). The CTRL experiment (Fig. 27b) largely underestimated the surface skin temperature

especially over the north and the southeast coast. In contrast, all three DA configurations well caught the patterns. Both 3D-Var and Hybrid slightly underestimate the surface skin temperature over Missouri and Illinois (Fig. 27c, d). Hybrid also slightly overestimate the surface skin temperature over Louisiana. Compared to 3D-Var and Hybrid, EnKF shows better results in these three states. The summer case study verifies that EnKF has more advantages in predicting temperature in summer (section 4.2.3.3).

4.3.2 Verification of the Precipitation

Secondly, the precipitation products from the CTRL experiment, and each DA configurations are compared to the GLDAS 3-h precipitation products. The major precipitation region is in the southeast coast of U. S. as shown in Fig. 23. The 3-h precipitation time-series is from GLDAS products, CTRL, 3D-Var, Hybrid and EnKF were plotted in Fig. 28. All three DA configurations have better correlations than the CTRL experiment in which 3D-Var and Hybrid give better correlations than EnKF. However, EnKF has the best RMSD compared to the other configurations. All experiments largely overestimate the precipitation amount over the precipitation peaks while the CTRL experiment shows better predictions of precipitation peaks during the last three days. In contrast, all DA configurations well predict the precipitation valleys. By comparing the performances of different DA configurations, the EnKF and Hybrid show better predictions in the later DA cycles than 3D-Var.

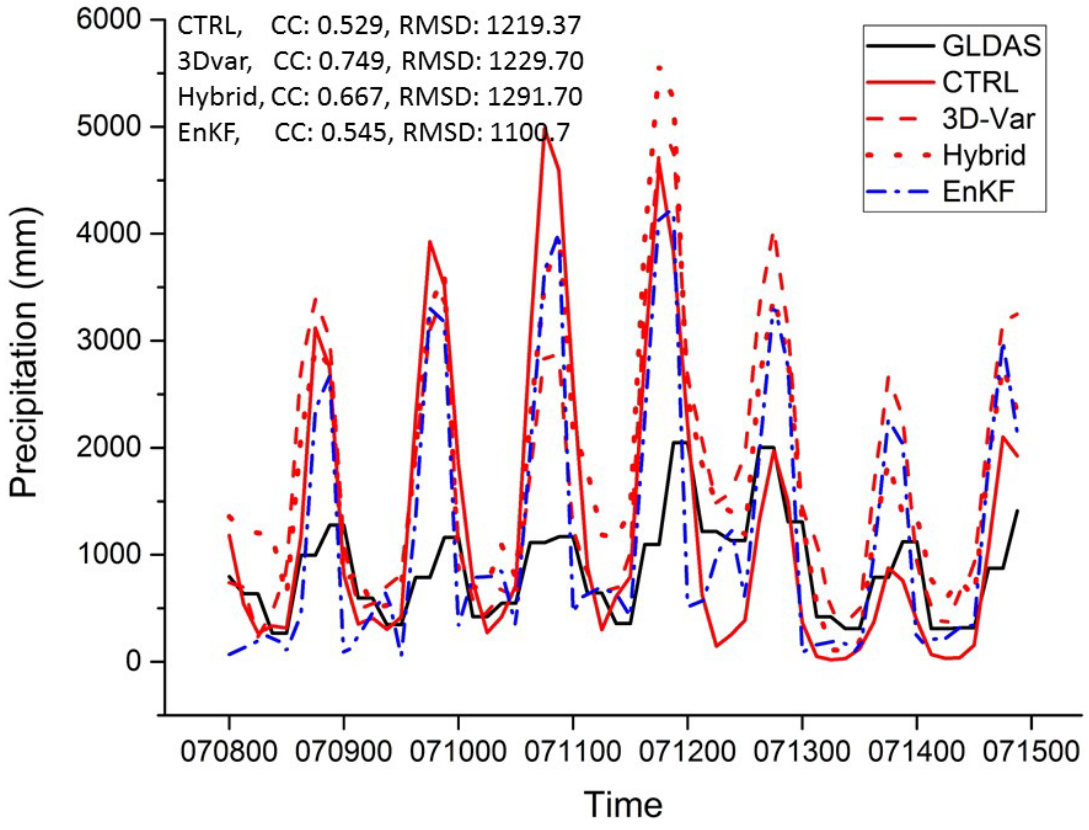

Figure 28 Time series of 3-h accumulated precipitation from different model results.

The mismatches of the accumulated precipitation may be related to the mismatch of storm center locations or predicting of fake precipitation patterns. The daily precipitation distributions from GLDAS (Fig. 29a, f), CTRL (Fig. 29b, g), 3D-Var (Fig. 29c, h), Hybrid (Fig. 29d, i), and EnKF (Fig. e, j) of July 10th (first row) and July 12th (second row) are plotted. In July 10th, all GSI configurations overestimate the total precipitation in major precipitation areas except the EnKF configuration, and a storm center was obtained over Texas and Oklahoma especially in CTRL and Hybrid experiments. The CTRL experiment failed to catch the storm center over the coast of

Gulf of Mexico, in contrast, the other configurations successfully caught this storm center but 3D-Var largely overestimate the total precipitation. In July 12th, the precipitation pattern in CTRL experiment moved to the east and the precipitation pattern in 3DVar moved to the west. In contrast, Hybrid, and EnKF show only slightly offset to the west of the precipitation pattern. Among Hybrid and EnKF, Hybrid largely overestimate the daily precipitation amounts, however, EnKF shows more reliable results compared to the other DA configurations.

The individual case study of a heavy precipitation event during the 2012 drought summer period shows that EnKF has the advantages in predicting both temperature and precipitation during summer which confirmed the results obtained in the previous sections.

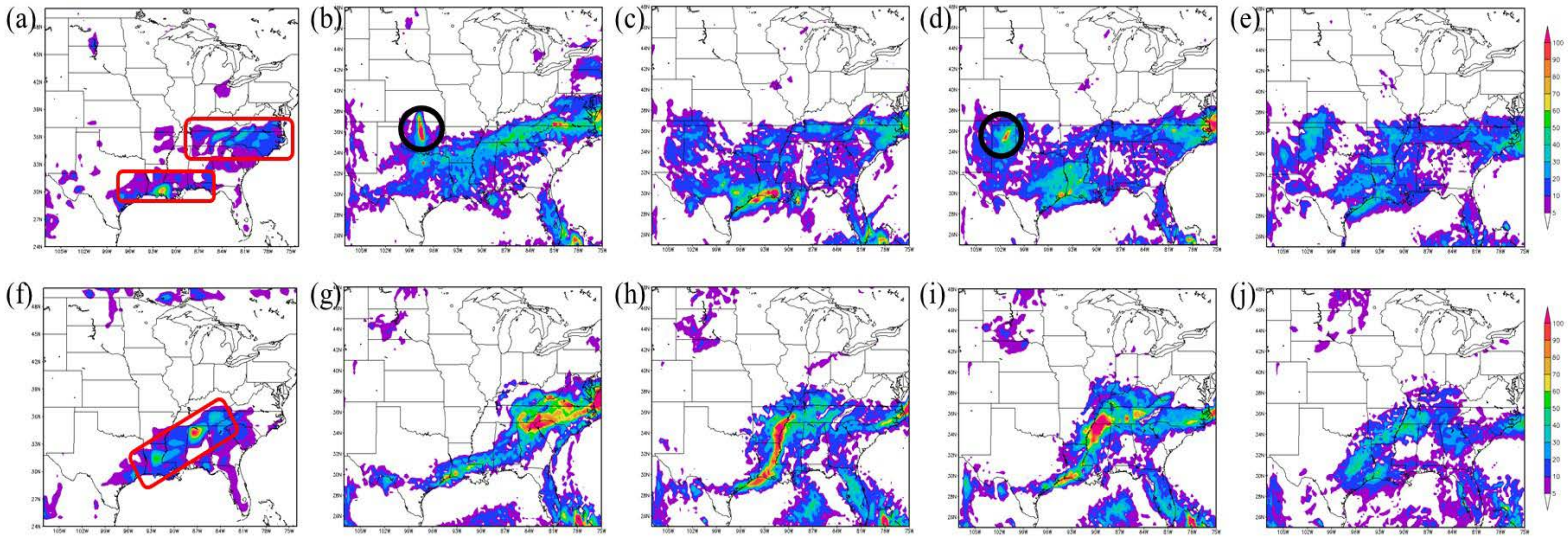

Figure 29 Daily precipitation (mm) distribution of July 10th and July 12th, 2012, from different model results.

4.4 Individual Case study – A Winter Case

Another heavy precipitation event happened in the Jan. 2nd to Jan. 4th, 2015 is used to verify the DA configurations during winter. The observed precipitation distribution during this period is concluded in Fig. 30. The observed precipitation data is obtained from NOAA's Advanced Hydrologic Prediction Service. As shown in Fig. 30, this precipitation event started at the east of Texas and moved eastward.

Also, the in-situ near-surface temperature observations from Manhattan, KS during Jan. 1st to Jan. 4th, 2015 are used to verify the model outputs from different configurations. Both 3D-Var and Hybrid show slightly improvements in CC and RMSDs compared to CTRL (Fig. 31). In contrast, EnKF shows a decrease of the CC but comparable value of RMSD with 3D-Var. When predicting near surface temperature, no obvious differences are found in the first few DA cycles between the CTRL and DA configurations, and all experiments underestimate the temperature. However, all DA configurations show smaller biases in late DA cycles especially in EnKF experiment. In the comparison of 3-h accumulated precipitation in the major precipitation area from GLDAS products (Fig. 32), EnKF shows the largest improvements in both CC and RMSD. In contrast, no obvious differences are found between 3D-Var, Hybrid, and CTRL experiments. However, EnKF underestimates the 3-h accumulated precipitation in the first few DA cycles compared to Hybrid configuration.

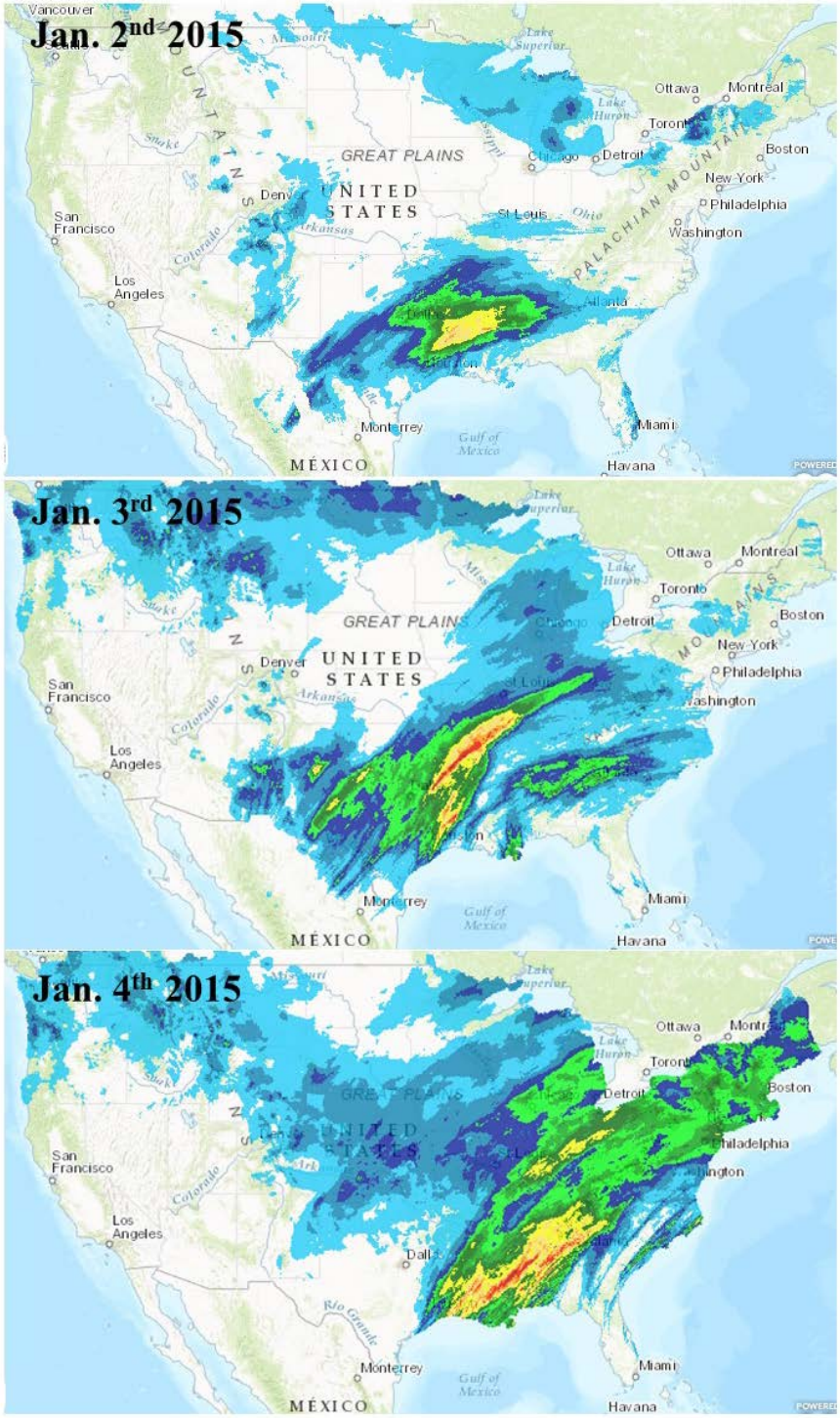

Figure 30 Observed precipitation distribution from Jan. 2nd to Jan. 4th, 2015 from NOAA.

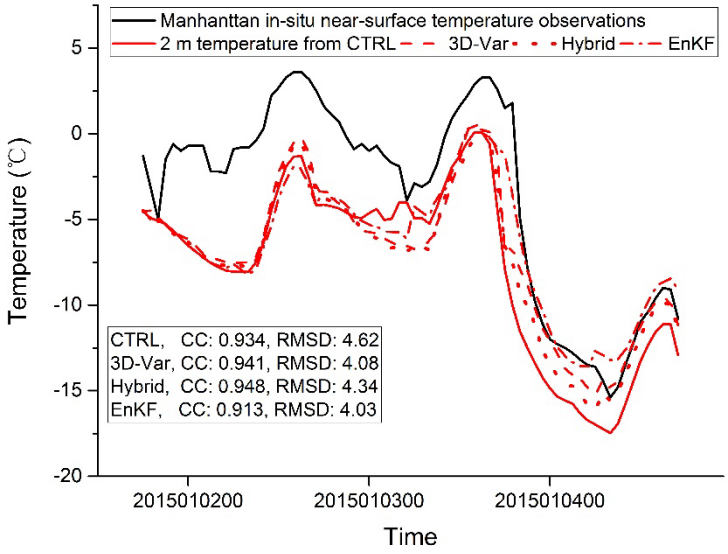

Figure 31 Time series of near-surface temperature from Manhattan, KS (39.102°N, 96.609°W) in-situ observational and the predicted 2 m temperature from different experiments.

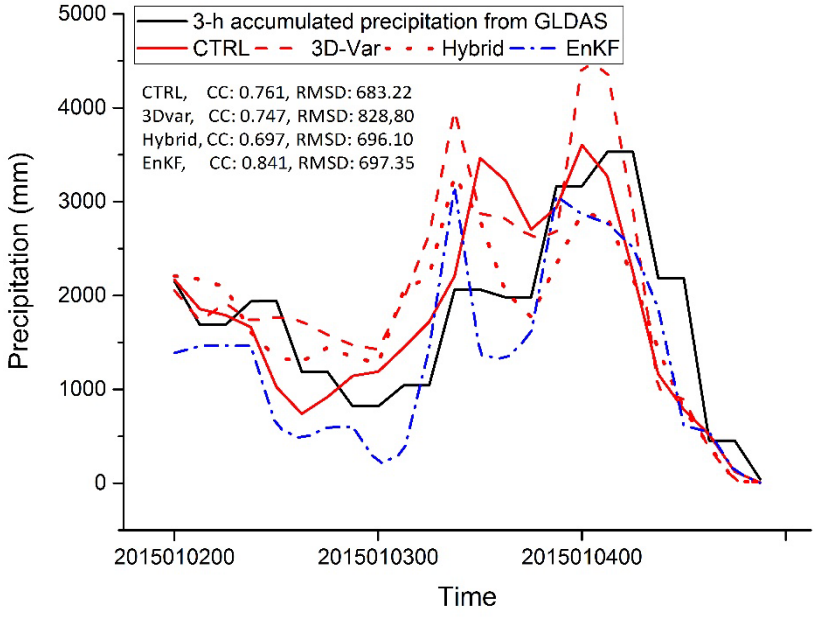

Figure 32 Time series of 3-h accumulated precipitation from different numerical experiments.

The distributions of the daily precipitation from GLDAS, CTRL, 3D-Var, Hybrid, and EnKF are plotted in Fig. 33. On Jan. 2nd, all experiments matched the major precipitation patterns, however, all experiments also overestimate the precipitation amounts over the Texas. No significant improvements are found in the first DA cycle. On Jan. 3rd, Hybrid (Fig. 33i) and EnKF (Fig. 33j) well matched the major precipitation patterns while 3D-Var (Fig. 33h) overestimates the total precipitation in the storm center. On Jan. 4th, the storm centers observed in the CTRL experiment (Fig. 33l) move to the Gulf of Mexico compared to the storm centers appeared over Alabama and Georgia in GLDAS products (Fig. 33k). Both Hybrid and EnKF configurations underestimate the precipitation amounts. In contrast, the 3D-Var configuration matched the two storm centers.

The individual case study of the heavy precipitation event during Jan. 2nd to Jan. 4th, 2015 shows that the Hybrid configuration shows overall better results than 3D-Var and EnKF. EnKF performs different from the summer event which underestimate the accumulated precipitation amounts in the first few DA cycles and then becomes comparable to the other configurations.

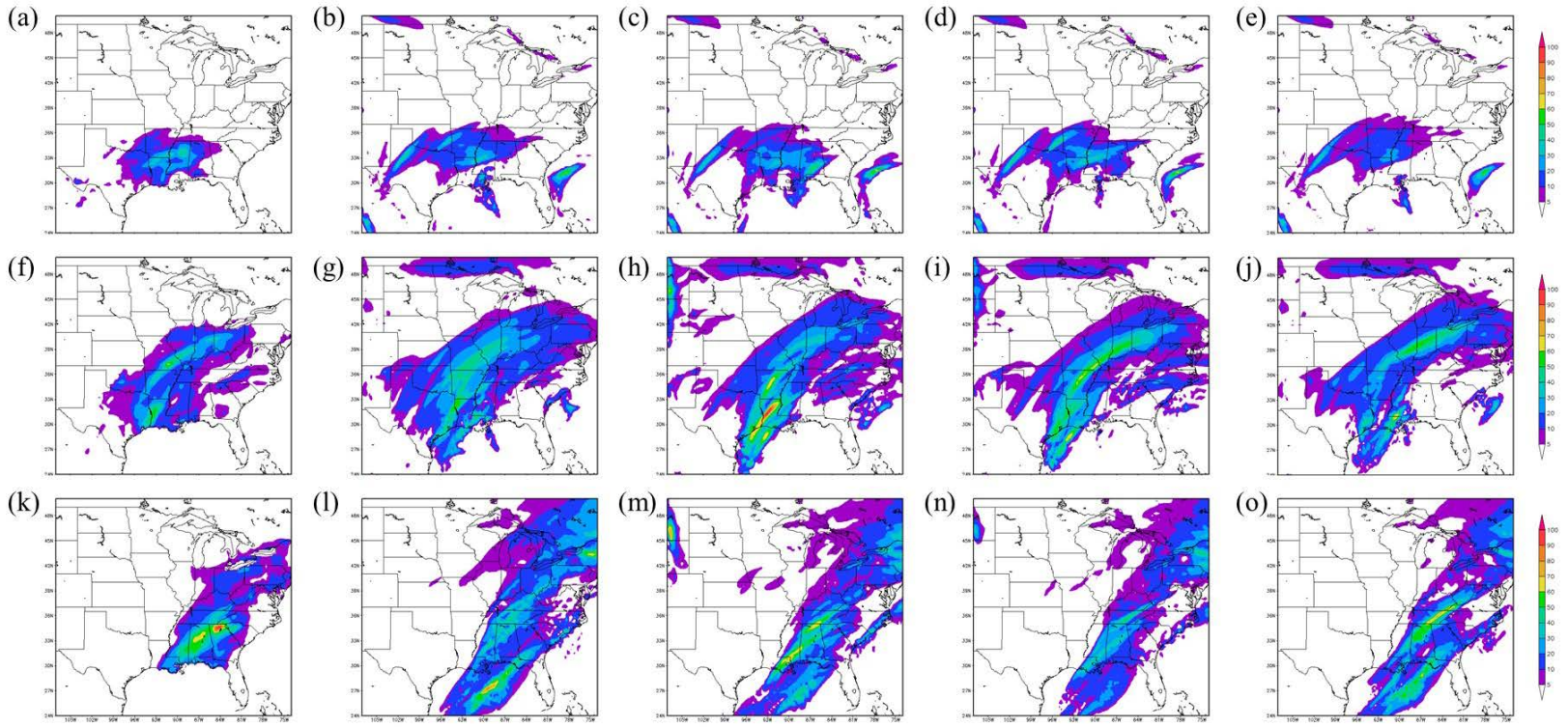

Figure 33 Daily precipitation (mm) distribution of Jan. 2nd, Jan. 3rd, and Jan. 4th, 2015, from different numerical results.

4.5 Summary

The performance of 3D-Var, 3D-Var based ensemble-variational hybrid (Hybrid), and EnKF on regional short-term weather forecasts over the continental U. S. in both winter and summer are investigated using the regional model WRF-ARW with a model top at 50-mb and the operational DA model GSI using all operationally available observations. The forecast results are verified against conventional observations.

The inclusion of ensembles in variational method can drive the convergence rate faster in summer. In winter, slightly slower convergence rate at first few iterations and then faster convergence rate at later iterations in both first and second outer loops when ensembles are included. When adjusting initial conditions, great improvements (10~20%) are found over the lower boundary layers and the tropopause layers. Beside the improvements, these three DA configurations show differences in adjusting different variables. 3D-Var and Hybrid show better improvements (3%) in adjusting surface pressure and wind in initial conditions while EnKF has better performance in adjusting temperature in both seasons.

Predictions made by three DA configurations also vary in different variables, heights, and seasons. All three DA configurations show better forecast skills (~10%) in summer than winter while bias differs from different variables. Generally, Hybrid shows more advantages in predicting surface pressure, wind, temperature, and RH in winter. In contrast, EnKF shows better skills in predicting summer atmospheric states which is similar as obtained in Meng and Zhang (2008). For wind and temperature profiles, all three DA configurations show better forecast skills in the middle tropospheric layers, but

less skills in the tropopause layers. EnKF shows less forecast skills in predicting tropopause wind but better skills in predicting tropopause temperature compared to the other two DA configurations. Hybrid has the advantages in predicting wind and temperature at lower levels.

The diurnal variation of biases observed in the experiments are mainly caused by two factors: systematic errors and one-time assimilation in a day. The temperature and surface pressure diurnal variations are largely caused by one-time assimilation in a day while the wind diurnal variations are strongly related to the systematic errors. When a 4-time assimilation is applied per-day, this diurnal variation features disappeared. Two individual heavy precipitation events occurred during summer and winter, respectively, are used to verify the statistical results. Individual case studies showed that EnKF do have better skills in predicting summer heavy precipitation events but less skills in predicting winter events compared to Hybrid, and EnKF tends to underestimate the total precipitation amounts. However, EnKF shows better performance in predicting atmospheric states (e.g., temperature) than the other DA configurations in later DA cycles.

To discuss the reasons for the different performance, analysis increments are firstly discussed. Similar increments are observed in different seasons. EnKF shows similar temperature increments to the variational schemes but tends to have more negative increments. In contrast, EnKF shows opposite wind incremental features to those in variational schemes. The reasons for the differences between different seasons and between using different DA configurations are complex. Absolutely, background

error covariance contributes a lot to the forecast qualities in both variational and Kalman filter data assimilations. The background error covariance used in 3D-Var is usually estimated via the so-called National Meteorological Center (NMC) model (Parrish and Derber, 1992) which is static. However, day-to-day variabilities are existed in the model forecast errors which can be as large as the average error and are ignored when the background error covariance is static. Compared to 3D-Var, the background error covariance used in EnKF is estimated form a set of ensembles which can provide flow-dependent information into the system. The inclusion of ensembles provided more accurate estimate of uncertainties, less error in the analysis and less diurnal variations. 3D-Var also benefited a lot by including flow-dependent ensembles in the background error covariance which the configuration here is called 3D-Var based ensemble Hybrid. The inclusion of ensembles greatly improved the analysis and have positive impacts on the forecasts especially in summer. However, there exists some deficiencies in the ensembles generated from regional model which lead to the decrease of predictabilities in winter when the atmospheric state shows less relations to the day-to-day errors. Also, the initial ensembles used in EnKF show more uncertainties when deeper convections exist.

CHAPTER FIVE COMPARISON OF THE INCLUSION OF INFRARED AND MICROWAVE IN DA

As we proved in chapter 4, different atmospheric variables in different seasons are sensitive to different DA configurations. In this chapter, the impacts of infrared and microwave satellite data when assimilated alone are investigated and compared. The major goal of this chapter is to seek the advantages of using microwave satellite data in DA system for the prediction of heavy precipitation events.

5.1 Introduction

In the fact that the emitted radiance from the earth-atmosphere system is much smaller than that of solar radiation, the wavelength for the radiance emitted from the earth-atmosphere system is usually longer than that of solar radiation which is usually referred to as the infrared or thermal and microwave radiation (Liao, 2002). Large differences exist between the infrared and microwave radiances and thus differs the ways how they observe the earth's key variables.

Carbon dioxide, water vapor and ozone are three major gases which absorb the infrared radiation significantly. Four regions in the infrared band are strongly related to these gases. As shown in Fig. 34, CO_2 absorbs the infrared radiation in the 15 μm band and the 4.3 μm band which overlaps with the solar radiation. Generally, satellite sensors (channels) that measure close to the spectral frequencies of CO_2 absorption lines are temperature sensitive sensors (channels). Ozone absorbs the infrared radiation mainly in

the 9.6 μm band. Water absorbs the infrared radiation over the entire infrared spectrum with the strongest region in 6.3 μm band. The channels which sensitive to the H_2O absorption lines are usually referred to the water vapor channels. The so called atmospheric window region is located between 800 to 1200 cm^{-1}. The radiance measurement in the atmospheric window region is more sensitive to the surface characteristics due to the little absorption by atmospheric components.

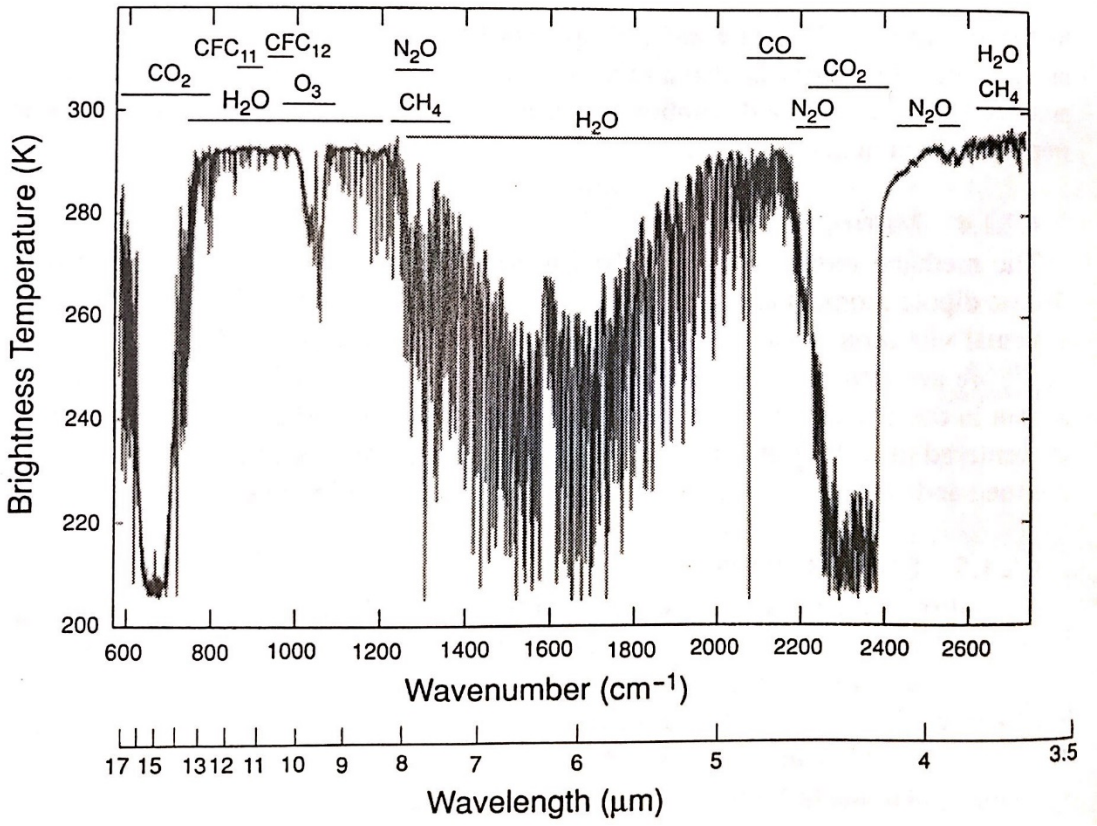

Figure 34 Observed brightness temperature for infrared spectrum with all absorption gases and their spectral locations. (Liao, 2002, Chapter 4.2).

For microwave, the wavelength is longer than infrared (usually at centimeter scale) and the microwave satellite sensors usually have much less channels than the infrared satellite sensors. Different from the infrared bands which are strongly absorbed by CO_2, H_2O, and O_3, only water vapor and molecular oxygen showed significant absorption lines. As shown in Fig. 35, the molecular oxygen strongly absorbs the radiation at the 60 GHz band and 118.75 GHz, and water vapor starts to absorb the radiation near 180 GHz. As Zou, et al. (2013) noticed, more valuable information of the cloud and atmosphere under cloudy conditions can be obtained when using Microwave radiance technologies because microwave radiation can penetrate through non-precipitation clouds and carries atmospheric humidity information within the clouds when compared to infrared humidity sensors. A comparison of the impacts of infrared and microwave satellite data in DA system on the NCEP's operational global forecast model was taken out by Cucurull and Anthes (2014). The study of the impacts on global forecast model showed that the infrared and microwave satellite observations affect the global temperature in a similar way but large differences existed in the lower troposphere. Furthermore, they found that by assimilating infrared and microwave alone will make a small positive impact on the global forecast system.

In this chapter, a set of experiments assimilate infrared or microwave satellite observations alone are taken out with the regional model top set at 10-mb. The impacts of infrared and microwave satellite observations when assimilated alone on our regional NWP system are investigated. Detailed channel selections of each sensor used in DA system is listed in appendix A.

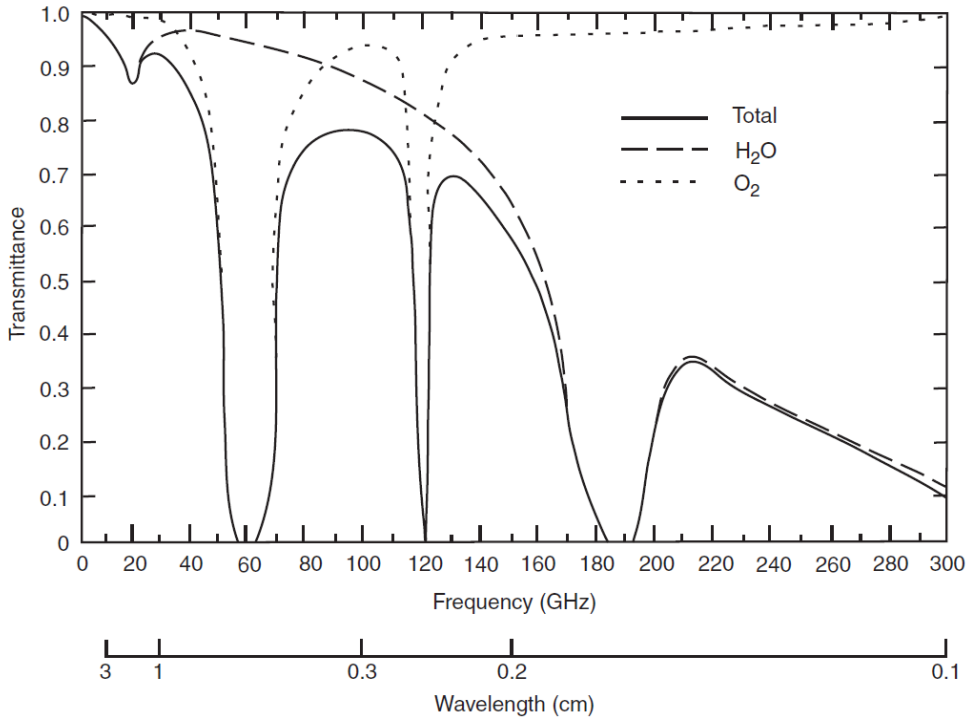

Figure 35 Atmospheric transmittances as a function of frequency and wavelength. (Liao, 2002, Chapter 7.5).

5.2 Statistical Results

As described in chapter 3, the domain configuration for the second set of experiments are the same in the horizontal direction as those in the first set of experiments. The model lid is raised from 50-mb to 10-mb and more model vertical levels are used. The DA configurations are selected based on the results obtained in chapter 4 which Hybrid and EnKF are selected for winter and summer predictions, respectively. Experiments are designed using different observations in the DA system and they are concluded in Table 5. The averaged biases and RMSDs fit to conventional observations during the study periods are compared in this section.

5.2.1 Comparison of Analysis

The surface pressure, wind, temperature, humidity, and precipitable water from the analysis assimilating infrared (IR) and microwave (MW) alone in the DA system are compared in this section. Table 8 concluded the differences of the analyzed surface pressure, all-level mean wind, all-level mean temperature, all-level mean humidity and precipitable water. No significant differences (less than 1%) are observed during summer when using EnKF configuration. In winter, MW configuration shows better results especially for precipitable water with 23% improvement in bias adjustment and 5.7% improvement in RMSD.

Table 6 Comparison of the analysis from IR and MW configurations

Surface Pressure (Pa)	Winter		Summer	
	IR	**MW**	**IR**	**MW**
Bias	0.0205	0.0295	0.1940	0.1955
RMSD	1.0206	1.0014	0.8224	0.8230
All-level mean wind ($m\ s^{-1}$)	**IR**	**MW**	**IR**	**MW**
Bias	0.2220	0.2170	0.3640	0.3705
RMSD	3.9168	3.8374	3.4618	3.4670
All-level mean T (K)	**IR**	**MW**	**IR**	**MW**
Bias	0.1325	0.0953	0.0891	0.0875
RMSD	1.2768	1.2430	1.4279	1.4307
All-level mean RH (%)	**IR**	**MW**	**IR**	**MW**
Bias	0.8394	0.9902	1.0935	1.1056
RMSD	11.0932	11.0298	11.4458	11.4607
Precipitable Water (mm)	**IR**	**MW**	**IR**	**MW**
Bias	0.3029	0.2364	0.5356	0.5291
RMSD	2.1297	2.0089	3.7197	3.7162

The differences in analyzed wind, temperature and RH profiles during both seasons (black for winter and red for summer) are calculated using MW results minus IR

results and plotted in Fig. 36. The blue solid line indicates the 0-demarcation. The negative values indicate that MW has more advantages in adjusting the initials, vice versa. No significant differences are observed in summer for both biases and RMSDs using EnKF configuration. The IR configuration shows slightly better RMSDs of wind (0.5%) and temperature (0.8%) over the tropopause layers, and better RMSDs of RH over higher tropospheric layers. In winter, the MW configuration shows overall better adjustments on wind and temperature profiles. For wind profiles, the MW configuration shows the largest advantages in adjusting wind in the tropopause with an extra 4% skill is obtained. In the lower troposphere, no significant differences are found in the biases, but MW shows better RMSDs (~2%). For temperature profiles, MW shows better performance in adjusting lower tropospheric biases and RMSDs. However, no big differences are found in the tropopause layers. Extra 6% skill is observed over the lower troposphere and lower stratosphere. For RH profiles, IR configuration shows better performance in adjusting biases. In contrast, the RMSDs show reverse features compared to summer results which MW configuration an extra 2% skill in the 500 hPa layers while IR configuration shows slightly better RMSDs in the lower troposphere.

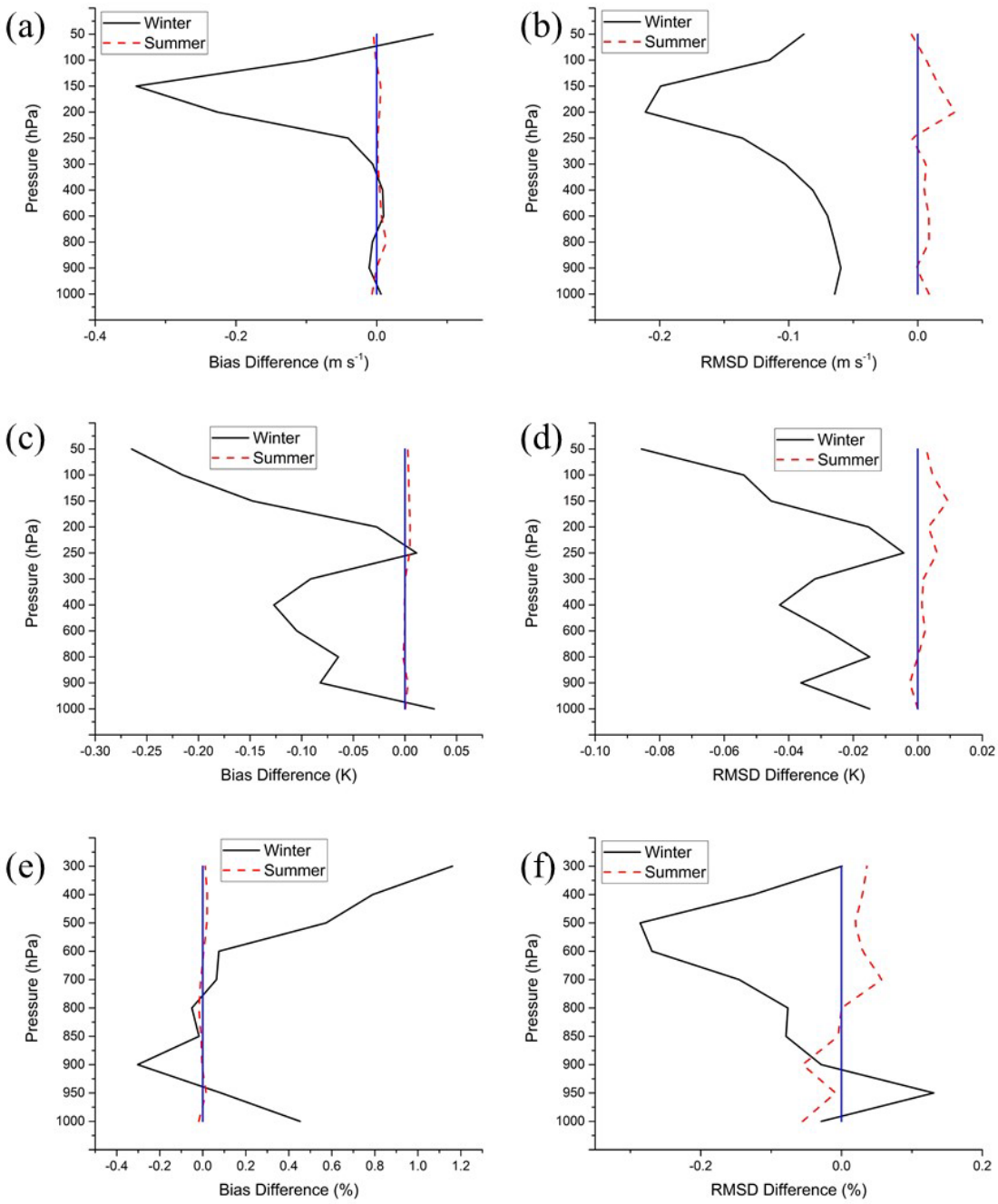

Figure 36 Bias and RMSD differences of initial wind, temperature, and RH profiles between the MW and IR configurations.

5.2.2 Comparison of Tropospheric Forecasts

5.2.2.1 Forecasts of Surface Pressure

For the fact that no significant differences are made in summer using EnKF configuration, only the differences in winter are plotted in this section. The averaged bias and RMSD differences of the predicted winter results between IR and MW configurations are plotted in Fig. 37. MW configuration shows advantages in predicting surface pressure at 12-h forecast lead time with an extra 7% predicting skill. In contrast, IR configuration shows better predicting skills at longer forecast lead times with an extra 7.7% predicting skill observed at 72-h forecast lead time. The MW configuration also shows less advantages in correcting bias at longer forecast lead times.

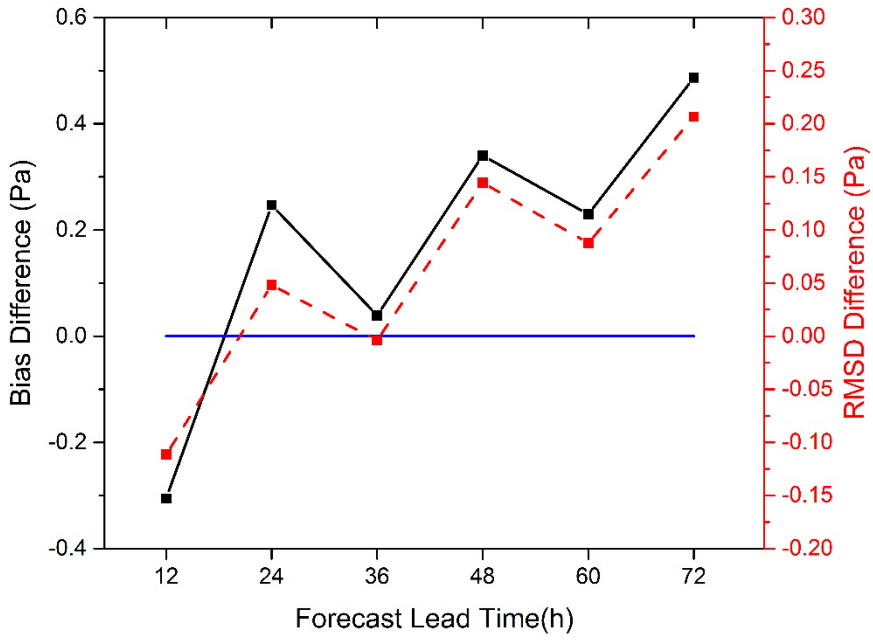

Figure 37 Bias and RMSD differences of the predicted winter surface pressure between MW and IR configurations.

5.2.2.2 Forecasts of Wind

The averaged bias and RMSD differences of the predicted all-level mean winter wind between IR and MW configurations are plotted in Fig. 38. MW and IR configurations tend to reach the same predictability level (red dashed line in Fig. 38) and bias magnitude (black solid line in Fig. 38) as the forecast lead time grows. Lower averaged biases and an extra 2% skill are obtained in predicting all-level mean winter wind when microwave observations are assimilated alone.

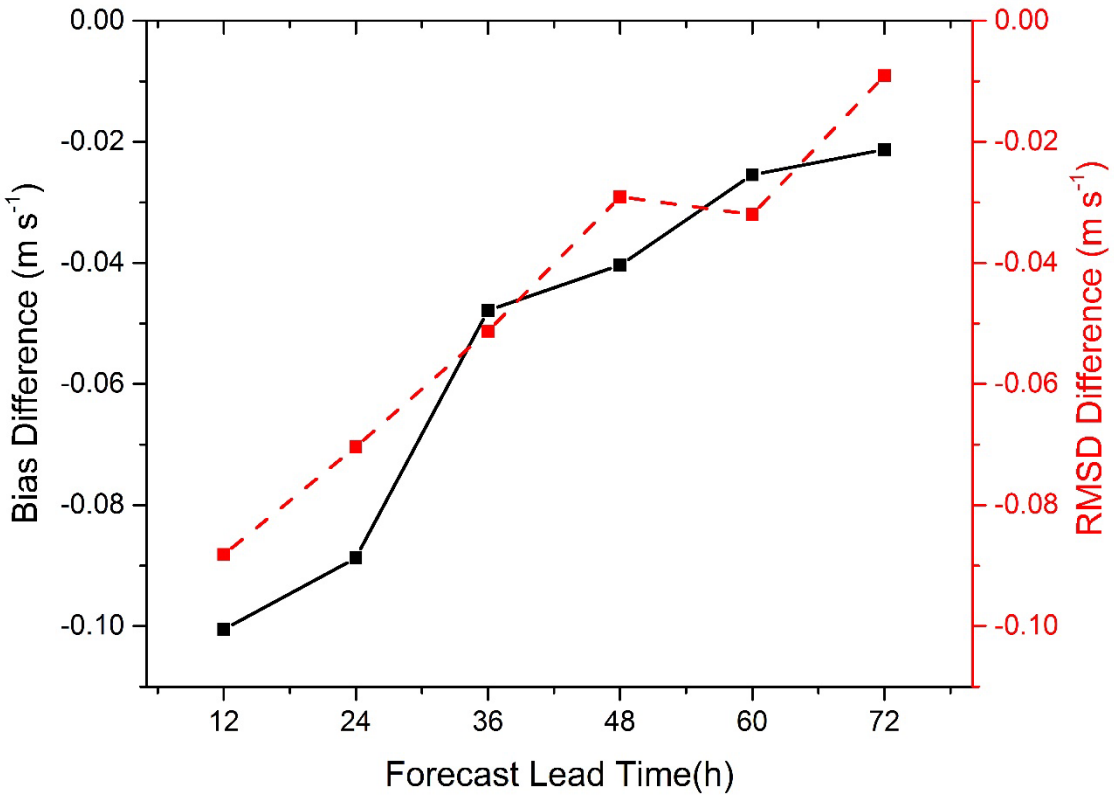

Figure 38 Bias and RMSD differences of the predicted all-level mean winter wind between MW and IR configurations.

The averaged biases and RMSDs differences of the predicted wind profiles are plotted in Fig. 39. The blue areas indicate the negative values which means MW configuration has the advantages over the IR configuration, vice versa. MW configuration predicts larger biases over the tropopause layer but smaller biases over the other layers (Fig. 39a). The RMSD differences in Fig. 39b indicate that extra skills (3% extra skill over the tropopause layers) in predicting wind at early forecast lead times are obtained when microwave observations are assimilated alone. IR configuration only shows better predicting skills in the lower troposphere at 60-, and 72-h forecast lead times.

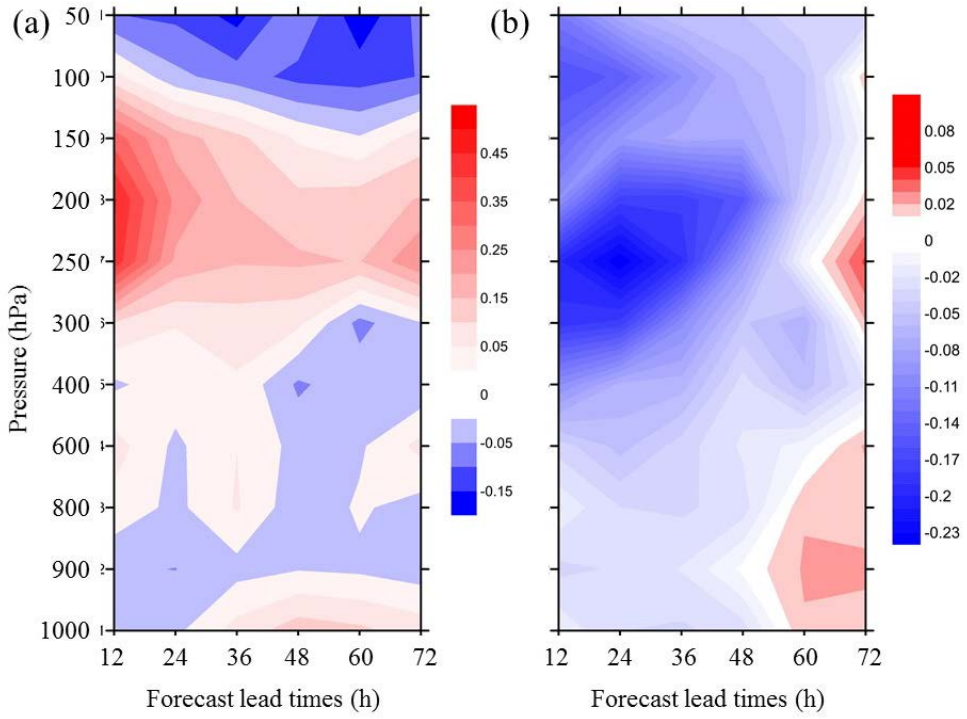

Figure 39 (a): Bias and (b): RMSD differences of the predicted winter wind profiles (m s^{-1}) at different forecast lead times between the MW and IR configurations.

5.2.2.3 Forecasts of Temperature

The differences between the predicted temperature from MW and IR configurations are similar to the prediction of surface pressure. As shown in Fig. 40, MW only shows advantages in predicting all-level mean temperature at 12-h forecast lead time with an extra 3% predicting skill. In contrast, IR configuration shows better performance at later forecast lead times with both smaller biases and RMSDs. An extra 1% skill were obtained using IR configuration at 72-h lead time. The bias of the predicted winter temperature in MW configuration also grows faster than that in IR configuration. Bias in MW configuration is smaller than IR configuration at 12-h forecast lead time and then grows larger than those in IR.

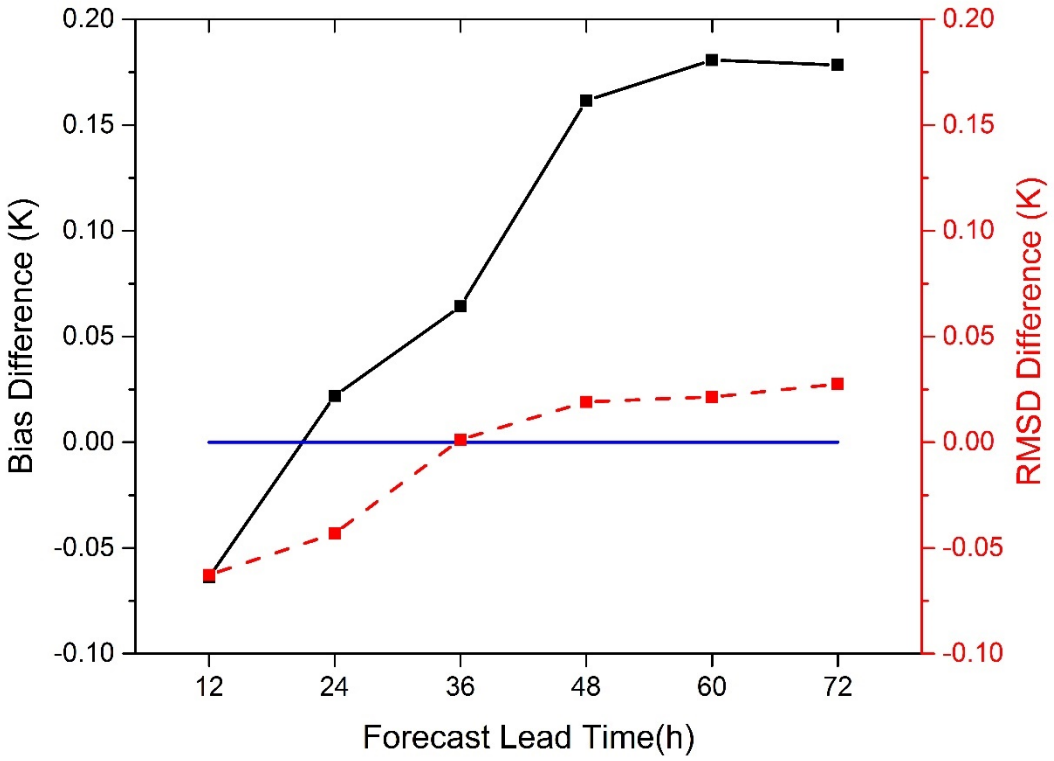

Figure 40 Bias and RMSD differences of the predicted all-level mean winter temperature between MW and IR configurations.

The differences of the averaged bias and RMSD of predicted temperature profiles from MW and IR configurations are plotted in Fig. 41. Similar to what Cucurull and Anthes (2014) obtained which large differences exist in the lower troposphere at later forecast lead times. Better performance in the lower troposphere with an extra 1.5% skill at 36-h lead time is observed in IR configuration while extra 1% skills at 12- and 24-h lead times are observed in MW configuration. However, large differences also exist in

the tropopause layers which an extra 15% skill is obtained in MW configuration in predicting tropopause temperature compared to IR configuration.

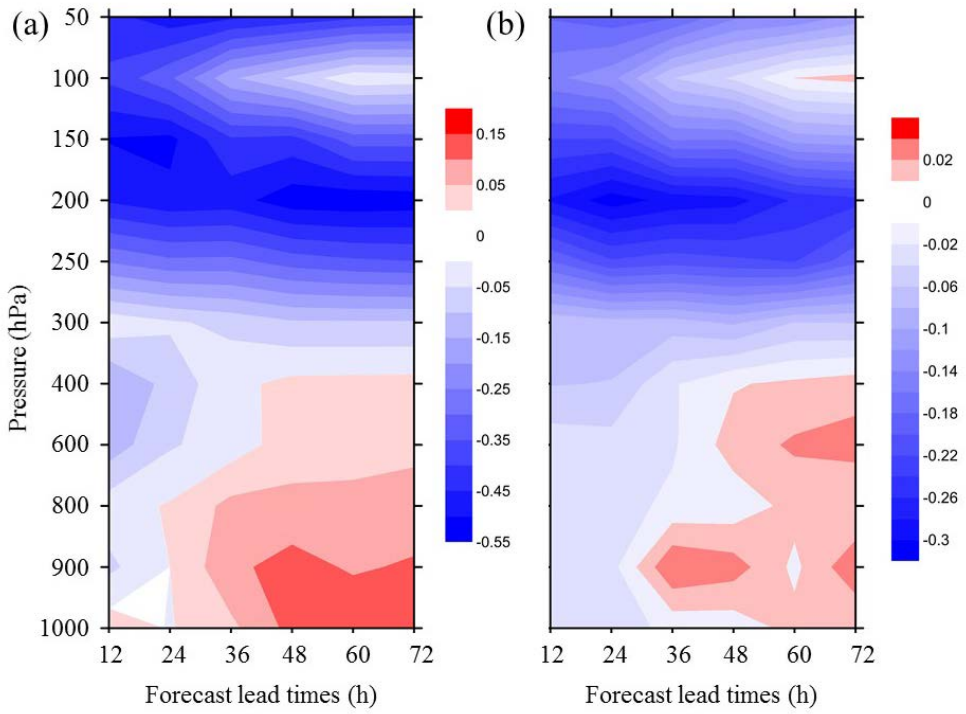

Figure 41 (a): Bias and (b): RMSD differences of the predicted winter temperature profiles (K) at different forecast lead times between MW and IR configurations.

5.2.2.4 Forecasts of RH

The averaged bias and RMSD differences of the predicted all-level mean RH between the MW and IR configurations (Fig. 42) also have similar results to the predicted all-level mean T and surface pressure. Both the biases and RMSDs in the predictions of RH and T show that the IR and MW configurations reached the same predictabilities at 24- or 36-h forecast lead times. An extra 2.5% skill is obtained from the MW

configuration at 12-h lead time while only an extra 1% skill is observed in the IR configuration at 72-h lead time.

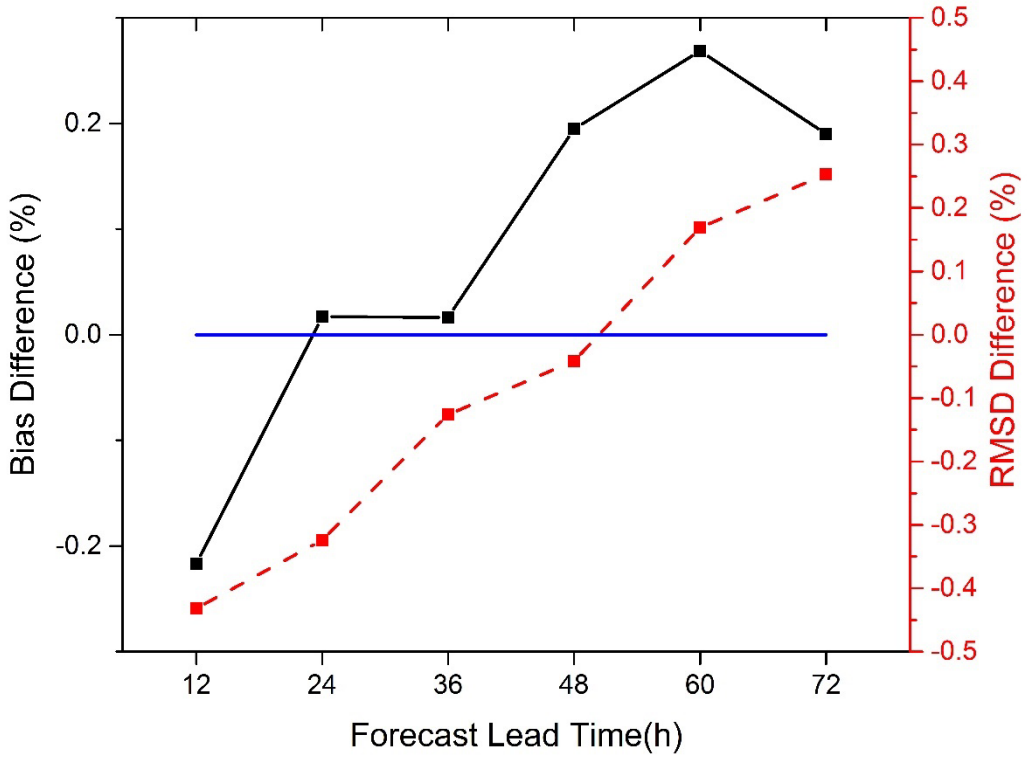

Figure 42 Bias and RMSD differences of the predicted all-level mean winter RH between MW and IR configurations.

The characteristics of RH profiles assimilating MW and IR alone (Fig. 43) are slightly similar to that of temperature. Smaller biases (Fig. 43a) at lower troposphere at 12-h lead time and smaller RMSDs (Fig. 43b) at the mid tropospheric layers with an extra 4% skill are obtained from the MW configuration. In contrast, smaller biases at higher troposphere and lower troposphere at later forecast lead times are observed in the IR

configuration. A small amount of extra skill is obtained at 72-h lead time over higher troposphere.

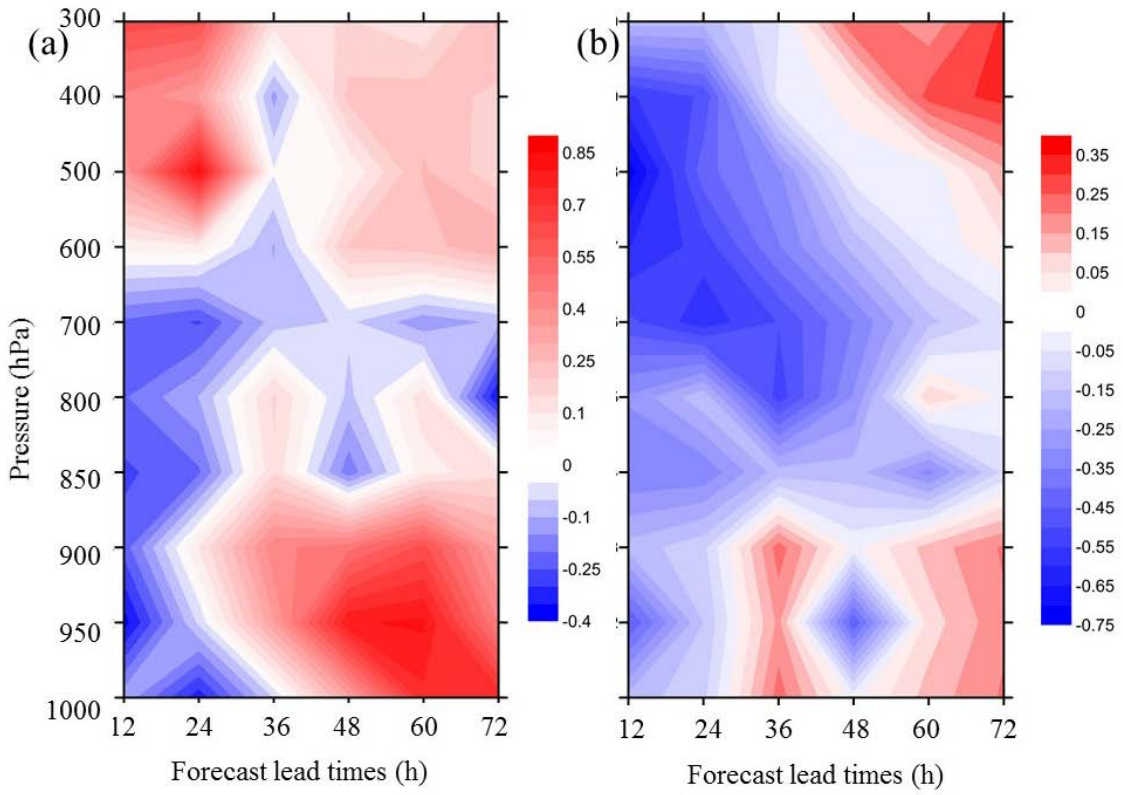

Figure 43 (a): Bias and (b): RMSD differences of the predicted winter RH profiles (%) at different forecast lead times between MW and IR configurations.

5.3 Individual Case Study

The small differences in EnKF configuration applied on summer may mainly due to the usage of ensemble members which the predictions are an average state of the ensemble forecasts. To investigate the differences between MW and IR configurations during summer, the summer case used in chapter 4 section 4.3 with Hybrid configuration

is simulated. Both the regional model lids at 50-mb and 10-mb are tested using the same horizontal configuration in section 4.3. Also, the drought condition occurred over the Corn Belt region and the heavy precipitation occurred in the south-east of U. S. are verified using both MW and IR configurations. A set of four experiments including the CTRL, IR, MW, and CON experiments are set up to investigate the differences between using different satellite sensors in DA system. The descriptions of the experiment set ups are concluded in Table 6.

5.3.1 Results Obtained from WRF-50mb experiment

5.3.1.1 Verification of Drought

The near-surface temperature is firstly verified against the in-situ observations. A comparison of the in-situ observation and the model results from three DA configurations (Hybrid, Hybrid-IR, and Hybrid-MW) is plotted in Fig. 44. Three DA configurations showed similar results – all-three experiments overestimate the near-surface temperature at first few DA cycles, then underestimate it at later DA cycles. However, slightly improvements (an extra 2% skill) are obtained in the Hybrid-IR configuration compared to the Hybrid configuration, and the Hybrid-MW configuration shows a decrease of the predicting skill.

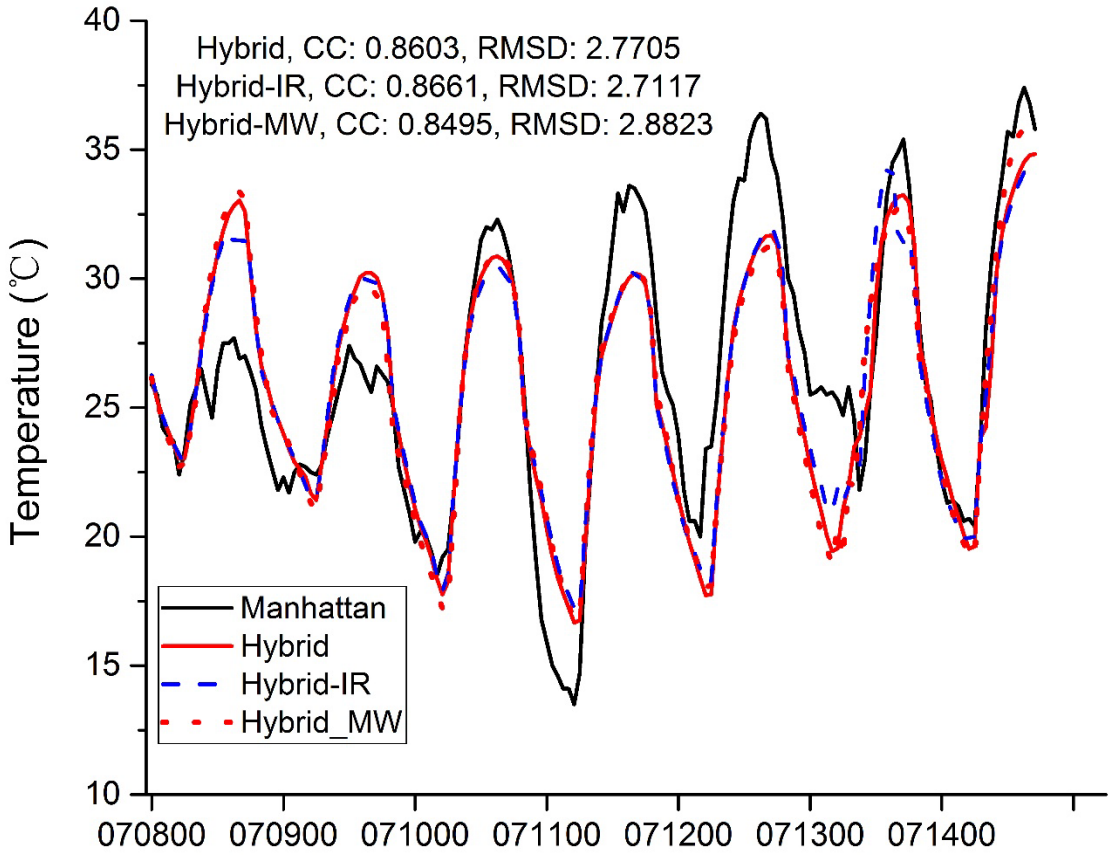

Figure 44 Time series of near-surface temperature observations from Manhattan, KS (39.102°N, 96.609°W) and the predicted 2 m temperature from different experiments.

The differences of the SCC and RMSDs between the GLDAS surface skin temperature and the model results (Fig. 45) are calculated in the same way as in Fig. 26. The larger positive values in Fig. 45a and the smaller negative values in Fig. 45b indicate more improvements. Hybrid-IR shows better performances in the early DA cycles while Hybrid-MW shows better performances in the late DA cycles. However, no significant differences are found in the averaged distribution of surface skin temperature.

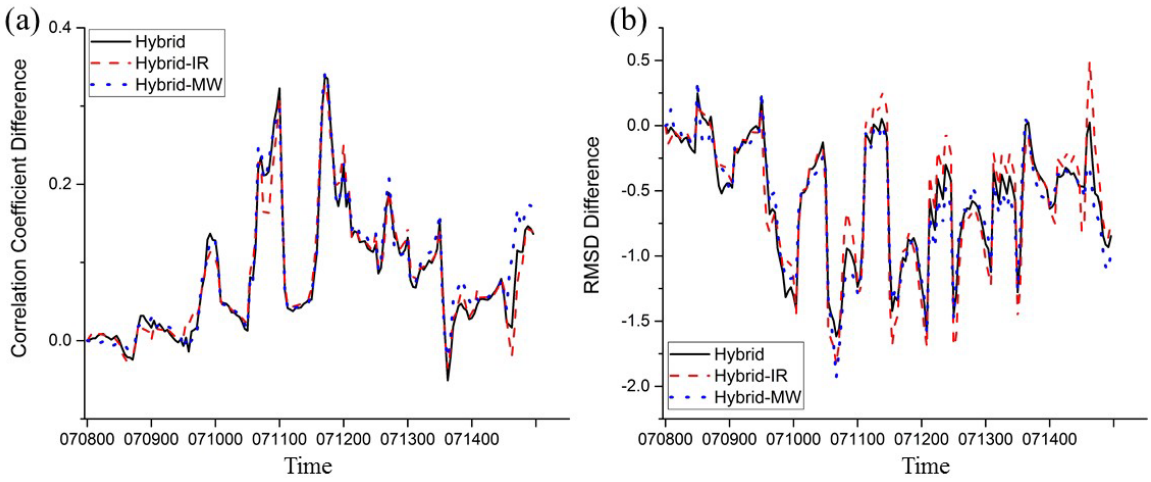

Figure 45 (a): Spatial correlation coefficients and (b): RMSD differences of surface skin temperature between IR and MW configurations with the regional model top at 50-mb.

5.3.1.2 Verification of Precipitation

The comparison of the precipitation time series over the major precipitation region between the three DA configurations are shown in Fig. 46. Different from the near-surface temperature predictions, less CC and larger RMSD (a decrease of 15% prediction skill) are observed in the Hybrid-IR configuration. The Hybrid-IR configuration shows even stronger overestimation of the precipitation amounts in the early DA cycles, and becomes comparable in the late DA cycles. In contrast, the Hybrid-MW configuration shows better performance in the early DA cycles compared to the infrared experiment.

The comparison of the distribution of daily precipitation is shown in Fig. 47. In July 8th (the first row in Fig. 47), the Hybrid (Fig. 47b) and Hybrid-IR (Fig. 47c) configurations overestimate the daily precipitation compared to the GLDAS products (Fig. 47a). In contrast, the Hybrid-MW (Fig. 47d) configuration shows much better

results with much smaller precipitation areas compared to the other two experiments. When it comes to July 12th (the second row in Fig. 47), the precipitation patterns successfully match the GLDAS products with slightly swift to the west. Among these three DA configurations, the Hybrid-MW predicts better precipitation patterns than Hybrid-IR.

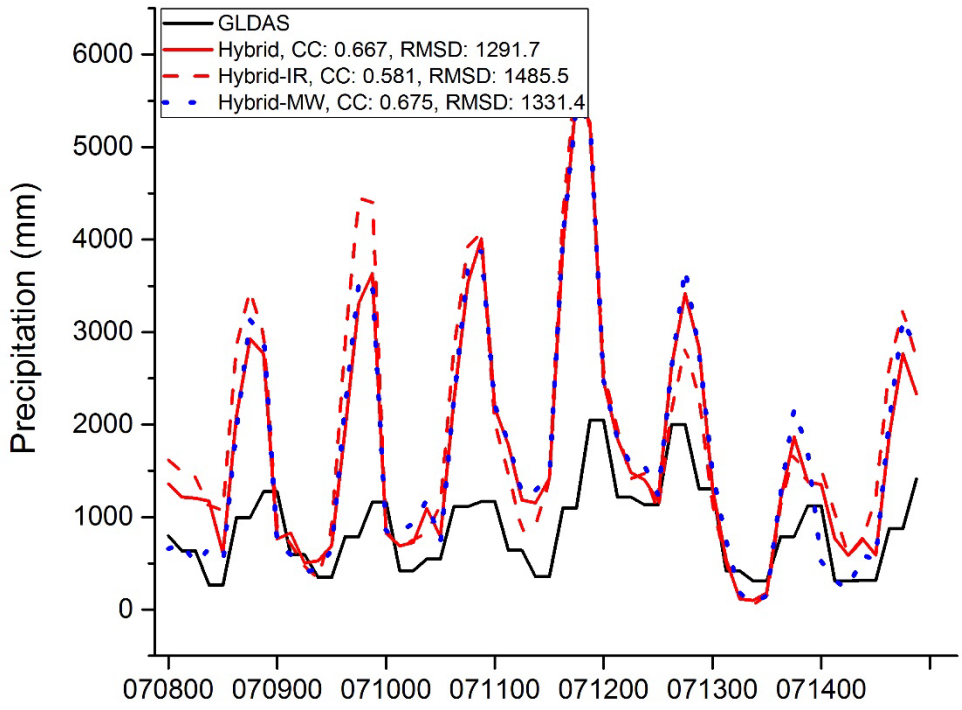

Figure 46 Time series of the 3-h accumulated precipitation from different numerical results with the regional model top at 50-mb.

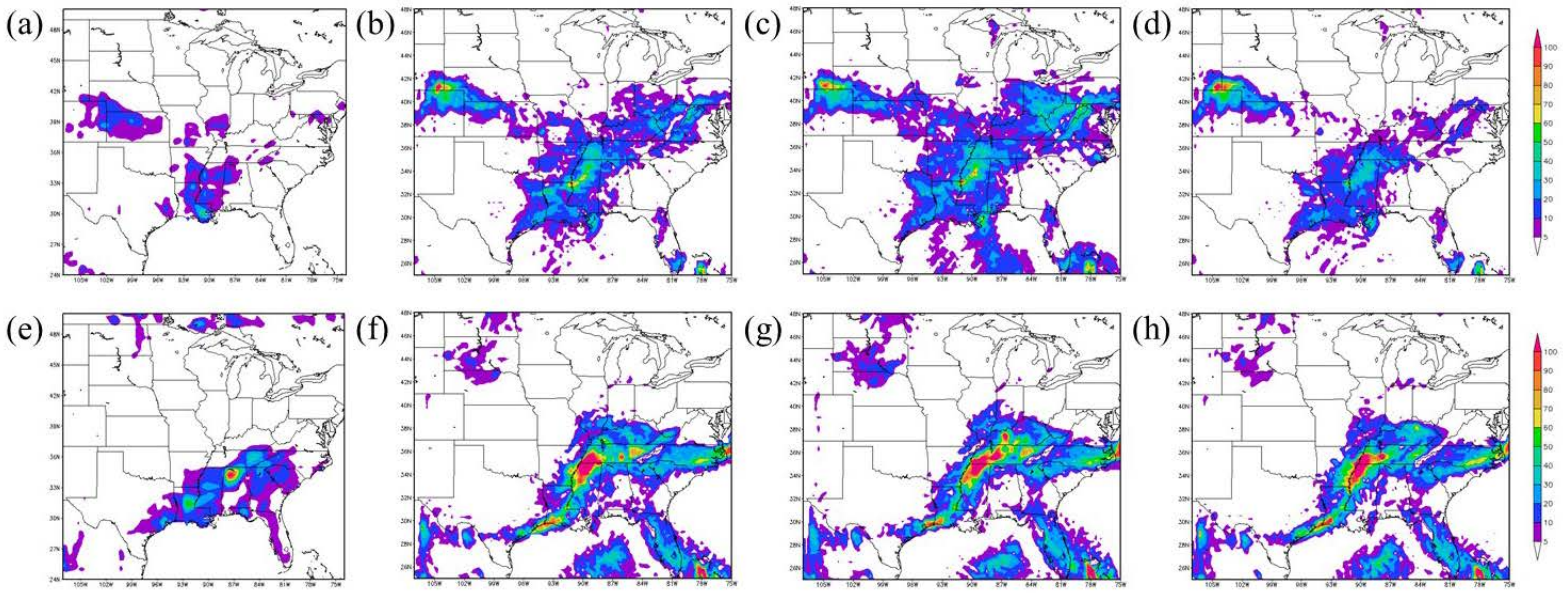

Figure 47 Daily precipitation (mm) distributions of July 8th, and July 12th, 2012, from different numerical results with the regional model lid at 50-mb.

5.3.2 Results obtained from WRF-10mb Experiment

5.3.2.1 Verification of Drought

The same observations are used for the verification of the model outputs with model lid at 10-mb. A comparison of the CTRL experiments with different model lids are firstly made (Fig. 48). Slightly improvements are made by raising the model lids to 10-mb. The major differences are observed in the early two days. The CTRL-10mb experiment shows better performance in the first day prediction while the CTRL-50mb experiment shows better performance in the second day prediction.

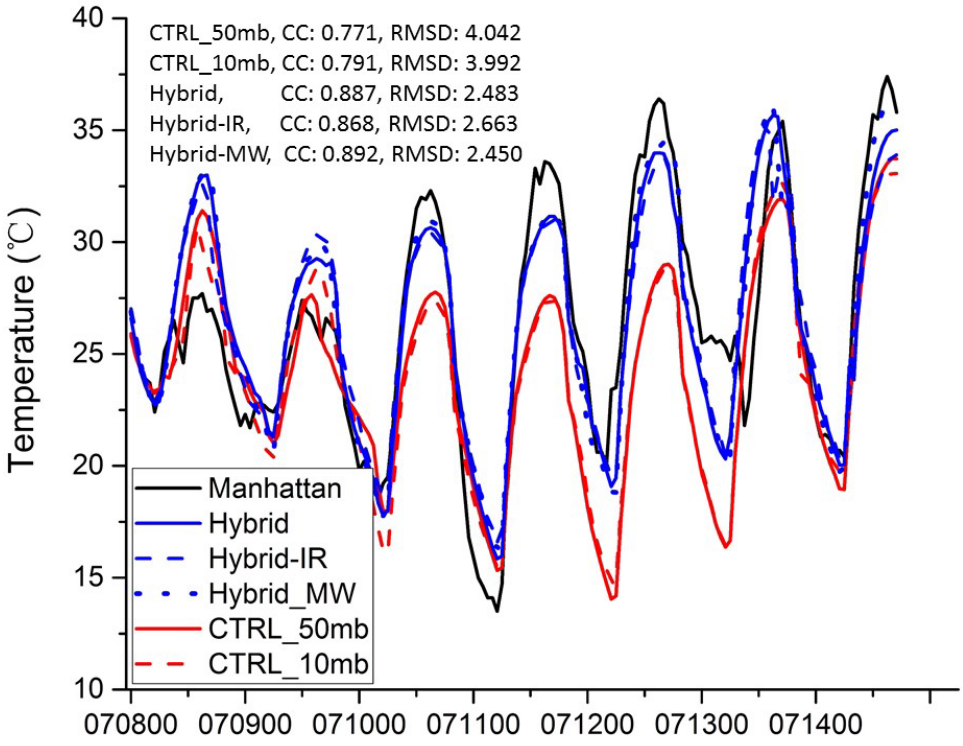

Figure 48 Time series of near-surface temperature observations from Manhattan, KS (39.102°N, 96.609°W) and the predicted 2 m temperature from different experiments with model top at 10-mb.

Similar to Fig. 45, the differences of SCC and RMSDs are plotted in Fig. 49. The impacts of the applied DA on regional forecasts show that the model lid at 10-mb predicts better than the model which model lid is set at 50-mb. The largest improvements by raising model lid to 10-mb are made in the Hybrid-MW configuration with an extra 15% skill in predicting near-surface temperature. For the Hybrid-IR configuration, no significant improvements are made when model lid is raised. The differences between the infrared and microwave configurations also changed. When the model lid was set at 50-mb, the Hybrid-IR shows better scores than the Hybrid-MW configuration. In contrast, when the model lid is set at 10-mb, the performance of the Hybrid-MW configuration exceeded the Hybrid-IR configuration with an extra 8% skill in predicting near-surface temperature. The significant improvement in the microwave experiment is believed as a result of the included extra stratospheric information via raising the model lid. Further discussion of the impacts of involving more stratospheric information into the system is addressed in chapter 6.

The assimilation of MW alone makes a small positive impact in the first few DA cycles compared to all observations configuration. In the later DA cycles (on July 13th), larger improvements are made in the MW configuration compared to the all observations configuration. In contrast, the assimilation of IR alone makes smaller positive impacts compared to the MW configuration and the all observations configuration.

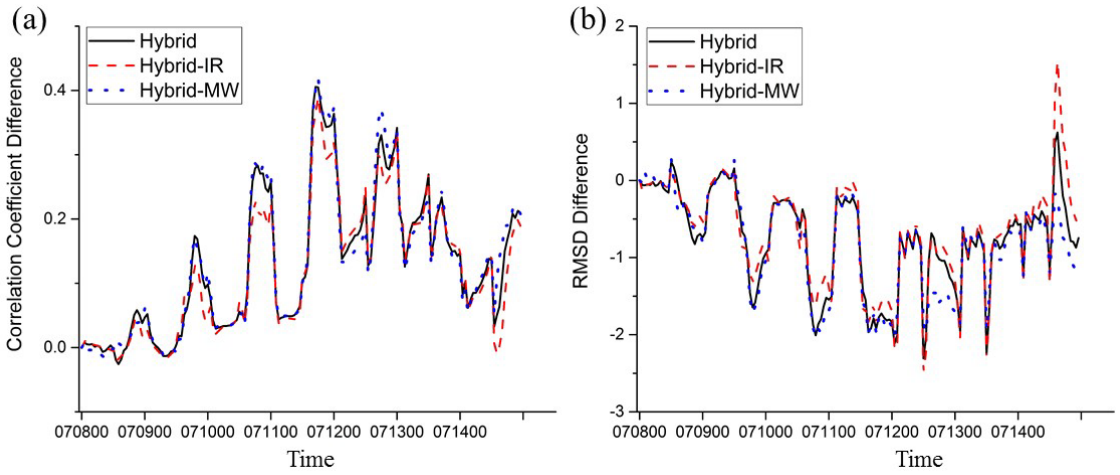

Figure 49 Spatial correlation coefficients (a) and RMSD (b) differences of surface skin temperature between IR and MW configurations with the regional model top at 10-mb.

5.3.2.2 Verification of Precipitation

All three DA configurations still overestimate precipitation amounts after the raising of model lid (Fig. 50). Smaller correlation coefficients are found in the Hybrid and Hybrid-MW configurations compared to the results obtained in the model results with 50-mb model top. In contrast, better RMSDs are found in these two configurations. The differences of the RMSD between the MW and IR configurations are enlarged by raising the model lid to 10-mb. Generally, an average of 45% more precipitation is generated in the Hybrid-IR configuration than the Hybrid-MW configuration. The largest difference was found at the early predictions where an average of 115% more precipitation is obtained in the Hybrid-IR configuration than the MW configuration.

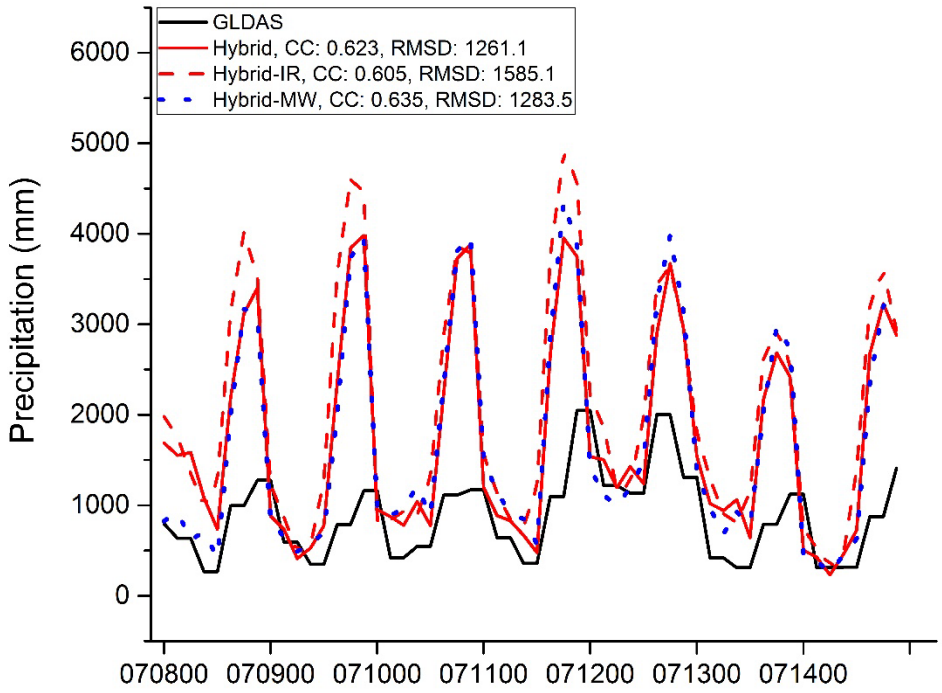

Figure 50 Time series of the 3-h accumulated precipitation from different numerical results with the regional model top at 10-mb.

The distributions of daily precipitation on July 08th, and 12th produced after the application of Hybrid, Hybrid-IR, and Hybrid-MW configurations on WRF system with model lid set at 10-mb are shown Fig. 51. The daily precipitation generated with a higher model lid shows similar characteristics to those with a lower model lid (Fig. 47). However, the daily precipitation amount is largely reduced in July 12th (second row in Fig. 51). The Hybrid (Fig. 51f) and Hybrid-IR (Fig. 51g) configurations again largely overestimate precipitation areas. In July 12th, an overestimation over the northwest was found in both Hybrid and Hybrid-MW configurations. In contrast, the Hybrid-MW shows more reliable results.

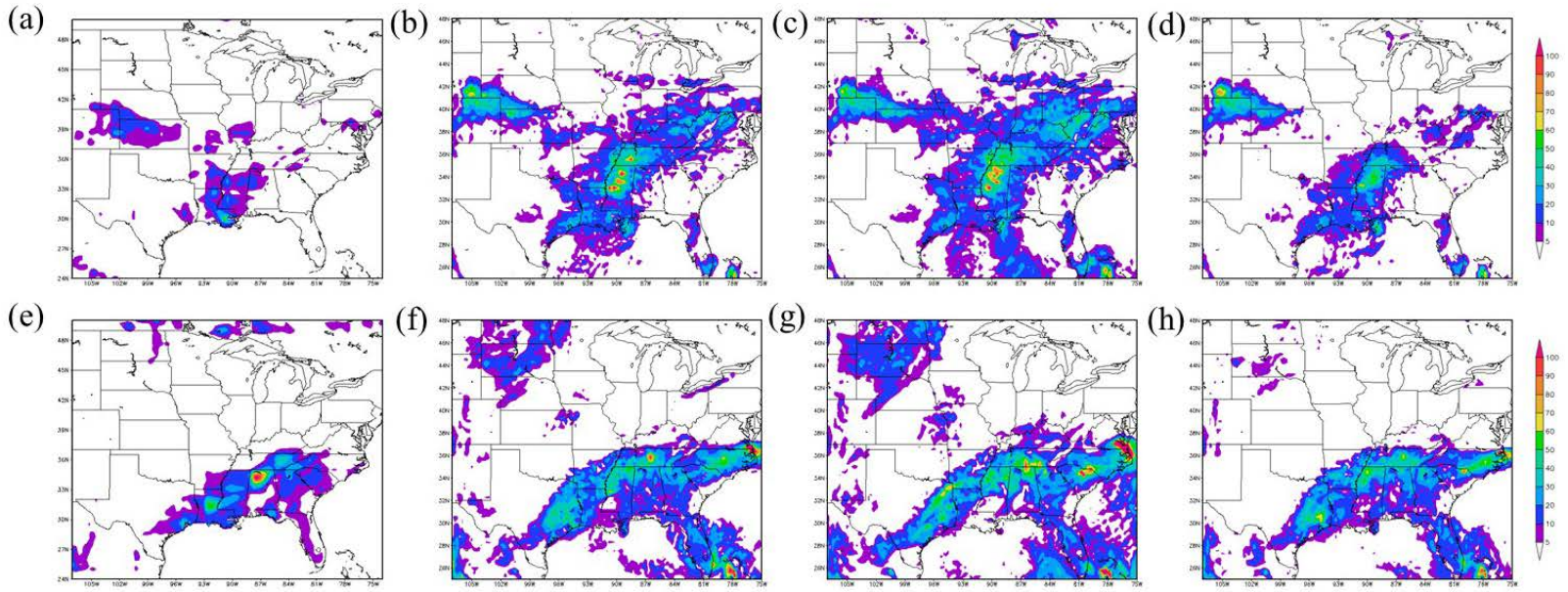

Figure 51 Daily precipitation (mm) distributions of July 8th, and July 12th, 2012, from different numerical results with the regional model lid at 10-mb.

5.4 Summary

The impacts of assimilating infrared and microwave satellite observations alone in DA system on regional short-term weather forecasts over the continental U. S. are investigated using the regional model WRF-ARW with a model top at 10-mb and the operational DA model GSI. The 3D-Var based ensemble-variational Hybrid algorithm is used in winter and the EnKF is used in summer. The forecast results are verified against conventional observations.

In summer, no significant differences are found between the MW and IR configurations. The IR configuration performs slightly better than the MW configuration. The smaller differences found in summer may mainly due to the usage of ensembles as the initial conditions. The analysis and final predictions are results of the average states. In contrast, large differences are found in winter using the Hybrid configuration. The MW makes overall advantages compared to the IR when assimilated alone. In the analysis, larger advantages of the MW configuration are found in the tropopause layers for wind profiles. For analyzed temperature profiles, the MW configuration shows larger advantages in the lower troposphere and the lower stratosphere. For analyzed RH profiles, the IR configuration shows better skills in lower troposphere. The MW provids smaller RMSDs in the higher troposphere but also with larger biases.

Predictions made by the IR and MW assimilations also vary in different variables and heights. In general, the MW has better predicting skills in the first 12-h predictions (except for wind predictions which MW shows overall better skills in short-period forecasts) compared to the IR when assimilated alone. An extra 7% skill in predicting

surface pressure and an extra 3% skill in predicting other variables at 12-h forecast lead time are obtained in MW configuration when compared to IR configuration. In contrast, an extra 7.7% skill in predicting surface pressure and an extra 1.5% skill in predicting other variables at later forecast lead times are obtained in IR configuration when compared to MW configuration. For different layers, MW configuration usually has better predicting skills in the higher layers. Extra 3% and 15% skills are found in predicting tropopause wind and temperature when microwave observations are assimilated alone, respectively. For RH profiles, MW configuration shows better skills (4%) in the higher tropospheric layers. IR shows a small extra 1% skill in predicting lower tropospheric temperature in later forecast lead times.

Individual case studies are also conducted to verify the impacts of MW and IR satellite observations when assimilated alone. Two sets of vertical layers are used in model lid at 50-mb and 10-mb, respectively. When the model lid is set at 50-mb, the IR configuration shows extra skills in predicting temperature but tends to enlarge the overestimation of precipitation peaks while the MW configuration shows extra skills in predicting heavy precipitation. The advantages of predicting temperature when IR is assimilated alone are the results that infrared channels have more temperature channels. In contrast, the MW channels can penetrate through non-precipitation clouds and carry atmospheric humidity information within the clouds (Zou, et al., 2013). However, when the model lid is raised to 10-mb, more advantages are found in predicting both temperature and heavy precipitation when MW satellite observations are assimilated alone. The largely improved temperature predictions in MW configuration may due to the

extra stratospheric microwave information included in the assimilation system. In the next chapter, the impacts of the stratospheric microwave information are studied.

CHAPTER SIX IMPACTS OF STRATOSPHERIC MEASUREMENTS ON REGIONAL NWP SYSTEM

In chapter five, the assimilation of microwave satellite observations alone advanced the regional NWP system in early forecast lead times. Extra skills in predicting wind and temperature in the tropopause layers are found when MW satellite observations are assimilated alone. MW configuration also shows advantages in predicting regional heavy precipitation events. Furthermore, large improvements are found when extra stratospheric microwave information is included in the DA system. In this chapter, we will discuss about the impacts of raising model lids on regional NWP predictions by raise the model lid to 1-mb. And the impacts of more stratospheric microwave information on regional NWP will be tested. At last, a FSO analysis will be taken out aiming at an optimal selection of the microwave channels. The performance of the optimal selected microwave channels is compared in individual case studies.

6.1 Introduction

In the early 20th century, many researches (e.g., Baldwin and Dunkerton, 1999 & 2001; Baldwin, et al., 2003) suggested that by including the stratospheric state in NWP systems, some prediction skills can be gained in the troposphere. Later in the early 2000s, Charlton and his group tested the impacts of stratospheric state on troposphere forecasts and found that a small amount of extra skill (~5%) can be obtained by including stratospheric information in a simple statistical forecasting model of the troposphere, and

at the same time, based on three cases, they also found that the tropospheric flow and tropospheric synoptic-scale systems can be statistically significantly influenced by including the stratospheric initial conditions (Charlton et al., 2004). Recently, due to the significant theoretically improvements in data assimilation fields and the application of ensemble methods in NWP systems, the operational data assimilation system began to not only assimilate the traditional meteorological data but also assimilate multiple atmosphere constituents extending from ozone to aerosols, particle matters (e.g., $PM_{2.5}$), greenhouse gases, etc. With a better representation of the atmosphere including the valuable stratospheric information, Gerber et al. (2012) found that an improvement of short-range forecasts can also be investigated and at the same time, the stratospheric information can provide additional skill on seasonal time scales forecasts.

As described in chapter 3, the CTRL experiments in all three sets of experiments are used to investigate the impacts of raised model lids. The vertical resolutions are relatively coarser than those in studying convective gravity waves (150 levels or more, Costantino, et al., 2015). The impacts of the extra stratospheric microwave information on regional NWP system will be brought out based on the vertical weighting function of each channel. The vertical weighting function is the measurements of the level that contribute the most to the observed signal and it depends on the frequency of the observing channel. The weighting functions of AMSU-A, ATMS, and SSMI/S are shown in Fig. 52. Based on the weighting function of each sensor, a selection of the stratospheric microwave channels can be brought out. The detailed stratospheric channel selections of the microwave sensors are shown in appendix B.

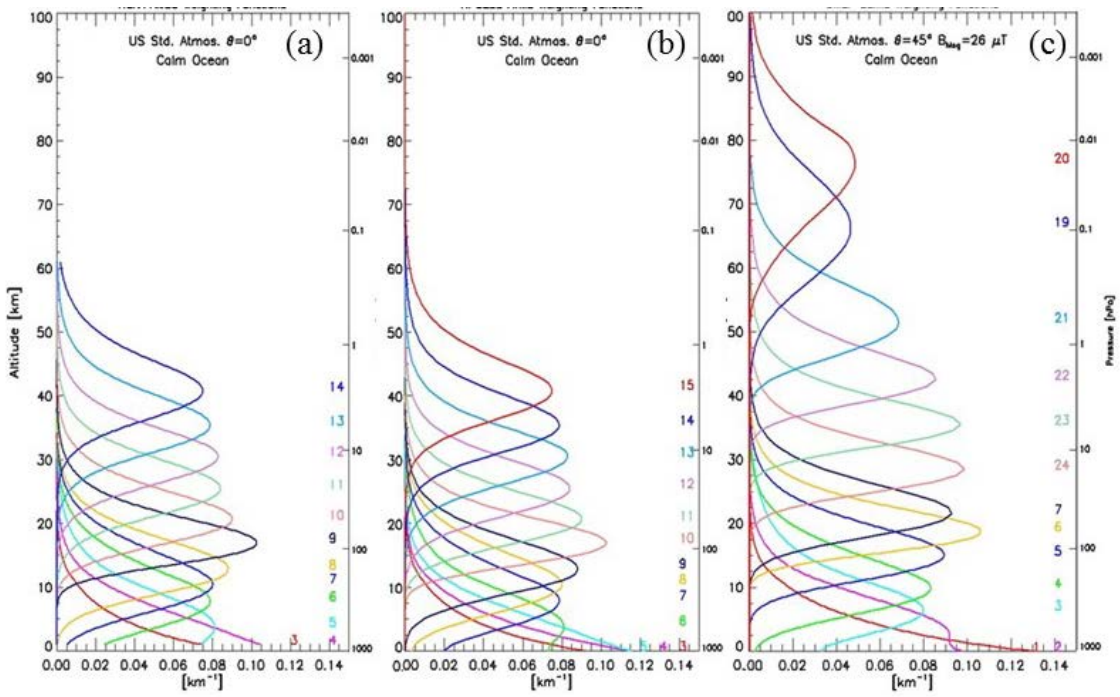

Figure 52 Weighting functions of microwave sensors, (a): AMSU-A, (b): ATMS, and (c): SSMI/S.

6.2 Impacts of Raised Model Lids with More Assimilated Stratospheric Observations on NWP System

6.2.1 Impacts on Initials

6.2.1.1 Systematic Differences on Initials

Firstly, the systematic differences between the model results with different model lids ("WRF-50", "WRF-10", and "WRF-1" for model lid at 50-mb, 10-mb, and 1-mb, respectively) during winter are investigated. The detailed experiment configurations are described in chapter 3. The averaged biases and RMSDs fit to conventional observations during the study periods are compared in this section.

The comparison of the impacts of raising model lid from 50-mb to 10-mb and then further to 1-mb on the initial conditions are concluded in Table 9. The WRF-50 is used as the baseline, results showed in Table 9 are calculated using WRF-10 and WRF-1 results minus the WRF-50 results. Generally, the configuration with raised model lid has better performances. The configuration with model lid set at 1-mb shows smaller RMSDs of surface pressure, temperature and precipitable water in initial conditions. However, the raising of model lids decrease the performance of adjusting initial wind.

Table 7 Comparison of the initials with different model lids

Surface Pressure (Pa)	Winter	
	10-mb – 50-mb	**1-mb – 50-mb**
Bias	0.1511	0.1264
RMSD	-0.0433	-0.0926
All-level mean wind (m s^{-1})	**10-mb – 50-mb**	**1-mb – 50-mb**
Bias	0.0380	0.0356
RMSD	0.8965	0.8446
All-level mean T (K)	**10-mb – 50-mb**	**1-mb – 50-mb**
Bias	-0.4819	-0.3688
RMSD	-0.1894	-0.2028
All-level mean RH (%)	**10-mb – 50-mb**	**1-mb – 50-mb**
Bias	-0.1592	-0.2949
RMSD	2.3534	2.0512
Precipitable Water (mm)	**10-mb – 50-mb**	**1-mb – 50-mb**
Bias	-0.0215	0.0040
RMSD	-0.0881	-0.0980

The differences between the initials in WRF-10 (black solid lines), WRF-1 (red solid lines) and the initials in WRF-50 are plotted in Fig. 53. The negative values indicate that the raising of model lids had positive impacts on the initials, vice versa. Generally, the WRF-1 shows more positive impacts than WRF-10 with both smaller biases and

RMSDs on initial tropopause wind, temperature, and RH profiles. Close values are found in the middle troposphere.

The raised model lids show overall positive impacts on the biases of the initials. Only the biases of wind at near surface layers are enlarged. Slightly larger wind and temperature biases are also observed at the tropopause layers in WRF-10 experiment. Biases of RH profiles are improved over all tropospheric layers. The RMSDs show different characteristics. Negative impacts are observed over the mid- and lower-troposphere (under 400 hPa) for all three profiles. For wind profiles, less skills are observed in lower troposphere and at lower stratosphere. However, 2% and 8% more skills are obtained in WRF-1 configuration than WRF-10 over the lower troposphere and the tropopause. Temperature profiles show similar results, not only shows 10% and 13% more skills are obtained in WRF-1 configuration over the lower troposphere and tropopause, but also shows better skills over the tropopause and lower stratosphere when compared to WRF-10 configuration. RH and temperature have similar structures with less skills over the lower troposphere, and WRF-1 also shows some more skills (~4%) than WRF-10.

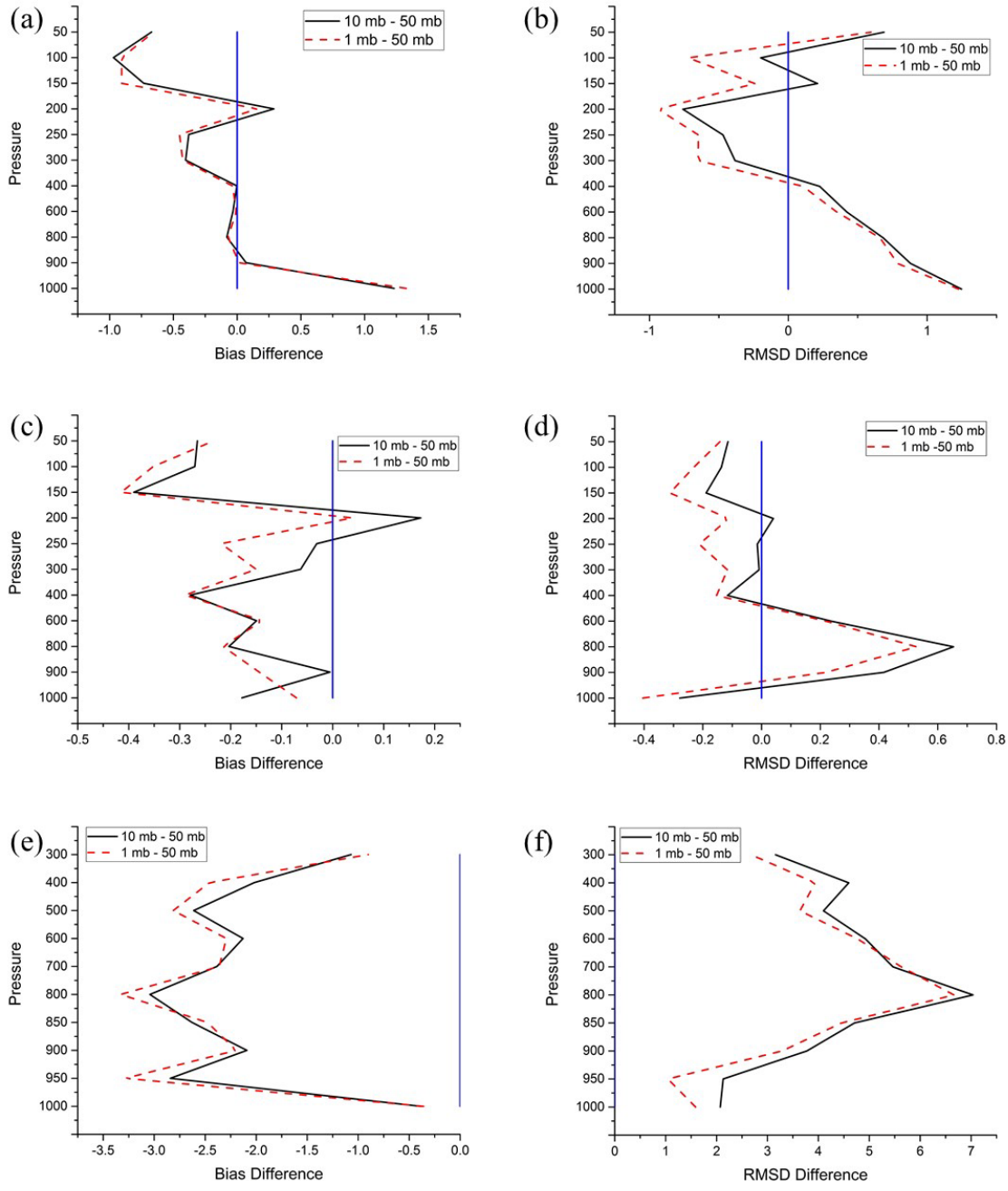

Figure 53 Bias (left panel) and RMSD (right panel) differences between model results with different model lids. (a, b): wind profiles (m s^{-1}); (c, d): temperature profiles (K); (e, f): RH profiles (%).

6.2.1.2 DA impacts on initials

The Hybrid scheme is used for the comparison of DA impacts with different model lids (Hybrid-50, Hybrid-10, and Hybrid-1 for model lids at 50-mb, 10-mb, and 1-mb). The impacts of DA on the initials are concluded in Table 10. The results are calculated using the differences between the results from different model lid configurations and then remove the systematic differences. The negative values indicate that more improvements are made after DA applications and the smaller values the more improvements are made by raising the model lids. As shown in Table 10, overall positive impacts are made after the application of DA except that larger biases are obtained in all-level mean temperature. By raising the model lid from 10-mb to 1-mb, more improvements are obtained in initial wind, temperature and precipitable water. But for initial surface pressure and RH, Hybrid-10 shows better results than Hybrid-1.

Table 8 Comparison of the initials after DA with different model lids

Surface Pressure (Pa)	Winter	
	10-mb – 50-mb	**1-mb – 50-mb**
Bias	-0.1518	-0.1226
RMSD	-0.1745	-0.1540
All-level mean wind (m s^{-1})	**10-mb – 50-mb**	**1-mb – 50-mb**
Bias	-0.2119	-0.2149
RMSD	-0.3895	-0.3910
All-level mean T (K)	**10-mb – 50-mb**	**1-mb – 50-mb**
Bias	0.3823	0.2348
RMSD	-0.1954	-0.1983
All-level mean RH (%)	**10-mb – 50-mb**	**1-mb – 50-mb**
Bias	-0.2558	-0.1989
RMSD	-1.7030	-1.1670
Precipitable Water (mm)	**10-mb – 50-mb**	**1-mb – 50-mb**
Bias	-0.0844	-0.1356
RMSD	-0.1179	-0.1710

The impacts of the DA applications on initial profiles are also calculated in a similar way to those in Table 10 (Fig. 54). The negative values indicate that more improvements are made after DA application than raising the model lids alone. And the smaller the scores are, the more improvements are made. After the application of DA, improvements are made mainly in the troposphere. Biases of wind profiles differ from the temperature and RH profiles. Positive impacts on initial wind profiles are found over the lower troposphere. In contrast, small negative impacts are observed over the lower troposphere in initial temperature and RH profiles. In contrast, the positive impacts are found in the tropopause layers for temperature. RMSDs show overall improvements after DA application. Larger improvements for wind profiles are observed at lower troposphere with an extra 15% skill. Smaller improvements are also observed at the tropopause. Large improvements in initial temperature and RH profiles are also observed over the lower troposphere with extra 40% and 20% skills, respectively. Another large improvement for temperature is observed at the tropopause with an extra 50% skill.

For the differences between the Hybrid-10 and Hybrid-1, no significant bias differences are found in the wind profile. For temperature and RH profiles, the Hybrid-10 shows slightly smaller biases over the tropopause and higher in tropospheric layers. Hybrid-1 shows overall smaller RMSDs for wind and temperature profiles. The largest improvements of raising model lid from 10-mb to 1-mb are found over the tropopause layers with extra 3% and 15% for initial wind and temperature. Near surface temperature also meet larger improvements in Hybrid-1 with an extra 17% skill. In contrast, Hybrid-10 shows better adjustment of initial RH profiles with an extra 5% skill.

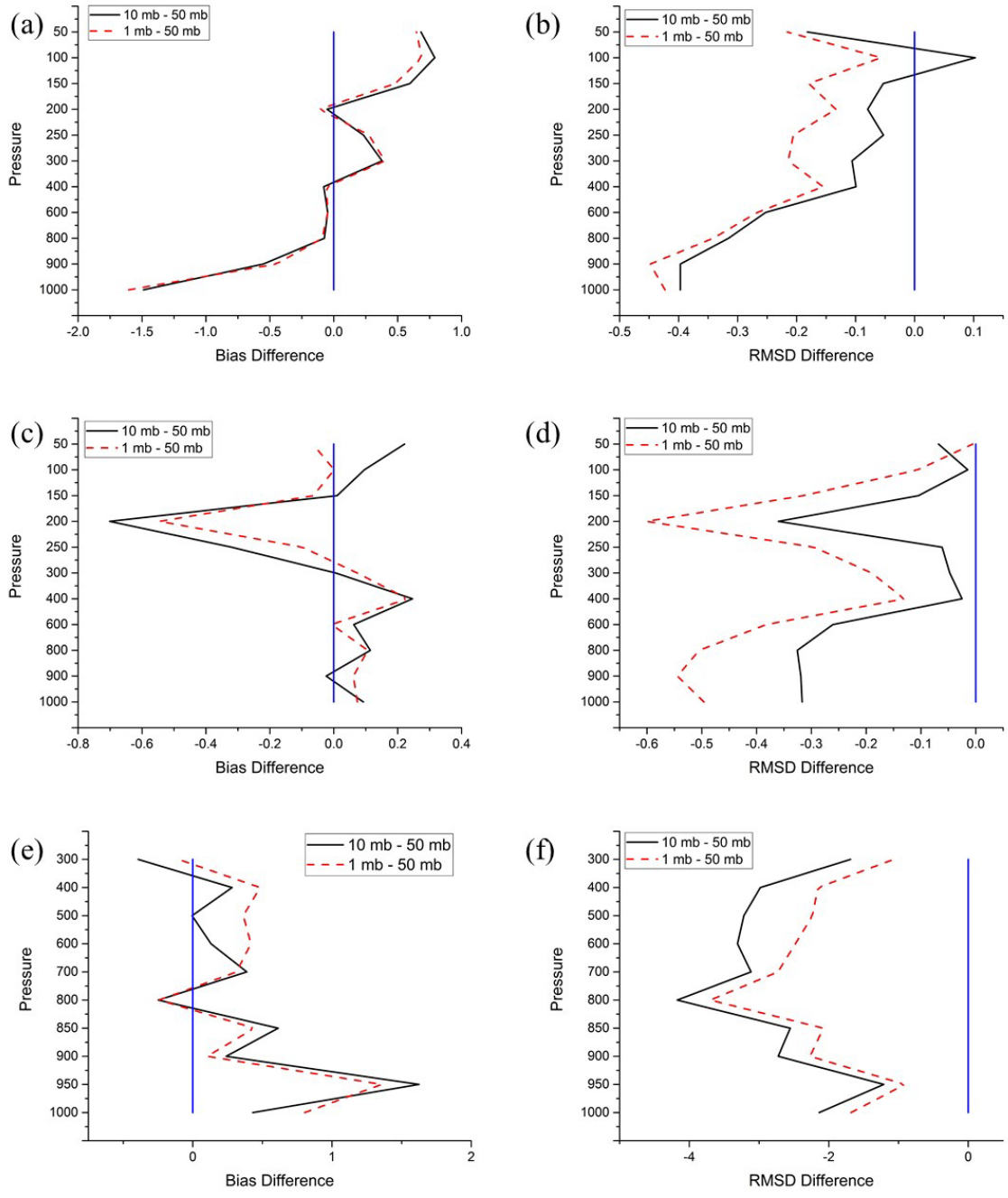

Figure 54 Bias and RMSD differences between model results with different model lids after the application of DA.

6.2.2 Impacts on Tropospheric Forecasts

As shown in section 6.2.1, more positive impacts are found on initial wind and temperature when more stratospheric observation is assimilated. In this section, whether the extra stratospheric observation has more positive impacts on the forecasts is tested. In this section, only the RMSDs are analyzed in the fact that the bias differences show similar results as in RMSD differences.

6.2.2.1 Forecasts of surface pressure

The systematic differences of the predicted surface pressure without the application of DA by raising the model lid to 10-mb and 1-mb are shown in Fig. 55. Similar to the initial conditions, the WRF-1 shows more improvements than the WRF-10 experiments. An extra 3% skill in predicting near surface pressure in the first few lead times is observed in the WRF-10 configuration. The predictabilities obtained in WRF-10 then reach the same level in WRF-50. In contrast, the WRF-1 shows overall improvements during the short-period forecasts with an extra 8% skill at the first 48-h forecast lead times.

The improvements of the predicted surface pressure after the application of DA and the removal of systematic differences are shown in Fig. 56. As shown in Fig. 56a, the negative values in both Hybrid-10 and Hybrid-1 show improvements (4.5% and 10%, respectively) compared to the Hybrid-50 experiment. The Hybrid-1 still yield larger improvements than the Hybrid-10 experiment. However, in Fig. 56b, after removing the systematic differences, the Hybrid-1 only shows a small extra 0.5% skill than the Hybrid-10 at 12-h forecast lead time when compared to the Hybrid-50 experiment. While at later

forecast lead times, Hybrid-10 shows extra 0.5% to 3.5% skills than the Hybrid-1 experiment.

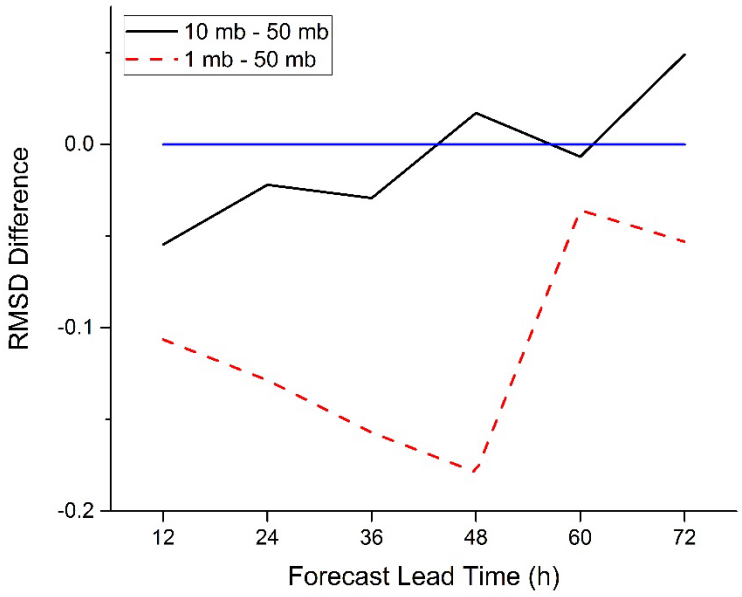

Figure 55 Systematic RMSD differences of the predicted surface pressure (Pa).

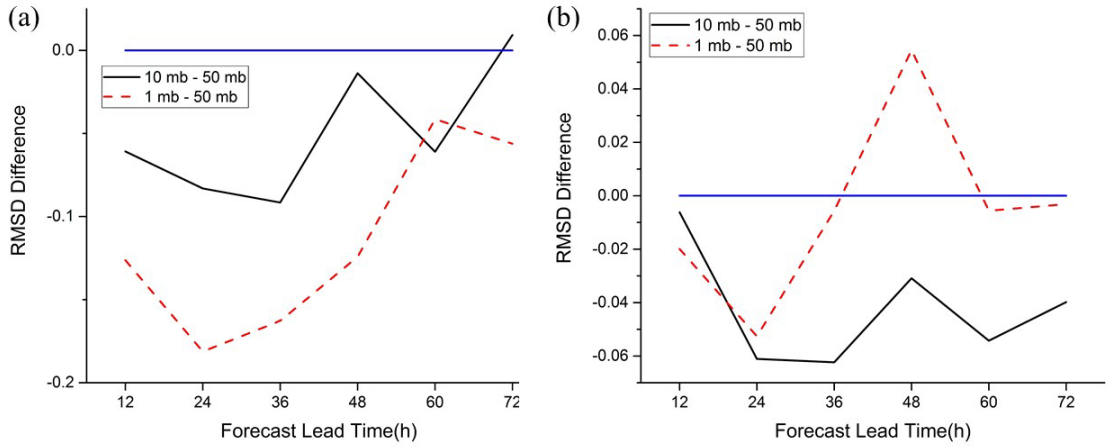

Figure 56 (a): RMSD differences of the predicted surface pressure (hPa); (b): same as (a) but removed systematic differences.

6.2.2.2 Forecasts of Wind

The systematic differences of the predicted all-level mean wind by raising the model lid alone are shown in Fig. 57. The WRF-1 shows more improvements at early forecast lead times than the WRF-10 experiment. Averaged 1.5% and 2% extra skills over the predicting period are obtained in the WRF-10 and WRF-1 configurations, respectively. The daily variations of the predictabilities of wind are discussed in chapter 4 which are results of the assimilation once per-day at 00:00 UTC. The largest improvement is found at 36-h forecast lead time in the WRF-1 experiment in which an extra 5.5% skill is found.

After the application of DA, the RMSD differences of the predicted all-level mean wind and the results after the removal of systematic differences are shown in Fig. 58. Both DA experiments showed improvements in the early forecast lead times. The Hybrid-1 shows better RMSDs in the first two-day forecasting. However, when a 3-day

forecasting is made, smaller improvements are obtained compared to the Hybrid-10 experiment. The improvements of both experiments are also smaller than raise the model lids alone in longer forecast lead times. A small extra 1% skill is obtained by including more stratospheric information below 10-mb after the removal of systematic differences. In contrast, an extra of 4% skill is obtained in the early forecast lead time when more stratospheric information up to 1-mb is included in the DA system after the removal of systematic differences.

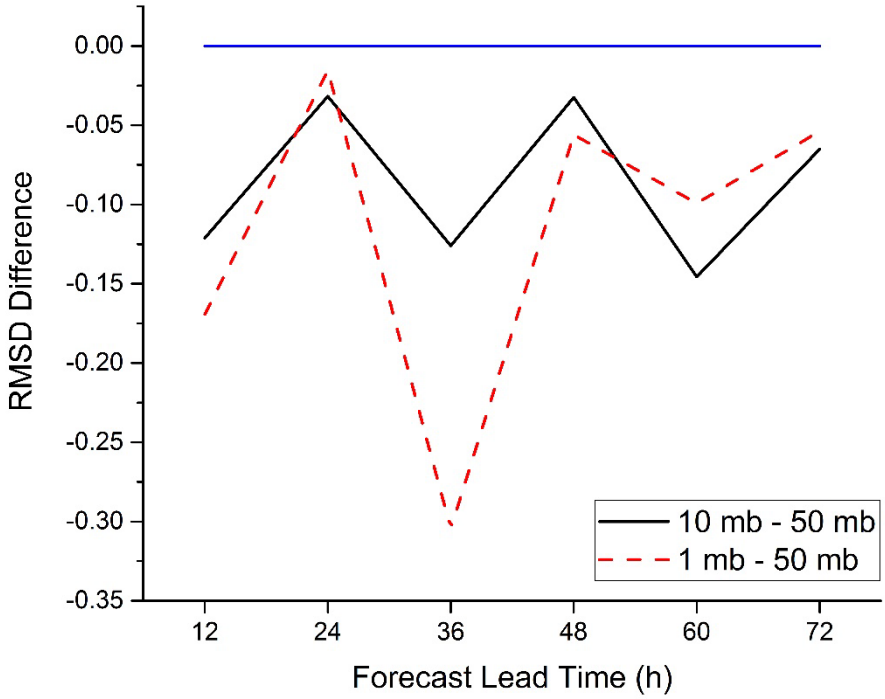

Figure 57 Systematic RMSD differences of the predicted all-level mean wind (m s^{-1}).

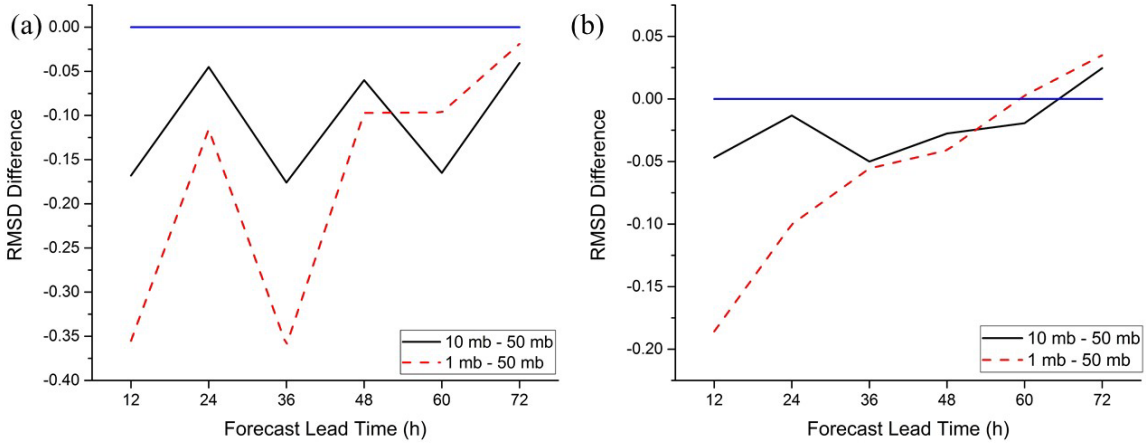

Figure 58 (a): RMSD differences of the predicted all-level mean wind (m s^{-1}); (b): same as (a) but removed systematic differences.

The RMSD differences between the predicted wind profiles with a model lid at 50-mb and the results with raised model lids are plotted in Fig. 59. The negative values (blue shaded areas) in Fig. 59a, b, d, and e indicate improvements are made by raising model lids, while the negative values (blue shaded areas) in Fig. 59 c, f (a removal of systematic differences are applied) indicate that larger improvements are made by including more stratospheric information in the DA system than raise the model lids alone. The major improvements are made in the tropopause layers for both model lids at 10-mb and 1-mb. Averaged extra 6.5% and 11.5% skills are obtained by raising the model lid to 10-mb and 1-mb alone at 12-h forecast lead time, respectively. In the DA experiments, the major improvements are also obtained in the tropopause layers with averaged extra 7.7% and 15% skills for model lid raised to 10-mb and 1-mb at 12-h forecast lead time, respectively. Both raising the model lids alone and applying DA with extra stratospheric information show less predicting skills over the near surface level at

all forecast lead times. In Fig. 59c, f, the major contributions of the extra stratospheric included in the DA system are also in the tropopause layers. The Hybrid-10 shows less improvements in the lower stratosphere (100-150-mb) and lower troposphere. In contrast, the Hybrid-1 shows more improvements over all layers at early forecast lead times. An extra 5% skill is obtained over the tropopause layers after the removal of systematic differences. Less improvements are obtained over the lower troposphere at longer forecast lead times.

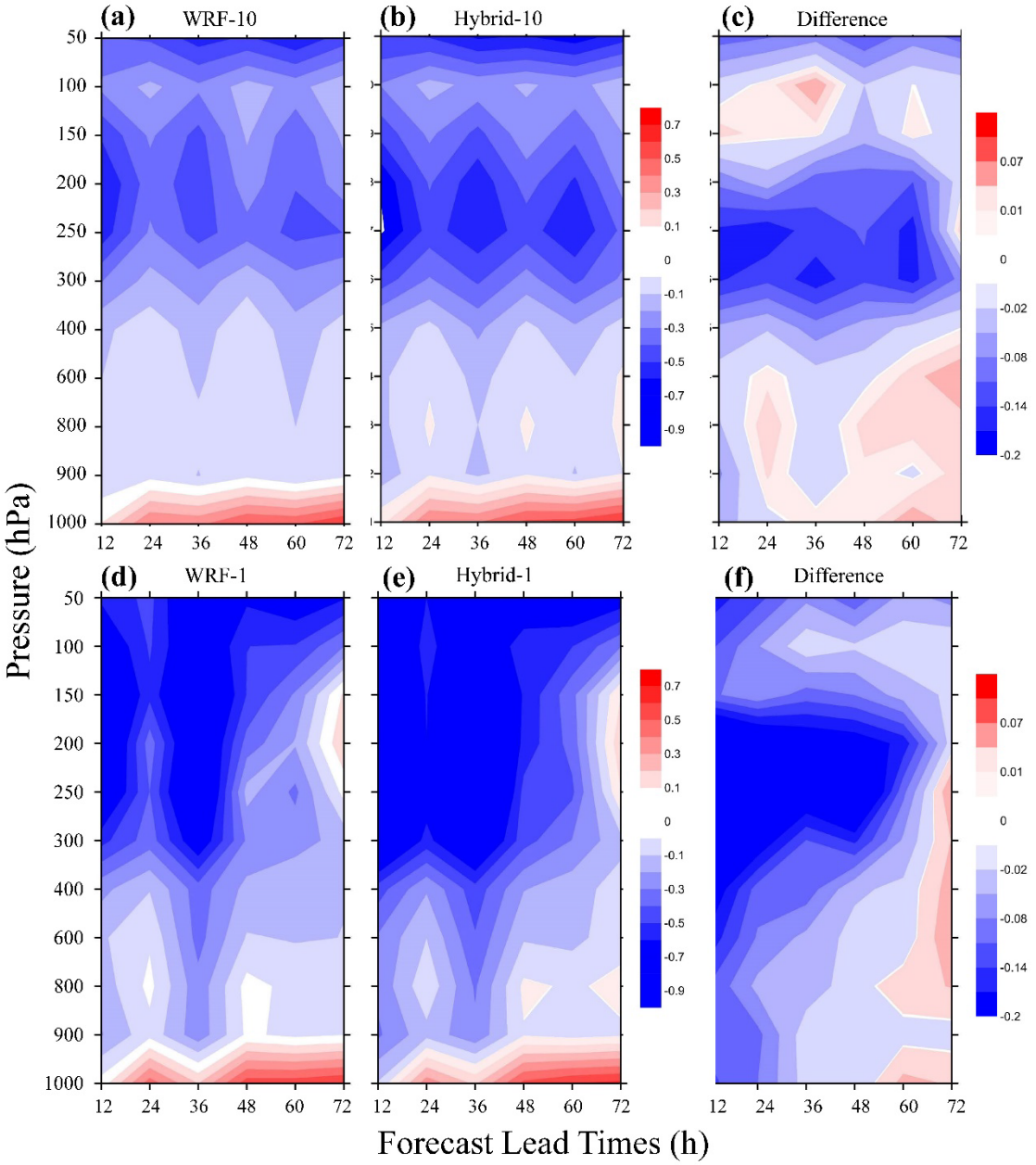

Figure 59 RMSD differences between the predicted wind profiles (m s^{-1}) as a function of forecast lead time (h) with different model lids.

6.2.2.3 Forecasts of Temperature

For temperature predictions without the application of DA (Fig. 60), only a small extra 3% skill is obtained at the 12-h forecast lead time when raising the model lid to 10-mb. When longer predictions are made, the predictabilities dropped about 3% in the WRF-10 experiment when compared to the WRF-50 experiment. Comparable improvement is found at the 12-h forecast lead time when the model lid is raised to 1-mb. However, for longer predictions, larger improvements are obtained where an averaged extra 7% skill is found compared to the WRF-50 experiment, aiming at that the information between 10-mb and 1-mb in the stratosphere is critical for the prediction of all-level mean temperature.

The differences of RMSDs after the application of DA are shown in Fig. 61a. The configuration with higher model lid still predicts better all-level mean temperature. The Hybrid-10 reaches the same predictability level as in Hybrid-50 at 48-h forecast lead time instead of 12-h forecast lead time without DA application. When the systematic differences are removed (Fig. 61b), improvements are made in both experiments. The Hybrid-1 shows larger improvements at 12-h forecast lead time with an extra 5.4% skill compared to an extra 2.9% skill in Hybrid-10. However, the extra information in the 10-1-mb level included in the DA system only shows positive impacts on the prediction of temperature at early forecast lead time and no significant impacts are found when the forecast lead time reaches to 48 hours. In contrast, the extra information in the 50-10-mb level included in the DA system shows longer impacts.

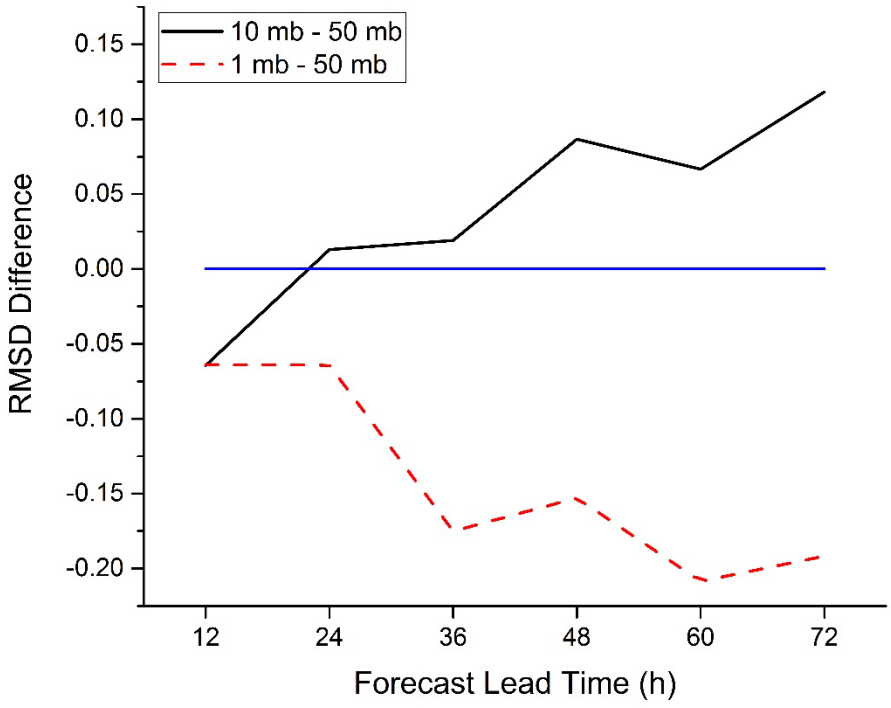

Figure 60 Systematic RMSD differences of the predicted all-level mean temperature (K).

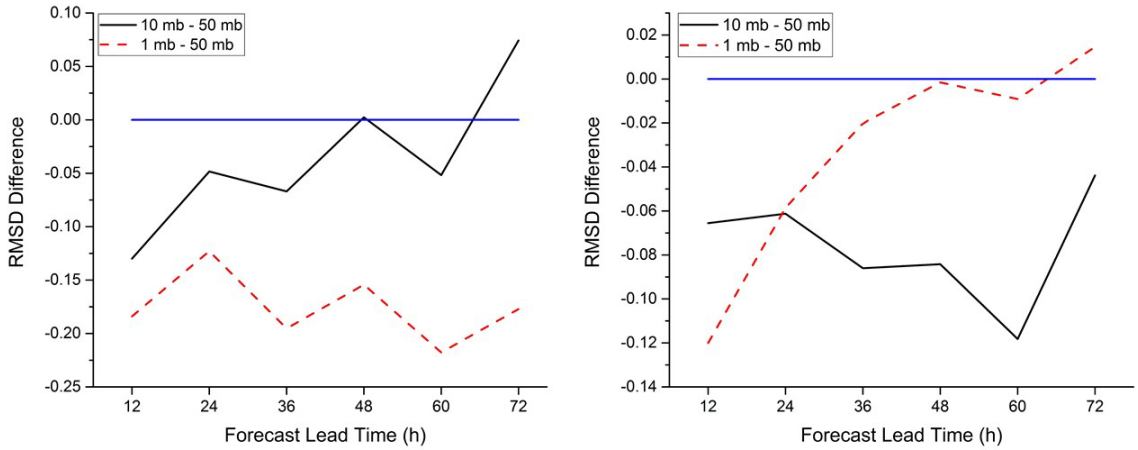

Figure 61 (a): RMSD differences of the predicted all-level mean temperature (K); (b): same as (a) but removed systematic differences.

For the temperature profiles (Fig. 62), major improvements made by raising the model lid are mainly in higher levels and near surface level. By raising the model lid to 10-mb alone, averaged extra 22%, 13%, and 20% skills are obtained at early forecast lead times in predicting temperature at near surface level, tropopause layers, and lower stratospheric layers, respectively. However, at longer forecast lead times, negative impacts are found in the lower tropospheric layers with an averaged decrease of 3% skill. When the model lid is raised to 1-mb, improvements are found in all vertical layers. The layers with major improvements show averaged extra 25.7%, 18.8%, and 22.4% skills which are slightly better than raising model lid to 10-mb.

After the application of DA, similar structures are obtained in both experiments. As shown in Fig. 62b, c, slightly improvements are obtained in the lower troposphere while larger improvements are made in the tropopause layers. After the removal of the systematic differences showed in Fig. 62a, d, the gross impacts of the inclusion of extra stratospheric information in the DA system are shown in Fig. 62c, f. Unlike the prediction of wind profiles, the inclusion of extra stratospheric information in DA system shows less impact in the lower stratospheric layers than raising the model lid alone. However, larger improvements over the tropopause layers are obtained in predicting both wind and temperature. Averaged extra 4.8% and 8% skills are obtained over the tropopause layers after the removal of systematic differences in the Hybrid-10 and Hybrid-1 experiments, respectively. Thus, the information in the 10-1-mb layers has more positive impacts on predicting the tropopause temperature. But for the near surface and lower tropospheric temperatures, more stratospheric information in the DA system

doesn’t show better improvements. The Hybrid-10 shows more improvements (an extra 2.3% skill) over the lower levels at early forecast lead times than the Hybrid-1 experiment (an extra 0.5% skill). Thus, the extra stratospheric information in the 10-1-mb layers has no significant impacts on the lower troposphere and near surface temperatures.

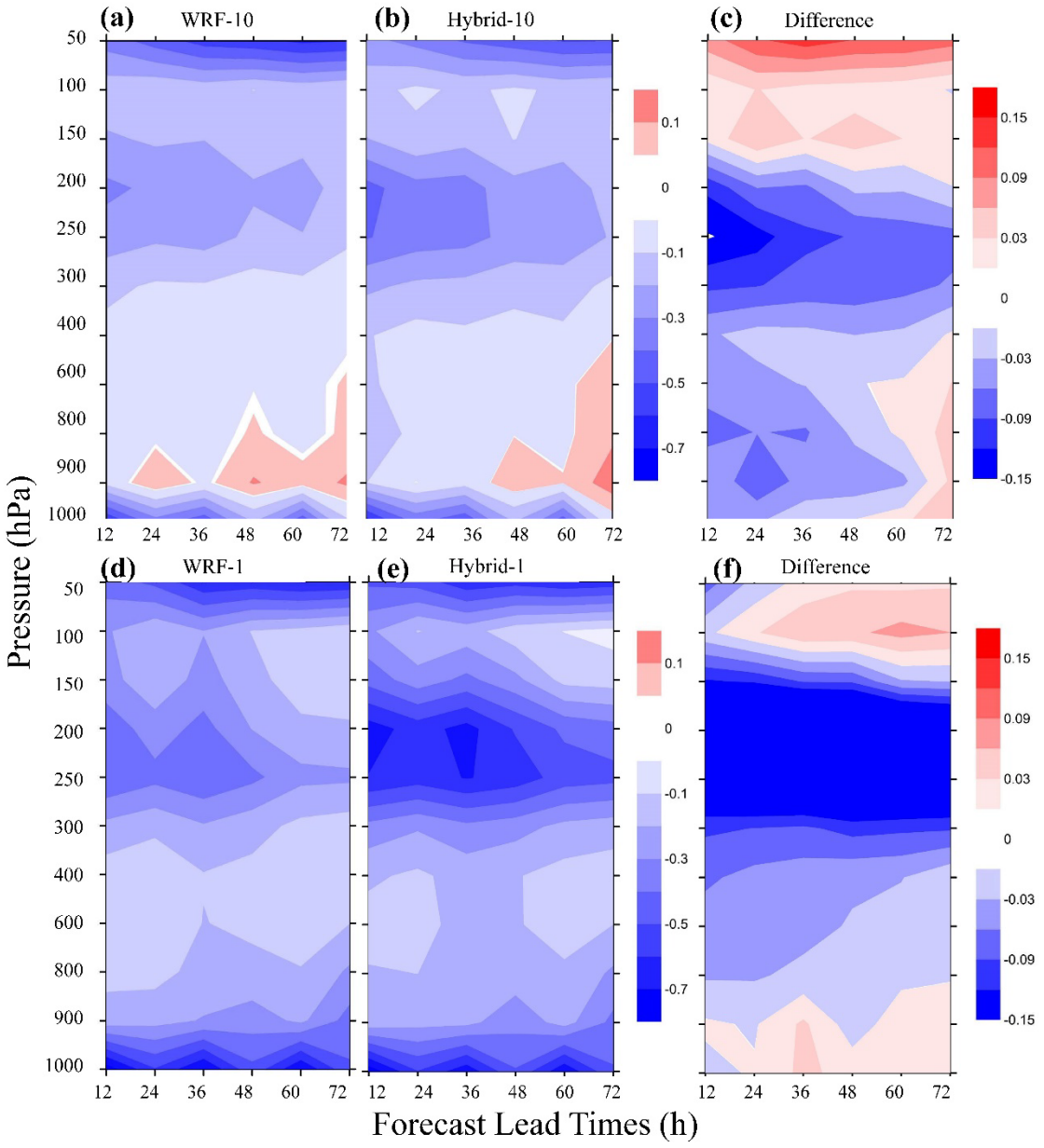

Figure 62 RMSD differences between the predicted temperature profiles (K) as a function of forecast lead time (h) with different model lids.

6.2.2.4 Forecasts of Relative Humidity

Similar to the prediction of temperature, by raising the model lid to 10-mb alone only shows a small extra 2.6% skill in predicting RH at early forecast lead times and less predictabilities at longer forecast lead times than the WRF-50 experiment (Fig. 63). In contrast, when the model lid is raised to 1-mb alone, more improvements are found at longer forecast lead times. About extra 1% skill is found at the first day forecasting, but almost extra 5% skill is found at the third day forecasting compared to the WRF-50 experiment.

After the application of DA, no significant differences are found in the Hybrid-10 experiment (Fig. 63a) compared to raising the model lid alone. The Hybrid-10 also shows less predictabilities at longer forecast lead times than the Hybrid-50 experiment. After the removal of systematic differences (Fig. 63b), only small extra 0.6-1% skills are found at 12-, 36-, and 60-h forecast lead times in the Hybrid-10 experiment. In contrast, the Hybrid-1 shows more positive impacts on the early forecast lead times. An extra 5% skill is found at 12-h forecast lead time and it drops as forecast lead time increases. At 48-h forecast lead time, the predictability of Hybrid-1 reached a comparable level with the Hybrid-50 experiment. Thus, the extra stratospheric information in the 10-1-mb level included in the DA system shows more positive impacts on the prediction of humidity for two days.

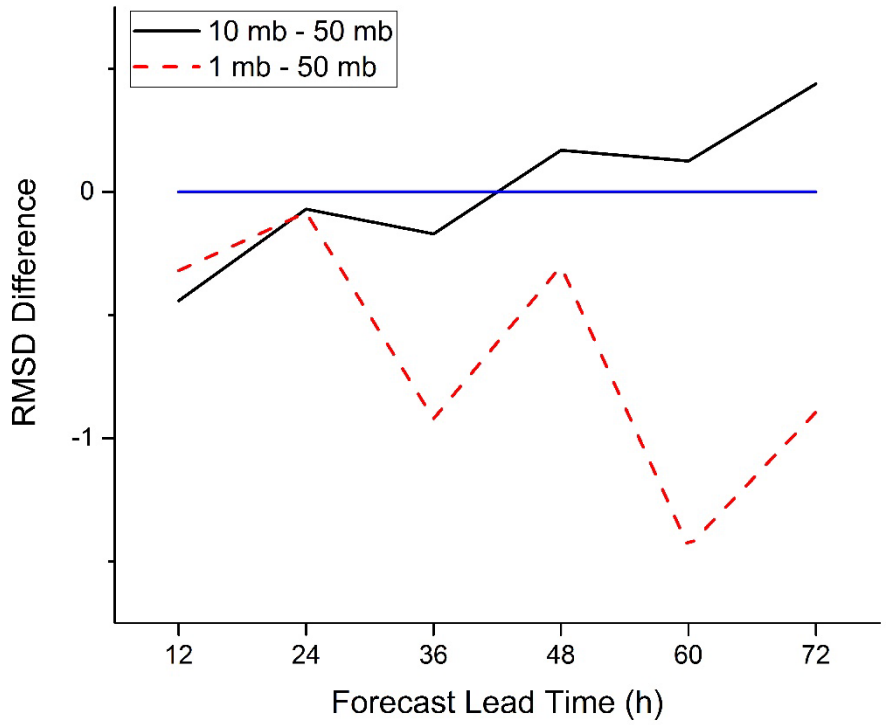

Figure 63 Systematic RMSD differences of the predicted all-level mean RH (%).

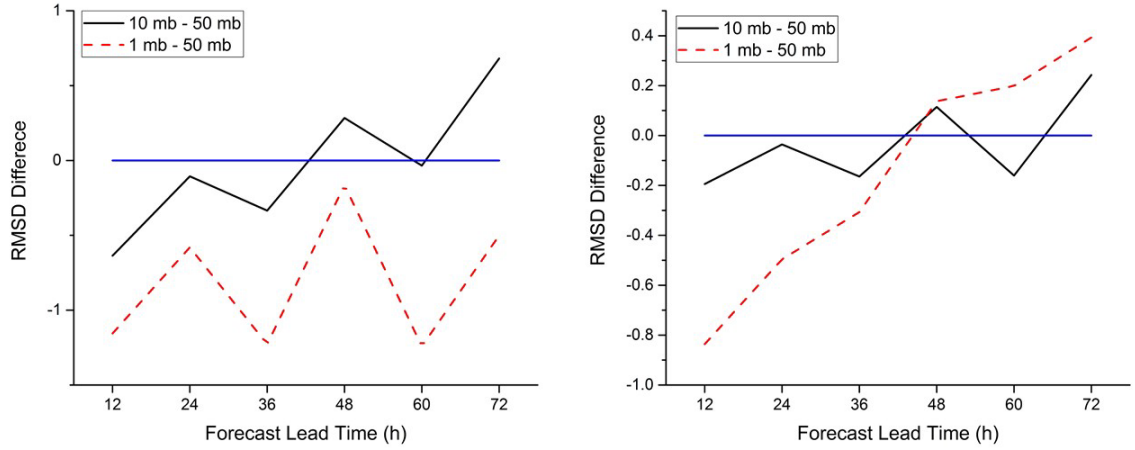

Figure 64 (a): RMSD differences of the predicted all-level mean RH (%); (b): same as (a) but removed systematic differences.

In the prediction of RH profiles, similar to the prediction of wind profiles, both the raising of model lids to 10 and 1-mb alone (Fig. 65a, d) show negative impacts on the near surface level with decrease of 40% and 27% skills at 72-h forecast lead time, respectively. In contrast, the improvements are made in lower tropospheric layers. An extra 5% skill is obtained at 800 mb level at 12-h forecast lead time when the model lid is raised to 10-mb. A smaller extra 4% skill is obtained at 800 mb level when the model lid is further raised to 1-mb. In contrast, the largest improvements are obtained in at later forecast lead times over lower troposphere with averaged extra 15% skill when the model lid is further raised to 1-mb.

After the inclusion of extra stratospheric information, the impacts are shown in Fig. 65b, e. The impacts of DA show similar structures with negative impacts on the near surface levels and positive impacts on the lower troposphere. The results after the removal of systematic differences (Fig. 65c, f) indicate that more positive impacts are obtained by including extra stratospheric information over the 10-1-mb layers. The inclusion of extra stratospheric information over the 50-10-mb layers in the DA system only show extra 3% skill over lower levels. While an extra 10% skill is obtained at early forecast lead times when the information in the 10-1-mb is included in the DA system.

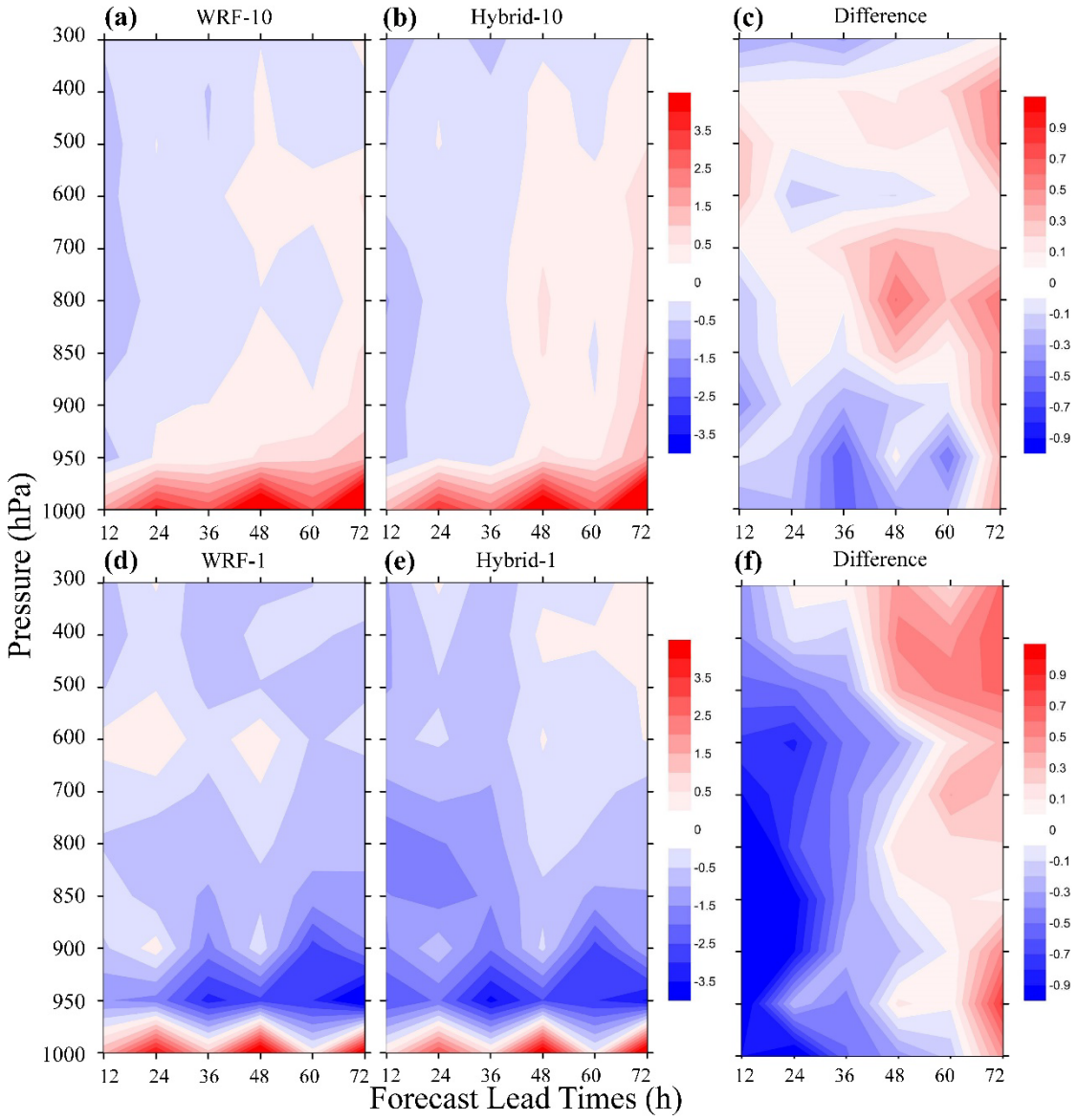

Figure 65 RMSD differences between the predicted RH profiles (%) as a function of forecast lead time (h) with different model lids.

6.3 Impacts of Stratospheric Microwave Measurements on DA system

As described in section 6.2, the raising of model lid to 1-mb has more positive impacts on the short-period regional weather forecasting. The inclusion of more

stratospheric observations in the DA system also show extra skills in regional NWP systems, especially over the tropopause layers. In this section, the impacts of the selected stratospheric microwave channels on regional weather forecasts are compared with the tropospheric microwave channels in a week-long prediction. The selection of microwave channels is based on the vertical weighting functions of each channel shown in Fig. 52. The detailed configurations of the experiments are described in Table 5.

6.3.1 Statistical Results

The bias and RMSD differences of the predicted atmospheric states between the Whole and TROPO experiments are analyzed. The negative values (or negative areas) indicating positive impacts are made by including stratospheric microwave channels in the DA system.

6.3.1.1 Forecasts of Surface Pressure

In the prediction of surface pressure (Fig. 66), positive impacts on both bias and RMSD are obtained when the stratospheric microwave channels are included. Good correlation (the CC is 0.6398) is found between the bias and RMSD differences with a low p value of 0.0137. The largest improvements for both bias and RMSD are found at 48-h forecast lead time with an extra 1.1% skill. Thus, the stratospheric microwave information included in the DA system can propagate through the tropopause layers into the troposphere and then influence the forecasts of surface pressure within 2 days. At the same time, the biases also meet its largest improvements. For longer predictions, the predictability then drops as forecast lead time increases. The predictability of surface pressure by including stratospheric microwave information reaches a stable level

compared to the inclusion of tropospheric microwave channels alone after 4-day forecasting.

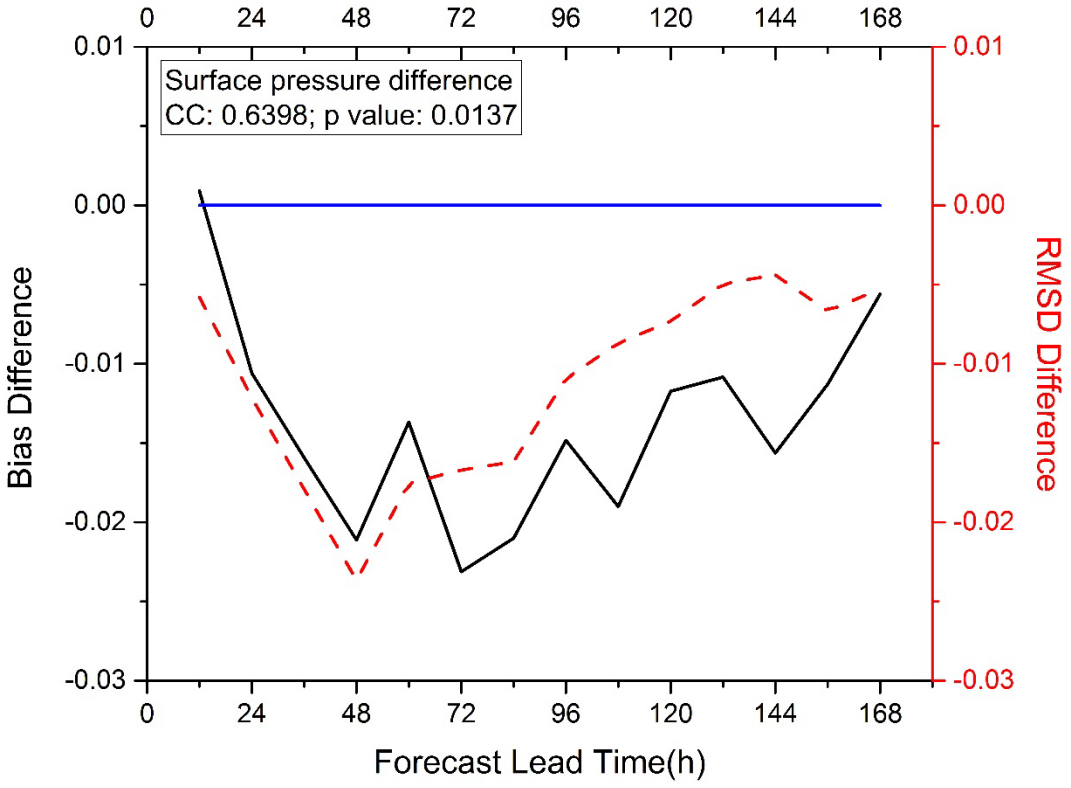

Figure 66 Bias and RMSD differences of the predicted surface pressure (Pa) between the Whole and TROPO experiments.

6.3.1.2 Forecasts of Wind, Temperature, Relative Humidity, and Precipitable Water

The predicted all-level mean wind, temperature, RH and precipitable water are plotted in Fig. 67. An averaged extra 0.4% skill is obtained in the prediction of one-week's all-level wind (Fig. 67a). The largest improvement is found at the third day prediction with an extra 0.6% skill. For longer predictions during the rest of the week, the

RMSD differences become smaller and more stable. In contrast, no significant differences are found by including the stratospheric microwave information. Similar to the prediction of wind, the prediction of precipitable water also shows the largest improvements at the third day forecasting. An extra 0.8% skill is found at 72-h forecast lead time. At 108-h forecast lead time, by including stratospheric microwave information, the RMSD increases at a faster rate and reaches a comparable predictability level to the results obtained in the TROPO experiment. Also, no significant differences are found in bias corrections. Small improvements are obtained at early forecast lead times. There are no significant correlations between the bias and RMSD differences in the prediction of wind and precipitable water. Thus, the stratospheric microwave information included in the DA system can propagate through the tropopause layers and affect the prediction of wind and precipitable water within 2 to 3 days.

The predictions of all-level mean temperature and RH show different features compared to the prediction of all-level mean wind and precipitable water. There exist very good correlations between the bias and RMSD differences in the prediction of temperature and RH with CCs of 0.9028 and 0.7968 and very small p values, respectively. For temperature predictions, the improvements are relatively smaller with an averaged extra 0.14% skill compared to the other atmospheric states. The improvements are made for both bias and RMSD when the forecast lead time reached 120-h. Larger improvements are obtained for 5-6 days' forecasts with an extra 0.9% skill. The improvements in the prediction of RH are relatively larger than the other variables with an averaged extra 1.1% skill. Larger improvements are obtained starting at the 48-h

forecast lead time with a maximum extra 1.5% skill. The stratospheric microwave information included in the DA system also can affect the prediction of humidity for 2-day or longer forecasts. However, the information contained in the stratosphere may need longer time (up to 5 days) to affect the prediction of temperature. The larger improvements obtained in the prediction of humidity are mainly related to moisture information contained in the ATMS and SSMI/S channels been brought into the system.

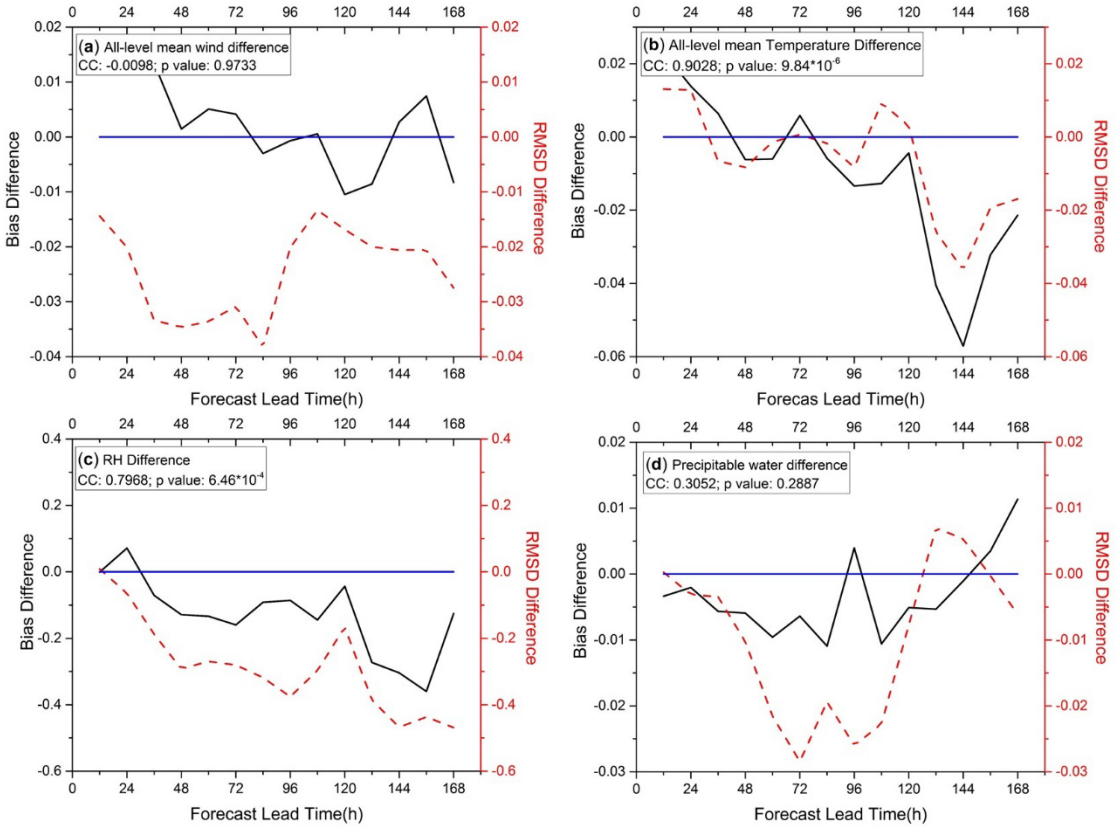

Figure 67 Bias and RMSD differences for (a): all-level mean wind speed (m s^{-1}); (b): all-level mean temperature (K); (c) all-level mean RH (%); and (d) precipitable water between the Whole and TROPO experiments.

The bias and RMSD differences of the predicted profiles are shown in Fig. 68. The inclusion of stratospheric microwave information in the DA system shows positive impacts on both bias and RMSDs in the troposphere at 24-72 forecast lead times in the prediction of wind (Fig. 68a, b). An averaged extra 0.5% skill is found in the troposphere. For longer predictions at 108-, and 144-h forecast lead times, some advantages of the inclusion of stratospheric microwave information can be found in the tropopause layers. An extra 1.1% skill is found at later forecasts of wind in the tropopause layers. For temperature forecasts (Fig. 68c, d), negative impacts are found on the lower stratosphere and tropopause layers by including the stratospheric microwave information. The predictability of the temperature dropped by 1.6% and 0.5% in the lower stratosphere layers and the tropopause layers, respectively. In contrast, positive impacts are found on both lower troposphere bias and RMSDs. Larger impacts on the lower troposphere are found starting at 48-h forecast lead times and the largest improvement is found around 132-h forecast lead time with an extra 3.6% skill. Compared to the wind and temperature, more positive impacts are obtained in the prediction of RH (Fig. 68e, f). Also, the impacts of the included stratospheric microwave information on the tropospheric humidity predictions started at 48-h forecast lead time for both bias and RMSDs. The largest improvements are also found in the lower tropospheric layers with an averaged extra 2% skill.

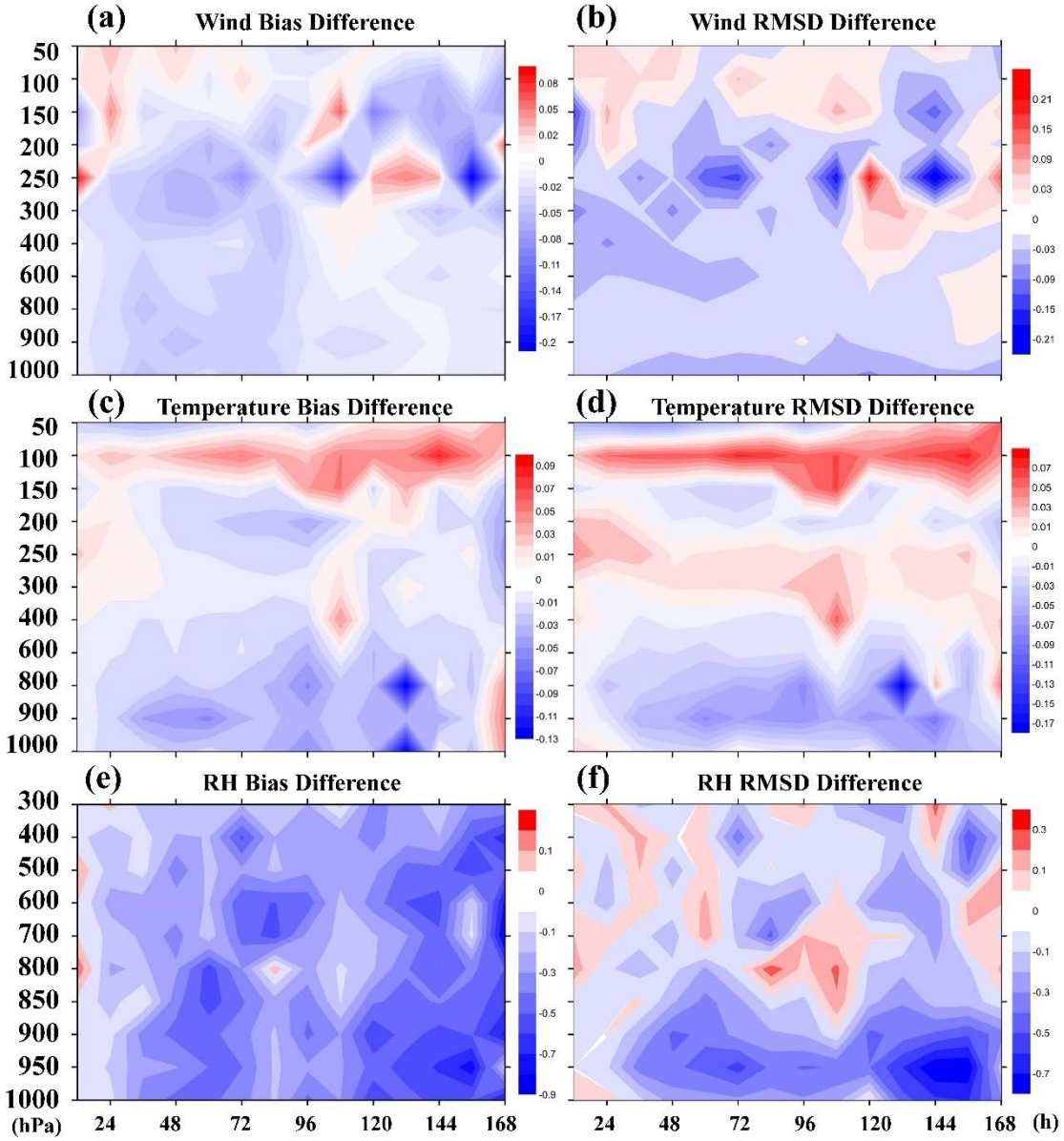

Figure 68 Bias and RMSD differences of the predicted (a, b): wind (m s^{-1}); (c, d): temperature (K); (e, f): RH (%) profiles between the Whole and TROPO experiments.

6.3.2 Forecast Sensitive to Observations

In the previous sections, we found that usually after 2 to 3 days' propagation, the stratospheric microwave information included in the DA system can go through the

tropopause layers and positively affect the prediction of tropopause and tropospheric variables at a regional scale. However, some negative impacts such as a “dropout” was found in the prediction of tropopause wind at 120-h forecast lead time (Fig. 68a, b). These negative impacts are usually believed as the results of using “flawed” observations in the DA system (Hotta, 2014).

To find out which observations degraded the forecasting skills, the traditional OSE method is usually used (Yamaguchi, et al., 2009; Lord, et al., 2016). This method uses two sets of experiments in which the control experiment assimilates a standard set of observations and the other one excludes/includes the observations to be tested. The impacts of the observations to be tested can be brought out by comparing the results from the two sets of experiments. Despite the useful answers this method can provide, the computational expensive is extremely expensive and new control experiments are needed when new observations are added.

A diagnostic technique called the Forecast Sensitivity to Observations was firstly developed by Langland and Baker in 2004 (Langland and Baker, 2004). This diagnostic technique enables us to identify the impacts of any observations on the forecasts all at once with the help of an adjoint model, and at the same time save lots of computational resources compared to OSE method. The detailed calculations of the impacts of observations can be found in Langland and Baker, 2004. In the FSO experiment, if the estimated errors were reduced (as negative values in the figures), thus the impact of the specified observation toward the forecasts is positive. In this thesis, to find out how observations affected the regional forecasts, the FSO technique without considering the

moisture observations and moist processes in the adjoint model (dry) is applied to the regional scale to match the domain configurations and study period in chapter 6. A pre-selection of channels is brought out based on the National Aeronautics and Space Administration (NASA) Global Modeling and Assimilation Office (GMAO) analysis (Zhu and Gelaro, 2008). The AMSU-A series FSO results are shown in Fig. 69, the ATMS FSO results are shown in Fig. 70, and the SSMI/S series FSO results are shown in Fig. 71. The performance of the selected channels is verified in the individual case study in the next section.

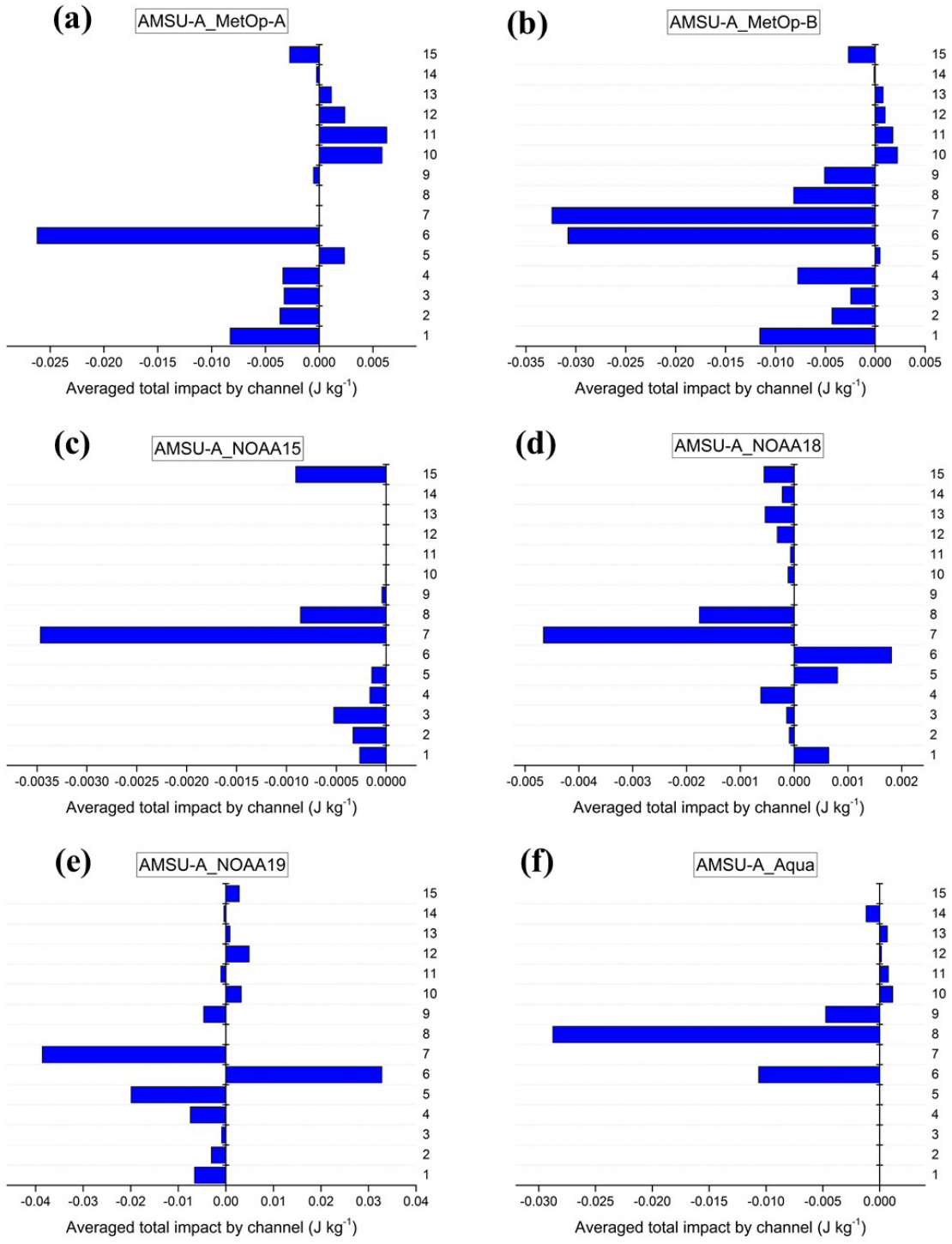

Figure 69 Averaged total impact of AMSU-A channels over the continental U. S. from (a): MetOp-A; (b): MetOp-B; (c): NOAA15; (d): NOAA18; (e): NOAA19; and (f): Aqua.

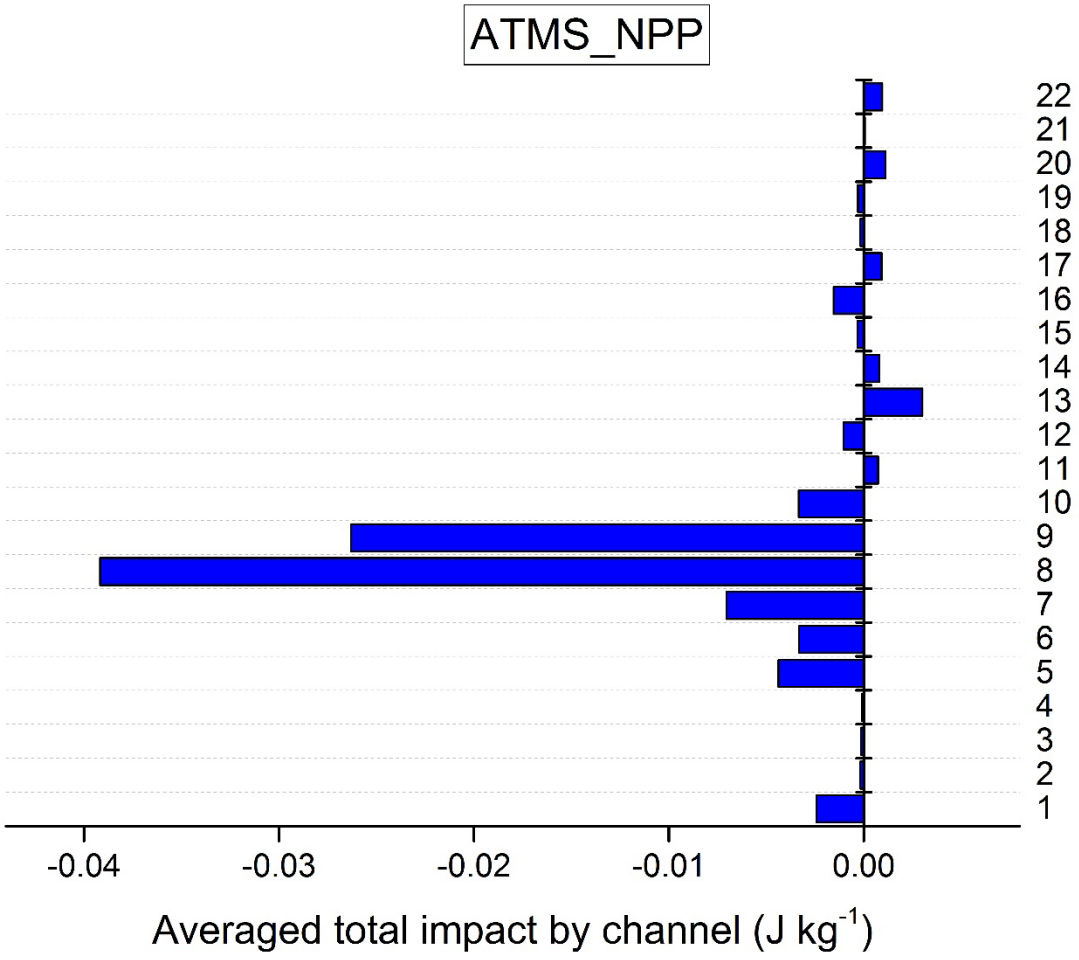

Figure 70 Averaged total impact of ATMS-NPP channels over the continental U. S.

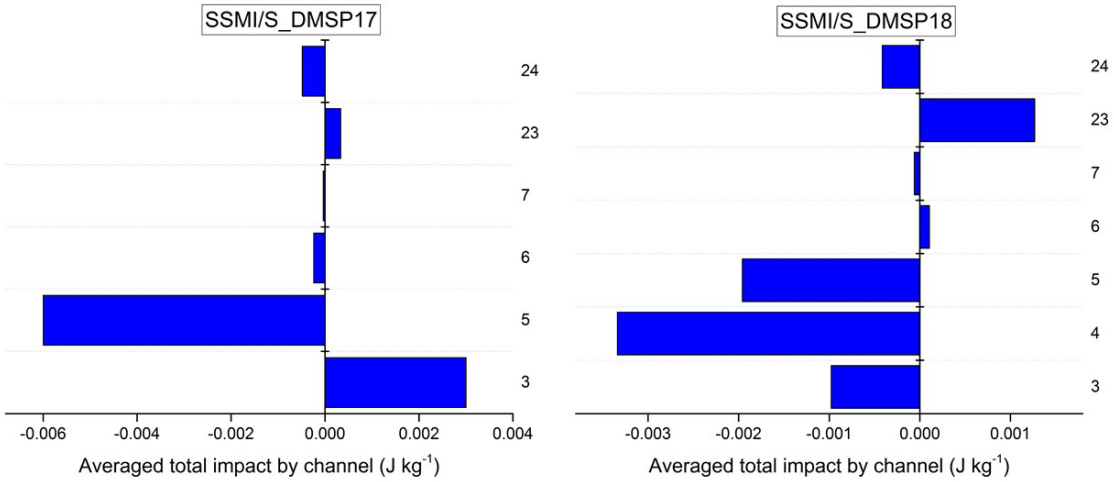

Figure 71 Averaged total impact of SSMI/S channels over the continental U. S. from (a): DMSP-17; and (b): DMSP-18.

6.4 Impacts of Stratospheric Microwave Temperature Measurements – A Two-Season Case Comparison

To explore the mechanisms of the impacts of the stratosphere on tropospheric weather forecast, DA configurations involving the microwave stratospheric temperature channels are conducted 4 times a day during Jan. 2015 and Jul. 2015. AMSU-A channels 7-14 (8-14), ATMS channels 8-15 (9-15), and SSMI/S channels 5-7 and 22-24 are selected in the DA system during winter (summer) as these channels mainly measure the stratospheric temperature.

Firstly, the stratospheric temperature and meridional wind analysis increment differences are plotted in Fig. 72. In winter temperature analysis increments (Fig. 72a), a warmer upper stratosphere (5-mb to 1-mb) is obtained by assimilating the microwave stratospheric measurements. The maximum warming region is located between 30-40°N with a value of 2.5K. In contrast, a cooled lower stratosphere is obtained especially over

the ozone layers. In summer (Fig. 72b), a warm pool is obtained between 22-40°N at upper stratosphere while a colder upper stratosphere with the maximum cooling effect of 1.4K is obtained over the north. The temperature analysis increments in the lower stratosphere are relatively weaker compared to winter. The cooled lower stratosphere in this case study agrees with the results obtained by Fu, et al. (2004) in which a cooling lower stratosphere is observed using the MSU channel 4 measurements. The zonal-mean meridional wind analysis increments (Fig. 72c&d) are also adjusted to respond to the temperature analysis increments caused by the assimilation of microwave stratospheric temperature measurements. Opposite features of the zonal-mean meridional wind analysis increments are obtained in winter and summer. The corresponded temperature and meridional wind adjustments may also related to the adjusted BDC at mid- and upper-stratosphere. Positive and negative meridional wind are obtained in winter and summer at upper-stratosphere, respectively. As a result, the BDC at upper-stratosphere is enhanced and weakened in winter and summer, respectively. Furthermore, the transportation of ozone and warm air from the tropical area at upper-stratosphere is enhanced and weakened in winter and summer, respectively. And thus, warmer and colder upper-stratosphere at correspond latitudes are obtained by assimilating the microwave stratospheric measurements.

As discussed in Karpechko et al. (2017), downward propagation of major sudden stratospheric warming events can affect the tropospheric weather forecast predictabilities due to its impacts on tropospheric circulations. However, the propagation usually takes one to three months to have significant impacts on troposphere. Also as Charlton et al.

(2004) discussed that consistent changes to the tropospheric synoptic-scale systems occur in response to the stratospheric initials starting at 5-day forecast lead times. In this study, faster response of the tropospheric circulations to the assimilation of microwave stratospheric temperature measurements. The predicted zonal-mean vertical velocity and meridional wind at 24-h forecast lead time are plotted in Fig. 73. In winter, the warmer upper stratosphere and the cooler ozone layers caused a more stable stratosphere and thus, strong downward vertical transportation anomaly is observed between 20-mb and 3-mb. In the upper troposphere, a relatively weaker upward vertical transfer is observed. The strongest upward vertical transfer in the upper troposphere is located between 22° and 30°N where the Hadley Cell and Ferrel Cell descend. Also, a relatively weaker downward vertical transfer is observed at 50°N over 300 hPa. Strong opposite meridional wind is obtained in upper stratosphere compared to initial analysis increments. Compared to the stratosphere, very weak changes have been made to the tropospheric general circulations. Negative meridional wind at 400-mb is observed between 22° and 30°N, slightly weaker negative meridional wind is observed at near surface layer between 35° and 50°N. Combined with the vertical velocity anomalies, the tropospheric general circulations are weakened in response to the stratospheric initials in winter. Compared to winter wind anomalies, opposite features are obtained in the summer predictions. The predicted summer vertical velocity anomaly (Fig. 73b), more perturbations are observed compared to a more flat vertical velocity anomaly in winter. Strong upward vertical transfer is observed at around 5-mb between 30° and 45°N. In the troposphere, downward

vertical transfer is observed at around 25°N between 200-mb and 1000-mb. Downward vertical transfer is also observed at near surface layers between 36° and 45°N. Small turbulence is also observed between 36° and 45°N with some upward transfer located at 800-mb height. The predicted summer meridional wind (Fig. 73d) also shows different features to winter predictions. Stronger negative meridional wind anomalies are observed at upper stratosphere. Negative meridional wind anomalies are also observed in the Ferrel Cell with slightly stronger northern wind at 200-mb between 37° and 45°N. Thus the tropospheric general circulation is slightly enhanced in response to the stratospheric initials in summer.

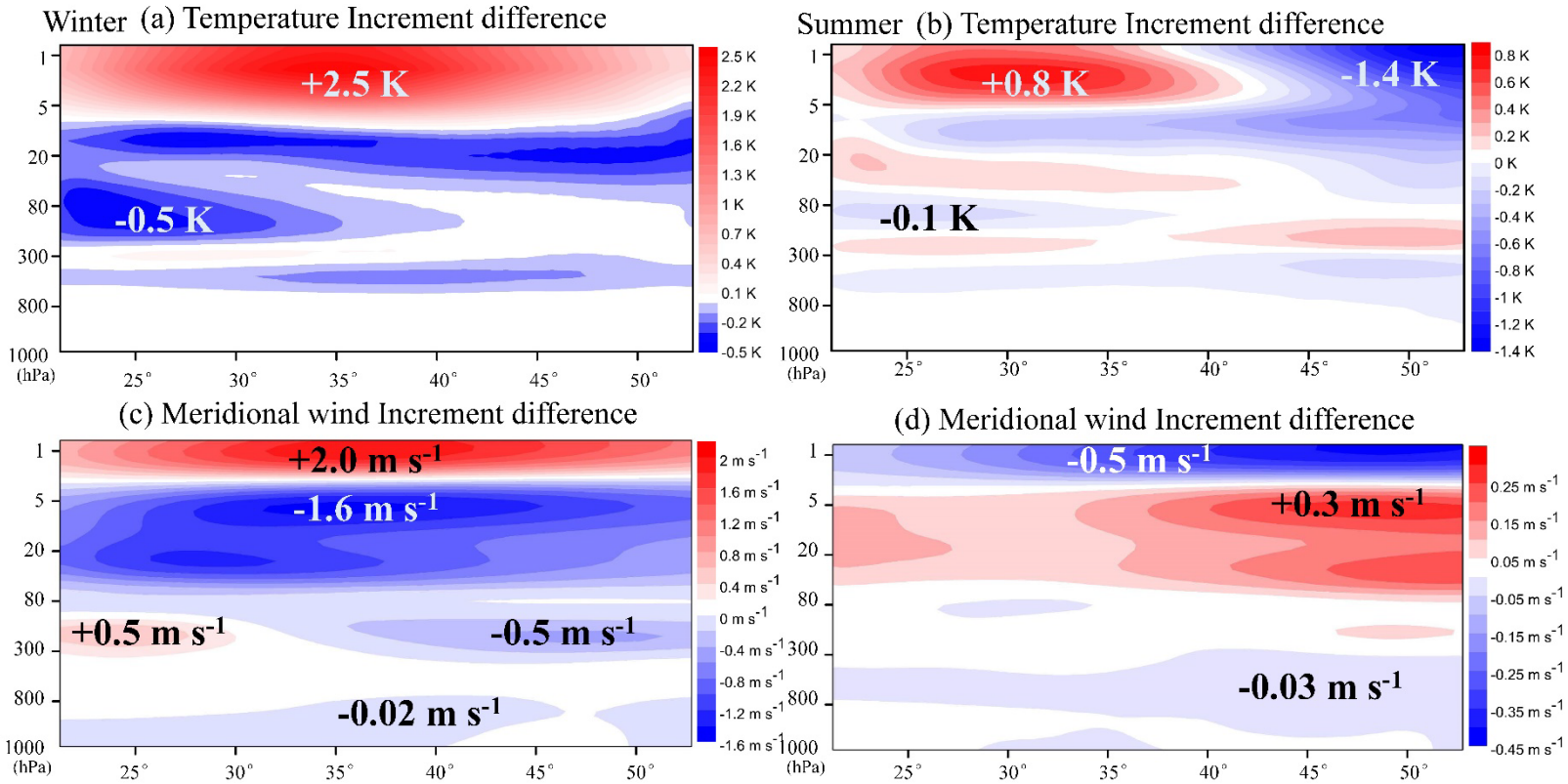

Figure 72 Zonal-mean vertical temperature (a, b) and meridional wind (c, d) analysis increment differences.

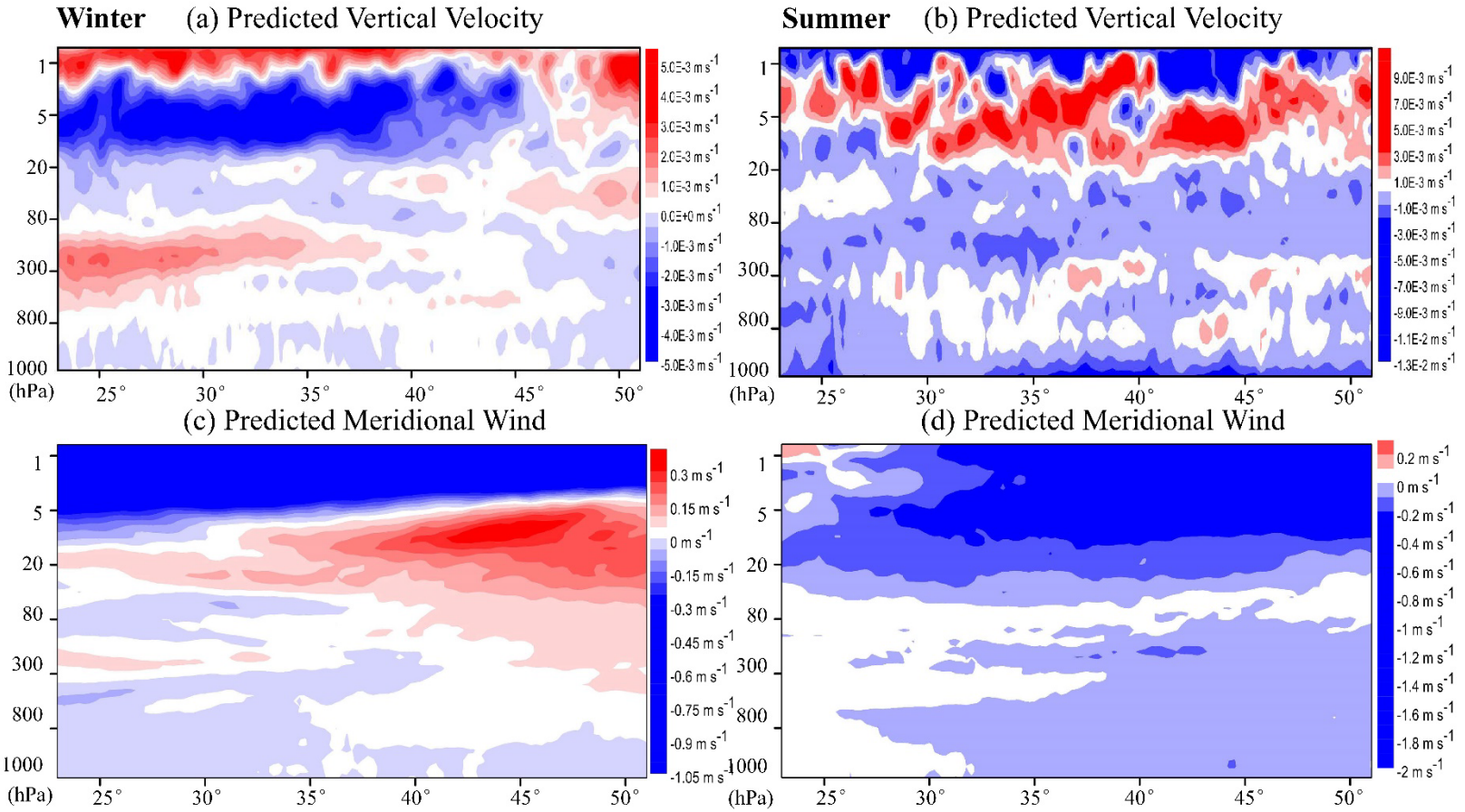

Figure 73 Predicted zonal-mean vertical velocity (a, b) and meridional wind (c, d) anomalies at 24-h forecast lead time.

The change of stratospheric vertical transfer and tropospheric general circulations also have strong impacts on the predicted atmospheric states. The predicted zonal-mean temperature and RH at 24-h forecast lead time are plotted in Fig. 74. In winter, strong upper stratospheric warming is obtained (Fig. 74a). In summer, a cooling pool is obtained at 5-mb between 30° and 45°N. Compared to vertical velocity and meridional wind anomalies (Fig. 73), the upper stratospheric temperature predictions are more related to the vertical transfers. In winter, strong downward vertical transfer is obtained in upper stratosphere around 5-mb. As a result, more energy is transferred from the high temperature area at high altitudes to the low temperature area at low altitudes in the stratosphere and caused the warming upper stratosphere. In summer, strong downward vertical transfer is observed at 5-mb between 30° and 45°N. A cooling pool responds the downward vertical transfer is also obtained in Fig. 74b. In the troposphere, slightly warming effect is obtained in winter. In summer, strong cooling effect is obtained at surface layer which is also related to the strong downward vertical transfer in Fig. 73b. Warming effect is obtained at 900-mb between 38° and 45°N which is also related to the upward vertical transfer in Fig. 73b.

The RH anomalies are mainly located in the troposphere due to the lack of water molecules in the stratosphere. In winter (Fig. 74c), decrease of RH is found in the tropopause and near surface layer. Increase of RH is obtained in the mid-troposphere except the ascending part of Ferrel Cell. Opposite features are obtained in summer, increase of RH is obtained in the tropopause and near surface layers. Decrease of RH is found in the mid-troposphere except ascending part of Ferrel Cell and the descending part

of Hadley Cell. The transport of tropospheric water vapor is strongly related to the tropospheric general circulations. As we discussed in Fig. 73, the tropospheric general circulations are weakened in winter but enhanced in summer. The weakened/enhanced winter/summer Ferrel Cell is responsible for the decrease/increase of RH in the tropopause and near surface layer with less/more water vapor from the tropical area. The changes of the RH in the mid-troposphere between 45° and 51°N are also related to the adjusted Ferrel Cell.

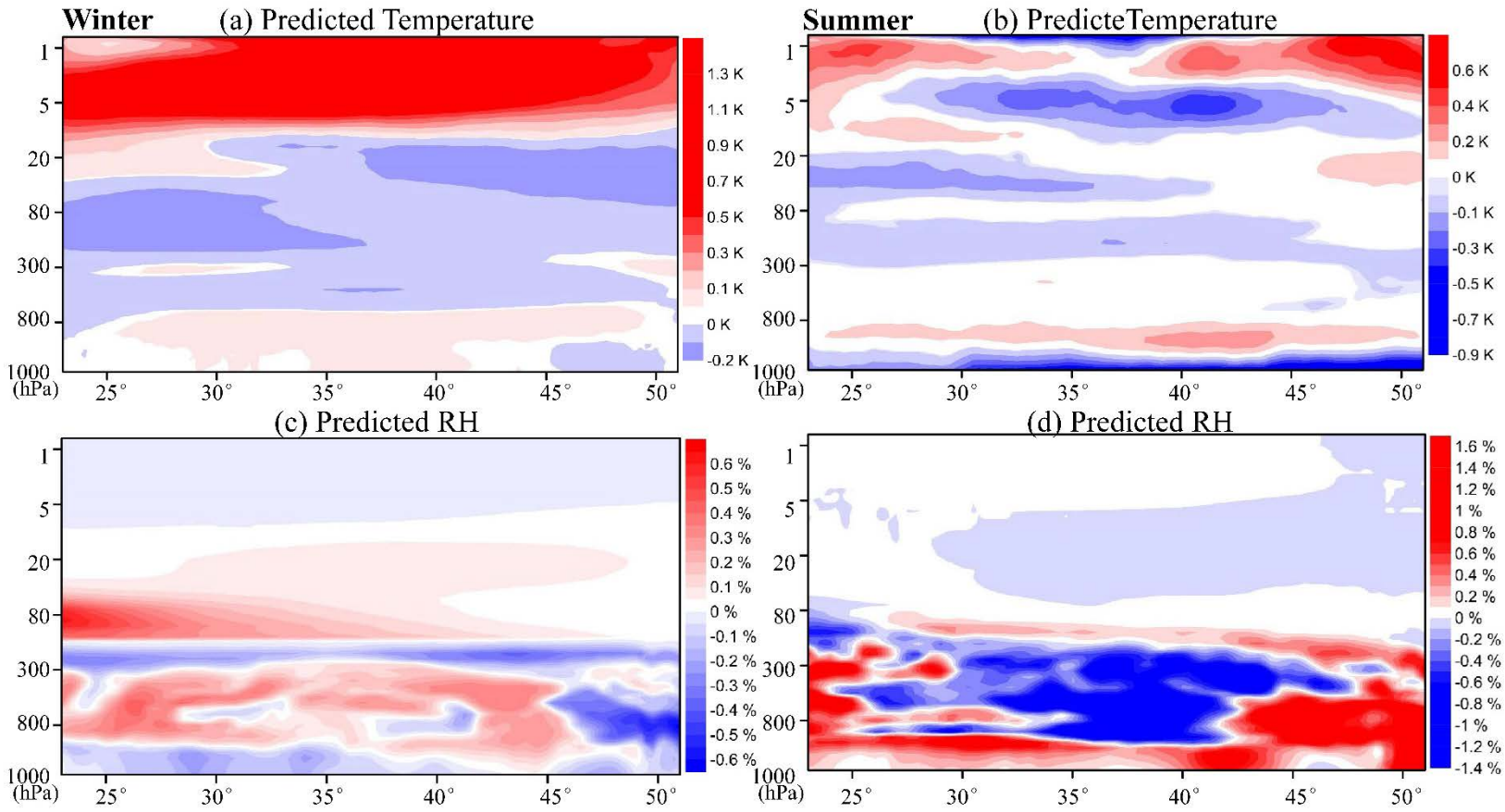

Figure 74 Predicted zonal-mean temperature (a, b) and RH (c, d) at 24-h forecast lead time.

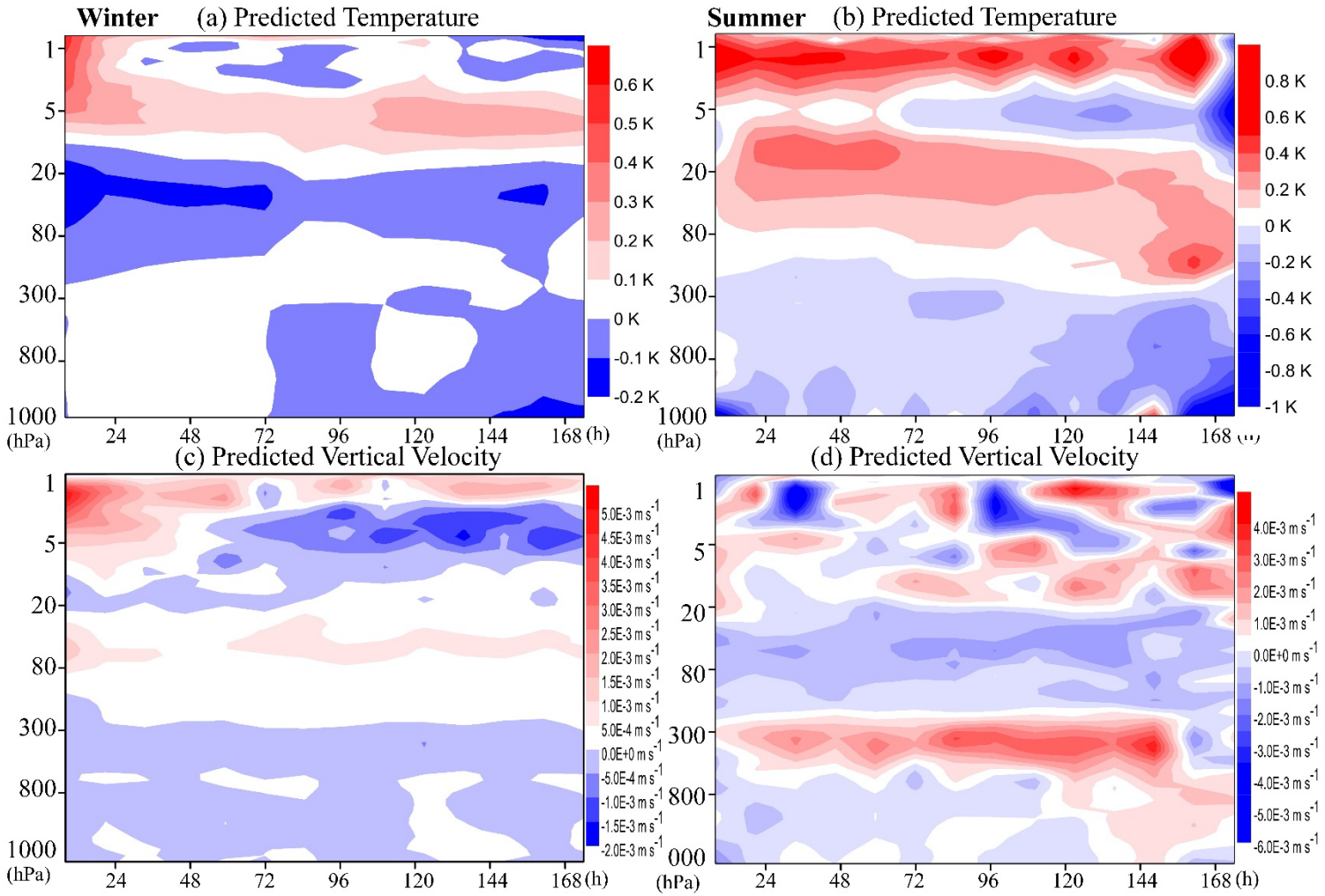

Figure 75 Predicted zonal-mean temperature (a, b) and vertical velocity (c, d) anomalies at 50°N as a function of forecast lead time (h).

Cross-sections of the zonal-mean temperature and vertical velocity anomalies at 50°N where the Ferrel Cell ascending are plotted in Fig. 75. Propagation of the temperature anomaly can be identified in Fig. 75. In winter, the temperature pattern is relatively flat in the upper stratosphere. In the troposphere, slightly weak adjustment to the synoptic-scale waves can be identified starting from 72-h forecast lead time. In summer, the propagation of the temperature and vertical velocity are more obvious. In the upper stratosphere, impacts on the planetary waves are found. Between 5-mb and 300-mb, the temperature pattern starts to propagate downward at 72-h forecast lead time and becomes stronger at 144-h forecast lead time. As shown in Fig. 75d, the magnitudes of the summer tropospheric synoptic-scale waves are also adjusted when microwave stratospheric measurements are assimilated.

The averaged bias and RMSD differences of predicted wind, temperature, and RH profiles over the continental of U. S. are calculated and plotted in Fig. 76. The blue area indicates better forecast skills are obtained while the red area indicates a drop of predictability is obtained. Overall improvements of both bias and RMSD are obtained. Large improvements are observed over the tropopause layers in predicting wind and temperature when microwave stratospheric temperature measurements are assimilated. Extra 1.1% and 2.7% skills are obtained for tropopause wind and temperature predictions, respectively. For tropospheric predictions, most of the improvements are made in the first 72-h forecast lead times. The improvements in the lower tropospheric wind predictions are relatively weaker than temperature. Extra 0.15% and 0.6% skills are obtained for lower tropospheric wind and temperature predictions, respectively. For

predictions of RH, the major improvements are made in the first 48-h forecast lead times. The largest improvement is obtained at 24-h forecast lead time at 800 hPa with an extra 2.7% skill. As the upward transfer becomes weaker as forecast lead time increases, the improvements moved upward. An extra 1.5% skill is obtained at 36-h forecast lead time at 600 hPa and an extra 1.6% skill is obtained at 72-h forecast lead time at 400 hPa.

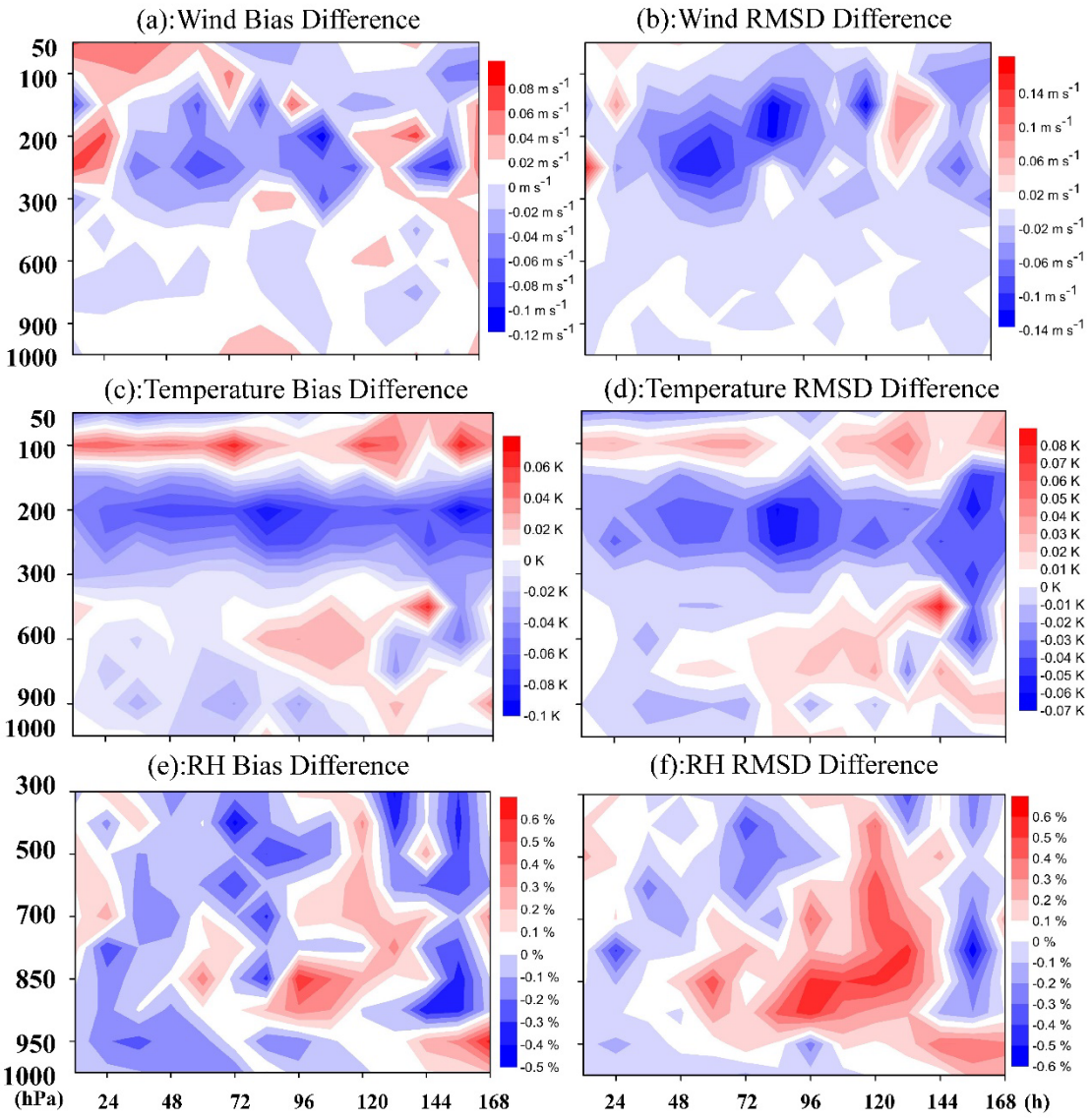

Figure 76 Bias and RMSD differences of predicted wind, temperature, and RH profiles.

6.5 Individual Case Study – The Winter Case in Section 4.4

The winter case used in chapter 4 is predicted with the selected channels in this section. Four experiments including a CTRL experiment and three different GSI configurations are conducted. The detailed descriptions about these four experiments are

shown in Table 6. Firstly, the near-surface temperature from the Manhattan in-situ observations and WRF 2 m high temperature are compared in Fig. 77. Similar to Fig. 31, all experiments also underestimate temperature predictions during the early DA cycles and less errors at later DA cycles. The CTRL experiment shows slightly smaller CC and larger RMSD than the results from the CTRL_50mb. In contrast, the temperature scores reach comparable levels with slightly smaller RMSD than the Hybrid experiment showed in Fig. 31. No significant differences are found between the three DA experiments.

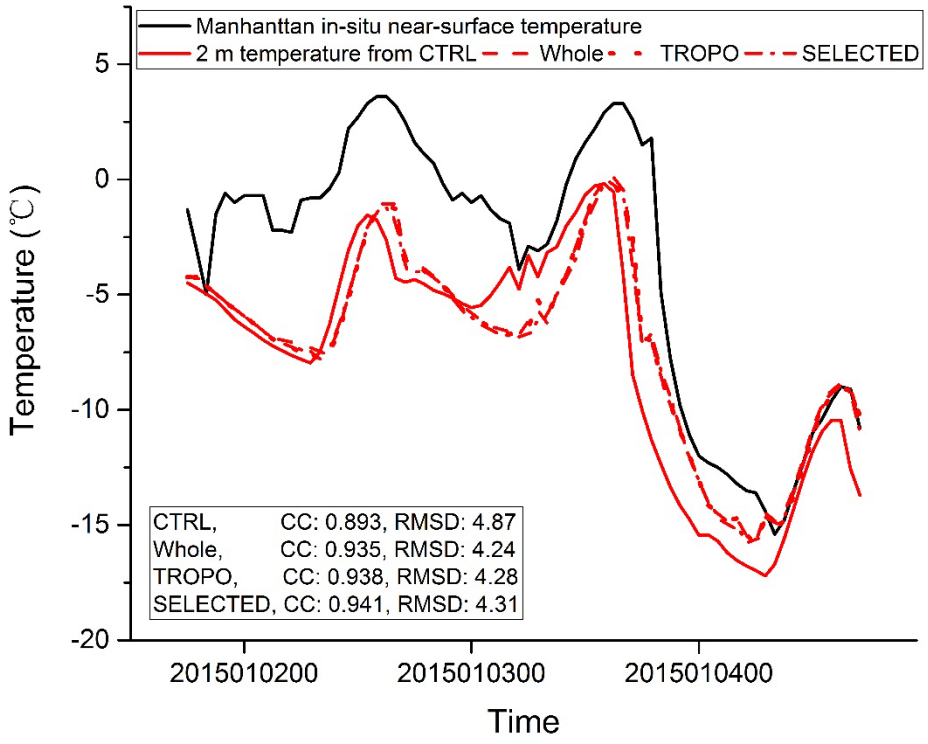

Figure 77 Time series of the near-surface temperature from Manhattan, KS (39.102°N, 96.609°W) and the predicted 2 m temperature from different experiments.

The comparison of the 3-h accumulated precipitation over the major precipitation area from the GLDAS products and regional weather model forecasts are shown in fig. 78. Slightly drop of the predictabilities of heavy precipitation is found by raising the model lid to 1-mb alone compared to the experiment with a model lid at 50-mb in Fig. 31. However, on one hand, by including the selected microwave channels alone in the SELECTED experiment yields results comparable to those of the Hybrid experiment in Fig. 31 which included all operationally available observations. On the other hand, the inclusion of stratospheric microwave information in the Whole experiment yields results better than those of the TROPO experiment.

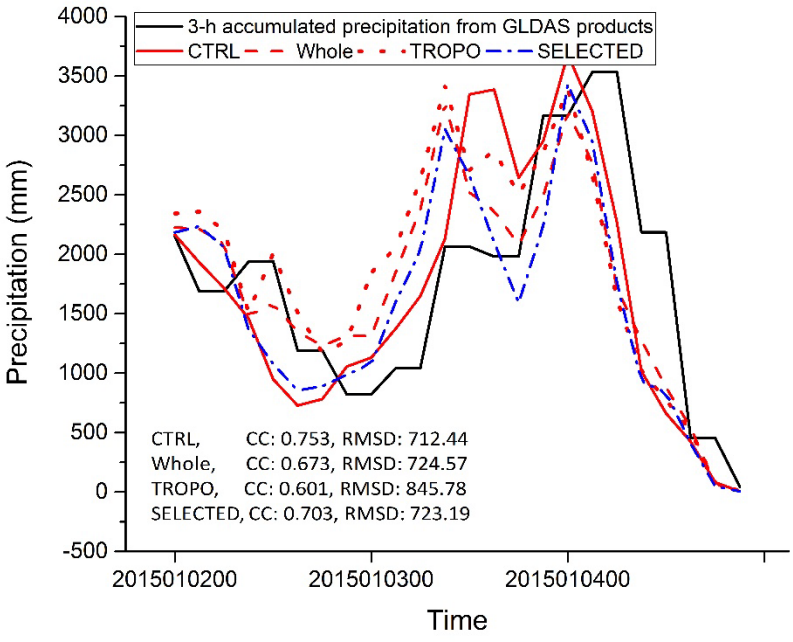

Figure 78 Analyzed and predicted 3-h accumulated precipitation from different experiments.

The daily precipitation distributions of Jan. 2nd (first row in Fig. 79), Jan. 3rd (second row in Fig. 79), and Jan. 4th (third row of Fig. 79) from different experiments are also compared with the GLDAS products. No significant differences are found in each experiment. However, the CTRL experiment lacks the ability to predict lighter precipitation events such as the miss-predicted precipitation area over the North Carolina and South Carolina states in Fig. 79g. The Whole (Fig. 79c, h, and m) and SELECTED (Fig. 79d, i, and n) experiments show comparable results while the TROPO (Fig. 79e, j and o) slightly overestimates precipitation amounts over the coast areas.

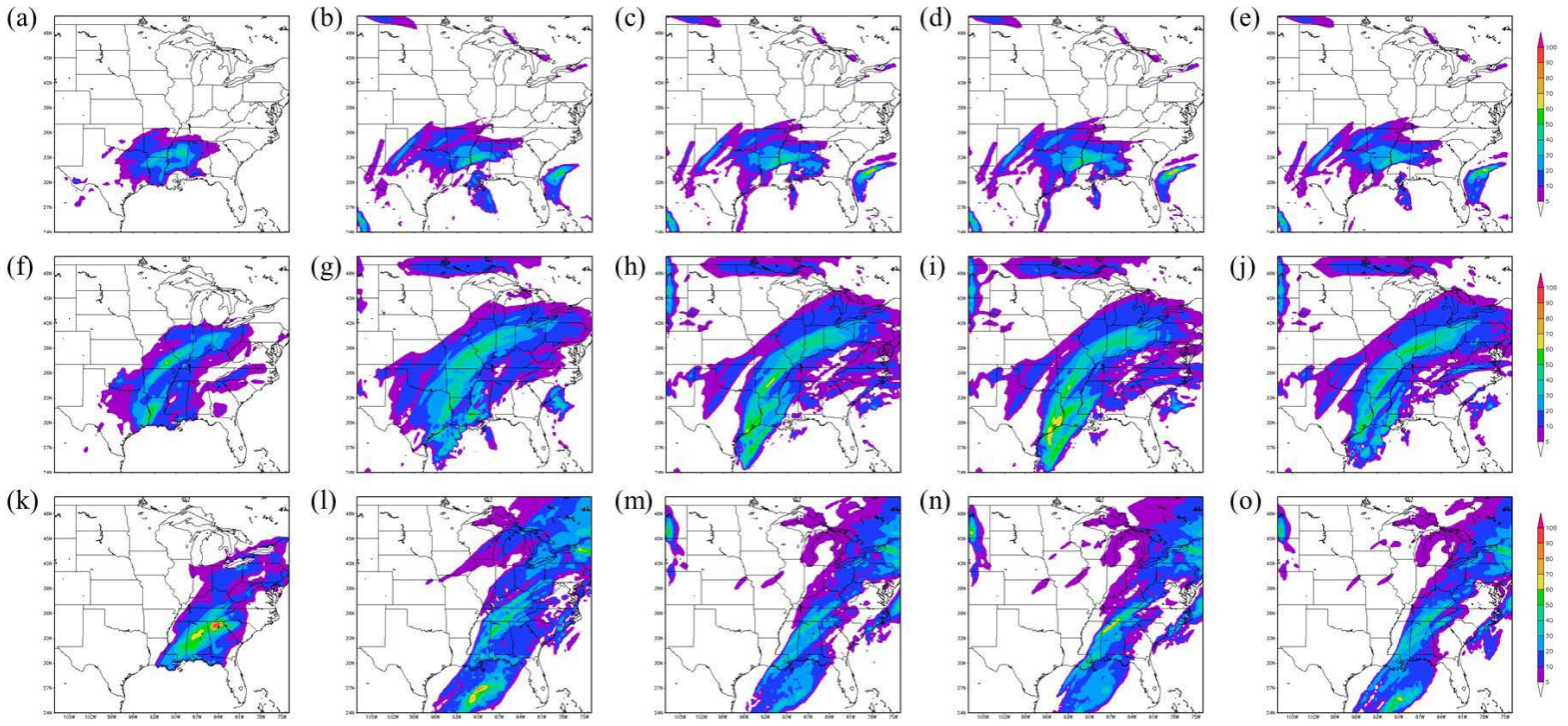

Figure 79 Daily precipitation (mm) distributions of Jan. 2nd, Jan. 3rd, and Jan. 4th, 2015, from different experiments.

6.6 Summary

The impacts of the raised model lids and the extra stratospheric information included in the DA system on winter short-period weather forecasts are investigated in this chapter also using the regional weather forecast model WRF-ARW and the GSI DA system. The model results are verified against conventional observations, and GLDAS products are used to verify the individual case studies.

Generally, the model with a lid at 1-mb generates better initials and forecasts than those with model lids at 10-mb and 50-mb. By raising the model lids alone, positive impacts are only found over the initial tropopause layers while negative impacts are obtained in the initial lower troposphere. However, after the application of DA, large improvements are obtained in the initials over both tropopause layers and lower troposphere layers. For the short-period forecasts, major improvements are mainly obtained over the tropopause layers at early forecast lead times. The impacts of the raised model lids on regional weather predictabilities compared to the model results with the model lid at 50-mb in percentage are summarized in Table 11 (by raising the model lids alone) and Table 12 (after the application of DA and a removal of systematic differences). Most of the improvements shown in Table 11 and 12 are made during the early forecast lead times. Despite the overall improvements by including extra stratospheric information in the DA system, decrease of the predictabilities of near surface wind, RH are observed.

Table 9 Impacts of the raised model lids alone on short-period weather forecast predictabilities

Predicted Variables		10-mb	1-mb
Surface Pressure		2.1%	7.4%
Wind	All-level Mean	1.7%	3%
	Tropopause	8%	12%
	Lower Troposphere	1.5%	3.5%
Temperature	All-level Mean	3%	3%
	Tropopause	13.5%	20%
	Lower Troposphere	1.8%	6%
RH	All-level Mean	2.7%	1.9%
	Lower Troposphere	2.2%	4%

Table 10 Impacts of the assimilated stratospheric observation on short-period weather forecast predictabilities after the removal of systematic differences

Predicted Variables		10-mb	1-mb
Surface Pressure		2.3%	1.4%
Wind	All-level Mean	0.7%	2.2%
	Tropopause	1.3%	3.8%
	Lower Troposphere	0.3%	1.5%
Temperature	All-level Mean	3%	2.9%
	Tropopause	3.9%	9%
	Lower Troposphere	2.4%	0.4%
RH	All-level Mean	0.7%	3%
	Lower Troposphere	0.7%	5.4%

After the investigation of how the raised model lids can affect regional weather forecasts. A specified set of experiments involving channel selections aiming at the impacts of stratospheric microwave channels on regional one-week weather forecasts are taken out. The inclusion of the stratospheric microwave channels in the DA system can propagate through the tropopause layers and affect the lower troposphere within 2-3 days. The impacts of the stratospheric microwave information on lower tropospheric temperature and RH are enlarged after 5 days' propagation. Large positive impacts are also found in the tropopause wind predictions. However, negative impacts are found over

the lower stratosphere layers especially for temperature. An optimized microwave channel selection for the continental U. S. is carried out using the FSO technique. The optimized microwave channel selection in DA system shows more advantages in predicting heavy precipitation events than the configuration used in the global operational system. No significant differences are found when predicting temperature.

Overall warmer stratosphere but cooler lower stratosphere in winter and summer 2015 are obtained when the microwave stratospheric temperature measurements are assimilated. The adjusted stratospheric temperature and meridional wind patterns are related to the adjusted BDC. Small impacts on the tropospheric general circulations are found. The tropospheric predictabilities are slightly improved in response to the stratospheric initial conditions and adjusted tropospheric general circulations. Summer still holds better improvements than winter. The major improvements are also found in the tropopause layers. Extra 1% and 2.2% skills are obtained in the tropopause wind predictions and extra 1.5% and 0.3% skills are obtained in the tropopause temperature predictions.

CHAPTER SEVEN CONCLUSION AND DISCUSSION

The technique of DA has been shown to provide significant impact to NWP systems. However, because of the large increasing amount of observations, the selection of DA schemes and observations are becoming more and more sensitive to forecasts of regional atmospheric states. The performance of three major DA schemes on regional weather forecasts were explored. The raised regional model lids and extra stratospheric information show the possibilities to better predicts weather on a regional scale. And a further application of FSO allows better forecasts of heavy precipitation events.

7.1 The Performance of the Current Assimilation Schemes on Regional Tropospheric Weather Forecasts

Chapter 4 explores the performances of three major assimilation schemes: 3D-Var, 3D-Var based ensemble-variational 3D-Var Hybrid with 20% weight on the statistical background covariance, and EnKF on regional weather forecasts during both winter and summer. Faster convergence rate is obtained by including ensembles in summer. For the impacts on initials or model outputs, Hybrid and 3D-Var give better performances (3%) on surface pressure and wind, while EnKF shows better performances in adjusting temperature in both seasons. Large improvements (10~20%) are observed over the tropopause and lower troposphere.

For the predictabilities involve these three DA schemes, better forecasting skills are obtained in all DA schemes in summer (~10% compared to winter forecasts). Among

these three DA schemes, Hybrid shows slightly better forecasting skills (~1%) in winter than 3D-Var. EnKF shows slightly better skills in summer compared to the variational methods. In contrast, EnKF shows ~6% less skills than the variational methods in winter predictions. The performances also vary in different vertical layers. Smaller biases and RMSDs are found in the mid-troposphere while larger ones are found in the tropopause layers. The incremental analysis shows that opposite impacts are obtained over the oceans and mountainous areas between the variational method and EnKF schemes. Furthermore, when enough DA cycles are performed in the individual case predictions, EnKF gains more predictabilities (10%) than the other two DA schemes in predicting heavy precipitation events.

Bias diurnal variations exist when testing the performance of three major DA schemes. The systematic errors and one-time DA per-day are believed to be the main reasons for the temperature and surface pressure bias diurnal variations, while wind bias diurnal variations are related to systematic errors alone. When DA is applied four times a day, these bias diurnal variations are disappeared.

7.2 Impacts of the Selection of Microwave and Infrared Satellite Observations in Data Assimilation system on Regional Tropospheric Weather Forecasts

Chapter 5 explores the different impacts of using microwave and infrared satellite observations in DA system on regional short-period weather forecasts. No significant differences are found between the usage of microwave and infrared observations in summer using the EnKF configuration in DA system. The use of infrared observation only shows less than 1% advantage than the microwave observation over the tropopause.

In contrast, large differences are obtained in winter using the Hybrid configuration. The MW generates overall advantages in adjusting initials compared to IR when assimilated alone. Large improvements are made for the tropopause wind, lower stratospheric temperature and higher tropospheric humidity when MW is assimilated alone.

For predictions, MW shows better skills than IR in the first 12-h predictions for most of the atmospheric variables (extra 7% skill for the prediction of surface pressure, 3% for temperature and 2.6% for humidity), and overall better skills in predicting wind (extra 2%). IR shows better skills at longer forecast lead times when assimilated alone. The predictabilities of assimilating MW and IR observations also vary in vertical layers. Great advantages in predicting tropopause wind and temperature are found (extra 3% and 15%, respectively) when MW is assimilated alone. For humidity, extra 4% skill is obtained when MW is assimilated alone. IR shows large advantages in predicting lower tropospheric variables when assimilated alone.

When verified in the summer heavy precipitation case study, MW shows better results in predicting this event. And when the model lid is raised to 10-mb, MW generates even better forecasts of near surface temperature compared to IR when assimilated alone.

7.3 Impacts of Extra Stratospheric Measurements on Regional Tropospheric Weather Forecasts

In the fact that extra stratospheric information used in the summer case study shows extra skills in predicting both temperature and heavy precipitation event when MW is assimilated alone. Chapter 6 explores the impacts of the raised model lids and the

extra stratospheric information included in the DA system on winter short-period regional weather forecasts.

Generally, the more stratospheric information, the better predictions the regional model can make. When the model lids are raised alone, positive impacts are mainly found over the initial tropopause layers while negative impacts are found in the initial lower troposphere. By including extra stratospheric information via DA systems, atmospheric states over both the tropopause and troposphere meet great improvements. Extra skills are also obtained in predictions when extra stratospheric information is brought into the system and the major improvements are also located over the tropopause layers.

A week-long prediction involving microwave observations alone are took out to investigate the impacts of microwave stratospheric measurements. The microwave measurements included in the DA system can propagate through the tropopause layers and affect the lower tropospheric predictions within 2-3 days. The microwave stratospheric measurements have more positive effects on the lower tropospheric temperature and humidity predictions after 5 days' propagation. Tropopause wind predictions also get more benefits from the stratospheric microwave information after 5 days. However, negative impacts are found over the lower stratospheric temperature predictions. An overall warmer stratosphere but cooler lower stratosphere in winter 2015 is obtained when the microwave stratospheric temperature measurements are assimilated. The warmed stratosphere then impacts the tropospheric general circulations by weaken the Hadley and Ferrel circulations. The weakened tropospheric general circulations then have impacts on the tropospheric predictions. Positive impacts are generally obtained at

the first 72-h forecast lead times. In the case study, extra 1.1% and 2.7% skills are obtained in the predictions of tropopause wind and temperature. The improvements of the tropospheric predictabilities are relatively weaker with extra 0.15% and 0.6% skills in the predictions of lower tropospheric wind and temperature. The weakened Hadley and Ferrel cell also affect the transport of air moisture. An extra 2.7% skill is obtained in the prediction of lower tropospheric RH.

Through the winter heavy precipitation case study, the extended microwave stratospheric measurements included in the DA system benefits the prediction of the heavy precipitation event. An optimized selection of the microwave channels over the regional scale is carried out using the FSO technique on regional models and the case study proved that the optimized selection of microwave channels can advantage the prediction of heavy precipitation events slightly. However, no significant improvements are found in predicting temperatures by including extended microwave stratospheric measurements.

7.4 Future Directions

This thesis aims to investigate the performance of three major DA schemes on regional NWP system, and to explore the impacts of extra stratospheric information on regional predictions of heavy precipitation events and other predictions. There are several works based on this thesis could be done in the future.

Firstly, in this thesis, the horizontal resolution of the regional model iss set at a relatively coarse resolution. Since some of the observations are very dense in the continental U. S., a finer resolution for the regional model may obtain more effective DA

results. And the DA schemes been tested in this thesis are the basic formations. More advanced DA schemes such as 4D-Var and ensemble Kalman filter-variational hybrid schemes can also be compared for predictions of different variables in different seasons. The inclusion of ensembles in DA systems showed particularly high forecast improvements. In this thesis, only 40 ensemble members are used and the preparing of the ensembles are adding random perturbations into the regional initials followed by a 6-h propagation. Do more ensemble members positively affect the DA performance? Furthermore, the deficiencies existed in the ensembles generated from regional model can greatly affect the forecast qualities especially during winter. Ensemble members with better qualities may have more positive impacts on the regional weather forecasts.

Second, the microwave and infrared satellite observations show significant different impacts on regional weather forecasts. The microwave and infrared channels can also be classified into temperature channels, water vapor channels, etc. How these different channels affect the predictions of regional corresponding atmospheric variables? Possible relations between the predictions of temperature and moisture may exist.

Finally, in chapter 7, only the impacts of stratospheric microwave channels over the continental U. S. been conducted in Hybrid scheme are investigated. For some of the stratospheric events, such as the Arctic Oscillation, are usually occurred over polar regions. For infrared satellite sensors, large amounts of information are distributed in different vertical layers. How the stratospheric infrared channels affect the tropospheric weather forecasts and how the combined stratospheric microwave and infrared information together affect the tropospheric weather forecasts. Further FSO results

investigating the infrared channels in regional scale can be obtained. In chapter 4, the EnKF scheme is proved to be more efficient in summer. How the extra stratospheric information been brought into the system via EnKF can affect the regional weather forecasts? An ensemble FSO (EFSO) technique can be applied on the reginal forecasts to investigate the impact of each channel from both microwave and infrared satellite sensors over the continental U. S. when one of the EnKF formats is used.

REFERENCES

Anderson, J. L., 2001: An ensemble adjustment Kalman Filter for data assimilation. *Mon. Wea. Rev.*, **129**, 2884-2903.

Anderson, E., and H. Jarvinen, 1998: Variational Quality Control. *Quarterly Journal Royal Met. Society*, **125 (554),** 697-722.

Anderson, E., J. Haseler, P. Courtier, G. Kelly, D. Vasiljevic, C. Brancovic, C. Cardinali, C. Gaffard, A. Hollingsworth, C. Jakob, P. Janssen, E. Klinker, A. Lanzinger, M. Miller, F. Rabier, A. Simmons, B. Strauss, J-N. Thepaut and P. Viterbo, 1998: The ECMWF implementation of three dimensional variational assimilation (3D-Var). Part III: Experimental results. *Quarterly Journal Royal Met. Society*, **124 (550)**, 1831-1860.

Andreas, P. W., M. A. Liniger, and C. Appenzeller, 2007: The Discrete Brier and Ranked Probability Skill Scores. *Mon. Wea. Rev.* **135**, 118-124.

Andrews, D. G., J. R. Holton, and C. B. Leovy, 1987: *Middle Atmosphere Dynamics.* Academic Press, 489 pp.

Badger, J., and B. J. Hoskins, 2001: Simple Initial Value Problems and Mechanisms for Baroclinic Growth. *Journal of the Atmospheric Sciences*, **58**, 38-49.

Baldwin, M. P., and T. J. Dunkerton, 1999: Propagation of the Arctic Oscillation from the Stratosphere to the Troposphere. *J. Geophys. Res.*, **104**, 30937-30946.

Baldwin, M. P., and T. J. Dunkerton, 2001: Stratospheric harbingers of anomalous weather regimes. *Science*, **294**, 581-584.

Baldwin, M. P., D. B. Stephenson, D. W. J. Thompson, T. J. Dunkerton, A. J. Charlton, and A. O'Neill, 2003: Stratospheric memory and skill of extended-range weather forecasts. *Science*, **301**, 636-640.

Bao, Y., J. J. Xu, A. M. Powell, M. Shao, J. Min, and Y. N. Pan, 2015: Impacts of AMUS-A, MHS, and IASI data assimilation on temperature and humidity forecasts with GSI-WRF over the western United States. *Atmos. Meas. Tech.*, **8**, 4231-4242.

Bergovind, P., and B. Döös, 1955: Numerical Weather map analysis. *Tellus*, **7**, 329-340.

Berri, G. J., and J. Paegle, 1990: Sensitivity of Local Predictions to Initial Conditions. *Journal of Applied Meteorology*, **29**, 256-267.

Black, R. X., B. A. McDaniel, and W. A. Robinson, 2006: Stratosphere-Troposphere Coupling during Spring Onset. *Journal of Climate*, **19**, 4891-4901.

Brewer, A. W., 1949: Evidence for a world circulation provided by the measurements of helium and water vapor distribution in the stratosphere. *Quart J. Roy. Meteor. Soc.*, **75**, 351-363, doi:10.1002/qj.49707532603.

Boville, B. A., and D. P. Baumhefner, 1990: Simulated Forecast Error and Climate Drift Resulting from the Omission of the Upper Stratosphere in Numerical Models. *Mon. Wea. Rev.*, **118**, 1517-1530.

Bouttier F., and P. Courtier, 1999: Data Assimilation concepts and methods, Meteorological Training Course Lecture Series, ECMWF

Calvo, N., R. R. Garcia, W. J. Randel, and D. R. Marsh, 2010: Dynamical mechanism for the increase in tropical upwelling in the lowermost tropical stratosphere during warm ENSO events. *Journal of the Atmospheric Science*, **67 (7)**, 2331-2340.

Caya, A., J. Sun, and C. Snyder, 2005: A Comparison between the 4DVAR and the Ensemble Kalman Filter Techniques for Radar Data Assimilation. *Mon. Wea. Rev.*, **133**, 3081-3094.

Chapman, S., 1930: On Ozone and atomic oxygen in the upper atmosphere. *Philosophical Magazine*, **10 (64)**, 369-383.

Charlton, A. J., A. O'Neill, W. A. Lahoz, and A. C. Massacand, 2004: Sensitivity of tropospheric forecasts to stratospheric initial conditions. *Q. J. R. Meteorol. Soc.*, **130**, 1771-1792.

Cohen, N. Y., E. P. Gerber, and O. Bühler, 2014: What Drives the Brewer-Dobson Circulation? *Journal of the Atmospheric Science*, **71**, 3837-3855.

Collard, A., F. Hilton, M. Forsythe, and B. Candy, 2011: From observations to forecasts – part 8: the use of satellite observations in numerical weather prediction. *Weather*, **66**, 31-36.

Collins, M., and M. R. Allen, 2002: Assessing the relative roles of Initial and Boundary Conditions in Interannual to Decadal Climate Predictability. *Journal of Climate*, **15**, 3104-3109.

Costantino, L., P. Heinrich, N. Mzé, and A. Hauchecorne, 2015: Convective gravity wave propagation and breaking in the stratosphere: comparison between WRF model simulations and lidar data. *Ann. Geophys.*, **33**, 1155-1171.

Courtier, P., E. Andersson, W. Heckley, J. Pailleux, D. Vasiljevic, M. Hamrud, A. Hollingsworth, F. Rabier and M. Fisher, 1998: The ECMWF implementation of three-dimensional variational assimilation (3D-Var). I: Formulation. *Quarterly Journal Royal Met. Society*, **124 (550)**, 1783-1807.

Cucurull, L., and R. A. Anthes, 2014: Impact of Infrared, Microwave, and Radio Occultation Satellite Observations on Operational Numerical Weather Prediction. *Mon. Wea. Rev.*, **142**, 4164-4186.

Delsole, T., 2004: Predictability and Information Theory. Part I: Measures of Predictability. *Journal of the Atmospheric Science*, **61**, 2425-2440.

Delsole, T., 2005: Predictability and Information Theory. Part II: Imperfect Forecasts. *Journal of the Atmospheric Science*, **62**, 3368-3381.

Derber, J. C., and W. S. Wu, 1998: The use of TOVS cloud-cleared radiances in the NCEP SSI analysis system. *Mon. Wea. Rev.*, **126**, 2287-2299.

Diak, G. R., 1995: Column Cloud Liquid Water Amounts for Nonprecipitating Clouds versus an "Effective Cloud Fraction" Derived from Microwave Data: A Simulation Study. *Journal of Atmospheric and Oceanic Technology*, **12**, 960-969.

Dickinson, R. E., 1968: Planetary Rossby Waves Propagating Vertically Through Weak Westerly Wind Wave Guides. *Journal of the Atmospheric Sciences*, **25**, 984-1002.

Dobson, G. M. B., 1956: Origin and distribution of the polyatomic molecules in the atmosphere. *Proc. Roy. Soc. London*, **236A**, 187-193, doi:10.1098/rspa.1956.0127.

Eliassen, A., 1954: Provisional report on calculation of spatial covariance and autocorrelation of the pressure field. *Dynamic Meteorology: Data Assimilation Methods*, L. Bengtsson, M. Ghil, and E. Kallen, Eds., Springer-Verlag, 319-330.

English, S. J., R. J. Renshaw, P. C. Dibben, A. J. Smith, P. J. Rayer, C. Poulsen, F. W. Saunders, and J. R. Eyre, 2000: A comparison of the impact of TOVS and ATOVS satellite sounding data on the accuracy of numerical weather forecasts. *Quart. J. Roy. Meteor. Soc.*, **126**, 2911–2931.

Epstein, E. S., 1969: The Role of Initial Uncertainties in Prediction. *Journal of Applied Meteorology*, **8**, 190-198.

Evensen G., 1994: Sequential data assimilation with a nonlinear quasi-geostrophic model using Monte-Carlo methods to forecast error statistics. *J. Geophys. Res.*, **99**, 10143-10162.

Evensen G., 2003: The ensemble Kalman filter: Theoretical formulation and practical implementation. *Ocean Dynamics*, **53**, 343-367.

Fu, Q., C. M. Johanson, S. G. Warren, and D. J. Seidel, 2004: Contribution of stratospheric cooling to satellite-inferred tropospheric temperature trends. *Nature*, **429**, 55-58.

Gandin, L. S., 1963: Objective Analysis of Meteorological Fields. (Translated by Israel Program for Scientific Translations).

Garcia-Moya, J.-A., A. Callado, P. Escriba, C. Santos, D. Santos-Munoz, and J. Simarro, 2011: Predictability of short-range forecasting: a multimodel approach. *Tellus*, **63(A)**, 550-563.

Garcia, R. R., and W. J. Randel, 2008: Acceleration of the Brewer Dobson circulation due to increases in greenhouse gases. *Journal of the Atmospheric Sciences*, **65 (8)**, 2731-2739.

Geber, E. P., A. Butler, N. Calvo, A. Charlton-Perez, M. Giorgetta, E. Manzini, J. Perlwitz, L. M. Polvani, F. Sassi, A. A. Scaife, T. A. Shaw, S.-W. Son, and S. Watanabe, 2012: Assessing and Understanding the Impact of Stratospheric Dynamics and Variability on the Earth System. *Bull. Amer. Meteor. Soc.*, **93**, 845-859.

Gelaro R., C. A. Reynolds, R. H. Langland, and G. D. Rohaly, 2000: A Predictability Study Using Geostationary Satellite Wind Observations during NORPEX. *Mon. Wea. Rev.*, **128**, 3789-3807.

Gibson, J. K., P. Kallberg, S. Uppala, A. Nomura, A. Hernandez, and E. Serrano, 1997: The ECMWF Re-Analysis: ERA description. ECMWF Re-Analysis Project Rep. Series, No. 1, 71pp.

Gregory, D., J. -J. Morcrette, C. Jakob, A. C. M. Beljaars, and T. Stockdale, 2000: Revision of convection, radiation and cloud schemes in ECMWF Integrated Forecasting System. *Quart. J. Roy. Meteor. Soc.*, **126**, 1685-1710.

Grise, K. M., D. W. J. Thompson, and P. M. Forster, 2009: On the Role of Radiative Processes in Stratosphere- Troposphere Coupling. *Journal of Climate*, **22**, 4154-4161.

Goncalves, L., J. Shuttleworth, S.C. Chou, Y. Xue, P. Houser, D. Toll, J. Marengo, and M. Rodell, 2006: Impact of different initial soil moisture fields on Eta model

weather forecasts for South America. *J. Geophys. Res.*, **111**, D17102, doi:10.1029/2005JD006309.

Hamiltion, K., 1993: 'The GFDL SKYHI general circulation model: some results of relevance for numerical weather prediction.' In proceedings of ECMWF workshop on Stratosphere and Numerical Weather Prediction. Reading, UK.

Hamrud, M., M. Bonavita, and L. Isaksen, 2015: EnKF and Hybrid Gain Ensemble Data Assimilation. Part I: EnKF Implementation. *Mon. Wea. Rev.*, **143**, 4847-4864.

Haynes, P. H., C. J. Marks, M. E. Mcintyre, T. G. Shepherd, and K. P. Shine, 1991: On the "Downward Control" of extratropical diabatic circulation by eddy induced mean zonal forces. *Journal of Atmospheric Sciences*, **48 (4)**, 651-678.

Hoinka, K. P., 1997: The tropopause: Discovery, definition and demarcation. *Meteorologische Zeitschrift*, **6**, 281-303.

Holton, J. R., P. H. Haynes, M. E. Mcintyre, A. R. Douglass, and R. B. Rood, 1995: Stratosphere-troposphere exchange. *Review of Geophysics*, **33 (4)**, 403-439.

Hotta, D., 2014: Proactive Quality Control Based on Ensemble Forecast Sensitivity to Observations. PhD thesis, University of Maryland.

Houekamer, P. L., and H. L. Mitchell, 1998: Data Assimilation using an ensemble Kalman Filter technique. *Mon. Wea. Rev.*, **126**, 796-811.

Hu M., H. Shao, D. Stark, K. Newman, and C. Zhou, 2015: GSI Community Version 3.4: User's Guide. *Developmental Testbed Center, National Center for Atmospheric Research, NOAA*, pp 143

Hu, S., S. Gu, X. Zhuang, and H. Luo, 2007: Automatic identification of storm cells using Doppler radars. *Acta Meteor. Sinica*, **21**, 353–365.

John, W. J., and V. H. Peter, 2006: *Atmospheric Science: an introductory survey*. Vol. 92, Academic press, 483 pp.

Justus, C. G., and A. Woodrum, 1973: Upper Atmospheric Planetary-Wave and Gravity-Wave Observations. *Journal of the Atmospheric Science*, **30**, 1267-1275.

Kalman, R. E., 1960: A New Approach to Linear Filtering and Prediction Problems. *J. Basic Eng.*, **82(1)**, 35-45.

Kalnay, E., 2003: *Atmospheric Modeling, Data Assimilation and Predictability*. Cambridge University Press, 341 pp.

Karpechko, A. Y., P. Hitchcock, D. H. W. Peters, and A. Schneidereit, 2017: Predictabilities of Downward Propagation of Major Sudden Stratospheric Warmings. *Quarterly Journal of the Royal Meteorological Society*, doi: 10.1002/qj.3017.

Kelly, G. A., P. Bauer, A. J. Geer, P. Lopez, and J. Thépaut, 2008: Impact of SSM/I observations related to moisture, clouds, and precipitation on global NWP forecast skill. *Mon. Wea. Rev*., **136**, 2713–2726.

Kleist, D. T., 2012: An evaluation of hybrid variational-ensemble data assimilation for the NCEP GFS. Ph.D dissertation, University of Maryland.

Kleist, D. T., D. F., Parrish, J. C. Derber, R. Treadon, R. M. Errico, and R. Yang, 2009a: Improving incremental balance in the GSI 3DVAR analysis system. *Mon. Wea. Rev.*, **137(3)**, 1046-1060.

Kleist, D. T., D. F. Parrish, J. C. Derber, R. Treadon, W. -S. Wu, and S. Lord, 2009b: Introduction of the GSI into the NCEP Global Data Assimilation System. *Weather & Forecasting*, **24(6)**, 1691-1705.

Klinker, E., F. Rabier, G, Kelly, and J. -F. Mahfouf, 2000: The ECMWF operational implantation of four-dimensional variational assimilation. III: Experimental results and diagnostics with operational configuration. *Quarterly Journal Royal Met. Society*, **126 (564)**, 1191-1215.

Kharin V. V., and F. W. Zwiers, 2003: On the ROC scores of Probability Forecasts. *Notes and Correspondence*, **16**, 4145-4150.

Kolstad, E. W., T. Breiteig, and A. A. Scaife, 2010: The association between stratospheric weak polar vortex events and cold air outbreaks in the Northern Hemisphere. *Q. J. R. Meteorol. Soc.*, **136 (649)**, 886-893.

Kulie, M. S., R. Bennartz, T. J. Greenwald, Y. Chen, and F. Z. Weng, 2010: Uncertainties in Microwave Properties of Frozen Precipitation: Implications for Remote Sensing and Data Assimilation. *Journal of the Atmospheric Sciences*, **67**, 3471-3487

Langland, R. H., and N. L. Baker, 2004: Estimation of observation impact using the NRL atmospheric variational data assimilation adjoint system. *Tellus*, **56(A)**, 189-201.

Lahoz, W. A., Q. Errera, R. Swinbank, and D. Fonteyn, 2007: Data Assimilation of stratospheric constituents: a review. *Atmos. Chem. Phys.*, **7**, 5745-5773.

Lee, S., and S. B. Feldstein, 2013: Detecting ozone- and greenhouse gas- driven wind trends with observational data. *Science*, **339 (6119)**, 563-567

Liao, K. N., 2002: *An Introduction to Atmospheric Radiation*. Academic press, 583 pp.

Lord, S., G. Gavno, and F. L. Yang, 2016: Analysis of an Observing System Experiment for the Joint Polar Satellite System. *Bulletin of the American Meteorological Society*, **97(8)**, 1409-1425.

Lorenc, A. C., 1981: A global three-dimensional multivariate statistical analysis scheme. *Mon. Wea. Rev.*, **109**, 701-721.

Lorenc, A. C., 1986: Analysis methods for numerical weather prediction. *Q. J. R. Meteorol. Soc.*, **112**, 1177-1194.

Lorenc, A. C., N. E. Bowler, A. M. Clayton, S. R. Pring, and D. Fairbairn, 2015: Comparison of Hybrid-4DEnVar and Hybrid-4DVar Data Assimilation Methods for Global NWP. *Mon. Wea. Rev.*, **143**, 212-229.

Mahouf, J.-F., and F. Rabier, 2000: The ECMWF operational implantation of four-dimensional variational assimilation. II: Experimental results with improved physics. *Quarterly Journal Royal Met. Society*, **126 (564)**, 1171-1190.

Mahfouf, J.-F., P. Bauer, and V. Marécal, 2005: The assimilation of SSM/I and TMI rainfall rates in the ECMWF 4D-Var system. *Quart. J. Roy. Meteor. Soc.*, **131**, 437–458, doi:10.1256/qj.04.17.

Matsuno, T., 1971: A dynamical model of stratospheric warmings. *J. Atmos. Sci.*, **27**, 871-883.

Mears C. A., and F. J. Wentz, 2008: Construction on the Remote Sensing System V3.2 Atmospheric Temperature Records from the MSU and AMSU Microwave Sounders. *Journal of Atmospheric and Oceanic Technology*, **26**, 1040-1056

Meng, Z. Y., and F. Q. Zhang, 2008: Tests of an Ensemble Kalman Filter for Mesoscale and Regional-Scale Data Assimilation. Part III: Comparison with 3DVAR in a Real-Data Case Study. *Mon. Wea. Rev.*, **136**, 522-540.

Meng, Z. Y., and F. Q. Zhang, 2011: Limited-Area Ensemble-Based Data Assimilation. *Mon. Wea. Rev.*, **139**, 2025-2045.

Migliorini, S., C. Piccolo, and C. D. Rodgers, 2008: Use of the Information Content in Satellite Measurements for an Efficient Interface to Data Assimilation. *Mon. Wea. Rev.*, **136**, 2633-2650.

Mueller, B., S.I. Seneviratne, C. Jimenez, T. Corti, M. Hirschi, G. Balsamo, A. Beljaars, A.K. Betts, P. Ciais, P. Dirmeyer, J.B. Fisher, Z. Guo, M. Jung, C.D. Kummerow, F. Maignan, M.F. McCabe, R. Reichle, M. Reichstein, M. Rodell, W.B. Rossow, J. Sheffield, A. J. Teuling, K. Wang, and E.F. Wood, 2011: Evaluation of global observations-based evapotranspiration datasets and IPCC AR4 simulations, Geophys. Res. Lett., 38, L06402, doi:10.1029/2010GL046230,

Norton, W. A., 2006: Tropical wave driving of the annual cycle in tropical tropopause temperatures. Part II: model results. *Journal of the Atmospheric Sciences*, **63 (5)**, 1420-1431.

Ott, E., B. R. Hunt, I. Szunyogh, and J. A. Yorke, 2004: A Local Ensemble Kalman Filter for atmospheric data assimilation. *Tellus*, **56**, 415-428.

Parrish, D. F., and J. C. Derber, 1992: The National Meteorological Center's Spectral Statistical-Interpolation Analysis System. *Mon. Wea. Rev.*, **120**, 1747-1763.

Prigent, C., J. R. Pardo, and W. B. Rossow, 2006: Comparisons of the Millimeter and Submillimeter Bands for Atmospheric Temperature and Water Vapor Soundings for Clear and Cloudy Skies. *Journal of Applied Meteorology and Climatology*, **45**, 1622-1633.

Rabier, F., A. McNally, E. Andersson, P. Courtier, P. Unden, J. Eyre, A. Hollingsworth and F. Bouttier, 1998: The ECMWF implementation of three-dimensional variational assimilation (3D-Var). II: Structure Function. *Quarterly Journal Royal Met. Society*, **124 (550)**, 1809-1829.

Rabier, F. H. Jarvinen, E. Klinker, J.-F. Mahfouf and A. Simmons, 2000: The ECMWF operational implantation of four-dimensional variational assimilation. I: Experimental results with simplified physics. *Quarterly Journal Royal Met. Society*, **126 (564)**, 1143-1170.

Rabier, F. H., 2005: Overview of global data assimilation developments in numerical weather-prediction centers. *Q. J. R. Meteorol. Soc.*, **131**, 3215-3233.

Rajedran, K., A. Kitoh, R. Mizuta, S. Sajani, and T. Nakazawa, 2007: High-Resolution Simulation of Mean Convection and Its Intraseasonal Variability over the Tropics in the MRI/JMA 20-km Mesh AGCM. *Journal of Climate*, **21**, 3722-3739.

Reinecke P. A., and D. R. Durran, 2009: Initial-Condition Sensitivities and the Predictability of Downslope Winds. *Journal of the Atmospheric Sciences*, **66**, 3401-3418.

Reiter, E. R., and L. F. Whitney, 1969: Interaction between subtropical and polar-front jet stream. *Mon. Wea. Rev.*, **97**, 432-438.

Rodell, M., P. R. Houser, U. Jambor, J. Gottschalck, K. Mitchell, C. -J. Meng, K. Arsenault, B. Cosgrove, J. Radakovich, M. Bosilovich, J. K. Entin, J. P. Walker, D. Lohmann, and D. Toll, 2004: The Global Land Data Assimilation System. *Bull. Amer. Meteor. Soc.*, **85(3)**, 381-394.

Rood R. B., 2005: Assimilation of stratospheric meteorological and constituent observations: A Review. SPARC Newsletter No. 25, July.

Saito, K., T. Fujita, Y. Yamada, J. -I. Ishida, Y. Kumagai, K. Aranami, S. Ohmori, R. Nagasawa, S. Kumagai, C. Muroi, T. Kato, H. Eito, and Y. Yamazaki, 2006: The Operational JMA Nonhydrostatic Mesoscale Model. *Mon. Wea. Rev.*, **134**, 1266-1298.

Sasaki, Y. K., and J. S. Goerss, 1982: Satellite Data Assimilation Using NASA Data Systems Test 6 Observations. *Mon. Wea. Rev.*, **110**, 1635-1644.

Sato, K., and M. Nomoto, 2015: Gravity Wave-Induced Anomalous Potential Vorticity Gradient Generating Planetary Waves in the Winter Mesosphere. *Journal of the Atmospheric Science*, **72**, 3609-3624.

Schwaerz, M., G., Kirchengast, 2003: Joint Temperature, Humidity, and Sea Surface Temperature Retrieval from IASI Sensor Data. *The thirteenth International TOVS Study Conference*, 558-567.

Schwartz, C. S., J. S. Kain, S. J. Weiss, M. Xue, D. R. Bright, F. Kong, K. W. Thmoas, J. J. Levit, and M. C. Coniglio, 2009: Next-Day Convection-Allowing WRF Model Guidance: A Second Look at 2-km versus 4-km Grid Spacing. *Mon. Wea. Rev.*, **137**, 3351-3372.

Schwartz, C. S., Z. Liu, X. -Y. Huang, Y. -H. Kuo, and C. -T. Fong, 2013: Comparing Limited-Area 3DVAR and Hybrid Variational-Ensemble Data Assimilation Methods for Typhoon Track Forecasts: Sensitivity to Outer Loops and Vortex Relocation. *Mon. Wea. Rev.*, **141**, 4350-4372.

Scott, K. A., M. Buehner, A. Caya, and T. Carrieres, 2012: Direct Assimilation of AMSR-E Brightness Temperatures for Estimating Sea Ice Concentration. *Mon. Wea. Rev.*, **140**, 997-1013.

Sela, J., 1980: Spectral modeling at the National Meteorological Center. *Mon. Wea. Rev.*, **108**, 1279-1292.

Sela, J., 1982: The NMC Spectral Model, NOAA Technical Report, NWS-30, 36pp.

Simmons, A. J., and A. Hollingsworth, 2002: Some aspects of the improvement in skill of numerical weather prediction, *Q. J. R. Meteorol. Soc.*, **128**, 647-677.

Skamarock W. C., J. B. Klemp, J. Dudhia, D. O. Gill, D. M. Barker, M. G. Duda, X. Y. Huang, W. Wang, J. G. Powers, 2008: "A Description of the Advanced Research WRF Version 3", *Mesoscale and Microscale Meteorology Division and National Center for Atmospheric Research*, 124pp.

Sjoberg, J. P., and T. Birner, 2012: Transient tropospheric forcing of sudden stratospheric warmings. *Journal of the Atmospheric Sciences*, **69**, 3420-3432

Smith, N., W. L. Smith Sr., E. Weisz, and H. Revercomb, 2015: AIRS, IASI, and CrIS Retrieval Records at Climate Scales: An Investigation into the Propagation of Systematic Uncertainty. *Journal of Applied Meteorology and Climatology*, **54**, 1465-1481

Solonen, A., A. Bidov, J. M. Bardsley, and H. Haario, 2014: Optimization-Based Sampling in Ensemble Kalman Filtering. *International Journal for Uncertainty Quantification*, **4(4)**, 349-364.

Staelin, D. H., K. F. Kunzi, R. L. Pettyjohn, R. K. L. Poon, and R. W. Wilcox, 1976: Remote Sensing of Atmospheric Water Vapor and Liquid Water with the Nimbus 5 Microwave Spectrometer. *Journal of Applied Meteorology*, **15**, 1204-1214.

Stocker, T. F., et al., 2001: Intergovernmental Panel on Climate Change (IPCC) Climate Change. Tech. Rep., 417-457.

Stohl, A., H. Wernli, P. James, M. Bourqui, C. Forster, M. A. Liniger, P. Seibert, and M. Sprenger, 2003: A New Perspective of Stratosphere-Troposphere Exchange. *Bulletin of the American Meteorological Society*, **84(11)**, 1565-1573.

Storch, H. V., H. Langenberg, and F. Feser, 2000: A Spectral Nudging Technique for Dynamical Purposes. *Mon. Wea. Rev.*, **128**, 3664-3673.

Swnbank, R., and A. O'Neill, 1994: A Stratosphere-Troposphere Data Assimilation System. *Mon. Wea. Rev.*, **122**, 686-702.

Thépaut, J. -N., 2003: Satellite data assimilation in numerical weather prediction: An overview. *Proc. Seminar on Recent Developments in Data Assimilation for Atmosphere and Ocean*, Reading, United Kingdom, ECMWF, 75-95.

Tobin, D. C., H. E. Revercomb, C. C. Moeller, and T. S. Pagano, 2006: Use of Atmospheric Infrared Sounder high-spectral resolution spectra to access the calibration of Moderate Resolution Imaging Sepctroradiometer on EOS Aqua. *Journal of Geophysics Research*, **111**, D09S05, doi:10.1029/2005JD006095.

Torn, R. D., 2010: Performance of a Mesoscale Ensemble Kalman Filter (EnKF) during the NOAA High-Resolution Hurricane Test. *Mon. Wea. Rev.*, **138**, 4375-4392.

Uhlmann, J. K., 1992: Algorithms for multiple target tracking. *American Scientist*, **80(2)**, 128-141.

Wan, Q. L., and J. J. Xu, 2011: A numerical study of the rainstorm characteristics of the June 2005 flash flood with WRF/GSI data assimilation system over south-east China. *Hydrological Processes*, **25(8)**, 1327-1341.

Wan, Q. L., J. J. Xu, and J. H. He, 2009: Impacts of ATVOS Data Assimilation on Prediction of a Rainstorm over Southeast China. *Journal of Tropical Meteorology*, **15(2)**, 155-161.

Wang, L., and C. Cao, 2008: On-orbit calibration assessment of AVHRR longwave channels on MetOp-A using IASI. *IEEE Trans. Geosci. Remote Sen.*, **46**, 4005-4013.

Wang, L., C. Cao, and M. Goldberg, 2009: Intercalibration of GOES-11 and GOES-12 water vapor channels with MetOp IASI hyperspectral measurements. *J. Atmos. Oceanic Technol.*, **26**, 1843-1855.

Wang, F., L. Wang, T. Koike, H. Zhou, K. Yang, A. Wang, and W. Li, 2011: Evaluation and application of a fine-resolution global data set in a semiarid mesoscale river basin with a distributed biosphere hydrological model. *J. Geophys. Res.*, **116**, D21108, doi:10.1029/2011JD015990

Wang, W., C. Bruyere, M. Duda, J. Dudhia, D. Gill, M. Kavulich, K. Keene, H. C. Lin, J. Michalakes, S. Rizvi, X. Zhang, J. Berner, S. Ha, and K. Fossell, 2016: "ARW Version 3 Modeling System User's Guide". *Mesoscale and Microscale Meteorology Division and National Center for Atmospheric Research*, 361pp.

Wang, X. G., D. Parrish, D. Kleist, and J. Whitaker, 2013: GSI 3DVar-based Ensemble-Variational Hybrid Data Assimilation for NCEP Global Forecast System: Single-Resolution Experiments. *Mon. Wea. Rev.*, **141**, 4098-4117.

Waters, J. W., 1975: Remote Sensing of Atmospheric Temperature Profiles with the Nimbus 5 Microwave Spectrometer. *Journal of the Atmospheric Sciences*, **32**, 1953-1969.

Weng, F. Z., X. Zou, X. Wang, S. Yang, and M. D. Goldberg, 2012: Introduction to Suomi national polar-orbiting partnership advanced technology microwave sounder for numerical weather prediction and tropical cyclone applications. *Journal of Geophysical Research*, **117**, D19112, doi:10.1029/2012JD018144.

Wootten, A., J. H. Bowden, R. Boyles, and A. Terando, 2016: The Sensitivity of WRF Downscaled Precipitation in Puerto Rico to Cumulus Parameterization and Interior Grid Nudging. *Journal of Applied Meteorology and Climatology*, **55**, 2263-2281.

Wu D., J. Qu, and X.- J. Hao, 2015: Agricultural drought monitoring using MODIS based drought indices over the Corn Belt. *International Journal of Remote Sensing*, **36(21)**, 5403-5425

Wu, W. S., R. J. Purser, and D. F. Parrish, 2002: Three-dimensional variational analysis with spatially inhomogeneous covariance. *Mon. Wea. Rev.*, **130**, 2905-2916.

Xu, J., S. Rugg, M. Horner, and L. Byerle, 2009: Application of ATVOS Radiance with ARW WRF/GSI Data Assimilation System in the Prediction of Hurricane Katrina. *The Open Atmospheric Science Journal*, **3**, 13-28.

Xu, J. J., and A. M. Powell Jr, 2012: Dynamical downscaling precipitation over Southwest Asia: Impacts of radiance data assimilation on the forecasts of the WRF-ARW model. *Atmospheric Research*, **111**, 90-103.

Xu, J. J., and A. M. Powell Jr, 2015: Extreme events of stratospheric stationary waves and indications for stratosphere-troposphere coupling: simultaneous analysis in boreal winter. *Theoretical and Applied Climatology*, **120(3)**, 661-671.

Yamaguchi, M., T. Iriguchi, T. Nakazawa, and C. -C. Wu, 2009: An Observing System Experiment for Typhoon Conson (2004) Using a Singular Vector Method and DOTSTAR Data. *Mon. Wea. Rev.*, **137**, 2801-2816.

Yang, H., 2015: Dynamic Coupling and Chemical Transport Between the stratosphere and the Troposphere, PhD thesis, Cornell University.

Zhu, Y-Q, and R. Gelaro, 2008: Observation Sensitivity Calculations Using the Adjoint of the Gridpoint Statistical Interpolation (GSI) Analysis System. *Mon. Wea. Rev.*, **136**, 335-351.

Zou X. L., F. Z. Weng, and H. Yang, 2014: Connecting the Time Series of Microwave Sounding Observations from AMSU to ATMS for Long-Term Monitoring of Climate. *Journal of Atmospheric and Oceanic Technology*, **31**, 2206-2222.

Zou, X. L., Z. K. Qin, and F. Z. Weng, 2011: Improved coastal precipitation forecasts with direct assimilation of GOES-11/12 imager radiances. *Mon. Wea. Rev.*, **139**, 3711-3729.

Zou, X. L., Z. K. Qin, and F. Z. Weng, 2013: Improved Quantitative Precipitation Forecasts by MHS Radiance Data Assimilation with a Newly Added Cloud Detection Algorithm. *Mon. Wea. Rev.*, **141**, 3203-3221.

BIOGRAPHY

Min Shao was born in Dongtai, Jiangsu province, P. R. China. He received his Bachelor degree of Atmospheric Science from Nanjing University in 2011 and his Master degree of Environmental Science from Nanjing University in 2013. He joined the Ph.D. program of Earth Systems and Geoinformation Sciences at George Mason University in 2013. He was employed for 4 years as a graduate research assistant under the instruction of Dr. John J. Qu. His research area at the time of this dissertation is about integrated remote sensing and numerical weather models in coupling stratosphere-troposphere for better tropospheric weather forecasts such as heavy precipitation events.